Density split statistic in cosmic shear surveys: Generalisations and its application to the Kilo Degree Survey

DISSERTATION

zur
Erlangung des Doktorgrades (Dr. rer. nat.)
der
Mathematisch-Naturwissenschaftlichen Fakultät
der
Rheinischen Friedrich-Wilhelms-Universität Bonn

vorgelegt von
Pierre Alexander Burger
aus
Bad Honnef, Deutschland

Bonn, September 2022

Angefertigt mit Genehmigung der Mathematisch-Naturwissenschaftlichen Fakultät
der Rheinischen Friedrich-Wilhelms-Universität Bonn

1. Gutachter:	Prof. Dr. Peter Schneider
2. Gutachter:	Prof. Dr. Cristiano Porciani

Tag der Promotion:	07. März 2023
Erscheinungsjahr:	2023

For my parents

Abstract

Understanding the formation and evolution of the Universe's large-scale structure are fundamental in modern cosmology. Currently, the most accurate model to describe the LSS and other observations like the cosmic microwave background (CMB) is the so-called Λ Cold Dark Matter model (ΛCDM), which is therefore considered the standard model of cosmology.

An ideal tool to measure the total matter distribution in the Universe is gravitational lensing, which describes how massive objects, regardless of the matter's nature, bend light rays and distort the images of distant objects.

To extract the non-Gaussian information, Gruen et al. (2016) introduced the density split statistic (DSS). The DSS measures the mean tangential shear around line-of-sights of similar galaxy densities. Since the galaxy densities trace the matter densities, the tangential shear correlates strongly with the galaxy distribution in a manner that varies with cosmology. Therefore, the DSS captures information from the number of foreground galaxies in each density bin and the shape and amplitude of the shear profiles.

In the first part of this thesis, we construct a general filter function, which is used to smooth the galaxy density field. The filter function is adapted to the shear pattern. We find that the adapted filter yields a better correlation between the total matter and the galaxy distribution and a larger signal-to-noise ratio than the previously used top-hat filter function. The latter eases the detection of the shear signals compared to the previously used top-hat filter functions making them more suitable for real data analyses.

In the second part, we modify the analytical DSS model described in Friedrich et al. (2018) to general filter functions. Similar to the previous DSS model, we build on log-normal approximations of large deviation theory approaches to model the matter density probability distribution function and on perturbative calculations of higher-order moments of the density field.

In the third part, we validate the modified DSS model against several simulations. This validation reveals that the analytical model is accurate for stage III surveys like the fourth data release of the Kilo-Degree Survey (KiDS-1000). Furthermore, we find that the model is robust against baryonic feedback and intrinsic alignment.

In the last part, we perform a cosmological analysis of KiDS-1000 based on the DSS. The image shapes are taken from the fourth and fifth tomographic bin of KiDS-1000, and the foreground galaxy sample is constructed from a bright galaxy sample. After marginalising over the photometric redshift uncertainty and the residual shear calibration bias, we measure a structure growth parameter of $S_8 \equiv \sigma_8\sqrt{\Omega_\mathrm{m}/0.3} = 0.74^{+0.03}_{-0.02}$ that is competitive too and consistent with two-point cosmic shear results, a matter density of $\Omega_\mathrm{m} = 0.27 \pm 0.02$, and a constant galaxy bias of $b = 1.32^{+0.12}_{-0.11}$.

In conclusion, although higher-order statistics are complicated to model and usually rely on cosmological simulations, we show that the generalised model of the DSS is a powerful cosmological tool with a significant advantage in breaking the Ω_m-σ_8 degeneracy.

Contents

1

Introduction

> *'One of the basic rules of the universe is that nothing is perfect. Perfection simply doesn't exist. Without imperfection, neither you nor I would exist.'*
>
> Stephen Hawking.

The origin of astronomy dates back to ancient cultures like Mesopotamia, China and Central America. Back then, the Earth was believed to be the centre of the Universe, while all visible objects like the Sun, the Moon or the planets revolve around it. Since the telescope had not yet been invented, astronomy was concerned only with observing and predicting the motion of objects visible to the naked eye.

The scientific revolution of astronomy began with scientists like Galileo Galilei or Johannes Kepler using telescopes to observe objects in the sky. Kepler was the first to prove that planets move on elliptical orbits rather than circular and formulated his famous laws of planetary motion. However, it was not possible for him to formulate a theory behind the laws he wrote down. Isaac Newton, with his laws of gravitation published in Philosophiæ Naturalis Principia Mathematica in 1687 (Newton, 1966) made the motions of celestial bodies predictable based on first mathematical principles.

Newton's law of gravity was the dominant scientific description of gravitation until it was replaced by general relativity (GR) formulated by Einstein (1915). In GR, gravitation is described as a geometric property of space and time. It is, until today, the most accurate description of gravitation in modern physics. The first breakthrough of GR was the observation of Sir Arthur Eddington and Sir Frank Watson Dyson, who compared the apparent positions of stars in the Hyades cluster during the Solar eclipse of 1919 to the position of the stars at night. This was the first detection of a gravitational lensing effect (Dyson et al., 1920). Although such light deflection can also be estimated in the Newtonian description, its prediction differs by a factor of two from that in GR. Since the observation agreed with the prediction of GR, nothing could stop the triumph of GR. Another recent success of GR was the first image of a black hole at the centre of the galaxy Messier 87 shown in Fig. 1.1, measured by the Event Horizon Telescope (EHT). Before this image was taken, the existence of black holes (Schwarzschild, 1916) could only be shown indirectly, for instance, by measuring the stellar orbits around a black hole (Gillessen et al., 2009) or by the measurements of gravitational waves (Abbott et al.,

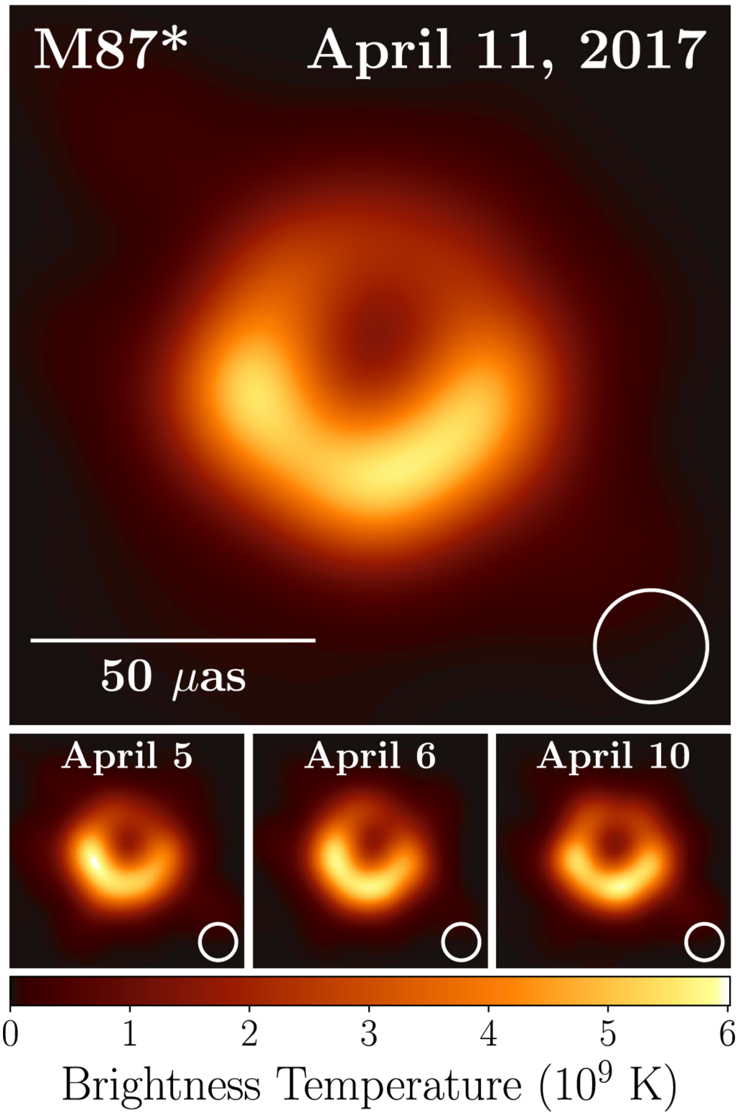

Figure 1.1: EHT image of M87* in units of brightness temperature. At the bottom, images of M87* are shown, which are measured on different days, showing the equivalence among different days. Figure taken from Event Horizon Telescope Collaboration: Akiyama et al. (2019).

2016). Gravitational waves are also predicted by GR and are distortions of space-time that can be created by collisions of black holes or neutron stars.

In modern astronomy, one differs between astrophysics, which employs the nature of the astronomical objects rather than their positions or motions in space, and cosmology, which studies the Universe as a whole.

The currently best cosmological model is the so-called ΛCDM model, which can describe many observations like the cosmic microwave background (CMB) first detected by Penzias and Wilson (1965), the abundance of Helium (Peebles, 1966) and other elements (Wagoner et al., 1967), and the existence and scale of baryonic acoustic oscillations (BAOs; Cole et al., 2005; Eisenstein et al., 2005). It assumes that the Universe contains baryonic matter[1] and dark matter. This "visible" baryonic matter, which accumulates in stars, gases, and planets, makes up only a tiny fraction (about 5%) of the total energy-matter content of the Universe. Nearly 75% of the energy-matter budget consists of a poorly understood dark energy, which accounts for the observed accelerated expansion of the Universe (Peebles and Ratra, 2003). The rest consists of matter that acts only gravitationally and is therefore invisible, which gives it the name dark matter.

The first hint of dark matter was found by measuring the velocities of galaxies in the Coma cluster (Zwicky, 1933). The visible mass estimated from the luminosity of the galaxies is insufficient to explain the high galaxy velocities, so Zwicky concluded that the cluster must contain an additional invisible mass component. Furthermore, the study of Rubin et al. (1980) found that the rotational velocities of stars inside spiral galaxies stay almost constant for large radii, which could only be explained by an additional invisible mass component.

One of the biggest successes of the ΛCDM model is its remarkable agreement with the observation of the CMB measured by the Planck satellite (Planck Collaboration: Aghanim et al., 2020). The CMB is a relic of the early Universe, where the Universe cooled enough such that photons decoupled for the first time from the baryonic matter. Since the temperature fluctuations of these CMB photons reflect the baryonic distribution directly, they give a snapshot of the Universe approximately 380 000 years after the Big Bang.[2] Based on the theory of gravitational instability for structure growth, one expects for a Universe without dark matter that the temperature fluctuations $\Delta T/T \sim 10^{-3}$. However, one finds that temperature fluctuations $\Delta T/T \sim 10^{-5}$, which can only be explained if the baryonic matter falls into potential wells that the dark matter formed before the decoupling of photons and baryons. Since the CMB is very well described as a Gaussian random field, two-point statistics like the two-point correlation functions or its Fourier counterparts, the power spectra, are excellent for extracting all information of the CMB.

In the late Universe, however, a significant amount of non-Gaussian features are generated by non-linear gravitational instabilities, whose information can only be completely extracted with higher-order statistics. An ideal tool to investigate the local (or late) Universe is gravitational lensing (Bartelmann and Schneider, 2001), which describes the deflection of light by massive objects, regardless of the nature of matter. However, even for the late Universe, most studies use second-order statistics both for weak lensing and galaxy clustering analyses because of their accurate theoretical description and control over systematic inaccuracies (see, e.g. Joudaki et al., 2018; Hamana et al., 2020; Asgari et al., 2021; DES Collaboration: Abbott et al., 2022; Amon et al., 2022, for recent analyses). With the ever-increasing accuracy of cosmological parameters, tensions arose between observations of the early and late Universe. Besides other interesting tensions, the most interesting tension for gravitational lensing manifests in the matter clustering parameter $S_8 = \sigma_8\sqrt{\Omega_\mathrm{m}/0.3}$, where it seems that the local Universe is less clustered than observations of the CMB suggest (Hildebrandt et al., 2017; Joudaki et al., 2020; Heymans et al., 2021; Di Valentino et al., 2021b).

---

[1] The cosmological convention is that all visible matter like neutrons, protons, and electrons is ‘baryonic’, even though electrons are leptons.

[2] The Big Bang is considered as the beginning of space and time.

One way to understand these tensions in more detail is to use higher-order statistics as they scale differently with cosmological parameters, which makes them very valuable to increase the constraining power on cosmological parameters (see, e.g. Kilbinger and Schneider, 2005; Bergé et al., 2010; Pires et al., 2012; Fu et al., 2014; Pyne and Joachimi, 2021), and to verify second-order statistic results. A model has to be constructed to access the information in higher-order statistics, which is usually more challenging, but can be done through simulations (Harnois-Déraps et al., 2021; Zürcher et al., 2022) or from analytical calculations (Reimberg and Bernardeau, 2018; Barthelemy et al., 2021). The simulation-based approach has the advantage that every measurable statistic can be modelled as long as enough simulations with varying cosmologies are available and the incorporation of critical systematic effects such as the intrinsic alignment (IA) of galaxies (Joachimi et al., 2015) or baryonic processes with hydro-dynamical simulations do not need complicated analytical modelling. However, if derivable, analytical models help to understand the underlying properties of the cosmic large-scale structure (LSS) and are usually faster to compute at any point in the cosmological parameter space. In Fig. 1.2 an image taken by the James Webb Space Telescope, which is about the size of a grain of sand when viewed at an arm's length distance, nicely demonstrates the LSS and the vast amount of galaxies that can be found in the Universe.

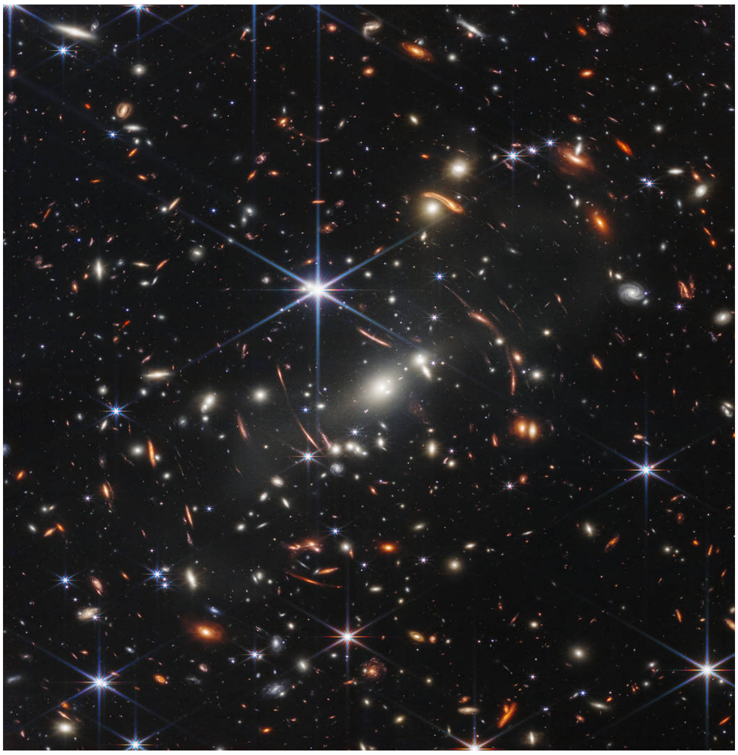

Figure 1.2: A $(2'.2)^2$ image taken by the James Webb Space Telescope (Pontoppidan et al., 2022), showing the galaxy cluster SMACS 0723. It is clearly seen how the massive foreground galaxy cluster distorts the image shapes of many background galaxies. Credit: NASA, ESA, CSA, STScI

One higher-order statistic was introduced by Gruen et al. (2016) and is called density split statistic (DSS). The idea of the DSS is to measure the mean tangential shear around sub-areas of the survey with similar foreground galaxy densities. High galaxy density regions generally trace large matter over-density regions, which result in higher tangential shear signals that vary with cosmology. Therefore, the DSS captures information from the shape and amplitude of the shear profiles and the distribution of the galaxy density field. Friedrich et al. (2018, hereafter F18) introduced an analytical model for the DSS that predicts the mean tangential shear profiles and the probability density function (PDF) of the galaxy counts in each mass density bin for a given cosmology by just providing it with the mean foreground galaxy density, and redshift distributions of the foreground and background galaxies. The F18 model was then used in Gruen et al. (2018, hereafter G18) to constrain cosmological parameters from measurements of the Dark Energy Survey (DES) First Year and Sloan Digital Sky Survey (SDSS) data, yielding results competitive with the main DES second-order analysis (Abbott et al., 2018).

The prime motivation for this work is to improve the filter function of the DSS, which we achieve by developing a pair of filter functions for the aperture mass and aperture number (see Schneider, 1996, 1998). These two statistics are strongly correlated if the local galaxy density distribution is proportional to the local matter density distribution. We adapt the filter functions to shear signals measured in the Millenium simulation (MS), giving it the name ‘adapted’ filter functions.

In the second part of this thesis, we modify the analytical model by F18 to general filter functions. As in the F18 model, we build on log-normal approximations to model the matter density probability distribution function and on perturbative calculations of higher-order moments of the density field.

The last part of this thesis consists of validating the analytical model on several simulations containing IA, baryonic feedback process, different redshift distributions and galaxy bias models. After showing that the model is accurate for Stage III surveys, we perform the first cosmological inference of Kilo-Degree Survey (KiDS) data using the DSS. To construct our foreground density maps, we use the dense sample of bright galaxies presented in Bilicki et al. (2021) and compute the tangential shear from the lensing catalogue constructed from the fourth data release of the Kilo-Degree Survey (KiDS-1000).

This work is structured as follows:

- In chapter 2, we review the cosmological standard model and cosmic structure formation, introduce the concepts of gravitational lensing and review the statistical methods we use.
- In chapter 3, we review all the observed and simulated data used in this work.
- The development of the adapted filter is done in chapter 4.
- The generalized model is described in chapter 5.
- The validation of the analytical model is done in chapter 6.
- In chapter 7, we show our results of the KiDS-1000 analysis.
- Chapter 8 concludes this thesis with a summary of our results and an outlook for future research.

Theoretical background

2

This chapter reviews the basics of cosmology and the usage of the gravitational lensing effect to explore the relationship between galaxies and the matter distribution of the Universe. The formation and evolution of galaxies and their relationship to the underlying dark matter depend on the cosmological model describing the dynamics of the Universe, the formation of the dark matter structure itself, and physical processes affecting only baryons. All three ingredients must be understood for measuring and modelling the DSS, whereas the baryonic processes are subdominant on the scales we are investigating later.

In Sec.2.1, we review the standard model of cosmology, cosmological distances, the formation of the LSS, and galaxy formation. We introduce the gravitational lensing effect and the DSS in Sect. 2.2. Finally, we give in Sect. 2.3.2 an overview of the statistical methods used in this work.

2.1 Cosmology

Cosmology is the science of the origin, evolution and future of the Universe. Common tasks of a cosmologist are to answer questions about the origin of the LSS of the universe or the age of the universe, and some cosmologists even try to answer what was before the birth of the universe, although this is rather a philosophical question. To answer the former questions, a fundamental theoretical description is needed.

2.1.1 Cosmological standard model

The current understanding of cosmology is based on the theory of GR by Einstein (1915), which describes space-time as a four-dimensional manifold, where gravitational attraction is a consequence of the curvature of space-time due to the energy and mass that is present inside the system. Mathematically this relation is described by Einstein's field equations

$$R_{\mu\nu} - \frac{R}{2} g_{\mu\nu} = \frac{8\pi G}{c^4} T_{\mu\nu} + \Lambda g_{\mu\nu} \ , \tag{2.1}$$

where $R_{\mu\nu}$ is the Ricci tensor describing the curvature of space-time and its trace being the Ricci scalar R. The space-time metric is $g_{\mu\nu}$ describing the spatial and temporal distances and local inertial frames. It also determines the world lines of freely falling particles or light rays (geodesics). Lastly, the energy-momentum tensor $T_{\mu\nu}$ describes the energy content of the Universe, G is the Newtonian gravitational constant, and Λ is the cosmological constant or energy density of the vacuum if written on the left side of Eq. (2.1).

Assumptions need to be made to solve these ten coupled non-linear differential equations. In cosmology, the *cosmological principle* is used. It states that the Universe is spatially *isotropic* on large angular scales[1] and that no place in the cosmos is privileged over any other place. It then follows directly that the Universe is *homogeneous*.

The distribution of galaxies or the temperature fluctuations of the CMB nicely demonstrates the isotropy of the cosmic matter distribution (Eisenstein et al., 2011; Planck Collaboration: Aghanim et al., 2020). Homogeneity is challenging to test because it is impossible to study the entire Universe at a fixed time or verify observers' measurements at other points in space. However, it is reasonable to assume that our spatial position is not unique so that the observed statistical properties are the same for the entire Universe.

The space-time for a homogeneous and isotropic universe is described by the Robertson-Walker metric (Robertson, 1935; Walker, 1937). In this idealised case the line element $\mathrm{d}s$, is the separation between two space-time points at (t, w, θ, ϕ) and $(t + \mathrm{d}t\,, w + \mathrm{d}w\,, \theta + \mathrm{d}\theta\,, \phi + \mathrm{d}\phi)$ as

$$\mathrm{d}s^2 = g_{\mu\nu}\mathrm{d}x^\mu \mathrm{d}x^\nu = -c^2\,\mathrm{d}t^2 + a^2(t)\left[\mathrm{d}\chi^2 + f_K^2(\chi)\left(\mathrm{d}\theta^2 + \sin^2(\theta)\;\mathrm{d}\phi^2\right)\right]\;. \tag{2.2}$$

Here, t is the cosmic time, $a(t)$ the cosmic scale factor which describes the expansion of the Universe observed by Hubble (1929) normalized that today $a(t_0) = 1$ and $a \longrightarrow 0$ at early times, χ is the comoving radial distance, θ and ϕ are angular coordinates. The comoving angular diameter distance

$$f_K(\chi) = \begin{cases} \frac{1}{\sqrt{K}}\;\sin\!\left(\sqrt{K}\,\chi\right) & \text{for } K > 0 \\ \chi & \text{for } K = 0 \\ \frac{1}{\sqrt{-K}}\;\sinh\!\left(\sqrt{-K}\,\chi\right) & \text{for } K < 0 \end{cases}\;, \tag{2.3}$$

where K describes the spatial curvature of the Universe, with a positive K corresponding to a closed (or positively curved) universe, $K = 0$ to flat space and a negative K to an open (or negatively curved) Universe.

Inserting the metric $g_{\mu\nu}$ given in Eq. (2.2) into Eq. (2.1) and using that for an ideal fluid with density ρ, pressure p and four-velocity u the energy momentum tensor

$$T_{\mu\nu} = \left(\rho + \frac{p}{c^2}\right)\,u_\mu\,u_\nu + p\,g_{\mu\nu}\;, \tag{2.4}$$

---

[1] Large scales are usually meant by scales larger than hundreds of Megaparsecs.

the Friedmann equations (Friedmann, 1922) follow to

$$\frac{8\pi\,\mathrm{G}}{3}\rho - \frac{K\,c^2}{a^2} + \frac{\Lambda\,c^2}{3} = \left(\frac{\dot{a}}{a}\right)^2 = H^2(a)\;, \tag{2.5}$$

$$-\frac{4\pi\,\mathrm{G}}{3}\left(\rho + 3\,\frac{p}{c^2}\right) + \frac{\Lambda\,c^2}{3} = \frac{\ddot{a}}{a}\;. \tag{2.6}$$

These equations describe the Universe's dynamics and expansion history, where $H = \frac{\dot{a}}{a}$ is the Hubble parameter determining the expansion rate. Its current value is the Hubble constant H_0. Interestingly, the actual value is uncertain, since early Universe measurements like the CMB or BAOs measure a value of $H_0 \approx 68\,\mathrm{km\,s^{-1}\,Mpc^{-1}}$, whereas local or late Universe observations like supernovae type Ia (SNIa) investigated by Riess et al. (2022) or strong gravitational lensing time delays (Wong et al., 2020) measure with a $5\,\sigma$ discrepancy a value of $H_0 \approx 73\,\mathrm{km\,s^{-1}\,Mpc^{-1}}$. Since this tension is currently not solvable and the fact that other parameters depend on it, the Hubble constant is frequently written as $H_0 = 100\,h\,\mathrm{km\,s^{-1}\,Mpc^{-1}}$.

The Friedmann equations can also be expressed in terms of cosmological parameters. This is done by solving the first law of thermodynamics transformed to comoving coordinates,

$$\mathrm{d}\left(\rho c^2 a^3\right) = -p\mathrm{d}\left(a^3\right)\;, \tag{2.7}$$

for each particle species separately by assuming that they all follow the ansatz $\rho_i = \rho_{i0} a^{\nu}$ but with different equation of state $w = p/(\rho\,c^2)$, the first Friedmann equation can also be written as

$$H(a)^2 = H_0^2\left[\Omega_\mathrm{r}\,a^{-4} + \Omega_\mathrm{m}\,a^{-3} + (1-\Omega_\mathrm{tot})\,a^{-2} + \Omega_\Lambda\right]\;. \tag{2.8}$$

where

$$\Omega_\mathrm{m} = \frac{\rho_\mathrm{m,0}}{\rho_\mathrm{crit}}\;,\; \Omega_\mathrm{r} = \frac{\rho_\mathrm{r,0}}{\rho_\mathrm{crit}}\;,\; \Omega_\mathrm{b} = \frac{\rho_\mathrm{b,0}}{\rho_\mathrm{crit}}\;,\; \Omega_\Lambda = \frac{\Lambda\,c^2}{8\pi G\,\rho_\mathrm{crit}}\;,\; \Omega_\mathrm{tot} = \Omega_\mathrm{m} + \Omega_\mathrm{r} + \Omega_\Lambda\;, \tag{2.9}$$

and

$$\rho_\mathrm{crit} = \frac{3\,H_0^2}{8\pi G}\;. \tag{2.10}$$

This cosmological model is the so-called ΛCDM model and assumes that the Universe contains baryonic matter ρ_b and cold dark matter ρ_CDM, since for hot dark matter, only the largest perturbations survive. Dark matter does not interact with electromagnetic radiation. Hence it is invisible but is detectable via its deformation of space-time. Together, baryonic and dark matter account for the total matter density parameter Ω_m, the radiation content by the density parameter Ω_r, and the non-zero cosmological constant Λ by Ω_Λ. Equation (2.8) reveals interesting results. First, it shows that the Universe's expansion history is fully determined by the density parameters and the Hubble constant, and second, the Universe experienced three different expansion epochs. In the early time, the Universe was dominated by radiation, and as soon as the scale factor grows above the matter-radiation equality at scale factor a_{eq} defined by

$$a_{\mathrm{eq}} = \frac{\Omega_{\mathrm{r}}}{\Omega_{\mathrm{m}}} \approx 3.2 \times 10^{-5}\, \Omega_{\mathrm{m}}^{-1}\, h^{-2}\,, \tag{2.11}$$

the matter density Ω_{m} starts to dominate. Measurements suggest that $\Omega_{\mathrm{tot}} = 1$ so the term proportional to a^{-2} vanishes. Furthermore, since $\Omega_{\Lambda} > \Omega_{\mathrm{m}}$ the current expansion of the Universe is dominated by the cosmological constant, where a increases exponentially.

Although the ΛCDM model is not able to describe all astrophysical observations, it is still referred to as the *cosmological standard model* since it does explain the observed accelerated expansion of the Universe (Riess et al., 1998; Perlmutter et al., 1999) and is also confirmed by several observations like the spatial galaxy distribution, distances to SNIa and its strongest proponent the CMB. One of the most famous 'problems' is the *H_0 Tension* between the Hubble constant measurements from the local Universe to the one from the early Universe (Di Valentino et al., 2021a). To solve this tension, either the ΛCDM model needs to be revised or even replaced, or observational reasons for this discrepancy need to be found, like the fact that the galactic supernovae are measured inside a void which would yield a larger local value for the Hubble constant (Shanks et al., 2019).

Another tension that is of more interest for our work describes the tension between local Universe measurements and early Universe measurement of the structure growth parameter of $S_8 \equiv \sigma_8\sqrt{\Omega_{\mathrm{m}}/0.3}$ (Hildebrandt et al., 2021; Joudaki et al., 2020), where σ_8 is the normalisation of the matter power spectrum (see Sect. 2.1.5).

Since this work does not aim to solve these tensions, we rely on the ΛCDM model, which is still the best description of our Universe.

2.1.2 Redshift and other cosmological distances

Considering two flashes of radiation at cosmic time t and $t + \Delta t_{\mathrm{e}}$, which an observer receives at time t_0 and $t_0 + \Delta t_{\mathrm{obs}}$ it follows from the expansion of the Universe that $\Delta t_{\mathrm{e}} = a(t)\Delta t_{\mathrm{obs}}$. The first consequence of this result is that two events separated by Δt_{e} in the rest-frame of the observer are measured by a time interval $\Delta t_{\mathrm{obs}} = \Delta t_{\mathrm{e}}/a(t)$ which can be studied in the context of SNIa. The second consequence is that for Δt_{obs} and Δt_{e} being the inverse of the observed and emitted frequency ν it follows that

$$\frac{\nu_{\mathrm{obs}}}{\nu_{\mathrm{e}}} = \frac{\lambda_{\mathrm{e}}}{\lambda_{\mathrm{obs}}} = a(t) \equiv (1+z)^{-1}\,, \tag{2.12}$$

where z is called the redshift, since it describes how photons are redshifted due to time dilation. In the following parts, we are interested in the redshift of galaxies. However, for galaxies, the true redshift is unknown, and to estimate their redshift, a distinction is made between *spectroscopic* and *photometric* redshifts.

Spectroscopic redshifts, z_{sp}, are assumed to be the most accurate and reliable estimates of the true redshift. They are determined by fitting templates of galaxy spectra with the various emissions and absorption lines to the measured spectra of the galaxy. According to Eq. (2.12) the emission and absorption lines move towards longer wavelengths for larger redshifts, as shown in Fig. 2.1.

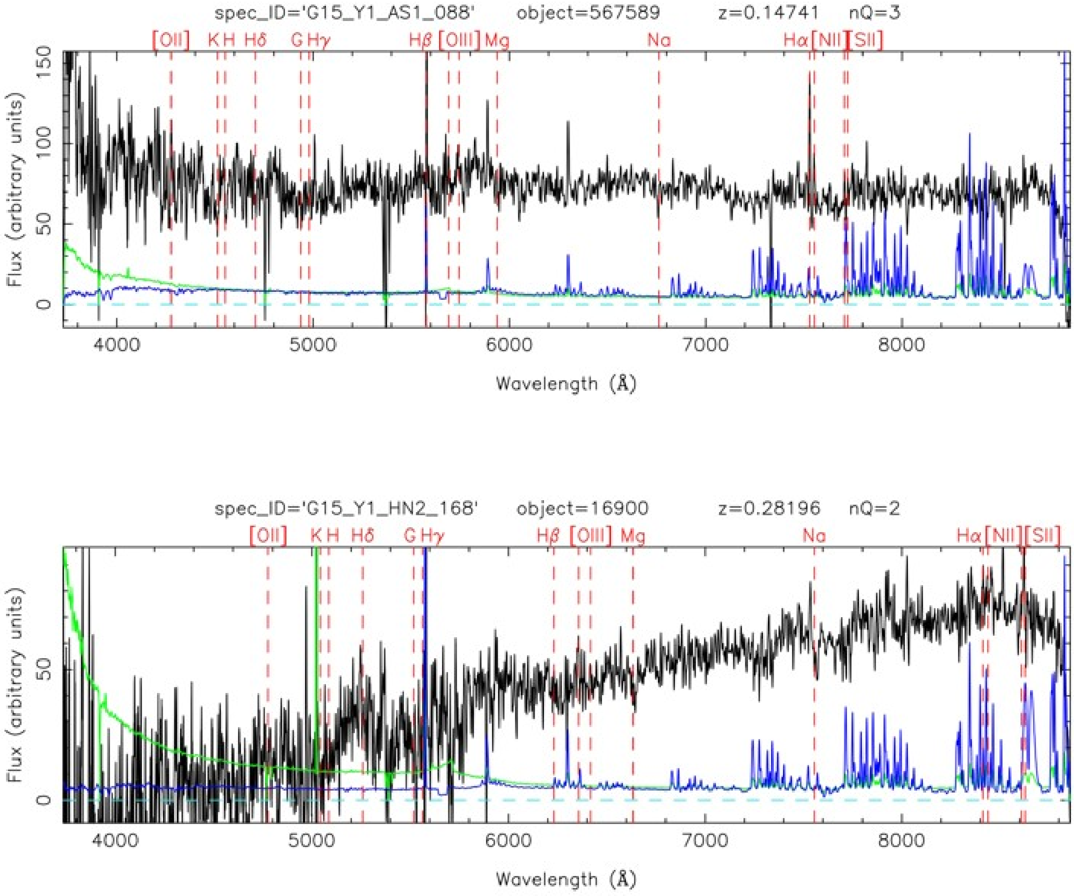

Figure 2.1: Galaxy spectra measured from the Galaxy And Mass Assembly survey (GAMA) for two different redshifts. In black, the spectrum itself; in green, the $1\,\sigma$ error; and in blue, the mean sky spectrum is displayed. The vertical dashed red lines, which mark common nebular emission and stellar absorption lines, clearly show how the emission and absorption lines shift towards higher wavelengths λ for increasing redshifts. Figures are taken from Driver et al. (2011).

Photometric redshifts, z_{ph}, are estimated by measuring the magnitude of galaxies in n broad-band filters, which form $n-1$ independent colours. If the star formation histories of galaxies are assumed to be similar, starting at a given redshift z_{f} and lasting for some time τ, then they occupy a certain two-dimensional subspace in $(n-1)$-dimensional colour space. This two-dimensional space changes with redshift $z < z_{\mathrm{f}}$ because the photometric filters correspond to different rest-frame spectral regions, and the spectral energy distributions differ for stellar populations at different cosmic epochs. This allows estimating the photometric redshifts rapidly from its broad-band energy distribution for a large number of galaxies, as illustrated in Fig. 2.2.

However, photometric redshifts are usually inaccurate and have large outliers. Since the more accurate spectroscopic redshifts are very expensive to determine, in many realistic scenarios, a small spectroscopic redshift sample is used to calibrate a large photometric redshift sample. Since the high-dimensional colour space of the photometric images is only imperfectly covered by the spectroscopic calibration sample, Wright et al. (2020) uses self-organising maps (SOMs) to discard the data part that can not be calibrated with sufficient precision.

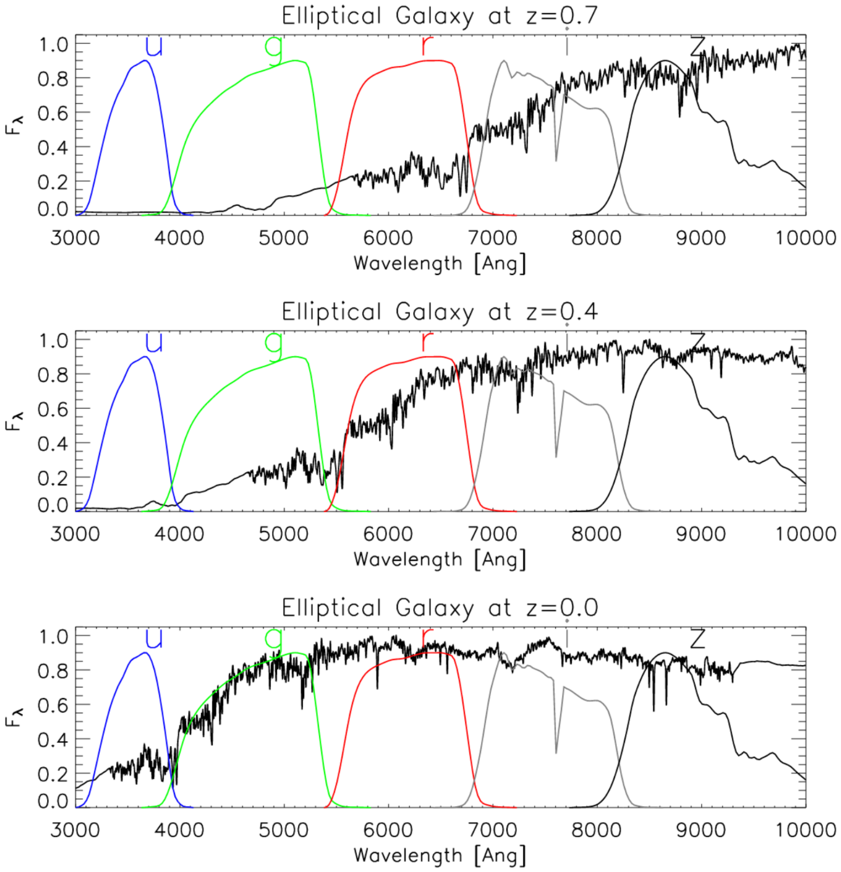

Figure 2.2: A model spectrum of an elliptical galaxy shown at three redshifts with five broad-band filters illustrating the idea of photometric redshift estimates. With increasing redshift the whole spectrum moves towards higher wavelengths, such that the measured flux, F_λ, at low wavelength filters decreases. The figure is taken from Padmanabhan et al. (2007).

Another important distance measure is the comoving distance. It is defined through the fact that in the framework of GR light rays follow null geodesics, $\mathrm{d}s^2 = 0$, such that for light rays that arrive at the centre of the coordinate system

$$c\,\mathrm{d}t = -a(t)\,\mathrm{d}\chi. \tag{2.13}$$

Solving this equation, the comoving radial distance

$$\chi(t) = \int_t^{t_0} \frac{c\,\mathrm{d}t'}{a(t')} = c\int_{a(t)}^{a(t_0)} \frac{\mathrm{d}a'}{a'^2\,H(a')}\,, \tag{2.14}$$

where $\chi(t_0) = 0$. In that context, it is interesting to mention the proper distance or physical distance is defined as $r(t) = a(t)\chi$, which describes the actual distance if the comic expansion is included.

To this point, the source's distance to the observer or the time at which the light was emitted to the observer is characterised in terms of χ, t, $a(t)$ and z. In Euclidean space-time, distance is defined as the length of a line connecting two simultaneous events, where all distance measures give coherent results. But in general space-time, two complications occur. The first is that the space might be curved and the second is that distances change over time, so the unique meaning of time does not exist anymore. Therefore, different types of 'distances' are used in cosmology, but of particular interest for this work is the angular diameter distance D_{ang}. This distance relates the angular diameter δ of an object at redshift z to its physical diameter $2R$ by

$$D_{\text{ang}}(z) = \frac{2R}{\delta} = a(z) f_K(\chi) \; . \tag{2.15}$$

2.1.3 Large scale structure formation

The foregoing sections introduced the standard model of cosmology, which is based on the assumption of a (spatially) homogeneous and isotropic universe. But since objects like galaxies and stars are observable, this assumption is not justified on smaller scales. Galaxies gather together into clusters and groups of galaxies; even the clusters of galaxies are correlated and grouped together in superclusters. As illustrated in Fig. 2.3, the three-dimensional distribution of galaxies obtained from redshift surveys shows that the LSS is structured in large voids separated by filaments and, therefore, is also called the *cosmic web*.

At the epoch of the last scattering at $z \sim 1000$, where the CMB photons decoupled from the baryons, the density variations in the Universe were small on the order of 10^{-5} and Gaussian. Due to the dark matter that formed potential wells before $z \sim 1000$, today's observed structure assembled, where the density fluctuations grow over time due to their self-gravity. These fluctuations collapse once they reach a threshold density to form dark matter halos. According to the bottom-up structure formation (Coles and Lucchin, 2002), the halos merge into increasingly more massive halos. After the last scattering, baryons fell inside these potential wells to follow the dark matter distribution to form stars, which eventually build galaxies, galaxy groups and galaxy clusters.

To describe the growth of dark matter density fluctuations in the matter-dominated epoch quantitatively, it is practical to define the density, velocity, and gravitational potential in terms of the comoving coordinate $\boldsymbol{x}$ as the comoving density

$$\rho(\boldsymbol{x}, t) = \rho\,[a(t)\,\boldsymbol{x}, t] =: \bar{\rho}(t)\,[1 + \delta(\boldsymbol{x}, t)] \;\; , \tag{2.16}$$

the comoving velocity

$$\boldsymbol{u}(\boldsymbol{x}, t) = \mathrm{v}\,[a(t)\,\boldsymbol{x}, t] - H(t)\,a(t)\,\boldsymbol{x} \;, \tag{2.17}$$

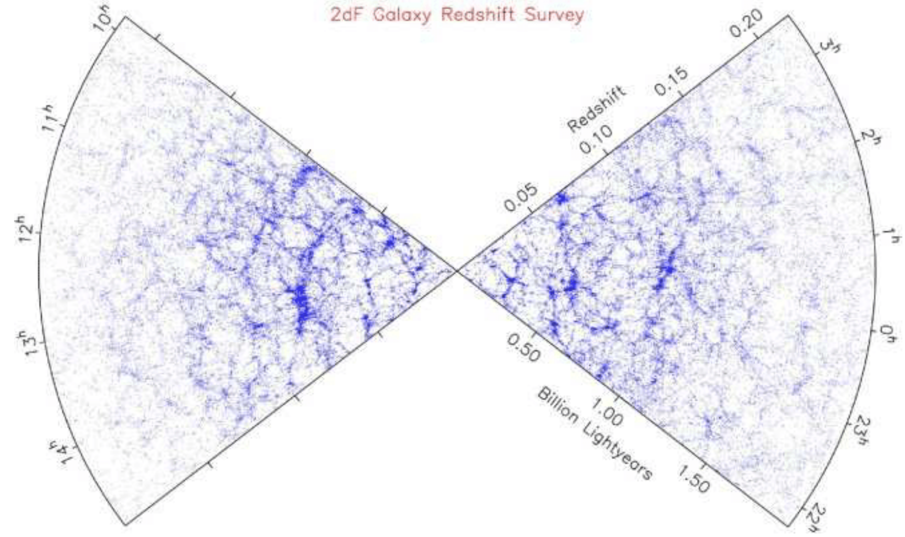

Figure 2.3: Three-dimensional galaxy redshift distribution in the complete 2dF Galaxy Redshift Survey. The distance of the galaxies to our Galaxy at the centre is given in terms of escape velocity, or redshift, and the polar angle is given in right ascension. Credit: M. Colless and the 2dF Galaxy Redshift Survey team

and the comoving potential

$$\mathit{\Phi}(\boldsymbol{x},t) = \Phi\left[a(t)\,\boldsymbol{x},t\right] + \frac{\ddot{a}\,a}{2}\,|\boldsymbol{x}|^2 \,, \tag{2.18}$$

where $\bar{\rho}$ is the mean density and δ is the three-dimensional matter *density contrast.* Assuming gravity is weak and well-described by the Newtonian framework with the potential Φ, and structure formation occur on length scales much smaller than the *comoving horizon* (defined in Eq. 2.14 if one integrates from 0 to scale factor a), three coupled differential equations emerge

$$\frac{\partial\delta}{\partial t} + \frac{1}{a}\boldsymbol{\nabla}_x \cdot \left[(1+\delta)\ \boldsymbol{u}\right] = 0 \,, \tag{2.19}$$

$$\frac{\partial\boldsymbol{u}}{\partial t} + H\,\boldsymbol{u} + \frac{1}{a}\left(\boldsymbol{u}\cdot\boldsymbol{\nabla}_x\right)\cdot\boldsymbol{u} = -\frac{1}{a}\boldsymbol{\nabla}_x\mathit{\Phi} \,, \tag{2.20}$$

$$\nabla_x^2\mathit{\Phi} = 4\pi G\bar{\rho}\delta \,, \tag{2.21}$$

where the first is called the continuity, the second the Euler and the third the Poisson equation. Since these equations are still not solvable analytically, it is common practice to consider small deviations from the homogeneous solution, where $\delta = 0$, $\mathbf{u} = 0$, $\mathit{\Phi} = 0$ and $\rho = \bar{\rho}$, such that $|\delta| \ll 1$ and $|\boldsymbol{u}| \ll H\,\boldsymbol{r}$, and all terms of second or higher order in δ and $\boldsymbol{u}$ can be neglected. This regime is also called *linear perturbation theory* (see, e.g. Peebles, 1980), where the linearized differential Eq. (2.19-2.21) read as

$$\frac{\partial \delta}{\partial t} + \frac{1}{a}\boldsymbol{\nabla}_x \boldsymbol{u} = 0 \,, \tag{2.22}$$

$$\frac{\partial \boldsymbol{u}}{\partial t} + H\,\boldsymbol{u} = -\frac{1}{a}\boldsymbol{\nabla}_x \Phi \,, \tag{2.23}$$

$$\nabla_x^2 \Phi = 4\pi G\,\bar{\rho}\,\delta \,, \tag{2.24}$$

which combined yield the *linear growth equation* for the density fluctuations,

$$\frac{\partial^2 \delta}{\partial t^2} + 2\frac{\dot{a}}{a}\frac{\partial \delta}{\partial t} = 4\pi\,G\,\bar{\rho}\,\delta \,. \tag{2.25}$$

This equation does not contain derivatives with respect to spatial coordinates, nor do the coefficients depend on x. This implies that Eq. (2.25) is solved by

$$\delta(\boldsymbol{x},t) = D_+(t)\,\Delta_+(\boldsymbol{x}) + D_-(t)\,\Delta_-(\boldsymbol{x}) \,, \tag{2.26}$$

where it has a growing mode $D_+(t)\,\Delta_+(\boldsymbol{x})$ and a decaying mode $D_-(t)\,\Delta_-(\boldsymbol{x})$, which decreases with time, and is therefore irrelevant at later cosmic time t. Consequently the growth of structures in the matter-dominated epoch is determined by the *linear growth function*

$$D_+(t) = D\,H(t)\int_0^{a(t)} \mathrm{d}a' \left[\Omega_\mathrm{m}\,a'^{-1} + \Omega_\Lambda\,a'^2 - (\Omega_\mathrm{m} + \Omega_\Lambda - 1)\right]^{-3/2} \,, \tag{2.27}$$

where the normalisation constant D is given by the fact that today $D_+(t_0) = 1$.

2.1.4 Formation and evolution of galaxies

For a cosmologist, galaxies, their distribution and their connection to the underlying matter distribution are of invaluable importance. Whereas their distribution and connection to the underlying matter distribution will be discussed in the next section, this section reviews some basic knowledge of their formation and evolution (see Cole et al., 2000, for more details).

Besides the fact that galaxy differs in terms of colour, morphology, size and gas content, they can be divided roughly into early-type galaxies and late-type galaxies. The former are typically red ellipticals with little star formation and gas, and the latter are bluer spiral galaxies with active star formation. The cooling gas, like the dark matter halo itself, accumulates finite angular momentum due to the gas friction in a disk perpendicular to the angular momentum of the gas. The gas in the disk then reaches densities at which efficient star formation can begin. In this way, the formation of disk galaxies, or spirals, with active star formation can be understood qualitatively. Early-type galaxies are mainly in denser environments like the centres of galaxy clusters because, in denser environments, more galaxies are found, which increases the merger events that decrease the star formation and, therefore, are seen as reddish. Late-types, however, are found frequently in regions with lower density (Kauffmann et al., 2004). Next, we give an overview of a general picture of galaxy formation and evolution as described in Mo et al. (2010).

Before recombination at $z \sim 1000$, baryons were coupled to the photons and, therefore, are hindered by the intense pressure to fall into the potential wells formed by dark matter inhomogeneities. After recombination, the decoupled baryonic matter became pressure-free and accumulated inside the already formed dark matter haloes. Due to gravitational attraction, the gas in these halos got compressed and heated, which was then cooled by the Bremsstrahlung of free electrons or excitation and recombination processes. These processes released some thermal energy and thus pressure, allowing the baryons to collapse into even denser structures and eventually form stars, which in turn gathered to form galaxies and even larger structures.

The galaxy halos gain mass by accreting further surrounding matter through the filaments of the large-scale density field or by merging with other galaxy halos. The outcome of a merger event depends mainly on the mass ratio of the halos: If one halo is much lighter than the other, the lighter halo is simply absorbed by the more massive halo. If the masses of the two objects are of the same order, the stars in both objects obtain a large random velocity component, such that any forgoing structure in the objects is destroyed, resembling an elliptical galaxy. The closer objects are, the more frequent merger events happen, meaning many merger events happen at high redshifts or high-density regions. We note here during a merger event that the space between individual stars is enormous, so the collision of different stars is very rare.

Various observations show that only a fifth of the baryons is in stars, and most are in the hot intracluster medium (Roberts et al., 1991; Mathews and Brighenti, 2003). This implies that 'feedback' processes hinder the gas from cooling, which in turn reduces the star formation. The two main feedback processes are core-collapse *supernovae* and Active Galactic Nuclei (AGN). The more massive a star is, the shorter its time scale, such that shortly after star formation starts, the most massive stars explode as a core-collapse supernova, where the mechanical energy is partly transferred to the surrounding gas and obstructs cooling. Whereas the decreasing conversion of gas into stars in low-mass halos can be explained by supernova, in higher mass halos AGN heating is the responsible process. The feedback from AGNs with high accretion rates is presumably by heating the gas through jets, which are relativistic outflow streams. At a low accretion rate, the main feedback is the injection of mechanical energy into the surrounding gas.

Furthermore, galaxies' compositions and morphology are affected by their motion through the potential of the halo galaxies by tidal forces that are able to remove material like gas and stars in a process called *tidal stripping*. Galaxies also interact with the hot gas surrounding them, which causes a drag force which eventually removes cold gas from the galaxy in a process called *ram pressure stripping* (Gunn and Gott, 1972). These processes change the structure of the galaxies and their colour as fewer new stars form. Since massive halos contain more gas, this could also explain why in dense environments, predominantly galaxies with suppressed star formation are found.

Lastly, several galaxies can find themselves inside the same gravitational well, where lower mass *satellite* galaxies move around a higher mass central galaxy. If satellites meet during their motion, they can disrupt each other, where they are unlikely to merge but lose some of their gas and stars due to their large velocities. The tidal forces in these encounters can destroy the disks of spiral galaxies (Farouki and Shapiro, 1981) or ignite a short period of intense star-formation, a so-called 'starburst'. If satellites lose enough kinetic energy, they merge with the central galaxy due to dynamical friction, which explains the observed large masses of central galaxies in galaxy clusters (De Lucia and Blaizot, 2007).

2.1.5 Correlation functions and polyspectra

As mentioned above, this works aims to describe the distribution and correlation of the galaxy distribution to the underlying matter distribution, i.e., how to quantify the large-scale structures of an inhomogeneous universe. Since the observed $\delta(\boldsymbol{x}, t)$ depends on the unobservable initial conditions, it cannot be modelled. Therefore, $\delta(\boldsymbol{x}, t)$ is considered as a realisation of a *random field*, whose statistical properties we explore and model. A random field is the statistical ensemble of all fields with the same statistical properties, where the individual realisations $\delta(\boldsymbol{x}, t)$ are different due to their initial conditions.

Assuming that the realisations of the random field are determined at n grid point $\delta(\boldsymbol{x}_i, t) = \delta_i$, then the random field is quantitatively characterised by the joint probability distribution

$$p\left(\delta_1 ... \delta_n\right) \mathrm{d}\delta_1 ... \mathrm{d}\delta_n \tag{2.28}$$

that $\delta(\boldsymbol{x}_i, t)$ lies within $\mathrm{d}\delta_i$ of δ_i. By building the ensemble average over multiple, independent realisations of the Universe, the *n-point correlation functions* is defined as

$$\begin{aligned} \xi^{(n)}(\boldsymbol{x}_1, \dots, \boldsymbol{x}_n, t) &\equiv \langle \delta(\boldsymbol{x}_1, t)\, \delta(\boldsymbol{x}_2, t) \dots \delta(\boldsymbol{x}_n, t) \rangle & (2.29) \\ &= \int \mathrm{d}\delta(\boldsymbol{x}_1, t) \dots \mathrm{d}\delta(\boldsymbol{x}_n, t)\;\; \delta(\boldsymbol{x}_1, t) \dots \delta(\boldsymbol{x}_n, t)\, p[\delta(\boldsymbol{x}_1, t), \delta(\boldsymbol{x}_2, t) \dots]\,. & (2.30) \end{aligned}$$

The ensemble averages above, in principle, require to average over all possible realisations of the random field. However, we can explore the properties of the one observable Universe. To still measure our Universe's statistical properties, the ergodicity of random field is used (Peebles, 1980), which implies that the ensemble averages are equivalent to spatial averages, such that Eq. (2.30) can be calculated as

$$\xi^{(n)}(\boldsymbol{x}_1, \dots, \boldsymbol{x}_n, t) = \frac{1}{V^n} \int_V \mathrm{d}^3 x_1 \cdots \int_V \mathrm{d}^3 x_n \;\; \delta(\boldsymbol{x}_1, t) \dots \delta(\boldsymbol{x}_n, t)\,, \tag{2.31}$$

with V being an arbitrary volume.

An equivalent description of the statistical properties of the matter distribution is the polyspectra $P^{(n)}$, which are Fourier transforms of the n-point correlation functions. The equivalence to the two-point correlation function $\xi^{(2)}(\boldsymbol{x}_1, \dots, \mathrm{x}_2, t)$ for which $n = 2$ is the so-called power spectrum $P(k)$, which describes the level of structure as a function of the length-scale $L = 2\pi/k$ with k being the comoving wave number.

By defining the Fourier transform of the density contrast $\delta(\boldsymbol{x}_i, t)$ as

$$\hat{\delta}(\boldsymbol{k}, t) = \int \mathrm{d}^3x \;\, \delta(\boldsymbol{x}, t) \; \exp(-\mathrm{i}\, \boldsymbol{k} \cdot \boldsymbol{x}) \; , \tag{2.32}$$

the polyspectra follow to

$$(2\pi)^3 \, \delta_\mathrm{D} \left(\boldsymbol{k}_1 + \dots + \boldsymbol{k}_n\right) \; P^{(n)}(\boldsymbol{k}_1, \dots, \boldsymbol{k}_n, t) = \left\langle \hat{\delta}(\boldsymbol{k}_1, t), \dots, \hat{\delta}(\boldsymbol{k}_n, t) \right\rangle \; , \tag{2.33}$$

with δ_D being the Dirac delta function. Making use of the cosmological principal, the power spectrum depends aside from the comsic time t on one, and the bispectrum on three parameter, such that

$$P(\boldsymbol{k}, -\boldsymbol{k}, t) =: P(k, t) \; , \tag{2.34}$$

$$B(\boldsymbol{k}_1, \boldsymbol{k}_2, -\boldsymbol{k}_1 - \boldsymbol{k}_2, t) =: B(k_1, k_2, \phi, t) \; , \tag{2.35}$$

where k is the norm of $\boldsymbol{k}$ and ϕ is the angle between $\boldsymbol{k}_1$ and $\boldsymbol{k}_2$. Most studies deal only with the matter power spectrum, which contains only second-order or Gaussian information. Since the CMB is Gaussian, it can be fully characterised by analysing the power spectrum. However, the bispectrum also contains information about the skewness of the matter distribution, which is of huge importance for the LSS that are observed in low-redshift surveys.

Since this work uses the information of the power spectra and models higher order statistics indirectly from it, the following description focus on the prediction of the power spectrum using linear perturbation theory. Given a primordial power spectrum $P_\mathrm{prim}(k)$, which characterises the initial density fluctuations at some early time, all perturbations in the matter-dominated area grow proportional to the growth factor D_+ given in Eq. (2.27), such that

$$P(k, t) = D_+^2(t) \, P_\mathrm{prim}(k) \, . \tag{2.36}$$

At an early time during the radiation-dominated era, no natural length scale existed in the Universe to which a wavelength could be compared. Therefore, it is expected that the initial power spectrum follows a power law, $P_\mathrm{prim}(k) \propto k^{n_\mathrm{s}}$, since this is the only mathematical function that depends on a length but does not contain any characteristic scale. The spectrum with $n_\mathrm{s} = 1$ is called the Harrison–Zeldovich spectrum or scale-invariant spectrum because for $n_\mathrm{s} = 1$, the amplitude of the fluctuations of the gravitational potential prefers neither small nor large scales. Most popular inflation models, however, predict a n_s slightly smaller than 1. Inflation is a period of time right after the Big Bang where the Universe expanded exponentially, which added to the ΛCMD to explain the ‘flatness problem’ (Dicke et al., 1965) and ‘horizon problem’ (Rindler, 1956). The flatness problem arises from the fact that to measure $\Omega_\mathrm{tot} \approx 1$ today, it must have been extremely close to 1 at earlier times. The horizon problem deals with the problem that the temperature fluctuations of the CMB are of the order of 10^{-5}, which is surprising as no signal can travel faster than light and regions of CMB separated more than one degree were not in causal contact, meaning they could not have exchanged any information since the birth of the Universe. The different evolution of perturbations in different eras also affects the power spectrum. To account for this, the power spectrum is modified by the transfer function $T(k)$, which describes how dark matter density fluctuations evolve at different scales k. For instance, during the matter-dominated epoch, fluctuations at all scales evolved proportionally to the scale factor a. However, during the radiation-dominated epoch, fluctuations at scales smaller than the comoving horizon d_{H} were suppressed, which is described by the so-called Meszaros-effect (Meszaros, 1974), where the Universe's expansion counteracts the growth of the fluctuations. Fluctuations at large scales, however, without causal contact, evolved proportionally to a^2, such that the power spectrum $P(k)$ is suppressed for wave numbers $k \geq \frac{2\pi}{d_{\mathrm{H}}}$.

Combining all ingredients, the linear power spectrum $P_{\mathrm{lin}}(k,t)$ is

$$P_{\mathrm{lin}}(k,t) = A\, D_+^2(t)\, T^2(k)\, P_{\mathrm{prim}}(k)\ , \tag{2.37}$$

where A is a normalisation constant that is obtained by setting the variance of matter fluctuations to one within spheres of comoving radius $R = 8\,h^{-1}\,\mathrm{Mpc}$ defined as

$$\sigma^2(R) \equiv \langle|\delta_R^2((x))\rangle = \frac{1}{2\pi^2}\int_0^\infty \mathrm{d}k\ \ k^2\, P(k,t_0)\, |\hat{W}(k\,R)|^2\ . \tag{2.38}$$

Here t_0 is the cosmic time today and $\hat{W}$ is the Fourier transform of a tophat filter, given as

$$\hat{W}(x) = \frac{3}{x^3}(\sin x - x\ \cos x)\ . \tag{2.39}$$

Using the fact that in spheres of radius $R = 8\,h^{-1}\,\mathrm{Mpc}$, galaxies count fluctuations $\Delta N/N \approx 1$, or

$$\left\langle \frac{(N-\langle N\rangle)^2}{\langle N\rangle^2} \right\rangle \approx 1\,, \tag{2.40}$$

and the assumption that the distribution of galaxies follows that of dark matter, the normalisation of the power spectrum can be determined by using that

$$\sigma_8^2 = \sigma^2(8\,h^{-1}\,\mathrm{Mpc}) \approx 1\,, \tag{2.41}$$

whereas current observations yield $\sigma_8 \approx 0.8$. This description ignores that galaxies are biased tracers of the underlying mass distribution, where the biasing usually depends on scale and galaxy properties such as luminosity, morphology, colour and redshift. On large spatial scales, however, a valid assumption is that the relative number fluctuations of galaxies are proportional to the density contrast,

$$\delta_g \equiv \frac{\Delta n}{n} = b\,\delta\,, \tag{2.42}$$

where b is called the bias factor. If the bias factor of galaxies is scale-independent, then the shape of the power spectrum of galaxies is the same as that of underlying (dark) matter, such that

$$P_g(k) = b^2 P(k)\,, \tag{2.43}$$

and equivalently, the correlation functions of galaxies and the underlying matter are correlated as

$$\xi_g(r) = b^2 \xi(r)\,. \tag{2.44}$$

2.1.6 Non-linear regime

While in the linear and quasi-linear regime of density fluctuations, the power spectrum can be computed for any given initial conditions and cosmological parameters using perturbation theory (Bernardeau et al., 2002), it fails to predict as shown in Fig. 2.4 the power spectrum for $k > 0.3\,h\,\mathrm{Mpc}^{-1}$, which corresponds roughly to spatial scales above $20\,h^{-1}$ Mpc.

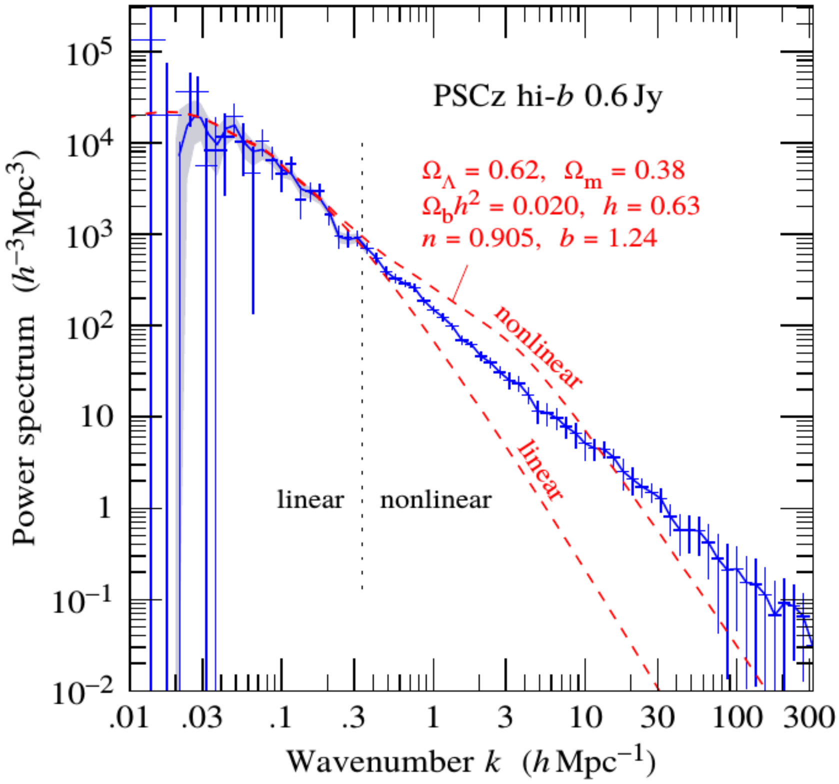

Figure 2.4: Shown as the blue crosses is the power spectrum, measured in the IRAS Point Source Catalog. The linear and non-linear perturbation theory predictions with the cosmological parameters marked in the figure are shown in red. Figure is taken from Hamilton and Tegmark (2002).

N-body simulations

For $k > 0.3\,h\,\mathrm{Mpc}^{-1}$, which is called the *non-linear regime*, cosmological N-body simulations are the ideal tool to study the non-linear structure formation. The creation of dark matter only N-body simulations that can be summarised to:

1. Choose the number of particles per box. For instance the MS have 2160^3 dark matter particles of mass $8 \times 10^8\,\mathrm{M}_\odot/h$.
2. Choose the volume L^3 of the box in which the particles are enclosed. The MS fixed it to $(500\,\mathrm{Mpc}/h)^3$.
3. Choose an N-body code (Springel et al., 2001; Springel et al., 2021) to compute the gravitational evolution of the particles starting from initial Gaussian random fields.

4. Add galaxies using a semi-analytical galaxy-formation model (Henriques et al., 2015; Smith et al., 2017) or, as we do it for most mocks, use a Poisson process.
5. Compute the shear information at redshift z by tracing the light-ray trajectories from the observer to z (Hilbert et al., 2009).

Simulations including dark matter particles and baryons have been done more recently. However, they require to include gas physics and radiation processes, which are considerably more complicated; see Chisari et al. (2015) and Huang et al. (2019) for recent comparisons of hydrodynamical simulations. Due to the limited mass resolution of N-body simulation, small scales which enclose regions with less than ~ 100 particles should not be trusted. Scales larger than $1/3$ of the box-size L are affected by the periodic boundary conditions and should not be trusted. Despite their limitations and the fact that N-body simulations are expensive to create, they are still the most accurate way to model non-linear structure formation.

The halo model and its application

Besides the fact that it is computationally expensive to run N-body simulations from which statistics (like the power spectrum) can be modelled, physically motivated analytical or semi-analytical models can provide insight into complex processes and allow predictions for cosmologies that have not been simulated. A famous analytical clustering model is the halo model (Ma and Fry, 2000; Peacock and Smith, 2000; Seljak, 2000), where all matter is contained within haloes. The clustering problem is then divided into the clustering that arises between different haloes (two-halo) and the clustering that arises within individual haloes (one-halo). The halo model needs several ingredients: the halo-mass distribution function, the halo profile, and the bias recipe for the clustering between haloes with respect to the matter. Assumptions must be made for all components, contributing to the halo model's inaccuracies. Smith et al. (2003) developed, based on the halo model, the popular semi-analytical model HALOFIT, which predicts the non-linear power spectrum. Given a functional form, the parameters were fitted to simulated data over a wide range of cosmologies to account for the inaccuracy of the halo model for the matter spectrum. The fitting function was updated in Takahashi et al. (2012) to account for inaccuracies that arose from the limited resolution of the used simulations. It also provides a more accurate model for dark energy cosmologies with a fixed equation of state parameter w. A different halo model ansatz is described in Mead et al. (2015), called HMCODE, which differs from HALOFIT in that the halo model is the starting point rather than a fitting function that is based on the halo model.

Tree-level perturbation theory

If the perturbation is no longer small, which happens already inside galaxy clusters with an average density contrast that exceeds unity by about two orders of magnitude, the linearisation breaks down. This implies that the neglected second-order term in the fluid equations has to be included. To do that, we follow the appendix of F18 by introducing the conformal time $\mathrm{d}t = a\,\mathrm{d}\tau$ such that Eq. (2.25) read as

$$\frac{\partial^2 \delta}{\partial \tau^2} + \mathcal{H}\frac{\partial \delta}{\partial \tau} = 4\pi\, G\, \bar{\rho}\, a^2\, \delta\ , \tag{2.45}$$

where $\mathcal{H} = \frac{\mathrm{d}}{\mathrm{d}\tau}\ln(a)$ and at linear (first) order in Fourier space

$$\delta_1(\boldsymbol{k},\tau) = D_+(\tau)\delta_1(\boldsymbol{k},\tau_0)\,. \tag{2.46}$$

The second-order term results to

$$\delta_2(\boldsymbol{k},\tau) = \int \mathrm{d}^3k_1\,\mathrm{d}^3k_2\,\delta_\mathrm{D}(\boldsymbol{k}-\boldsymbol{k}_{12})F_2(\boldsymbol{k}_1,\boldsymbol{k}_2,\tau)\delta_1(\boldsymbol{k}_1,\tau_0)\delta_1(\boldsymbol{k}_2,\tau_0)\,, \tag{2.47}$$

where $\boldsymbol{k}_{12} = \boldsymbol{k}_1 + \boldsymbol{k}_2$ and in a general ΛCDM universe

$$F_2(\boldsymbol{k}_1,\boldsymbol{k}_2,\tau) = \mu(\tau) + \frac{1}{2}\frac{\boldsymbol{k}_1\cdot\boldsymbol{k}_2}{k_1k_2}\left(\frac{k_1}{k_2}+\frac{k_2}{k_1}\right) + [1-\mu(\tau)]\frac{(\boldsymbol{k}_1\cdot\boldsymbol{k}_2)^2}{k_1^2k_2^2}\,. \tag{2.48}$$

In the forgoing equation $\mu(\tau) = 1 - D_{2,2}(\tau)/D_+^2(\tau)$, where $D_{2,2}$ is defined trough

$$\frac{\partial^2 D_{2,2}(\tau)}{\partial\tau^2} + \mathcal{H}\frac{\partial D_{2,2}(\tau)}{\partial\tau} - \frac{3\Omega_\mathrm{m}H_0^2}{2a}D_{2,2}(\tau) = \left(\frac{\partial D_+(\tau)}{\partial\tau}\right)\,. \tag{2.49}$$

Since in perturbation theory

$$\tilde{\delta}(\boldsymbol{k},\tau) = \sum_{n=1}^{\infty}\delta_n(\boldsymbol{k},\tau)\,, \tag{2.50}$$

the variance at leading order or at tree-level simplifies to

$$\langle\tilde{\delta}(\boldsymbol{k}_1,\tau)\tilde{\delta}(\boldsymbol{k}_2,\tau)\rangle_\mathrm{tree} = D_+^2\langle\delta_1(\boldsymbol{k}_1,\tau_0)\delta_1(\boldsymbol{k}_2,\tau_0)\rangle\,, \tag{2.51}$$

and the skewness

$$\langle\tilde{\delta}(\boldsymbol{k}_1,\tau)\tilde{\delta}(\boldsymbol{k}_2,\tau)\tilde{\delta}(\boldsymbol{k}_3,\tau)\rangle_\mathrm{tree} = D_+^2\langle\delta_1(\boldsymbol{k}_1,\tau_0)\delta_1(\boldsymbol{k}_2,\tau_0)\delta_2(\boldsymbol{k}_3,\tau_0)\rangle\,, \tag{2.52}$$

where it is assumed that the linear density field is well approximated as a Gaussian random field $\tilde{g}(\boldsymbol{k})$, for which the correlator $\langle\tilde{g}(\boldsymbol{k})_1...\tilde{g}(\boldsymbol{k}_N)\rangle$ vanishes for any odd number N per definition, whereas for even numbers it can be decomposed into second-order correlations

$$\langle\tilde{g}(\boldsymbol{k}_1)\tilde{g}(\boldsymbol{k}_2)\tilde{g}(\boldsymbol{k}_3)\tilde{g}(\boldsymbol{k}_4)\rangle = \langle\tilde{g}(\boldsymbol{k}_1)\tilde{g}(\boldsymbol{k}_2)\rangle\langle\tilde{g}(\boldsymbol{k}_3)\tilde{g}(\boldsymbol{k}_4)\rangle \tag{2.53}$$

$$+ \langle\tilde{g}(\boldsymbol{k}_1)\tilde{g}(\boldsymbol{k}_3)\rangle\langle\tilde{g}(\boldsymbol{k}_1)\tilde{g}(\boldsymbol{k}_4)\rangle \tag{2.54}$$

$$+ \langle\tilde{g}(\boldsymbol{k}_1)\tilde{g}(\boldsymbol{k}_4)\rangle\langle\tilde{g}(\boldsymbol{k}_2)\tilde{g}(\boldsymbol{k}_3)\rangle\,. \tag{2.55}$$

In that context, we note that in leading order (tree-level), the bispectrum can be expressed in terms of the power spectrum and F_2 as

$$B(k_1,k_2,k_3,\tau)_\mathrm{tree} = F_2(\boldsymbol{k}_1,\boldsymbol{k}_2,\tau)P_\mathrm{lin}(k_1,\tau_0)P_\mathrm{lin}(k_2,\tau_0) \tag{2.56}$$

$$+ F_2(\boldsymbol{k}_1,\boldsymbol{k}_3,\tau)P_\mathrm{lin}(k_1,\tau_0)P_\mathrm{lin}(k_3,\tau_0) \tag{2.57}$$

$$+ F_2(\boldsymbol{k}_2,\boldsymbol{k}_3,\tau)P_\mathrm{lin}(k_2,\tau_0)P_\mathrm{lin}(k_3,\tau_0)\,. \tag{2.58}$$

In the literature, also other approaches exist, like the large deviation theory (LDT) to infer statistical properties of the cosmic density fields beyond the linear regime. The LDT is a branch of probability theory that deals with the rate at which probabilities of certain events decay as a natural parameter of the problem varies (Varadhan, 2008).

2.2 Gravitational lensing

As predicted by GR, masses distort space-time. Therefore, since light propagates along null geodesics, it seems like the mass bends light rays similarly to optical lenses (Einstein, 1936), which gives it the name gravitational lensing. The strength of the deflection of the light ray depends on the encountered mass and its separation from that mass. Therefore, light bundles of distant objects appear distorted, such that by measuring the deflection, the total matter distribution of the Universe can be investigated since gravitational lensing acts identically to baryonic and dark matter.

The breakthrough of the theory of gravitational lensing started with the expeditions led by Sir Arthur Eddington, director of the Cambridge Observatory, and Sir Frank Watson Dyson. By comparing the apparent positions of stars in the Hyades cluster during the Solar eclipse of 1919 to the position of the stars at night, they made the first detection of the gravitational lensing effect (Dyson et al., 1920). The measured shifts in the position of the stars caused by the Sun were consistent with the predictions by GR, which led to its tremendous triumph over the Newtonian description.

Nowadays, gravitational lensing is divided into different areas, but in this work, we restrict ourselves to the area of the weak lensing effect, where measuring the distortion of galaxy shapes is used to infer information about the matter distribution, as first proposed by Zwicky (1937a,b). With today's instruments, the distortion of galaxies can be determined so well that the age of precise cosmologies has begun. See Bartelmann (2010) for a general and recent review of gravitational lensing.

2.2.1 Basic equations of gravitational lensing

If the light ray impact parameter ξ (see Fig. 2.5) is much larger than the Schwarzschild radius of the mass, $\xi \gg R_s \equiv 2GM/c^2$, then GR predicts that the deflection angle $\hat{\alpha}$ as shown in Fig. 2.5 is

$$\hat{\alpha} = \frac{4GM}{c^2\xi} \ll 1\,, \tag{2.59}$$

which is twice the value obtained from the Newtonian framework. Considering only small deflection angles is equivalent to considering gravitational lensing only in the weak-field limit of GR, where the field equations of GR can be linearised. The weak-field limit further requires that the gravitational potential Φ, its typical scales L and intrinsic velocity $\mathbf{v}$ are small:

$$|\Phi| \ll c^2\,, \qquad L \ll \frac{c}{H_0}\,, \qquad |\mathbf{v}| \ll c\,. \tag{2.60}$$

As discussed by Cuesta-Lazaro et al. (2018) the assumption of weak-field limit is satisfied even for Stage IV surveys. Another consequence of the deflection angle being small is the Born approximation, which states that a light ray can be approximated as a straight line in the neighbourhood of a deflecting mass. While with increasing redshift, this approximation gets violated, it is negligible for second-order shear statistics (Cuesta-Lazaro et al., 2018).

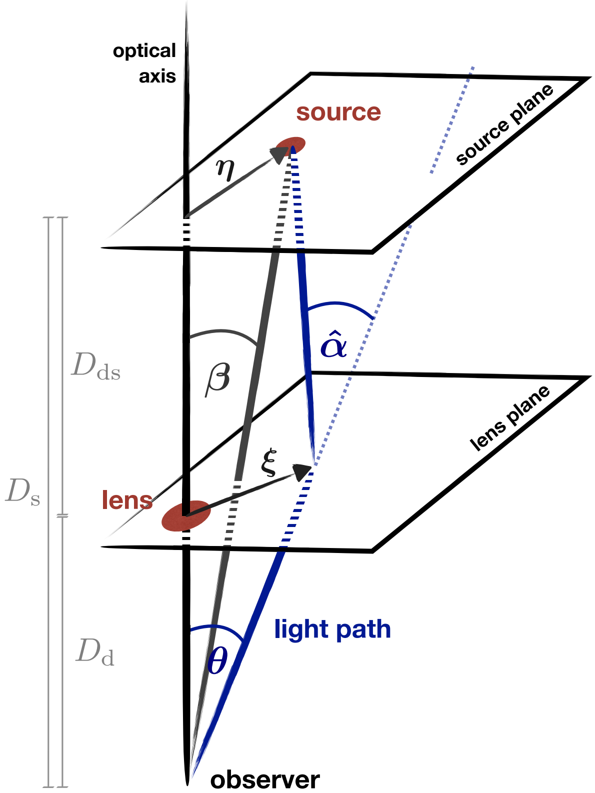

Figure 2.5: Sketch of a gravitational lensing system. The distances D_{s}, D_{d}, and D_{ds} are the angular diameter distances from the observer to the source plane, to the lens plane, and from the lens to source plane, respectively. The angles $\boldsymbol{\theta}$, $\boldsymbol{\beta}$, and $\hat{\alpha}$ are the apparent, true and deflection angles, respectively. Image adapted from Bartelmann and Schneider (2001) by Sandra Unruh.

In Fig. 2.5 a sketch of a typical gravitational lens system is displayed. A *source* is located at the distances D_{s} from the observer, with a mass concentration (*lens*) at distance D_{d}. An optical axis (dashed line) connects the observer and the centre of the mass concentration. The lens and source planes are both perpendicular to the optical axis, where the lens plane is at the mass concentration at distance D_{d} and the source plane is at the distance of the source D_{s}. The intersections of the optical axis and the planes are chosen as the origins of the respective coordinate systems. A light beam emitted from the source at the point $\boldsymbol{\eta}$ or angle $\boldsymbol{\beta} = \boldsymbol{\eta}/D_{\mathrm{s}}$ in the source plane intersects the lens plane at the point $\boldsymbol{\xi}$ or angle $\boldsymbol{\theta} = \boldsymbol{\xi}/D_{\mathrm{d}}$ and is deflected by an angle $\hat{\boldsymbol{\alpha}}$. These quantities are all two-dimensional vectors. From the theorem of intersecting lines, it follows that the source is observed in the direction $\boldsymbol{\theta}$ and is given by the lens equation,

$$\boldsymbol{\beta} = \boldsymbol{\theta} - \frac{D_{\mathrm{ds}}}{D_{\mathrm{s}}}\hat{\boldsymbol{\alpha}} =: \boldsymbol{\theta} - \boldsymbol{\alpha} \, , \tag{2.61}$$

where $\boldsymbol{\alpha}$ is the *scaled deflection angle*. The scaled deflection angle can also be expressed in terms of the surface mass density

$$\Sigma(\boldsymbol{\xi}) = \int \mathrm{d}r \, \rho(\xi_1, \xi_2, r) \, , \tag{2.62}$$

with $\boldsymbol{\xi} = (\xi_1, \xi_2)$ and r the propagation direction of the light ray, as

$$\boldsymbol{\alpha}(\boldsymbol{\theta}) = \frac{1}{\pi} \int \mathrm{d}^2\theta' \kappa(\boldsymbol{\theta}') \frac{\boldsymbol{\theta} - \boldsymbol{\theta}'}{|\boldsymbol{\theta} - \boldsymbol{\theta}'|^2} \, . \tag{2.63}$$

The definition of the dimensionless surface mass density or convergence is

$$\kappa(\boldsymbol{\theta}) = \frac{4\pi G}{c^2}\frac{D_\mathrm{d}D_\mathrm{ds}}{D_\mathrm{s}}\Sigma(\boldsymbol{\theta}) =: \frac{\Sigma(\boldsymbol{\theta})}{\Sigma_\mathrm{crit}}\,, \tag{2.64}$$

where Σ_crit is the critical surface mass density. Given the definition of the convergence and the identity $\nabla \ln|\boldsymbol{\theta}| = \boldsymbol{\theta}/\boldsymbol{\theta}^2$, the lensing potential Ψ is defined, as

$$\Psi(\boldsymbol{\theta}) = \frac{1}{\pi}\int \mathrm{d}^2\theta' \;\kappa(\boldsymbol{\theta}')\;\ln(|\boldsymbol{\theta} - \boldsymbol{\theta}'|)\,, \tag{2.65}$$

such that $\boldsymbol{\beta}$ is related to the lensing potential by

$$\boldsymbol{\beta} = \boldsymbol{\theta} - \nabla\Psi\,. \tag{2.66}$$

This also allows to determine the Poisson equation in two dimensions as

$$\nabla^2\Psi = 2\kappa\,. \tag{2.67}$$

Taking the gradient of Eq. (2.66) with respect to $\boldsymbol{\theta}$, it follows

$$\partial_j\beta_i = \delta_{ij} - \partial_i\partial_j\Psi =: \mathcal{A}_{ij}, \tag{2.68}$$

where $\mathcal{A}$ is the Jacobian determinant, and is given by

$$\mathcal{A}(\boldsymbol{\theta}) = \left(\delta_{ij} - \frac{\partial^2\Psi}{\partial\theta_i\partial\theta_j}\right) =: \begin{pmatrix} 1-\kappa-\gamma_1 & -\gamma_2 \\ -\gamma_2 & 1-\kappa+\gamma_1 \end{pmatrix} = (1-\kappa)\begin{pmatrix} 1-g_1 & -g_2 \\ -g_2 & 1-g_1 \end{pmatrix}\,, \tag{2.69}$$

where the *complex shear* $\gamma = \gamma_1 + \mathrm{i}\,\gamma_2 = |\gamma|\mathrm{e}^{2\mathrm{i}\phi}$ and the reduced shear

$$g \equiv \frac{\gamma}{1-\kappa} = \frac{|\gamma|}{1-\kappa}\mathrm{e}^{2\mathrm{i}\phi}\,, \tag{2.70}$$

got introduced, where the phase ϕ is the orientation of distortion. The reduced shear g is as γ a complex number. As illustrated in Fig. 2.6, the term $1-\kappa$ only yields an isotropic stretching of the image without any shape distortion. The components of g determine the change of shape from the source to the image. For instance, it can be shown that a circular source of unit radius is mapped onto an ellipse with axes $|(1-\kappa)(1+|g|)|^{-1}$ and $|(1-\kappa)(1-|g|)|^{-1}$.

Furthermore, it is often more convenient to express the shear relative to a direction φ instead of a reference Cartesian coordinate frame. Since the shear is polar, it must be multiplied by $\exp(-2i\psi)$ for a rotation of ψ, such that the rotated shear $\gamma_\mathrm{rot}(\boldsymbol{\theta})$ is given by

$$\gamma_\mathrm{rot}(\boldsymbol{\theta}) = -\mathrm{e}^{-2\mathrm{i}\varphi}\,\gamma(\boldsymbol{\theta}) =: \gamma_\mathrm{t}(\boldsymbol{\theta};\varphi) + \mathrm{i}\,\gamma_\times(\boldsymbol{\theta};\varphi)\,, \tag{2.71}$$

where γ_t is the *tangential shear* and $\gamma_\times$ is the *cross shear.* Given the definition of the tangential shear, an important relation between the mean convergence and mean tangential shear on a circle of radius θ is

$$\langle\gamma_\mathrm{t}\rangle(\theta) = \bar{\kappa}(<\theta) - \langle\kappa\rangle(\theta)\,, \tag{2.72}$$

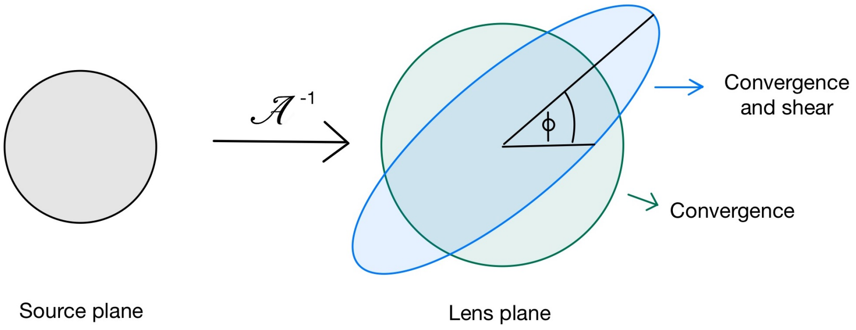

Figure 2.6: Illustration of the mapping of a circular shape to an ellipse by the inverse Jacobian $\mathcal{A}^{-1}$. In the absence of shear, the convergence κ modifies the radius of the image. The shear is responsible for the change into an ellipse, whereas the orientation depends on the phase of the shear.

where $\bar{\kappa}$ is the mean convergence inside θ.

A big challenge of gravitational lensing is the mass-sheet degeneracy (MSD; Falco et al., 1985), which provides a transformation of the mass profile, which leaves all lensing observables exactly invariant. In particular, this means that $\kappa(\boldsymbol{\theta})$ cannot be distinguished from the whole family of lens models defined as

$$\kappa_\alpha(\boldsymbol{\theta}) = (1-\alpha) + \alpha\,\kappa(\boldsymbol{\theta})\,. \tag{2.73}$$

The first term adds a homogeneous surface mass density to the mass distribution, and the second term scales the original surface mass density. One consequence of the MSD is the introduction of the aperture statistic described later.

2.2.2 Weak gravitational lensing

The investigation of strongly distorted images as arcs, complete rings, or even multiple images belong to the regime of *strong lensing*, where $\kappa \gtrsim 1$. However, we are interested in the *weak lensing* regime, where $\kappa \ll 1$ or the Jacobi matrix $\mathcal{A}$ is close to unity, which implies as seen in Eq. (2.68) weak distortions (see Bartelmann and Schneider, 2001, for a review). Since the intrinsic shape of a galaxy is larger than the shape distortion due to weak lensing, it is not possible to measure the weak lensing shape distortion of each galaxy individually. However, it is possible to measure the effect of weak lensing statistically. Assuming that the intrinsic orientation of galaxies is uncorrelated, averaging over many galaxy shapes yields shape distortion caused by gravitational lensing. Therefore, weak lensing is an ideal statistical tool for the measurements of the matter distribution.

To measure the shapes and shears of galaxies, the ellipticity of a galaxy needs to be defined. Assuming the brightness distribution, $I(\boldsymbol{\theta})$, of an image is isolated in the sky, then the centre of the image is defined as

$$\bar{\boldsymbol{\theta}} = \frac{\int \mathrm{d}^2\theta\, I(\boldsymbol{\theta})\, q_I[I(\boldsymbol{\theta})]\,\boldsymbol{\theta}}{\int \mathrm{d}^2\theta\, I(\boldsymbol{\theta})\, q_I[I(\boldsymbol{\theta})]}\,, \tag{2.74}$$

where $q_I(I)$ is a suitably chosen weight function. The second brightness moments are defined as

$$Q_{ij} = \frac{\int \mathrm{d}^2\theta \, I(\boldsymbol{\theta}) \, q_I[I(\boldsymbol{\theta})] \, (\theta_i - \bar{\theta}_i) \, (\theta_j - \bar{\theta}_j)}{\int \mathrm{d}^2\theta \, I(\boldsymbol{\theta}) \, q_I[I(\boldsymbol{\theta})]} \, . \tag{2.75}$$

The size of the image is described by the trace of Q, and ellipticities are given by the traceless part as

$$\epsilon = \frac{Q_{11} - Q_{22} + 2\mathrm{i}Q_{12}}{Q_{11} + Q_{22} + 2(Q_{11}Q_{22} - Q_{12}^2)^{1/2}} \, . \tag{2.76}$$

If Q is multiplied by a constant factor, the ellipticities remain unchanged, which is important since the ellipticity should not depend on the size of the image. By defining in analogy the second brightness moments Q^{s} for the sources by just exchanging $\boldsymbol{\theta}$ with $\boldsymbol{\beta}$ in Eq. (2.75) the relation

$$Q^{\mathrm{s}} = AQA \tag{2.77}$$

follows, which results with Eq. (2.69) in

$$\epsilon^{\mathrm{s}} = \frac{\epsilon - g}{1 - g^* \epsilon} \quad \text{and} \quad \epsilon = \frac{\epsilon^{\mathrm{s}} + g}{1 + g^* \epsilon^{\mathrm{s}}} \, . \tag{2.78}$$

With the assumption that in the Universe, the intrinsic orientation galaxies are random, the expectation value, $\langle \rangle$, of source ellipticities vanishes, $\langle \epsilon^{\mathrm{s}} \rangle = 0$, such that in the weak lensing regime, with $\kappa \ll 1$,

$$\gamma \approx g \approx \langle \epsilon \rangle \, . \tag{2.79}$$

This relation implies that the averaged ellipticity over N galaxies in a local region provides an unbiased estimate of the local reduced shear, where the noise of this estimator is the so-called shape noise and is determined by the intrinsic ellipticity dispersion

$$\hat{\sigma}_\epsilon = \sqrt{\epsilon^{\mathrm{s}} \epsilon^{\mathrm{s}*}} \, . \tag{2.80}$$

The standard deviation on the averaged ellipticity is given by $\hat{\sigma}_\epsilon / \sqrt{N}$, such that the noise becomes smaller the more galaxies are used for the average.

2.2.3 Cosmic shear

This section reviews the principles of cosmic shear.

In order to determine the effective convergence the three-dimensional convergence is projected along the comoving line-of-sight, χ, weighted by the redshift distribution of sources, $n_{\mathrm{s}}(z)\mathrm{d}z = n_{\mathrm{s}}^{\chi}(\chi)\mathrm{d}\chi$ as

$$\kappa(\boldsymbol{\theta}) = \int \mathrm{d}\chi \, n_{\mathrm{s}}^{\chi}(\chi) \, \kappa(\boldsymbol{\theta}, \chi) \tag{2.81}$$

$$= \frac{3H_0^2 \Omega_{\mathrm{m}}}{2c^2} \int \mathrm{d}\chi \, g(\chi) \, f_K(\chi) \, \frac{\delta(f_K(\chi)\boldsymbol{\theta}, \chi)}{a(\chi)} \tag{2.82}$$

where δ is the three-dimensional matter density contrast, f_K is defined by Eq. (2.3), and

$$g(\chi) = \int_{\chi}^{\infty} \mathrm{d}\chi' \; n_{\mathrm{s}}^{\chi}(\chi') \, \frac{f_K(\chi' - \chi)}{f_K(\chi')} \tag{2.83}$$

is the source redshift-weighted lens efficiency factor. By considering the projected κ as a two-dimensional random field, we define similar to Eq. (2.33) that

$$(2\pi)^2 \, \delta_{\mathrm{D}}(\boldsymbol{\ell} + \boldsymbol{\ell}') P_{\kappa\kappa}(\ell) = \langle \hat{\kappa}(\boldsymbol{\ell}) \, \hat{\kappa}(\boldsymbol{\ell}') \rangle \ , \tag{2.84}$$

where $\hat{\kappa}$ is the Fourier transformation of κ, and the *projected convergence power spectrum*

$$P_{\kappa\kappa}(\ell) = \frac{9 H_0^4 \, \Omega_{\mathrm{m}}^2}{4 c^4} \int_0^{\infty} \mathrm{d}\chi \; \frac{g^2(\chi)}{a^2(\chi)} \, P(\ell / f_K(\chi), \chi) \ . \tag{2.85}$$

Similarly, the angular power spectrum of the projected galaxy density field, $P_{gg}(\ell)$, or the cross-correlation of galaxies and matter, $P_{\kappa g}(\ell)$, can be determined with the corresponding $n(z)$ to

$$P_{i,j}(\ell) = \int_0^{\infty} \mathrm{d}\,\chi \frac{q_i(\chi) \, q_j(\chi)}{f_K^2(\chi)} \; P(\ell / f_K(\chi), \chi) \, , \tag{2.86}$$

where the indices i, j are placeholder for either the galaxy g or convergence κ projection, such that $q_g(\chi) = n_{\mathrm{l}}(z[\chi]) \frac{\mathrm{d}z[\chi]}{\mathrm{d}\chi}$ and the lensing efficiency

$$q_\kappa(\chi) = \frac{3 \Omega_{\mathrm{m}} H_0^2}{2 c^2} g(\chi) \frac{f_K(\chi)}{a(\chi)} \ . \tag{2.87}$$

In the projections above, the Limber approximation (Kaiser, 1992) is used, assuming that the weight functions $q(\chi)$ vary slightly. This assumption is valid if the angular scales on which, for instance, $P_{\kappa\kappa}$ is evaluated are small, and the weight functions are broad enough. As found by Kilbinger et al. (2017) the Limber approximation is accurate for cosmic-shear power spectrum at the sub-percent level for $\ell > 3$.

Next, using the tangential and cross shear definition (Eq. 2.71) the two-point correlation functions (2PCF), $\xi_\pm$ (Kaiser, 1992), are formally defined as

$$\xi_\pm(\theta) = \langle \gamma_{\mathrm{t}} \gamma_{\mathrm{t}} \rangle(\theta) \pm \langle \gamma_\times \gamma_\times \rangle(\theta) \, . \tag{2.88}$$

These quantities can also be expressed in terms of the projected convergence power spectrum to

$$\xi_+(\theta) = \int_0^{\infty} \frac{\mathrm{d}\ell \, \ell}{2\pi} J_0(\ell\theta) \, P_\kappa(\ell) \quad \text{and} \quad \xi_-(\theta) = \int_0^{\infty} \frac{\mathrm{d}\ell \, \ell}{2\pi} J_4(\ell\theta) \, P_\kappa(\ell) \, , \tag{2.89}$$

where $J_n(x)$ is the n-th Bessel function of first kind. The $\xi_\pm$ are not independent of each other as one can derive

$$\int_0^{\infty} \frac{\mathrm{d}\ell \, \ell}{2\pi} J_0(\ell\theta) \, \xi_+(\theta) = \int_0^{\infty} \frac{\mathrm{d}\ell \, \ell}{2\pi} J_4(\ell\theta) \, \xi_-(\theta) \, . \tag{2.90}$$

However, the observed shear field generally does not fulfil this relation due to noise and other systematic effects. In particular, 2PCF are a mixture of *E-modes*, which are expected to carry the cosmological signal and satisfy Eq. (2.90), and *B-modes*, which do not satisfy Eq. (2.90). B-modes can only be created by a variety of systematic effects like IA or violations of the Born approximation and, therefore, provide a valuable null test. As a result of this mixing of modes, the $\xi_\pm$ are unsuitable for systematic tests that utilise B-modes.

Schneider et al. (2010) introduced 2PCF defined on a finite angular range $\{\theta_{\rm min}, \theta_{\rm max}\}$ that separates all well-defined E- and B-modes within that range, and removes any ambiguous modes that are not uniquely identified as E- or B-modes. This complete orthogonal sets of E/B-integrals (COSEBIs) form discrete values and can be measured through 2PCFs as

$$E_n = \frac{1}{2}\int_{\theta_{\rm min}}^{\theta_{\rm max}} \mathrm{d}\theta\, \theta\, [T_{+n}(\theta)\xi_+(\theta) + T_{-n}(\theta)\xi_-(\theta)] \ , \tag{2.91}$$

$$B_n = \frac{1}{2}\int_{\theta_{\rm min}}^{\theta_{\rm max}} \mathrm{d}\theta\, \theta\, [T_{+n}(\theta)\xi_+(\theta) - T_{-n}(\theta)\xi_-(\theta)] \ , \tag{2.92}$$

where $T_{\pm n}$ are filter functions defined for the given angular range $\{\theta_{\rm min}, \theta_{\rm max}\}$.

B-modes can also emerge from the intrinsic correlations of galaxy ellipticities, known as IA (Joachimi et al., 2015). The correlator of galaxies' ellipticities at redshift z_i with the ellipticities of galaxies at redshift $z_j > z_i$ read as

$$\langle \epsilon_i \epsilon_j^* \rangle = \langle \gamma_i \gamma_j^* \rangle + \langle \epsilon_i^{\rm s} \epsilon_j^{\rm s*} \rangle + \langle \epsilon_i^{\rm s} \gamma_j^* \rangle + \langle \gamma_i \epsilon_j^{\rm s*} \rangle \, . \tag{2.93}$$

The first term $\langle \gamma_i \gamma_j^* \rangle$, known as the GG term, is the quantity for a cosmological analysis. The second term $\langle \epsilon_i^{\rm s} \epsilon_j^{\rm s*} \rangle$, known as the II term, is generated by the fact that galaxies align with each other. The last two terms are known as the GI terms, which are generated from the fact that galaxies align with the LSS that also contributes to the gravitational deflection of light from background galaxies. The GI term $\langle \gamma_i^* \epsilon_j^{\rm s} \rangle$, is expected to vanish as the shear acting on a galaxy in the foreground z_i cannot be affected by the ellipticity of a galaxy in background z_j. The term II is only important for galaxies that are in a close neighbourhood, $\langle \epsilon_i^{\rm s} \epsilon_j^{\rm s*} \rangle \neq 0$ for $z_i \approx z_j$. Hence, if redshift information is available (e.g., photometric redshifts), then galaxy distribution with similar redshifts should not be correlated to get an unbiased cosmic shear signal. The non-vanishing GI term, however, is important for adjacent redshift bins and becomes stronger with increasing distance between bins, since it depends on the lensing efficiency q_κ.

2.2.4 Aperture Statistics

One of the major problems of determining the mass profile of clusters from weak lensing techniques is the MSD, which corresponds to adding a uniform surface mass density. However, weak lensing is very well suited to finding mass concentrations and measuring mass density distributions. This is achieved by defining quantities in terms of the surface mass density, which are invariant under the MSD, summarised in the so-called *aperture statistics*.

Given a convergence field $\kappa(\boldsymbol{\theta})$, the aperture mass map is defined as

$$M_{\mathrm{ap}}(\boldsymbol{\theta}) := \int \mathrm{d}^2\theta' \, \kappa(\boldsymbol{\theta} + \boldsymbol{\theta}') \, U(|\boldsymbol{\theta}'|) \,, \tag{2.94}$$

where $\boldsymbol{\theta}$ is the flat sky position, and $U(\vartheta)$ is a compensated, axisymmetric filter function, such that $\int \vartheta \, U(\vartheta) \, \mathrm{d}\vartheta = 0$. The compensation of U ensures that adding a uniform surface mass density does not affect the aperture mass. The aperture mass, M_{ap}, can also be expressed in terms of the tangential shear γ_{t} as

$$M_{\mathrm{ap}}(\boldsymbol{\theta}) = \int \mathrm{d}^2\theta' \, \gamma_{\mathrm{t}}(\boldsymbol{\theta} + \boldsymbol{\theta}') \, Q(|\boldsymbol{\theta}'|) \,, \tag{2.95}$$

where

$$Q(\vartheta) = \frac{2}{\vartheta^2} \int_0^{\vartheta} \mathrm{d}\vartheta' \, \vartheta' \, U(\vartheta') - U(\vartheta) \,, \tag{2.96}$$

and can be determined by Eq. (2.72) and the fact that U is compensated. The inversion from filter Q to U is given by

$$U(\vartheta) = 2 \int_{\vartheta}^{\infty} \mathrm{d}\vartheta' \, \frac{Q(\vartheta')}{\vartheta'} - Q(\vartheta) \,. \tag{2.97}$$

This allows working in principle either with convergence maps or shear catalogues.

Another important definition for this work is the aperture number counts, or simply aperture number (Schneider, 1998), where the convergence in Eq. (2.94) is replaced by the foreground galaxy number count $n(\boldsymbol{\theta})$,

$$N_{\mathrm{ap}}(\boldsymbol{\theta}) := \int \mathrm{d}^2\theta' \, n(\boldsymbol{\theta} + \boldsymbol{\theta}') \, U(|\boldsymbol{\theta}'|) \,. \tag{2.98}$$

2.2.5 Density split statistic method

Using the quantities defined so far, the general idea of the DSS is as follows:

1. Determine the aperture number, N_{ap}, by use of Eq. (2.98). An illustration of a flat-sky field is shown in the left panel of Fig. 2.7.
2. Divide the area into quantiles Q according to the aperture number N_{ap}, illustrates in the middle panel of Fig. 2.7. For this illustration, five quantiles are used.
3. Correlate all pixels belonging to one quantile with the shear of the background galaxies to measure the mean tangential shear in the corresponding quantiles $\langle \gamma_{\mathrm{t}} | Q \rangle$, shown in the right panel of Fig. 2.7.

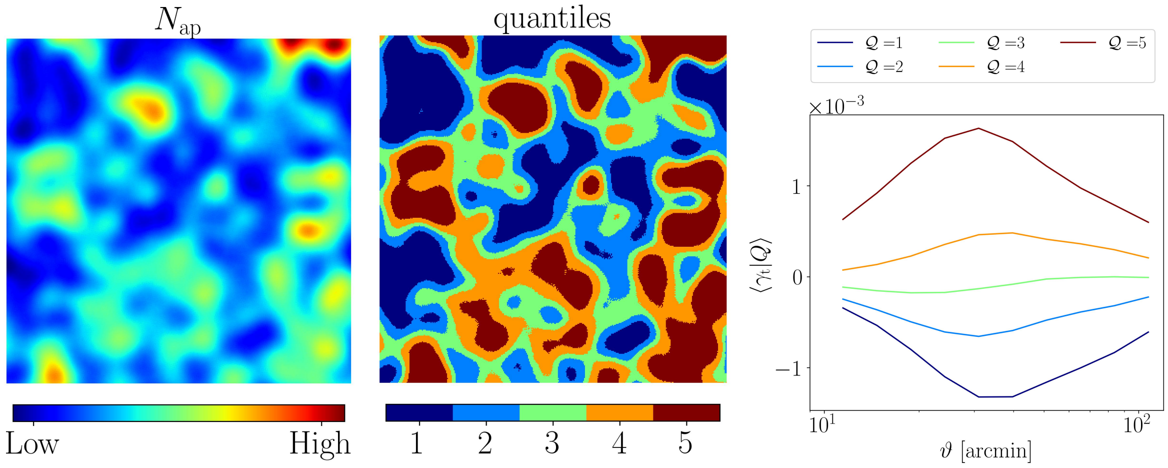

Figure 2.7: Illustration of a $N_{\rm ap}$ field on the left, the corresponding five quantiles in the middle, and on the right, the resulting mean tangential shear signals.

The DSS was introduced by Gruen et al. (2016) and was applied to real data for the first time in G18 to constrain cosmological parameters from measurements of the DES First Year and SDSS data. For this analysis, they used the model derived in F18, which is based on LDT approaches and log-normal approximations thereof to model the matter PDF, and on perturbation theory to determine higher-order moments of the density field.

Since the DSS captures information from the shape and amplitude of the shear profiles and the clustering of foreground galaxies according to which the quantiles are arranged, it counts as a higher-order statistic. Its main advantage is that it breaks the $\Omega_{\rm m}$-σ_8 degeneracy from which shear two-point statistic normally suffers. Furthermore, the DSS is also very powerful in measuring the galaxy bias.

2.3 Statistical methods

2.3.1 Probability density distributions

The following chapters use several different PDFs. The simplest is the multivariate normal or Gaussian distribution written as

$$p(\boldsymbol{x}|\boldsymbol{\mu},C) = \frac{1}{(2\pi)^{N/2}\sqrt{\det C}} \exp\left[-\frac{1}{2}(\boldsymbol{x}-\boldsymbol{\mu})^{\rm t}C^{-1}(\boldsymbol{x}-\boldsymbol{\mu})\right] , \tag{2.99}$$

where $\boldsymbol{x}$ is the multidimensional data vector, $\boldsymbol{\mu}$ is the expectation value of the same dimension, and C is the corresponding covariance matrix.

Another PDF of large relevance is a zero-mean shifted log-normal random field z, which is defined as

$$z : \mathbb{R}^D \to \mathbb{R} : \boldsymbol{x} \to z(\boldsymbol{x}) = \exp[n(\boldsymbol{x})] - \lambda \tag{2.100}$$

where n is a homogeneous and isotropic normal field with mean μ and variance σ^2, and the shift parameter $\lambda = \exp\left(\mu + \sigma^2/2\right)$, which ensures that the mean vanishes for z. The one-point distribution of the random field z is then given by (Hilbert et al., 2011)

$$p(z|\lambda,\sigma) = \begin{cases} \frac{1}{\sqrt{2\pi}(z+\lambda)\sigma} \exp\left(-\frac{1}{2\sigma^2}[\ln(z/\lambda+1)+\sigma^2/2]^2\right) & \text{for } z > -\lambda \\ 0 & \text{otherwise} \end{cases}, \tag{2.101}$$

where the negative of the shift parameter λ defines the lower limit of possible z values.

An important PDF for the parameter estimation is the t-distribution (Gosset, 1908), which arises when estimating the mean of a normally distributed population if the sample size is small and the population's standard deviation is unknown. This is the case for many cosmological situations since there is only one Universe to observe, and therefore, in many cases, only an estimate of the covariance matrix is available. For a multidimensional data vector $\boldsymbol{x}$, with mean $\boldsymbol{\mu} = \mathrm{E}[\boldsymbol{x}]$ and variance $\mathrm{Var}[\boldsymbol{x}] = \frac{\nu}{\nu-2}R$ for $\nu > 2$, where ν is the number of degrees of freedom (d.o.f.) and R the scale matrix defined trough the covariance matrix C to $R = \frac{\nu-2}{\nu}C$, the multivariate t-distribution reads

$$p_{t,\nu}(\boldsymbol{x}|\boldsymbol{\mu},R) = \frac{\Gamma([\nu+n_\mathrm{d}]/2)}{\Gamma(\nu/2)(\nu\pi)^{n_\mathrm{d}/2}|R|^{1/2}}\left[1+(\boldsymbol{x}-\boldsymbol{\mu})^\mathrm{t}(\nu R)^{-1}(\boldsymbol{x}-\boldsymbol{\mu})\right]^{-\frac{\nu+n_\mathrm{d}}{2}}, \quad \text{for } \nu > 2\,, \tag{2.102}$$

where n_d is the dimension of the data vector, and Γ is the gamma function defined as

$$\Gamma(z) = \int_0^\infty \mathrm{d}x\, x^{z-1}\mathrm{e}^{-x}\,. \tag{2.103}$$

A frequently utilised PDF that is used if the probability of a given number of events occurs with a constant mean rate in a fixed interval of time or space without being influenced by previous events is the Poisson distribution (Haight, 1967). Given the mean, μ, the Poisson PDF is defined as

$$p_\mu(k) = \frac{\mu^k \mathrm{e}^{-k}}{k!}\,, \tag{2.104}$$

where k is a discrete random variable. The interesting property of a Poisson PDF is that its mean and variance are given by μ. Of interest for this work is also a super-Poissonian distribution, which is a PDF with a larger variance than a normal Poisson distribution while having the same mean. Conversely, a sub-Poissonian distribution has a smaller variance.

Lastly, another important PDF is the χ^2-distribution (Abramowitz and Stegun, 1972), defined as

$$p_\nu(x) = \begin{cases} \frac{1}{2^{\nu/2}\Gamma(k/2)} x^{\nu/2-1}\,\mathrm{e}^{-x/2} & \text{for } x > 0 \\ 0 & \text{otherwise} \end{cases}, \tag{2.105}$$

where ν is the d.o.f.. The expectation value is ν, and the variance is 2ν. The χ^2-distribution allows a judgement on the compatibility of a presumed functional relationship with empirically determined measurement points. In other words, since the expectation value of the χ^2-distribution is ν, it follows that under the assumption that the measurement points are normally distributed the reduced χ^2/ν should be close to one, if the variance of the measurement points are estimated correctly.

2.3.2 Parameter estimation

In the following chapters, several parameter estimations will be performed. More specifically, the aim is to interpret measured data $\boldsymbol{d}$ in terms of a model $\boldsymbol{m}$, which depends on some parameters $\boldsymbol{\Theta}$. In other words, the idea is to find the probability of the parameters $\boldsymbol{\Theta}$ given the observed data $\boldsymbol{d}$, which is called the posterior probability $p(\boldsymbol{\Theta}|\boldsymbol{d})$. From $p(\boldsymbol{\Theta}|\boldsymbol{d})$ the expectation values and the errors of the parameters can be estimated, where we use the Bayesian view of probability as a degree of belief rather than a frequency of occurrence in a set of trials. In most cosmological scenarios it is easier to calculate the opposite, which is the probability distribution of the data given some parameters, $p(\boldsymbol{d}|\boldsymbol{\Theta})$, and is also called the likelihood function $\mathcal{L}(\boldsymbol{\Theta})$. Using Bayes theorem (Bayes, 1763) it is connected to the posterior probability as

$$p(\boldsymbol{\Theta}|\boldsymbol{d}) = \frac{\mathcal{L}(\boldsymbol{\Theta})p(\boldsymbol{\Theta})}{p(\boldsymbol{d})}\,, \tag{2.106}$$

where $p(\boldsymbol{\Theta})$ is the prior knowledge of the parameters that may result from previous experiments or theory. If no previous information is available, the prior is often assumed to be a constant in a given range (flat prior). The denominator is the evidence defined as

$$p(\boldsymbol{d}) = \int \mathrm{d}\Theta\, \mathcal{L}(\boldsymbol{\Theta})p(\boldsymbol{\Theta})\,. \tag{2.107}$$

Since the evidence does not depend on the parameters, it is usually ignored, such that for flat priors

$$p(\boldsymbol{\Theta}|\boldsymbol{d}) \propto \mathcal{L}(\boldsymbol{\Theta})\,. \tag{2.108}$$

In order to estimate $p(\boldsymbol{\Theta}|\boldsymbol{d})$ in practice, a process called Markov chain Monte Carlo (MCMC) is used, which generates a set of points in the parameter space (MCMC chain) whose distribution function is the same as the target density, here $\mathcal{L}(\boldsymbol{\Theta})$ or for flat priors $p(\boldsymbol{\Theta}|\boldsymbol{d})$. The general idea of an MCMC is

1. Compute the target density at some random point in the parameter space, $\boldsymbol{\Theta}$.
2. Choose another point in the parameter space, $\boldsymbol{\Theta}'$, by taking a proposal step and calculating the target density at this point.
3. Determine the probability of acceptance. For instance, this could be

   $$p(\text{accept}) = \min\left[1, \frac{\mathcal{L}(\boldsymbol{\Theta}')}{\mathcal{L}(\boldsymbol{\Theta})}\frac{q(\boldsymbol{\Theta}|\boldsymbol{\Theta}')}{q(\boldsymbol{\Theta}'|\boldsymbol{\Theta})}\right]\,, \tag{2.109}$$

   where $q(\boldsymbol{\Theta}'|\boldsymbol{\Theta})$ is the proposal distribution, which describes the probability to move from point $\boldsymbol{\Theta}'$ to $\boldsymbol{\Theta}'$.
4. Depending on the acceptance repeat step 2 and 3 from $\boldsymbol{\Theta}$ or $\boldsymbol{\Theta}'$.

To ensure that the whole posterior distribution is sampled, the foregoing steps are performed from multiple *walker*, where each walker starts at a different point in parameter space.

The 68% ($1\,\sigma$) credible interval is then determined by the area that contains 68% of the generated points. The parameters that yield the highest posterior probability are called the maximum a-posterior (MAP),

$$\mathbf{\Theta}_{\mathrm{MAP}} = \underset{\mathbf{\Theta}}{\mathrm{argmax}}\,[p(\mathbf{\Theta}|\boldsymbol{d})]\ . \tag{2.110}$$

But in general, the MAP is not necessarily the point of the MCMC chain with the highest likelihood, since the sampling might have missed that point. Therefore, we run a maximisation process of the likelihood to report the MAP values instead of using the point with the highest likelihood of the MCMC chain.

As most cosmological studies deal with multiple parameter dimensions, it is suitable for the illustration of the posterior to marginalise over parameters. In general, a marginal distribution of m parameters of $\mathbf{\Theta}$ is obtained by integrating over the other $n-m$ parameters

$$p(\mathbf{\Theta}^{(m)}|\boldsymbol{d}) \int \mathrm{d}\Theta^{n-m}\, p(\mathbf{\Theta}|\boldsymbol{d})\,. \tag{2.111}$$

For the MCMC chain, this means ignoring all parameters except the ones of interest.

A common assumption to determine the posterior distribution is the usage of a Gaussian likelihood function (see Eq. 2.99), which is only valid if the individual data vector measured from n_{r} number of realisations that are used to determine the covariance matrix follows a Gaussian distribution. Furthermore, due to the finite number of realisations, the inverse of the covariance matrix is not noise-free or unbiased, which would only be the case for an infinite number of realisations according to the central limit theorem. To unbias the inverse of the covariance matrix, a general approach is to multiply the covariance matrix by the so-called Hartlap factor (Anderson, 2003; Hartlap et al., 2007)

$$h = (n_{\mathrm{r}} - 1)/(n_{\mathrm{r}} - n_{\mathrm{d}} - 2)\,. \tag{2.112}$$

However, only unbiasing with the Hartlap factor is not sufficient. Therefore, Percival et al. (2022) suggests a more accurate method to unbias an estimated covariance matrix $\tilde{C}$, which is a random variable itself. It uses a more general joint prior of the mean and covariance matrix as the Jeffreys prior proposed in equation 6 in Sellentin and Heavens (2016). Interestingly, their method leads to credible intervals, which can also be interpreted as confidence intervals, which are valid for a frequentist, and are a set of ranges that contain, for instance, 68% the true parameters in repeated trials. If the model vector $\mathbf{m}$ depending on n_θ parameters $\mathbf{\Theta}$ the likelihood function, or posterior distribution for flat priors, scales as

$$p\left(\mathbf{m}(\mathbf{\Theta})|\mathbf{d},\tilde{C}\right) \propto |\tilde{C}|^{-\frac{1}{2}}\left(1+\frac{\chi^2}{n_{\mathrm{r}}-1}\right)^{-m/2}\ , \tag{2.113}$$

which is a t-distribution, and

$$\chi^2 = [\mathbf{m}(\mathbf{\Theta}) - \mathbf{d}]^{\mathrm{T}}\,\tilde{C}^{-1}\,[\mathbf{m}(\mathbf{\Theta}) - \mathbf{d}]\ . \tag{2.114}$$

The power-law index m is

$$m = n_\theta + 2 + \frac{n_\mathrm{r} - 1 + B(n_\mathrm{d} - n_\theta)}{1 + B(n_\mathrm{d} - n_\theta)}\,, \tag{2.115}$$

with n_d being the number of elements of the model or data vector and

$$B = \frac{n_\mathrm{r} - n_\mathrm{d} - 2}{(n_\mathrm{r} - n_\mathrm{d} - 1)(n_\mathrm{r} - n_\mathrm{d} - 4)}\,. \tag{2.116}$$

A correlated formalism is proposed by Sellentin and Heavens (2016) and is recovered by setting $m = n_\mathrm{r}$. Finally, to unbias the covariance matrix $\tilde{C}$ we transform it as

$$\tilde{C}' = \frac{(n_\mathrm{r} - 1)\,[1 + B(n_\mathrm{d} - n_\theta)]}{n_\mathrm{r} - n_\mathrm{d} + n_\theta - 1}\tilde{C}\,. \tag{2.117}$$

In the real data analysis, reporting the goodness-of-fit can be done either in terms of the reduced χ^2/d.o.f. or in terms of the p-value, which is the probability of finding χ^2 values that are larger for the given d.o.f.. For both, the d.o.f. needs to be estimated, which naively is done by d.o.f. $= n_\mathrm{d} - n_\theta$. However, if parameters are correlated and others are constrained by prior knowledge, the actual d.o.f. is bigger than d.o.f. $= n_\mathrm{d} - n_\theta$. Therefore, to estimate the 'true' d.o.f. we create mock data vectors from a multivariate Gaussian distribution, where the mean is the model prediction at the MAP values, and the covariance is the matrix that was used to get the MAP. For each mock data vector we determined the lowest χ^2 value. The d.o.f. results then from fitting a χ^2-distribution to the PDF of these χ^2.

Finally, we note that the model prediction is too slow to run an MCMC, with several ten thousand model predictions. Hence, for some analysis steps, we used a Gaussian process regression (GPR) emulator to emulate the χ^2 values directly or used an emulation tool contained in CosmoPower (Spurio Mancini et al., 2022) to emulate the model vector itself. CosmoPower was first developed to emulate power spectra but can easily be adapted for arbitrary vectors. The advantage of CosmoPower is that it can be trained on a graphics processing unit (GPU) and also the MCMC can be run on a GPU, which enables MCMC predictions in a couple of minutes for $\sim 10^4$ steps per walker, and the number of walkers is just limited by the available memory of the GPU. To train the emulator, the model is computed at several thousand different parameters values distributed in a Latin hypercube. To quantify the accuracy of the emulator, we calculated the model at 500 independent points determined with the emulator or directly with the model. For these independent points, we found that the error of the emulator is better than 2% of the standard deviation of the measured data (95% confidence level).

3

Observed and simulated data

This chapter summarises all the simulated and observed data used in this work, which is based on my three publications:

- B20: Burger, P., Schneider, P., Demchenko, V., Harnois-Deraps, J., Heymans, C., Hildebrandt, H., and Unruh, S., 2020. An adapted filter function for density split statistics in weak lensing. Astronomy & Astrophysics, 642:A161. doi:10.1051/0004-6361/20203869.
- B22a: Burger, P., Friedrich, O., Harnois-Déraps, J., and Schneider, P., 2022a. A revised density split statistic model for general filters. Astronomy & Astrophysics, 661:A137. doi:10.1051/0004-6361/202141628.
- B22b: Burger, P., Friedrich, O., and Harnois-Déraps, J., Schneider, P., Asgari, M., Bilicki, M., Hildebrandt, H., Wright, A., Castro, T., Dolag, K., Heymans, C., Joachimi, B., Martinet, N., Shan, H., and Tröster, T., 2022b. KiDS-1000 Cosmology: Constraints from density split statistics. Submitted to Astronomy & Astrophysics. arXiv:2208.02171.

The individual contributions will be made clear in the following chapters. These papers are also attached in the appendix for more details. Most of the data are public, but some are provided by my co-authors, especially Joachim Harnois-Déraps, so I use the scientific wording ‘we’ in this chapter.

3.1 Observed data

In our analysis, we focused on the fourth data release (Kuijken et al., 2019) of KiDS (Kuijken et al., 2015; de Jong et al., 2015, 2017), which is a public survey by the European Southern Observatory[1]. KiDS is a survey designed for excellent weak lensing applications, producing high-quality images with VST-OmegaCAM. Due to the infrared data from its partner survey, VIKING (VISTA Kilo-degree Infrared Galaxy survey, Edge et al., 2013) galaxies are observed in nine optical and near-infrared bands, $ugriZYJHKs$, where the fourth data release has enormous control over redshift uncertainties (Hildebrandt et al., 2021). The fact that it contains $\sim 1000\,\mathrm{deg}^2$ of images, which reduce to $777.4\,\mathrm{deg}^2$ after masking gives the fourth data release the name

---

[1] Data products are publicly available through `http://kids.strw.leidenuniv.nl/DR4`

KiDS-1000. In the following, we will discuss the used lens and source catalogues in more detail.

3.1.1 Lens catalogues

As the lens catalogue, we used the bright sample of the KiDS-1000 release (KiDS-bright) described in Bilicki et al. (2021), with photometric redshifts, $z_{\rm ph}$, that are derived using $ugriZYJHK_s$ photometry from KiDS-1000 and the large amount of spectroscopic calibration data measured by GAMA. The KiDS-bright sample spans the redshift range of $0 < z \lesssim 0.6$; however, our analytical model is inaccurate for very small redshifts, and these low redshift estimates are uncertain, we excluded all galaxies with $z_{\rm ph} < 0.1$.

Following the description of Peacock and Bilicki (2018), we estimated the redshift distribution by taking advantage of the very good match between the GAMA spectroscopic sample and the KiDS-bright sample. However, it still has some uncertainties, so we investigate the impact of the resulting posterior if we use instead of the best-estimated $n_{\rm be}(z)$, the photometric redshift distribution $n_{\rm ph}(z)$, or the spectroscopic redshift distribution $n_{\rm sp}(z)$, coming from the cross-match of the KiDS-bright sample with GAMA; both also shown in Fig. 3.1. The best estimated

$$n_{\rm be}(z) = \int n_{\rm ph}(z_{\rm ph})\, p_{\delta z}\left(z_{\rm ph} - z\right)\, {\rm d}z_{\rm ph}\,. \tag{3.1}$$

results from smoothing the $n_{\rm ph}(z)$ of the KiDS-bright sample with a photo-z error model

$$p_{\delta z}(\Delta z) \propto \left(1 + \frac{\Delta z^2}{2as^2}\right)^{-a}\,, \tag{3.2}$$

where $\Delta z = z_{\rm ph} - z_{\rm sp}$ is used to determine the parameters a and s by fitting $p_{\delta z}$ to the KiDS-bright galaxies that also have GAMA spectroscopic redshifts[2]. The best-fit a and s values for our selection are provided in the top row of Table 3.1, where we verified their robustness by measuring similar values for individual tiles of the survey. Finally, we allow the $n_{\rm be}(z)$, the $n_{\rm ph}(z)$ and the $n_{\rm sp}(z)$ to shift along the redshift axis of the order of 0.01, which we have chosen as an upper estimate because we expect them to be at the same order as the source' mean redshift $\delta\langle z\rangle$.

In addition to the full KiDS-bright sample, we also used an empirical split between red and blue galaxies based on their location on the absolute r-band magnitude, M_r, and the rest-frame $u - g$ colour diagram. We then used the same approach for the full sample to estimate their underlying redshift distributions.

---

[2] In the arXiv version of B22b, we erroneously determined the a and s by using $\Delta z = (z_{\rm ph} - z_{\rm sp})/(1 + z_{\rm sp})$. This resulted in posteriors that are barely distinguishable. The MAP are also almost identical as seen for instance in Table 3 of B22b and Table 7.2. In that context, we also changed the notation from the best-estimated $n(z)$ to $n_{\rm be}(z)$, the photometric redshift distribution $n(z_{\rm ph})$ to $n_{\rm ph}(z)$, and the spectroscopic redshift distribution $n(z_{\rm sp})$ to $n_{\rm sp}(z)$.

Table 3.1: Overview of the observational KiDS-1000 data, describing the lens and source catalogues in the upper and lower parts of this Table, respectively. The $\delta\langle z\rangle$ for the sources are taken from Hildebrandt et al. (2021), whereas the measured ellipticity dispersion per component, σ_ϵ, are measured in Giblin et al. (2021), and the shear multiplicative m-bias correction are updated in van den Busch et al. (2022). The lenses' $\delta\langle z\rangle$ are unknown, but we expect them to be in the same order as the source' $\delta\langle z\rangle$, so we used 0.01 as an upper estimate of them. Table taken from B22b.

name	$n_{\rm eff}\,[\rm arcmin^{-2}]$	$\delta\langle z\rangle$	a	s
Full KiDS-bright sample	0.325	0.0 ± 0.01	2.509	0.018
Red KiDS-bright sample	0.131	0.0 ± 0.01	2.630	0.016
Blue KiDS-bright sample	0.165	0.0 ± 0.01	2.619	0.020
name	$n_{\rm eff}\,[\rm arcmin^{-2}]$	$\delta\langle z\rangle$	σ_ϵ	m-bias $\times 10^3$
Source sample bin 4	1.26	0.011 ± 0.0087	0.25	8 ± 12
Source sample bin 5	1.31	−0.006 ± 0.0097	0.27	12 ± 10

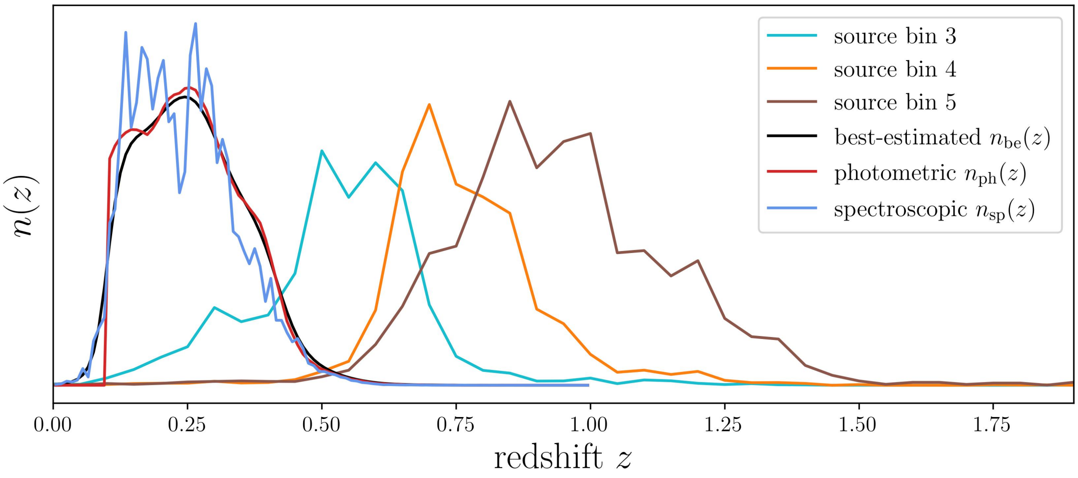

Figure 3.1: Redshift distributions, $n(z)$, of the galaxy samples. The cyan, orange, and brown lines show the third, fourth and fifth redshift bins of the KiDS-1000 data, as estimated in Hildebrandt et al. (2021). The lens sample is obtained from the KiDS-bright galaxies described in (Bilicki et al., 2021), where the blue line shows $n_{\rm sp}(z)$, the red line shows $n_{\rm ph}(z)$, and the black line shows our best-estimated $n_{\rm be}(z)$. Figure adapted from B22b.

3.1.2 Source catalogues

The KiDS-1000 cosmic shear catalogue consists of five tomographic bins, whose redshifts were calibrated using the self-organising map (SOM) method of Wright et al. (2020) and presented in Hildebrandt et al. (2021). However, if sources and lenses belong to the same gravitational potential, IA effects as discussed in Sect. 2.2.3 are important, such that we restricted our DSS analyses to the last two source bins. The uncertainty on the mean of the redshift distribution,

$\delta\langle z\rangle$, and the uncertainty on galaxy shear estimates are listed in the last two rows of Table 3.1.

3.1.3 Extracting the observed data vector

The aperture number in Eq. (2.98) assumes full knowledge of $n(\boldsymbol{\theta})$ on the sky, but in the observed data, it has to be modified in the presence of a mask $m(\boldsymbol{\theta})$. For a filter function U, with a finite filter radius Θ and exactly one transition from positive to negative values at $\theta_{\rm tr}$ the aperture number calculation modifies to

$$\begin{aligned} N_{\rm ap}(\boldsymbol{\theta}) = & \frac{\int_0^{\theta_{\rm tr}} U(\boldsymbol{\theta}')\,\mathrm{d}^2\theta'}{\int_0^{\theta_{\rm tr}} m(\boldsymbol{\theta}+\boldsymbol{\theta}')U(\boldsymbol{\theta}')\,\mathrm{d}^2\theta'} \int_0^{\theta_{\rm tr}} n(\boldsymbol{\theta}+\boldsymbol{\theta}')U(\boldsymbol{\theta}')\,\mathrm{d}^2\theta' \\ & + \frac{\int_{\theta_{\rm tr}}^{\Theta} U(\boldsymbol{\theta}')\,\mathrm{d}^2\theta'}{\int_{\theta_{\rm tr}}^{\Theta} m(\boldsymbol{\theta}+\boldsymbol{\theta}')U(\boldsymbol{\theta}')\,\mathrm{d}^2\theta'} \int_{\theta_{\rm tr}}^{\Theta} n(\boldsymbol{\theta}+\boldsymbol{\theta}')U(\boldsymbol{\theta}')\,\mathrm{d}^2\theta'\,. \end{aligned} \tag{3.3}$$

The integrals were measured on the curved sky using the HEALPY function SMOOTHING. By considering the negative and positive parts of the filter separately, we prevent, that missing area in the negative part of the filter from erroneously increases the $N_{\rm ap}$ or vice versa. Furthermore, we included only those pixels where the number of unmasked pixels within the given filter radius (effective area) is greater than 50% of the maximal area. For compensated filters, we restricted our selection to those pixels where the effective area for the positive and negative parts is greater than 50% of their maximal individual area. The 50% threshold was chosen to avoid as many corrupted pixels as possible without that the measured shear profiles are dominated by shot noise. The pixels that are above the threshold were then separated into different quantiles according to their aperture number. The correlation, which we call shear profiles, between the pixels of each quantile with shear of the background sources are measured with the TREECORR (Jarvis et al., 2004) software in 10 log-spaced bins with angular separation 10 arcmin $< \vartheta <$ 120 arcmin. The final data vector consists of the shear profiles and the mean aperture number of the highest two and lowest two quantiles. To avoid a singular covariance matrix, we had to exclude one quantile, as otherwise, different covariance matrix elements would be dependent on each other. This is because the average of all shear signals vanishes and the average over the mean aperture numbers of the quantiles are either fixed by the galaxy number density (positive filter) or vanish (compensated filter). We excluded the middle quantile as it has the lowest cosmological information. Overall we end up with a data vector of size $80 + 4 = 84$ elements.

3.2 Simulated data

This work aims to analyse the observed data described above by using an analytical model that predicts the DSS vector. However, to derive a filter function and a KiDS-1000 covariance matrix and to test, validate and calibrate the model, we made use of many different simulations. We restrict our description to the usage of the simulations, where detailed descriptions of the development of the simulations can be found in the attached papers.

3.2.1 Full-sky Log-normal Astro-fields Simulation Kit

Since an analytical covariance matrix for the DSS is currently unavailable, we needed to rely on a large set of simulations to estimate a reliable covariance matrix. As the DSS covariance matrices depend strongly on the used area from which the individual data vectors are measured, full-sky simulations are preferred against the small flat sky simulations, which would require a rescaling that biases the covariance matrix. Furthermore, since the mask $m(\boldsymbol{\theta})$ influences the resulting covariance matrix strongly, we use log-normal simulations created by the publicly available Full-sky Log-normal Astro-fields Simulation Kit (FLASK) tool[3] (Xavier et al., 2016). Log-normal random fields are a good approximation for the 1-point probability density function (PDF) of the weak lensing convergence/shear field (Hilbert et al., 2011; Xavier et al., 2016), and accurate enough for a good estimate of the covariance matrix for higher-order statistics (Gruen et al., 2018; Halder et al., 2021). For FLASK to predict projected density $\delta_{\mathrm{m,2D}}$ and shear maps, it needs to be provided with the angular power spectrum of the projected matter density field $P_{gg}(\ell)$, the projected convergence power spectrum $P_{\kappa\kappa}(\ell)$, and their combination $P_{\kappa g}(\ell)$, which are all determined by Eq. (2.86). Furthermore, FLASK needs the log-normal shift parameters, λ, for the convergence maps determined directly from the fitting formula equation (38) in Hilbert et al. (2011), and foreground density maps estimated from the model for a top-hat filter function.

We distribute galaxies using a Poisson distribution with parameter $\lambda = n(1 + b\,\delta_{\mathrm{m,2D}})$, where $b = 1.4$ is a constant linear galaxy bias estimated from preliminary analyses with a few realisations and $n = 0.325\,\mathrm{arcmin}^{-2}$ is the mean galaxy density of the bright sample. Lastly, we incorporate shape noise by use of Eq. (2.78), where the source ellipticities ϵ^{s} per pixel are generated by drawing random numbers from a Gaussian distribution with width

$$\sigma_{\mathrm{pix}} = \frac{\sigma_\epsilon}{\sqrt{n\,A_{\mathrm{pix}}}}\,, \tag{3.4}$$

where A_{pix} is the pixel area of the shear grid, shape noise per component $\sigma_\epsilon = \{0.254, 0.270\}$, and effective number density $n = \{1.26, 1.31\}\,\mathrm{arcmin}^{-2}$ for the two source bins.

Similar to the real data measurement, we used the HEALPY function SMOOTHING and used only pixels with an effective area greater than 50% of the maximal area. The corresponding shear profiles are measured also with the TREECORR software in 10 log-spaced bins with angular separation $10\,\mathrm{arcmin} < \vartheta < 120\,\mathrm{arcmin}$.

---

[3] Available here: `http://www.astro.iag.usp.br/~flask/`

3.2.2 The Millenium simulation

The MS is a N-body simulation and is described in Springel et al. (2005). In B20 we used the MS for the development of the adapted filter described in chapter 4. It consists of 64 pseudo-independent light cones of size $4 \times 4\,\mathrm{deg}^2$, where each of the Cartesian components of the shear was inferred from the lensing Jacobi matrix $\mathcal{A}$ on a 4096×4096 pixel grid for several source redshifts.

To create the galaxy number density field $n(\boldsymbol{\theta})$, we projected for each light cone the galaxies that were added to the simulation using a semi-analytical galaxy-formation model, with an SDSS r-band magnitude $m_r < 20.25\,\mathrm{mag}$. The magnitude cut was chosen such that the galaxy number density in the MS matches the one in Bilicki et al. (2018).

As B20 was done before the KiDS-1000 release, we mimicked the KiDS shear estimates by combining the shear information of each source plane weighted by the redshift distribution $n(z)$ of the third data release of the Kilo-Degree Survey (KV450), described in Hildebrandt et al. (2020). We considered only sources with $0.5 < z_{\mathrm{phot}} < 1.2$, such that our sources are mostly behind our low-redshift lenses. Since the MS is exclusively used to construct the adapted filter, we ignored shape noise.

3.2.3 Takahashi simulations

The full-sky N-body simulation described in Takahashi et al. (2017, hereafter T17), are used in B22a to test and validate the analytical model described in chapter 6.

With one out of 108 publicly available matter density contrast map δ, we created two realistic lens galaxy density maps, by projecting δ weighted by the corresponding $n(z)$ of the second and third redshift bins of the luminous red galaxies (LRG) sample constructed from the KiDS-1000 data (Vakili et al., 2019). For both projected density contrast maps δ_{2D}, we distributed galaxies following a Poisson distribution with parameter $\lambda = n(1 + b\,\delta_{\mathrm{2D}})$, where $b = \{1.72, 1.74\}$ is a constant linear galaxy bias, $n = \{0.028, 0.046\}\,\mathrm{arcmin}^{-2}$ is the galaxy number density.

We chose a noise-free shear grid at a single source plane located at $z = 0.8664$, which is at a noticeably higher redshift as the two LRG $n(z)$.

To estimate the uncertainties of the measured T17 signals, we divided the full-sky map into 48 sub-patches, such that each patch had a size of approximately $859.4\,\mathrm{deg}^2$. Although we used only one full T17 map to measure the signals, we used 10 full-sky maps divided into 48 sub-patches to measure a reliable covariance matrix from 480 realisations with shape noise. To create a realistic covariance matrix, we transformed the shear field into an observed ellipticity field using Eq. (2.78), where the source ellipticities ϵ^{s} per pixel are determined with Eq. (3.4) with an effective number density n and σ_ϵ that match the KiDS-1000 data. Finally, as the area of the sup-patches with an area of $859.4\,\mathrm{deg}^2$ is slightly larger than the KiDS-1000 area of $777.4\,\mathrm{deg}^2$, we re-scaled the covariance matrix by $859.4\,\mathrm{deg}^2/777.4\,\mathrm{deg}^2 \approx 1.1$.

To measure the quantities $\delta_{\mathrm{m},U}$, N_{ap} on the full-sky we used the HEALPY function SMOOTHING. The tangential shear profiles $\langle\gamma_{\mathrm{t}}|Q\rangle$ were measured for each quantile Q by the software TREECORR in 15 log-spaced bins with angular separation $\Theta/20 < \vartheta < \Theta$, where Θ is the size of the used filter. For the top-hat filter, we measured the shear signal up to $120'$.

3.2.4 Scinet Light Cone Simulations

The N-body Scinet Light Cone Simulations (SLICS), described in Harnois-Déraps et al. (2018), are used in B20 to compare the performance of the adapted filter to a top-hat filter, in B22a to construct a KiDS-1000 like covariance matrix, and in B22b to analyse the galaxy bias model. In total the SLICS are a set of over 800 fully independent realizations with underlying cosmological parameters fixed to $\Omega_{\mathrm{m}} = 0.2905$, $\Omega_{\Lambda} = 0.7095$, $\Omega_{\mathrm{b}} = 0.0473$, $h = 0.6898$, $\sigma_8 = 0.826$ and $n_{\mathrm{s}} = 0.969$ (see Hinshaw et al., 2013).

For the work in B20, the co-author Joachim Harnois-Déraps provided us with source galaxies that mimic the KV450 data. These mock galaxies are placed at random angular coordinates on $100\,\mathrm{deg}^2$ flat-sky light cones, with the KV450 number density $n = 6.93/\mathrm{arcmin}^2$ and $n(z)$ from Hildebrandt et al. (2020). The observed ellipticities ϵ^{obs} are obtained again by use of Eq. (2.78), where the source ellipticity ϵ^{s} are generated by drawing random numbers from a Gaussian distribution with width $\sigma_\epsilon = 0.29$. To decrease the overlap between the lens $n(z)$, we selected only photometric redshifts inside $0.5 < z_{\mathrm{phot}} < 1.2$, resulting in a galaxy number density of $n_{\mathrm{gal}} = 5.17/\mathrm{arcmin}^2$. For the lens sample in B20, we used GAMA SLICS mocks, which are based on a halo occupation distribution (HOD) prescription (Smith et al., 2017). The HOD describes the biasing of galaxies to trace the underlying dark matter density field by the probability that a halo of mass M contains N galaxies with a certain property. For the GAMA mocks, the galaxy number density is $n \sim 0.25\,,\mathrm{arcmin}^{-2}$, and on large scales, they follow a linear bias of about 1.2.

For the work in B22a, we used the KiDS-1000-like sources and KiDS-LRG-like lenses provided by co-author Joachim Harnois-Déraps to determine a covariance matrix. For these mocks, the source galaxy number density and $n(z)$ are matched to the one used in Asgari et al. (2021). The source mock galaxies were placed at random angular coordinates in $100\,\mathrm{deg}^2$ light cones, whereas the shear signal γ and the observed ellipticities ϵ^{obs} were obtained from several lensing maps following the KiDS-1000 fourth and fifth tomographic bins. Specifically, we used $\sigma_\epsilon = 0.25$ and 0.27 for the source bins, as reported in Giblin et al. (2021). To create the lens sample, galaxies were placed following a Poisson distribution with parameter $\lambda = n(1 + b\,\delta_{\mathrm{m,2D}})$ for the second and third tomographic bin of the LRG galaxies described in Vakili et al. (2019). In particular, the same linear galaxy bias $b = \{1.72, 1.74\}$, galaxy number density $n = \{0.028, 0.046\}$ gal/arcmin^2, and $n(z)$ as for the T17 were used.

For the work in B22b, we used the GAMA lens mocks used in B20 combined with the KiDS-1000-like sources used in B22a to test the galaxy bias model.

As the SLICS are flat-sky simulations, we used the SCIPY (Virtanen et al., 2020) function CONVOLVE to calculate the aperture number, and again TREECORR to measure the tangential shear profiles.

3.2.5 Cosmology-dependent Scinet Light Cone Simulations

The cosmo-SLICS, described in Harnois-Déraps et al. (2019), were used in B20 to investigate the sensitivity of the top-hat filter and the adapted filter to cosmological parameters, in B22a to validate the analytical model on an independent simulation suite, and in B22b to test the robustness of the model if the mocks are infused with IA.

The cosmo-SLICS are a suite of weak lensing simulations sampling 26 points in a broad ΛCDM parameter space distributed in a Latin hypercube. For every cosmology, 50 pseudo-independent realisations with $100\,\mathrm{deg}^2$ light cones are available. In these simulations, the matter density Ω_m, the dimensionless Hubble parameter h, the normalisation of the matter power spectrum σ_8 and the time-independent dark energy equation-of-state w_0 are varied over a range that is large enough to complement the analysis of current weak lensing data (see Hildebrandt et al., 2020).

For the work in B20, we were provided with KV450-like catalogues following the same pipeline as for the SLICS mocks, with the same galaxy number density and redshift distribution $n(z)$. However, the HOD-based mocks are unavailable for the lenses. To generate GAMA-like mocks, galaxies were distributed with a constant galaxy bias model of one to the projected density maps that follow the GAMA $n(z)$.

For the work in B22a, the cosmo-SLICS mocks were used for the validation of the model and were identically produced as the SLICS mocks. The only difference is that we used noise-free shear signals for this validation.

For the work in B22b, we used mocks that are created as in B22a to investigate the impact of IA. Specifically, we used $\sigma_\epsilon = 0.25$ and 0.27 per component for the source bins four and five, as reported in Giblin et al. (2021), and the $n(z)$ described in Hildebrandt et al. (2021). Following the methods described in Harnois-Déraps et al. (2022), the IA properties of these galaxies were computed as

$$\epsilon_1^\mathrm{IA} = -\frac{A_\mathrm{IA}\bar{C}_1\bar{\rho}(z)}{D_+(z)}(s_{xx} - s_{yy}) \;, \quad \epsilon_2^\mathrm{IA} = -\frac{2A_\mathrm{IA}\bar{C}_1\bar{\rho}(z)}{D_+(z)}s_{xy} \;, \tag{3.5}$$

where $s_{ij} = \partial_{ij}\phi$ are the Cartesian components of the projected tidal field tensors interpolated at their positions, with ϕ being the gravitational potential. The strength of the coupling between the ellipticities and the tidal field are captured by A_IA, where $\bar{\rho}(z)$ is the matter density, $D_+(z)$ is the linear growth factor, and the constant $\bar{C}_1 = 5 \times 10^{-14} M_\odot^{-1} h^{-2}\,\mathrm{Mpc}^3$, as calibrated in Brown et al. (2002). By use of Eq. (2.78), the intrinsic ellipticity components $\epsilon_{1/2}^\mathrm{IA}$ were combined with the cosmic shear signal, which resulted in an IA-contaminated weak lensing sample that is consistent with the NLA model of Bridle and King (2007). Furthermore, we used for the lens sample the $n(z)$ of the KiDS-bright sample, as they gave a cleaner signal in the real data analysis compared to the LRG sample. By populating the underlying dark matter field with galaxies following a Poisson distribution, we achieved an effective number density of $n_\mathrm{eff} = 0.325\,\mathrm{arcmin}^{-2}$, where we fixed the linear galaxy bias to 1.4.

3.2.6 Magneticum

The *Magneticum* lensing simulations[4] were first introduced in Hirschmann et al. (2014) and further used in Martinet et al. (2021). In B22b, we used the *Magneticum* to investigate the impact of baryon feedback to the DSS data vector.

Baryon feedback affects the distribution of LSS, as the sustained outflow of energy from stellar winds, supernovae, and AGN reduces the clustering on intra-cluster scales by tens of per cent (van Daalen et al., 2011). However, to which strength baryons affect the LSS (Chisari et al., 2015) is still largely uncertain. Since we expect the DSS to be only a little affected by baryons, we decided to use hydro-dynamical simulations for which the impact is quite high.

We used mocks with dark matter-only light-cones and dark matter+baryon light-cones to test the difference caused by the presence of baryons. The simulations provided were a cooperation work by the co-authors Klaus Dolag, Tiago Castro, Nicolas Martinet and Joachim Harnois-Déraps. The underlying matter field was constructed from *Run-2* and *Run-2b* data described in Hirschmann et al. (2014) and Ragagnin et al. (2017), which are based on the Gadget3 hydro-dynamical code (Springel, 2005). They can reproduce a large number of observations (Castro et al., 2021), where dark matter particles of mass $6.9 \times 10^8 h^{-1} M_\odot$ and gas particles with mass $1.4 \times 10^8 h^{-1} M_\odot$ are co-evolved in comoving volumes of side 352 and 640 h^{-1} Mpc, respectively. The essential mechanisms included are radiative cooling, star formation, supernovae, AGN, and their associated feedback on the matter density field. Lastly, the galaxy and shear catalogues were produced from sequences of projected mass planes to mimic the KiDS-1000 sources and KiDS-bright lenses for ten pseudo-independent 100 deg^2 light-cones.

Similar to the SLICS the *Magneticum* are flat-sky simulations, so we used the SCIPY function CONVOLVE to calculate the aperture number, and TREECORR to measure the tangential shear profiles.

---

[4] `www.magneticum.org`

4

An adapted filter for the density split statistic

This chapter is covered by B20, which analysis was mainly developed during my master's thesis. However, I improved, wrote and published it during the PhD. Therefore, and because it is essential for understanding the remaining work, we added it here as a separate chapter. The general framework was done by me in a corporation with Peter Schneider. Furthermore, since many discussions with Joachim Harnois-Déraps, Hendrik Hildebrandt and Sandra Unruh helped to develop this work, I use the scientific wording 'we' for this chapter.

In the work of B20 an adapted filter function to compute the aperture number, $N_{\rm ap}$, was developed and compared to the previously used top-hat filter function. The motivation for the adapted filter was that even if the (foreground) galaxy density $n(\boldsymbol{\theta})$ is proportional to the lensing convergence field $\kappa(\boldsymbol{\theta})$, the $N_{\rm ap}$ measured with a top-hat filter with radius θ is not perfectly correlated to aperture mass $M_{\rm ap}$, measured using the $\gamma_{\rm t}(\vartheta)$ with $\vartheta > \theta$. To improve the correlation between $N_{\rm ap}$ and $M_{\rm ap}$, we developed a pair of compensated filters in an iterative process using the MS with the setup described in Sect. 3.2.2 as follows: The first step was to calculate the aperture number $N_{\rm ap}$ with a compensated top-hat filter defined as

$$U_1(|\boldsymbol{\theta}|) := \begin{cases} 1\,\mathrm{arcmin}^{-2} & ,\ \text{if } \theta < 1' \\ -\frac{1}{\theta_{\rm max}^2/\theta_{\rm tr}^2-1}\,\mathrm{arcmin}^{-2} & ,\ \text{if } \theta_{\rm tr} \leq \theta < \theta_{\rm max} \\ 0\,\mathrm{arcmin}^{-2} & ,\ \text{if } \theta > \theta_{\rm max} \end{cases} \tag{4.1}$$

where $\theta_{\rm max}$ is the size of the filter and $\theta_{\rm tr}$ is the transition from positive to negative filter values. Next, we measured the tangential shear profile $\gamma_{\rm t}(\theta)$ up to $\theta_{\rm max}$ around the highest 10% $N_{\rm ap}$ values. With setting $Q(\theta) \propto \gamma_{\rm t}(\theta)$ and Eq. (2.97) we created a revised compensated filter $U_{\rm i+1}$. This process was repeated iteratively, starting with the revised filter U_{i+1} determined in the previous iteration. In B20 this iteration continues as long as the change in relative signal-to-noise $\Delta(S/N)/(S/N)_1 > 10^{-3}$ between consecutive iterations, where the noise was estimated from the 64 MS realisations and ended after eight iterations. After convergence was achieved, the last step was to extend the U and Q filters by measuring the shear signal up to radius Θ, which provides the large signal at $\Theta > \theta_{\rm max}$. Since the new filter is adapted to the shear profiles, it is called the adapted filter.

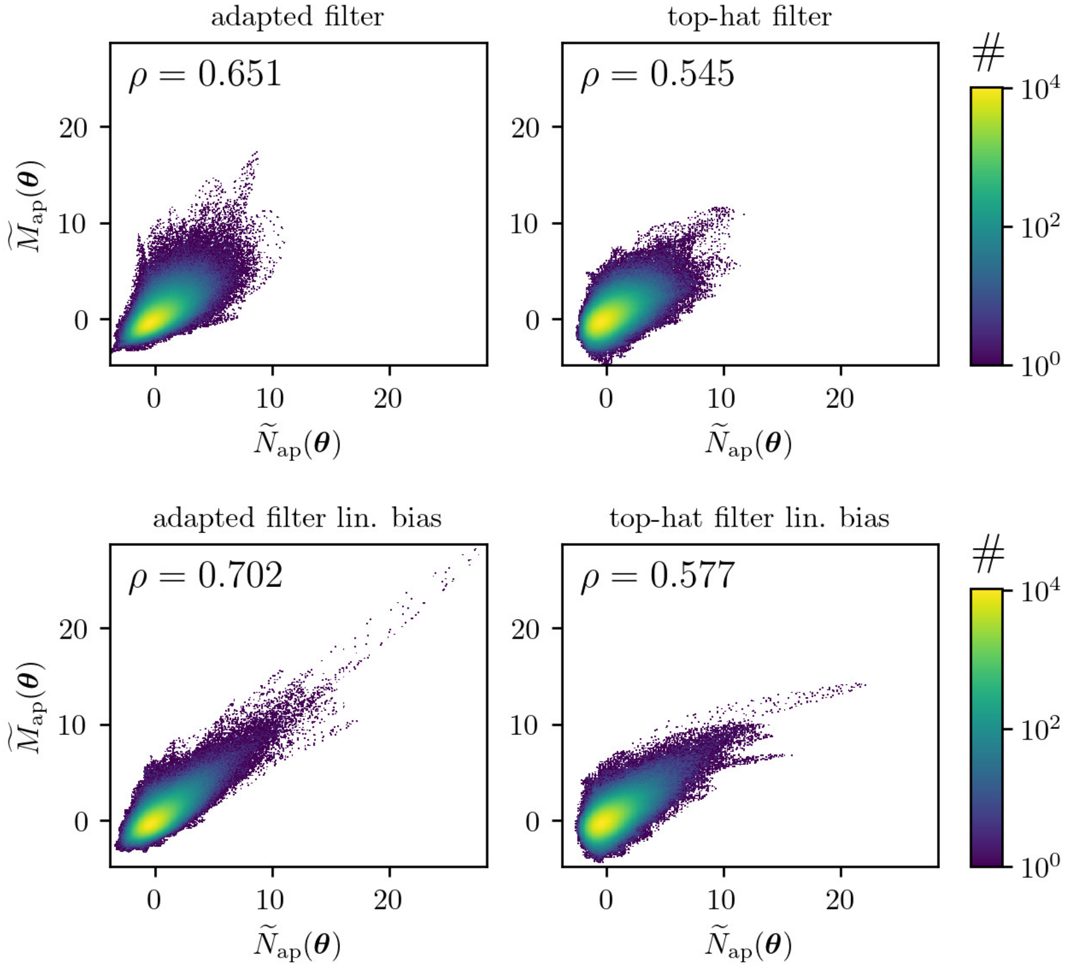

Figure 4.1: Pixel-by-pixel comparison of $M_{\rm ap}(\boldsymbol{\theta})$ vs. $N_{\rm ap}(\boldsymbol{\theta})$. To ease the comparison between $M_{\rm ap}(\boldsymbol{\theta})$ and $N_{\rm ap}(\boldsymbol{\theta})$ we re-scaled $M_{\rm ap}(\boldsymbol{\theta}) \rightarrow \widetilde{M}_{\rm ap}(\boldsymbol{\theta}) := (M_{\rm ap}(\boldsymbol{\theta}) - \langle M_{\rm ap}\rangle)/\sqrt{\langle (M_{\rm ap}(\boldsymbol{\theta}) - \langle M_{\rm ap}\rangle)^2\rangle}$, correspondingly $N_{\rm ap}(\boldsymbol{\theta}) \rightarrow \widetilde{N}_{\rm ap}(\boldsymbol{\theta})$, where $\langle ... \rangle$ is the ensemble average over all pixel positions. In the upper left corner of each plot we state also the Pearson correlation factor between $M_{\rm ap}(\boldsymbol{\theta})$ and $N_{\rm ap}(\boldsymbol{\theta})$. The left panels show the analysis with the adapted filter and the right with the top-hat filter. The upper panels deviate from the lower ones in respect to the used foreground galaxies. Figure taken from B20.

In the remaining part of the work in B20, the adapted filter was compared to a top-hat filter, where the size of the top-hat was adjusted such that the peaks of the resulting shear profiles of both filters were similar. Using the SLICS (Sect. 3.2.4), we measured with the adapted filter better S/N ratios than with the top-hat filter. For this comparison, the signal, S, was the mean from 64 SLICS realisations and the noise, N, was the standard deviation of 64 SLICS tangential shear profiles around random pixel positions. Since the top-hat filter does not have a corresponding Q-filter, we used the approach from Brouwer et al. (2018), where $Q(\theta) \sim 1/\sqrt{\theta}$ for $\theta_{\rm th} < \theta < \Theta$ with $\theta_{\rm th}$ the size of the top-hat filter. Especially for the highest and lowest quantiles, the adapted filter had a better S/N, meaning that the signal is more likely to distinguish from pure noise, which we exploit later in the real data analysis. To investigate which filter function creates signals more sensitive to cosmological parameters, we used the cosmo-SLICS (Sect. 3.2.5). For each cosmological node, we measured a χ^2 value as the deviation to the fiducial cosmology weighted by a covariance matrix measured from the 50 realisations of the fiducial cosmology. For most cosmological parameters, the adapted filter performs better in distinguishing between different cosmologies. In the last test, we compared the correlation between both filters' aperture number and aperture mass. As shown in Fig. 4.1, we performed this test once with the SLICS (upper panels), where galaxies are distributed with a HOD, and with the fiducial cosmology of cosmo-SLICS, where galaxies were distributed with a linear galaxy bias model (lower panel). In both cases, the adapted filter yielded a better relation, indicating that the overall aim of this work was achieved.

Since F18 states that their analytical model, which we will use in a modified version, is currently not accurate enough for top-hat filter functions smaller than $20'$, we can not use the adapted filter derived in B20 as it is too small. After several tests, we fixed the filter function size to $120'$. However, the MS with $4 \times 4\,\mathrm{deg}^2$ fields is too small to generate a filter function of that size. The $100\,\mathrm{deg}^2$ area of the SLICS simulations with a combined fourth and fifth tomographic bin of the KiDS-1000 source mocks and GAMA lens mocks are very suitable for this task, as we will analyse the real KiDS-bright sample that is calibrated with spectroscopic GAMA measurements.

For the iteration process, we fixed the transition scale $\theta_{\mathrm{tr}} = 4'$ and the maximum scale to $\theta_{\max} = 40'$. In the upper panel of Fig. 4.2, we show the filter functions after each iteration step, where the solid black line corresponds to the initial compensated top-hat filter. The corresponding shear profiles of the highest 10% N_{ap} values are shown in the lower panel of Fig. 4.2.

After ten iterations, we manually stopped the iteration process since the shapes' changes were significantly smaller than the expected uncertainties. Using Eq. (2.97) we extended the final adapted filter, which is shown as the solid blue line in Fig. 4.3. Although we test the DSS model also for other compensated filters with a similar angular extent in B22a, we display in Fig. 4.3 only the adapted and top-hat filter as we restrict the review in this thesis to these two filters.

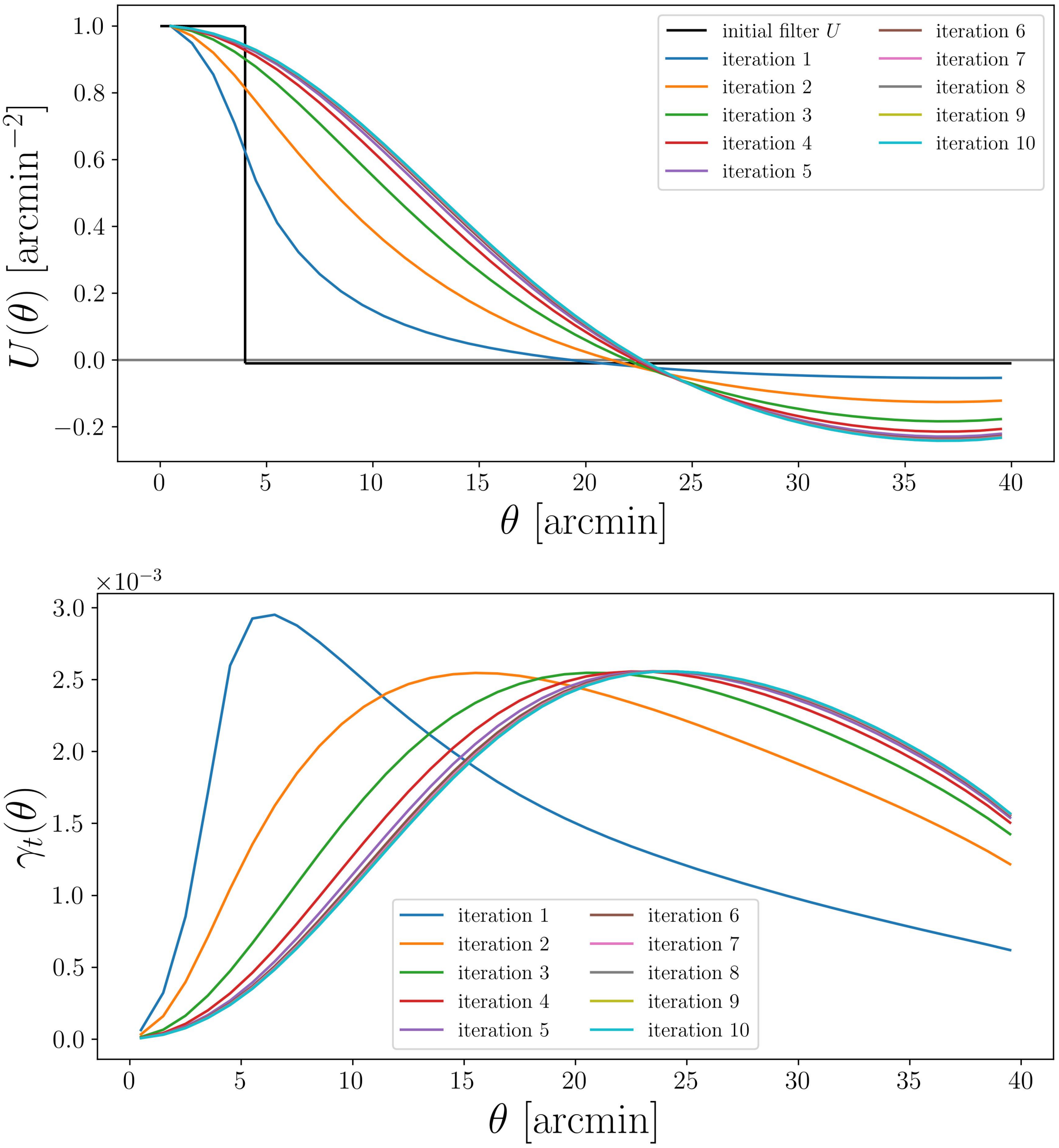

Figure 4.2: Resulting filter functions and corresponding shear profiles of the iteration process. The filter functions on the upper panel result from those shear profiles on the lower panel with the same colour.

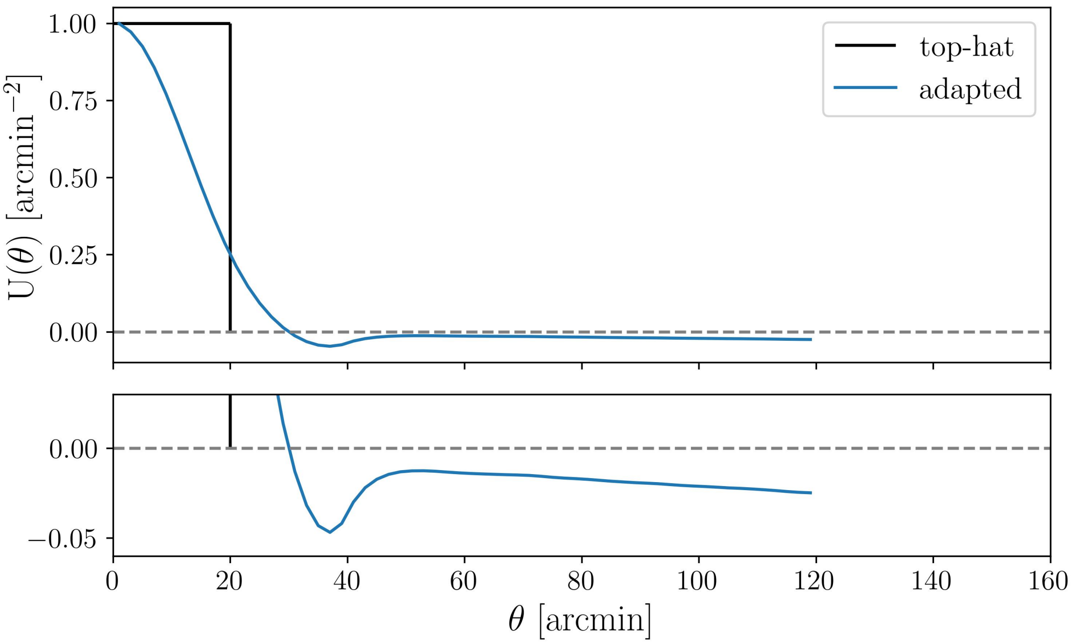

Figure 4.3: Adapted filter U used in the following chapters. To ease the comparison, we scaled the first bin value to $1/\text{arcmin}^{-2}$

.

5

Generalised model of density split statistic

This chapter reviews the essential ingredients of the analytical DSS model presented in B22a, and the slight modification presented in B22b. In general, we describe the modifications of the original F18 model, who showed that the full non-perturbative calculation of the PDF could be approximated with a log-normal PDF. The basic structure was taken from F18, but every step in the formalism and its implementation had to be redone for general filters. And although the work described here was done by me, it resulted from several discussions with Oliver Friedrich and Peter Schneider, so I use the scientific wording ‘we’.

In analogy to the definition of the convergence $\kappa(\boldsymbol{\theta})$ in Eq. (2.81), we defined for a flat universe ($K = 0$ in Eq. 2.3) the line-of-sight projection of the 3D matter density contrast δ_m, weighted by the projection kernel $q_\mathrm{g}(\chi) = n_\mathrm{l}(z[\chi])\frac{\mathrm{d}z[\chi]}{\mathrm{d}\chi}$ as

$$\delta_\mathrm{2D}(\boldsymbol{\theta}) = \int \mathrm{d}\chi\, q_\mathrm{g}(\chi)\, \delta(\chi\boldsymbol{\theta}, \chi)\,, \tag{5.1}$$

where χ is the co-moving distance and $n_\mathrm{l}(z[\chi])$ is the foreground (lens) galaxy redshift distribution. Next, the two-dimensional matter density contrast was smoothed with a filter U of size Θ:

$$\delta_{\mathrm{m},U}(\boldsymbol{\theta}) \equiv \int\limits_{|\boldsymbol{\theta}'|<\Theta} \mathrm{d}^2\theta'\, \delta_\mathrm{2D}(\boldsymbol{\theta}+\boldsymbol{\theta}')\, U(|\boldsymbol{\theta}'|)\,, \tag{5.2}$$

which simplifies in the case of a top-hat filter of size ϑ to

$$\delta^{\vartheta}_{\mathrm{m,th}}(\boldsymbol{\theta}) = \frac{1}{\pi\vartheta^2} \int\limits_{|\boldsymbol{\theta}'|<\vartheta} \mathrm{d}^2\theta'\; \delta_\mathrm{m,2D}(\boldsymbol{\theta}+\boldsymbol{\theta}')\,. \tag{5.3}$$

In analogy, the mean convergence inside an angular separation ϑ is

$$\kappa_{<\vartheta}(\boldsymbol{\theta}) = \frac{1}{\pi\vartheta^2} \int\limits_{|\boldsymbol{\theta}'|<\vartheta} \mathrm{d}^2\theta'\; \kappa(\boldsymbol{\theta}+\boldsymbol{\theta}')\,. \tag{5.4}$$

As the tangential shear profiles for given a quantile, $\langle\gamma_\mathrm{t}|Q\rangle$, is the average over all N_ap values that belong to quantile Q, it simplifies to the prediction of $\langle\gamma_\mathrm{t}|N_\mathrm{ap}\rangle$. This conditional expectation value can in turn be computed by use of Eq. (2.72) as

$$\langle\gamma_\mathrm{t}|N_\mathrm{ap}\rangle(\vartheta) = \langle\kappa_{<\vartheta}|N_\mathrm{ap}\rangle - \langle\kappa|N_\mathrm{ap}\rangle(\vartheta) = -\frac{\vartheta}{2}\frac{\mathrm{d}}{\mathrm{d}\vartheta}\langle\kappa_{<\vartheta}|N_\mathrm{ap}\rangle\,, \tag{5.5}$$

where κ and γ_t are the averages on circles of radius ϑ from the centre of the filter. In order to predict the $\langle\kappa_{<\vartheta}|N_\mathrm{ap}\rangle$ we use that

$$\langle\kappa_{<\vartheta}|N_\mathrm{ap}\rangle \approx \int \mathrm{d}\delta_{\mathrm{m},U}\ \langle\kappa_{<\vartheta}|\delta_{\mathrm{m},U}\rangle\, p(\delta_{\mathrm{m},U}|N_\mathrm{ap})\,, \tag{5.6}$$

where we assumed that the expected convergence within ϑ only depends on the projected matter density contrast $\delta_{\mathrm{m},U}$. Next, we used Bayes' theorem Eq. (2.106) to express the conditional PDF as

$$p(\delta_{\mathrm{m},U}|N_\mathrm{ap}) = \frac{p(N_\mathrm{ap}|\delta_{\mathrm{m},U})p(\delta_{\mathrm{m},U})}{p(N_\mathrm{ap})}\,, \tag{5.7}$$

where $p(N_\mathrm{ap}|\delta_{\mathrm{m},U})$ is the probability of finding N_ap given the smoothed density contrast $\delta_{\mathrm{m},U}$, and $p(N_\mathrm{ap})$ follows by integrating over the numerator.

Summarising, we were left with three ingredients in order to calculate $\langle\gamma_\mathrm{t}|Q\rangle$:

1. The PDF of the matter density contrast smoothed with the filter function U (used in Eqs. 5.7)
$$p(\delta_{\mathrm{m},U})\,. \tag{5.8}$$
2. The expectation value of the convergence inside a radius ϑ given the smoothed density contrast (used in Eq. 5.6)
$$\langle\kappa_{<\vartheta}|\delta_{\mathrm{m},U}\rangle\,. \tag{5.9}$$
3. The distribution of N_ap for the given filter function U given the smoothed density contrast (used in Eqs. 5.7)
$$p(N_\mathrm{ap}|\delta_{\mathrm{m},U})\,. \tag{5.10}$$

All three components are sensitive to the filter function U so we will discuss them in more detail next.

5.1 $p(\delta_{\mathrm{m},U})$

For the matter density PDF we assumed that it follows a shifted log-normal distribution with vanishing mean (see Eq. 2.101) as

$$p(\delta_{\mathrm{m},U}) = \frac{1}{\sqrt{2\pi}\sigma(\delta_{\mathrm{m},U}+\delta_0)}\exp\left(-\frac{\left[\ln\left(\delta_{\mathrm{m},U}/\delta_0+1\right)+\sigma^2/2\right]^2}{2\sigma^2}\right)\,. \tag{5.11}$$

The two free parameters, σ and δ_0 are determined in terms of the variance $\langle \delta^2_{\mathrm{m},U} \rangle$ and skewness $\langle \delta^3_{\mathrm{m},U} \rangle$ as

$$\langle \delta^2_{\mathrm{m},U} \rangle = \delta_0^2 \left[\exp(\sigma^2) - 1 \right] \,, \tag{5.12}$$

$$\langle \delta^3_{\mathrm{m},U} \rangle = \frac{3}{\delta_0} \langle \delta^2_{\mathrm{m},U} \rangle^2 + \frac{1}{\delta_0^3} \langle \delta^2_{\mathrm{m},U} \rangle^3 \,, \tag{5.13}$$

where the expression of $\langle \delta^2_{\mathrm{m},U} \rangle$ and $\langle \delta^3_{\mathrm{m},U} \rangle$ are derived in Appendix A in B22a, which are based tree-level perturbation theory discussed in Sec. 2.1.6. The plain log-normal ansatz works well for exclusively positive filters like a Gaussian. However, for compensated filters, $p(\delta_{\mathrm{m},U})$ is better described by considering the positive $U_<$ and negative $U_<$ part separately and then combining both with a bi-variate log-normal ansatz that read as

$$\begin{aligned} p(\delta_{\mathrm{m},U_>}, \delta_{\mathrm{m},U_<}) = & \frac{1}{2\pi\sigma_> (\delta_{\mathrm{m},U_>} + \delta_{0,>})\, \sigma_< (\delta_{\mathrm{m},U_<} + \delta_{0,<}) \sqrt{1-\rho^2}} \\ & \times \exp\left(-\frac{1}{2(1-\rho^2)} \left[\Delta_>^2 + \Delta_<^2 - 2\rho \Delta_> \Delta_< \right] \right) \,, \end{aligned} \tag{5.14}$$

with

$$\Delta_{>,<} = \frac{\ln\left(\delta_{\mathrm{m},U_{>,<}} / \delta_{0,>,<} + 1\right) + \sigma^2_{>,<}/2}{\sigma_{>,<}} \,, \tag{5.15}$$

and

$$\rho = \ln\left(\frac{\langle \delta_{\mathrm{m},U_>} \delta_{\mathrm{m},U_<} \rangle}{\delta_{0,>} \delta_{0,<}} + 1 \right) \frac{1}{\sigma_> \sigma_<} \,. \tag{5.16}$$

Using the convolution theorem (Arfken and Weber, 2008) it follows that

$$p(\delta_{\mathrm{m},U}) = \int_{-\infty}^{\infty} \mathrm{d}\delta_{\mathrm{m},U_>}\, p(\delta_{\mathrm{m},U_>}, \delta_{\mathrm{m},U_>} - \delta_{\mathrm{m},U}) \,. \tag{5.17}$$

5.2 $\langle \kappa_{<\vartheta} | \delta_{\mathrm{m},U} \rangle$

To calculate the expectation value of the mean convergence inside an angular radius ϑ, $\kappa_{<\vartheta}$, given the matter density contrast $\delta_{\mathrm{m},U}$, we assumed that both follow a joint log-normal distribution. In this case, the expectation value can be written as

$$\frac{\langle \kappa_{<\vartheta} | \delta_{\mathrm{m},U} \rangle}{\kappa_0} = \exp\left(\frac{C \left[2 \ln\left(\delta_{\mathrm{m},U} / \delta_0 + 1 \right) + V - C \right]}{2V} \right) - 1 \,, \tag{5.18}$$

where δ_0 is determined with Eq. (5.13) and

$$V = \ln\left(1 + \frac{\langle \delta_{\mathrm{m},U}^2 \rangle}{\delta_0^2}\right), \tag{5.19}$$

$$C = \ln\left(1 + \frac{\langle \kappa_{<\vartheta}\, \delta_{\mathrm{m},U} \rangle}{\delta_0 \kappa_0}\right), \tag{5.20}$$

$$\kappa_0 = \frac{\langle \kappa_{<\vartheta}\, \delta_{\mathrm{m},U} \rangle^2 \mathrm{e}^V}{\langle \kappa_{<\vartheta}\, \delta_{\mathrm{m},U}^2 \rangle - 2\langle \kappa_{<\vartheta}\, \delta_{\mathrm{m},U} \rangle \langle \delta_{\mathrm{m},U}^2 \rangle / \delta_0}, \tag{5.21}$$

where detailed derivations of the $\langle \kappa_{<\vartheta}\, \delta_{\mathrm{m},U}^k \rangle$ moments are given in Appendix A in B22a.

5.3 $p(N_{\mathrm{ap}}|\delta_{\mathrm{m},U})$

To derive an expression for $p(N_{\mathrm{ap}}|\delta_{\mathrm{m},U})$ we used its characteristic function (CF) (Papoulis and Pillai, 1991). The CF is an alternative representation of a probability distribution, similar to the moment generating functions (MF), but based on the Fourier transform of the PDF. Similar to the MF, the n-th derivative of the CF can be used to calculate the n-th moment of the PDF. A closed expression for the CF of $p(N_{\mathrm{ap}}|\delta_{\mathrm{m},U})$ was derived in Appendix A in B22a, and reads as

$$\Psi(t) = \exp\left(2\pi n_0 \int_0^\infty d\vartheta\ \vartheta\ \left(1 + b\,\langle w_\vartheta | \delta_{\mathrm{m},U} \rangle\right) \left[\mathrm{e}^{\mathrm{i}tU(\vartheta)} - 1\right]\right), \tag{5.22}$$

with n_0 being the mean number density of foreground galaxies in the sky, b is linear galaxy bias, and

$$w_\vartheta = \frac{1}{2\pi} \int_0^{2\pi} \mathrm{d}\phi\ \delta_{\mathrm{m},2D}(\vartheta, \phi), \tag{5.23}$$

is the averaged density contrast on a circle of radius ϑ. Hence, $n_0(1+b\,\langle w_\vartheta | \delta_{\mathrm{m},U} \rangle)$ is the effective number density at ϑ given $\delta_{\mathrm{m},U}$. Similar to $\langle \kappa_{<\vartheta} | \delta_{\mathrm{m},U} \rangle$, we also assumed that w_ϑ and $\delta_{\mathrm{m},U}$ follow a joint log-normal distribution in order to compute $\langle w_\vartheta | \delta_{\mathrm{m},U} \rangle$. As shown in B22a, using the inverse Fourier transformation of the CF is as accurate as using a log-normal distribution for $p(N_{\mathrm{ap}}|\delta_{\mathrm{m},U})$, but is significantly slower. Therefore, we calculate $p(N_{\mathrm{ap}}|\delta_{\mathrm{m},U})$ from

$$p(N_{\mathrm{ap}}|\delta_{\mathrm{m},U}) = \frac{1}{\sqrt{2\pi} S (N_{\mathrm{ap}} + L)} \exp\left(\frac{-\left[\ln(N_{\mathrm{ap}} + L) - M\right]^2}{2S^2}\right), \tag{5.24}$$

where the parameters S, M, L follow from the n-th derivative of the CF.

The model derived so far is accurate if galaxies are distributed with a Poisson process. However, real galaxies are not expected to be perfectly Poisson-distributed. Therefore, we modified in B22b the distribution of the aperture number to allow for super-Poissonian shot noise by scaling the galaxy number density n_0 with a free parameter $\alpha > 0$. In that case $n_0\,\alpha^{-1}$ can be interpreted as an effective number density of Poissonian tracers, which implies that instead of $p(N_{\mathrm{ap}}|\delta_{\mathrm{m},U})$

the quantity $p(N_{\mathrm{ap}}\,\alpha^{-1}|\delta_{\mathrm{m},U})$ follows a log-normal distribution. This modifies the characteristic function as

$$\Psi(t) = \exp\left(2\pi \frac{n_0}{\alpha} \int_0^\infty \mathrm{d}\vartheta\ \vartheta\ \left(1 + b\,\langle w_\vartheta|\delta_{\mathrm{m},U}\rangle\right)\left[\mathrm{e}^{\mathrm{i}tU(\vartheta)} - 1\right]\right), \tag{5.25}$$

and the mean aperture number remains constant if

$$p\left(N_{\mathrm{ap}}|\delta_{\mathrm{m},U}\right) \rightarrow \frac{1}{\alpha} p\left(\frac{N_{\mathrm{ap}}}{\alpha}|\delta_{\mathrm{m},U}\right). \tag{5.26}$$

With this PDF description we got that the expectation value $\langle N_{\mathrm{ap}}|\delta_{\mathrm{m},U}\rangle \propto \alpha$ and the variance $\langle(N_{\mathrm{ap}} - \langle N_{\mathrm{ap}}|\delta_{\mathrm{m},U}\rangle)^2|\delta_{\mathrm{m},U}\rangle \propto \alpha^2$, so their ratio is proportional to α as required to describe deviations from Poissonian distributions. For numerical reasons, similar to Friedrich et al. (2018), we allowed only $\alpha > 0.1$ in our parameter selection. Moreover, we also compared our modelling of the α parameter with that in Friedrich et al. (2018) and found no differences in the predictions.

We also tested if the cosmological results are robust for the linear galaxy bias assumption, by using galaxy samples distributed with a HOD and samples where we distributed galaxies with a Poisson process with mean $\lambda = n_{\mathrm{eff}}\left[1 + b_1\,\delta_{\mathrm{m,2D}}(\boldsymbol{\theta}) + b_2\,(\delta^2_{\mathrm{m,2D}}(\boldsymbol{\theta}) - \langle\delta^2_{\mathrm{m,2D}}\rangle)\rangle\right]$. The analysis using the HOD mocks showed that the smoothing scale of our filter function is large enough to give unbiased results. Furthermore, we found that a linear galaxy bias model seems to be sufficient if an analysis using shear and N_{ap} information is consistent with an analysis that uses exclusively shear information.

Model validation and calibration

6

This chapter reviews the validation and calibration of the model performed in B22a and further repeats the validation in B22b. Furthermore, we restrict this review to the results of the adapted filter shown in Fig. 4.3 and a top-hat filter of size $20'$. The used simulations described in chapter 3.1 are either publicly available or were provided by co-author Joachim Harnois-Déraps. Although the analysis described here is fully done by me, I continue for this part using the scientific wording 'we', since this work also resulted from discussion with the co-authors.

6.1 Testing the ingredients of the revised model

To test all the essential ingredients of the revised model, we used the T17 simulations described in Sect. 3.2.3. Although, in principle, the test for the top-hat filter could be done with the original model of F18, we also used the revised model for it and noted that both models yield almost identical results. Furthermore, we restrict the comparison the adapted filter of size $120'$ derived in chapter 4 and a top-hat of size $20'$, where other filters are also tested in B22a.

6.1.1 Validating $p(\delta_{\mathrm{m},U})$

The PDF of the smoothed two-dimensional density contrast for the top-hat (upper panel) and the adapted (lower panel) filter are shown in Fig. 6.1, for the second and third LRG bins. The predictions agree with the simulations for the two lens bins within $1\,\sigma$ for the expected variance of KiDS-1000, estimated with the 48 sub-patches of one realisation. For the adapted filter, the deviations are more substantial than for the top-hat filter when using a log-normal approximation. However, the results for a Gaussian filter and for the top-hat filter are well within $1\,\sigma$, indicating that the log-normal approximation is suitable for exclusively positive filters. That is the reason for using the bi-variate log-normal approach discussed in Sect. 5.1, which in principle combines two log-normal filters that are exclusively positive. With this approach, no significant differences in the match between predicted and measured PDF for compensated filters can be recognised.

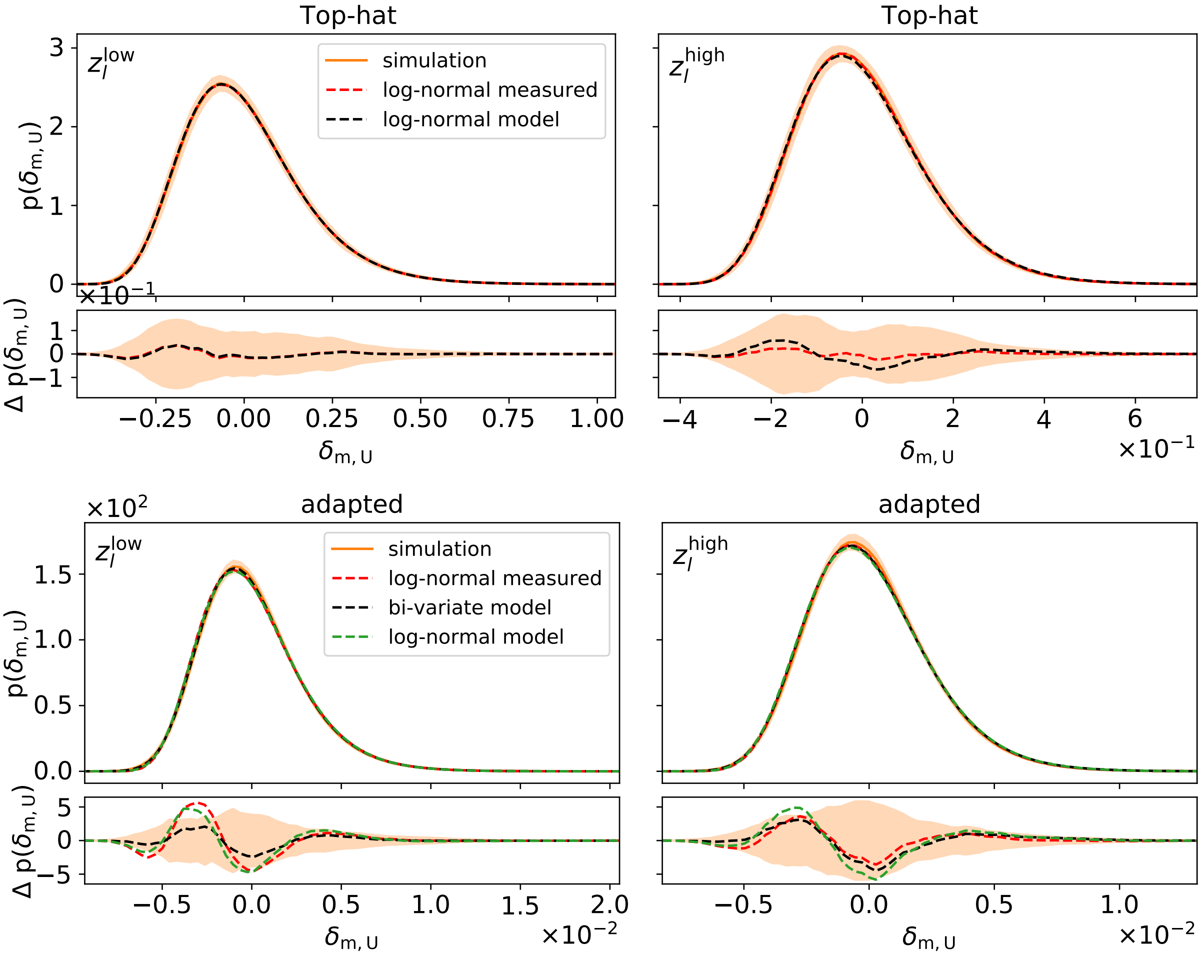

Figure 6.1: In this figure, the PDF of $\delta_{\mathrm{m},U}$ smoothed with the top-hat and adapted filter is shown, where the orange shaded region is the standard deviation of 48 sub-patches scaled by a 777.4/859.4, to mimic the effective survey area of KiDS-1000. The red dashed curve is a log-normal PDF with $\langle\delta^2_{\mathrm{m},U}\rangle$ and $\langle\delta^3_{\mathrm{m},U}\rangle$ measured from the smoothed T17 density maps, and indicates the accuracy using a log-normal PDF. The green and the black dashed lines are both from the model; the green corresponds to the PDF of $\delta_{\mathrm{m},U}$ when using log-normal and the black using the bi-variate approach described in Eq. (5.14). The lower panels show the residuals $\Delta p(\delta_{\mathrm{m},U})$ with respect to the simulations. Figure taken from B22a.

6.1.2 Validating $p(N_{\mathrm{ap}})$

Next, we discuss the validation of the modelled $p(N_{\mathrm{ap}})$ as shown in Fig. 6.2. For the adapted filter, we used the model with the bi-variate log-normal $p(\delta_{\mathrm{m},U})$ approach as it better agrees with the T17 simulations. The resulting $p(N_{\mathrm{ap}})$ show some discrepancies for the adapted filter, which indicates that either the remaining inaccuracies in $p(\delta_{\mathrm{m},U})$ propagate into $p(N_{\mathrm{ap}})$ or the term $\langle w_\vartheta|\delta_{\mathrm{m},U}\rangle$ is inaccurate. Since the deviations in $p(\delta_{\mathrm{m},U})$ are much smaller than in $p(N_{\mathrm{ap}})$, we expected that the assumptions made in computing $\langle w_\vartheta|\delta_{\mathrm{m},U}\rangle$ induce additional inaccuracies.

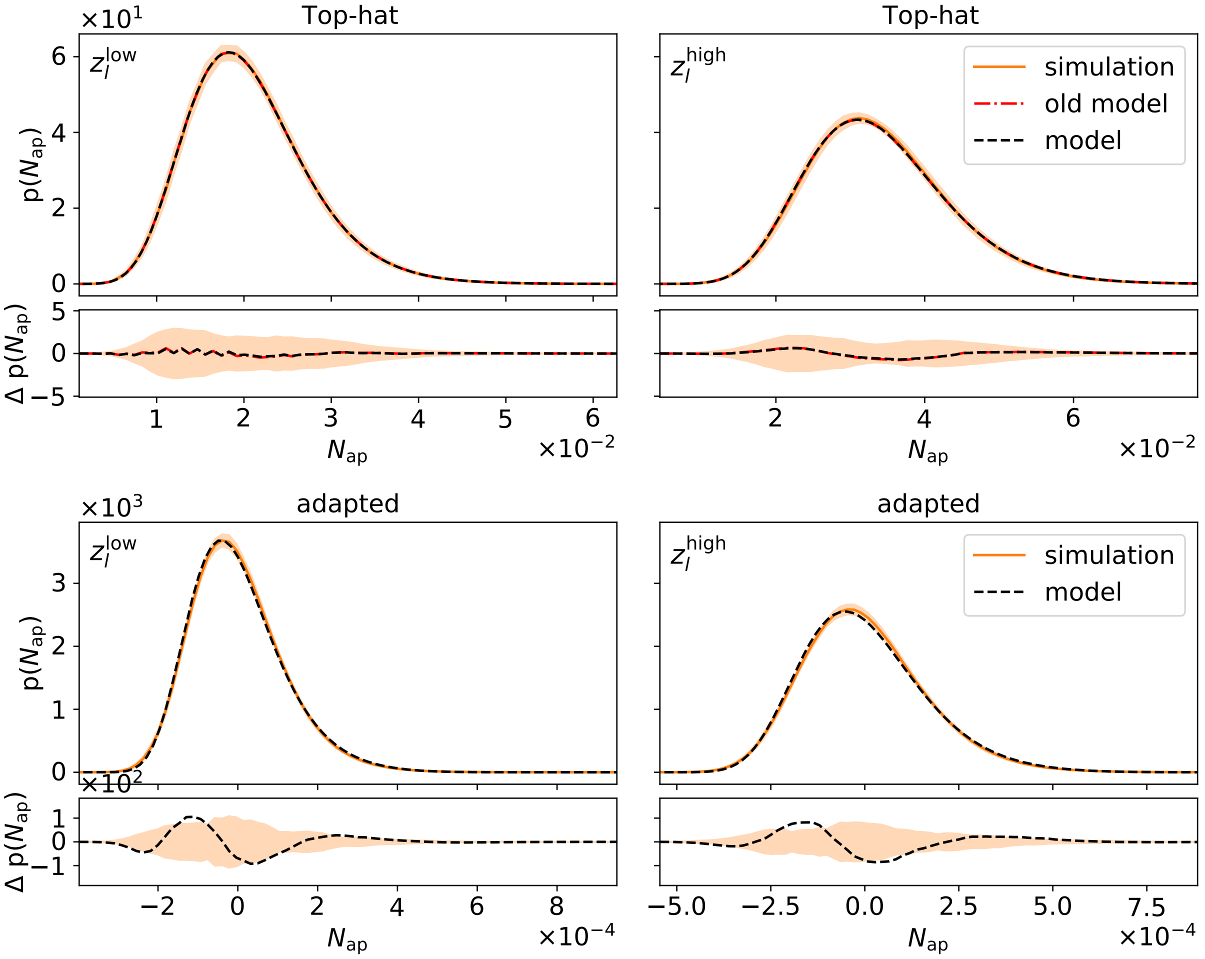

Figure 6.2: This figure shows the PDF of N_{ap}, where the orange lines are the expected KiDS-1000 uncertainties. The black dashed line is the prediction of the new model, and for comparison, the red dashed line for the top-hat filter is the prediction of the F18 model. The lower panels show the residuals $\Delta p(N_{\mathrm{ap}})$ with respect to the simulations. Figures are taken from B22a.

Nevertheless, these deviations result in shear signals with residuals well within the statistical uncertainties of KiDS-1000.

6.1.3 Validating $\langle \gamma_{\mathrm{t}} | Q \rangle$

The predicted and measured shear profiles, which are a major result of our work, are shown in Fig. 6.3. We measured the shear profiles up to 120′, using five quantiles as in G18. No significant deviations between the model and the simulations are visible for the top-hat, but for the adapted filter, minor discrepancies in some quantiles at large angular scales are seen, which are still consistent within the KiDS-1000 accuracy.

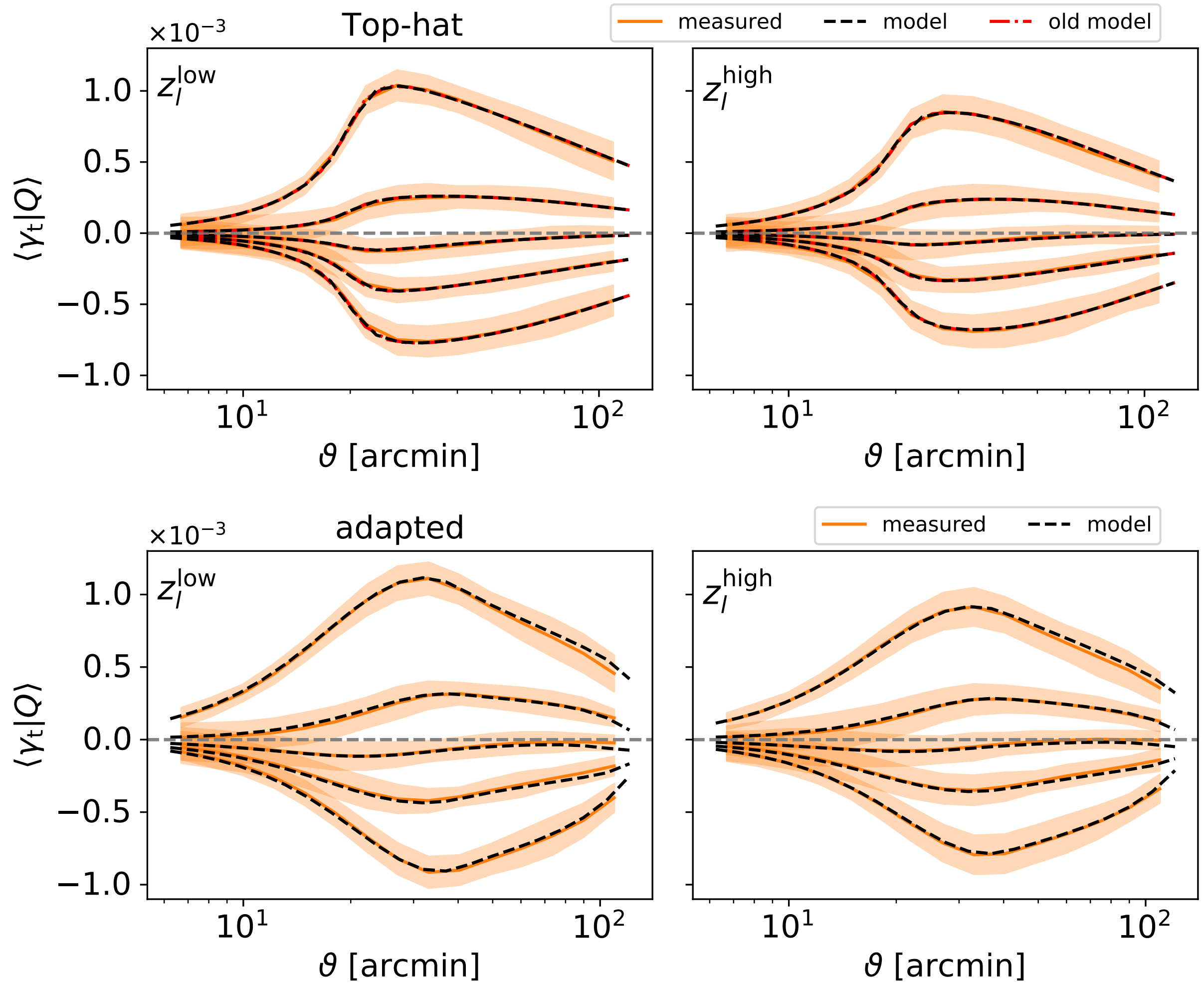

Figure 6.3: Predicted and measured shear profiles for the two lens samples and measured shear profiles for the new model, where the orange shaded region is the expected KiDS-1000 uncertainty. Figure taken from B22a.

Given the set-up described in Sect. 2.3.2 we ran an MCMC with a Gaussian likelihood for the adapted and top-hat filter, and use the covariance matrix described in Sect. 3.2.3 scaled by the Hartlap factor defined in Eq. (2.112). The left panel of Fig. 6.4 shows that the analysis with the adapted filter results in a biased inference for the Ω_{m}-σ_8-plane, which is still within $1\,\sigma$. By rescaling the prediction of the shear profiles of the highest quantile to the measured shear profile, we found that the bias is due to the systematic offset of the slope of the highest shear profile, which in turn is highly sensitive to Ω_{m}. The contours shift to smaller σ_8 values to compensate for the bigger Ω_{m} value as these two parameters are highly correlated. In the next section, we perform the calibration of the model to remove this systematic bias.

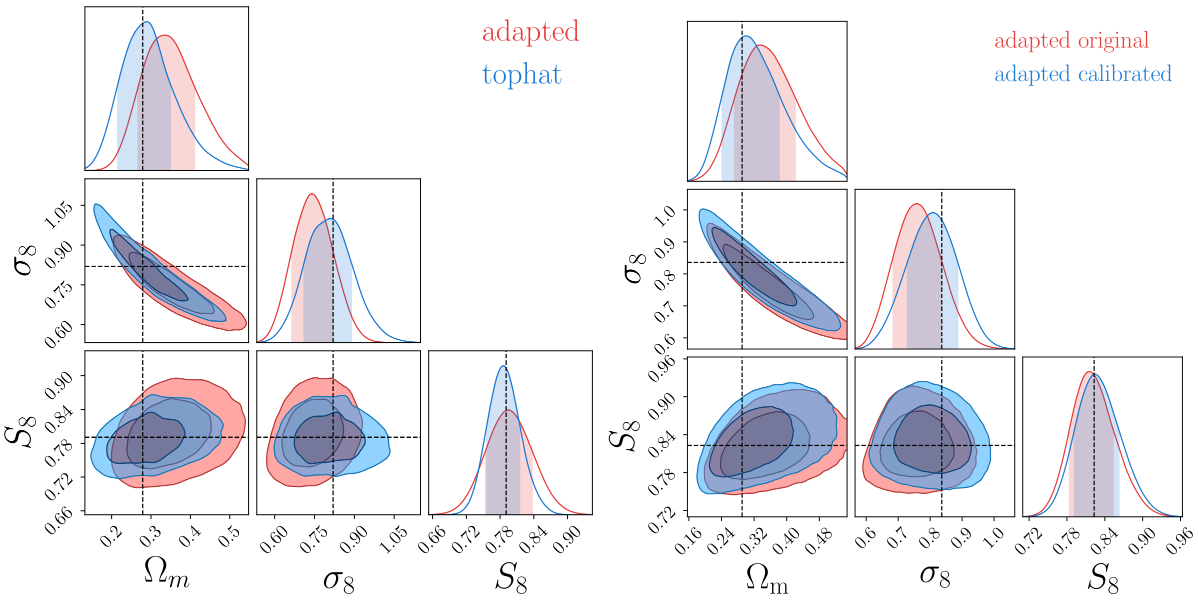

Figure 6.4: On the left side, the MCMC results are shown if the model and the T17 simulations for the data vector and covariance are used. The bias for the adapted filter can be removed by calibrating the model, as shown by the results of the MCMC on the right with the independent SLICS simulations. Here the data vector is calculated from the fiducial cosmology of cosmo-SLICS and the covariance matrix with 614 SLICS realisations. The contours are marginalised over the lens galaxy bias parameters. Figure taken from B22a.

6.1.4 Calibrating the model

In this chapter, we remove the remaining small inaccuracies of the adapted filter's analytical model. This calibration was done by rescaling the original model, $\gamma_{\rm t,ori}(\boldsymbol{\Theta})$, by the ratio of the measured shear profiles of the T17 simulations, $\gamma_{\rm t,T17}$, to the original predicted shear profiles at the T17 cosmology, $\gamma_{\rm t,ori}(\boldsymbol{\Theta}_{\rm T17})$. The calibrated model at parameters Θ was then defined as[1]

$$\gamma_{\rm t,cal}(\boldsymbol{\Theta}) = \gamma_{\rm t,ori}(\boldsymbol{\Theta})\frac{\gamma_{\rm t,T17}}{\gamma_{\rm t,ori}(\boldsymbol{\Theta}_{\rm T17})}\,. \tag{6.1}$$

In order to test our calibration on a independent suite of simulations, we made use of the cosmo-SLICS and SLICS, described in Sect. 3.2.5 and 3.2.5, respectively. Since the $n(z)$ of the cosmo-SLICS source galaxies extends over a larger redshift range, we averaged several T17 shear grids at different redshifts weighted by the source $n(z)$ of the cosmo-SLICS. For the calibration test, we performed another MCMC, where we discarded the middle quantile with the lowest signal to avoid a singular covariance matrix. The shear signals are measured from the fiducial cosmology of the cosmo-SLICS without shape noise, and the uncertainty was measured from 614 SLICS realisations with shape noise, scaled by the Hartlap factor in Eq. (2.112), and scaled to mimic the KiDS-1000 effective area. As shown in the right panel of Fig. 6.4 the calibrated model for the adapted filter resulted in an unbiased inference.

---

[1] We changed the notation from B22a in order to be consistent with rest of this work.

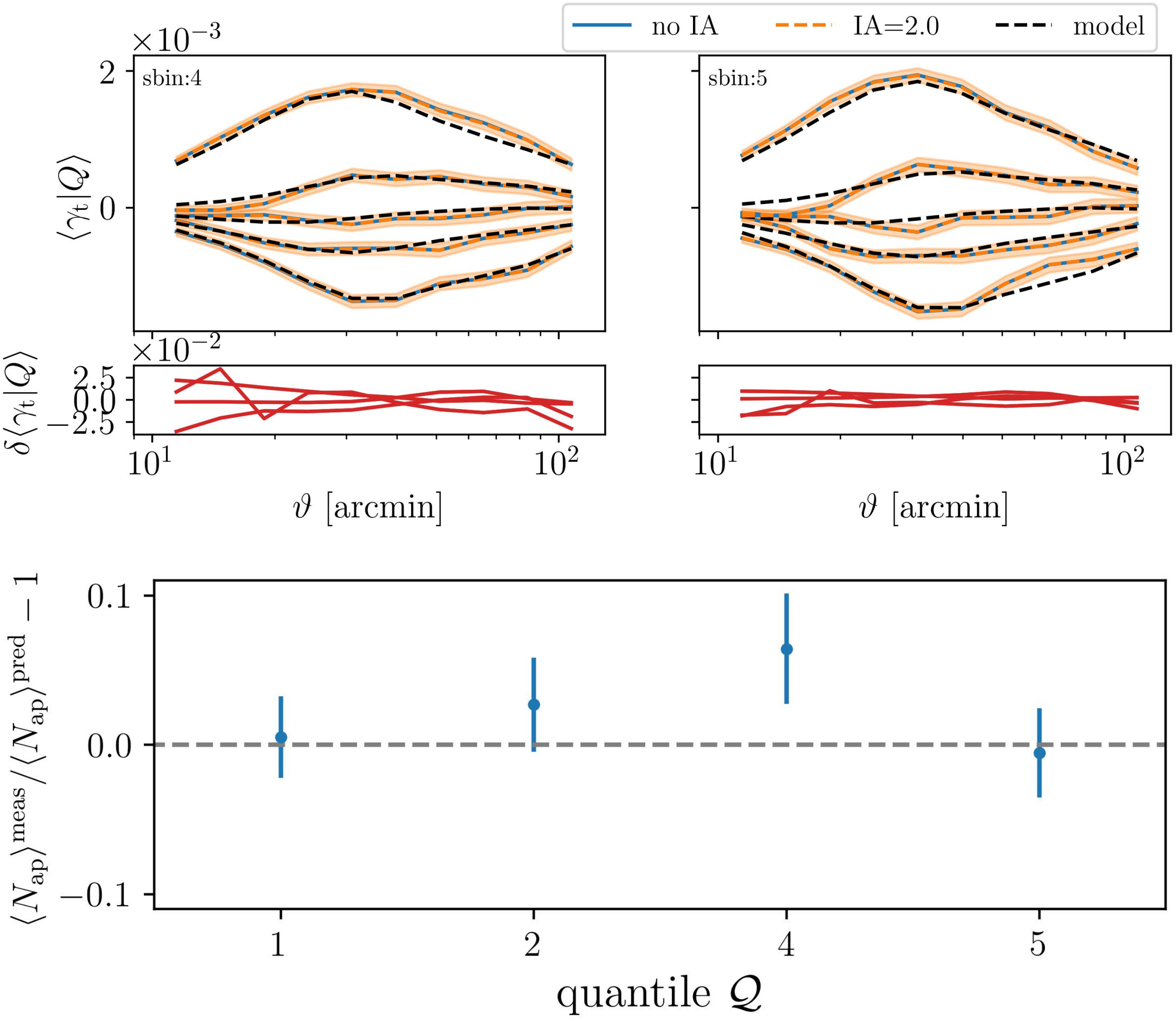

Figure 6.5: On the top: Shear profiles measured for the KiDS-bright-like lenses and KiDS-1000 sources from the cosmo-SLICS with two different IA amplitudes (see Eq. 3.5). On the bottom: Relative difference between the mean $\langle N_{\rm ap}\rangle$ measured in the cosmo-SLICS KiDS-bright mocks and the prediction from the model. The uncertainties for both figures are estimated from the FLASK mocks with the expected KiDS-1000 statistical uncertainty. Figure adapted from B22b.

6.2 Validation on realistic mock data

This section reviews the validation of the model that is performed in B22b restricted to the adapted filter, which is important as we used the KiDS-bright sample instead of the LRG in the real data analysis, which has an $n(z)$ that is shifted towards lower redshifts, where the model is slightly less accurate. Additionally, for the real data analysis, the mean of the aperture number values for each quantile was added to the data vector, so we had to verify if the extended data yields unbiased inferences. In this validation, we also tested the robustness of our analysis with respect to the IA in the sources by using the simulations described in Sect. 3.2.5 that are infused

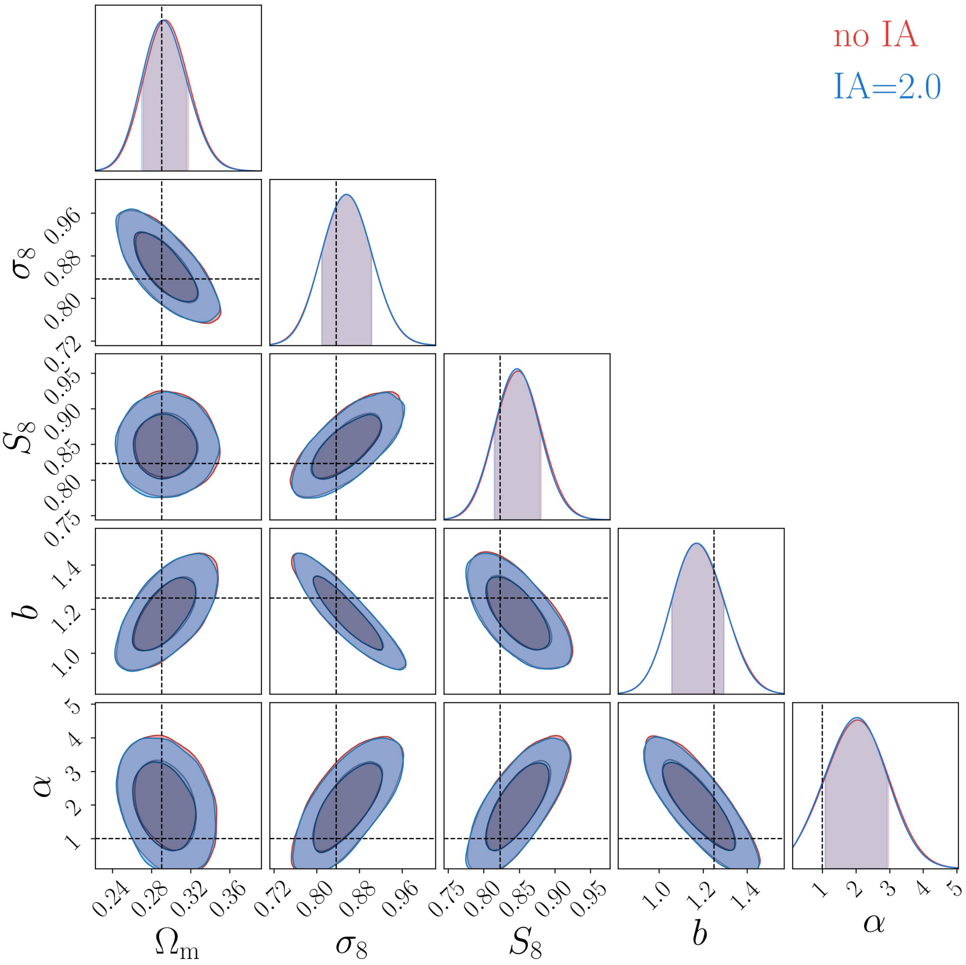

Figure 6.6: Cosmological inference with the adapted filter using the cosmo-SLICS simulations with and without IA infusion, analysed with our model that ignores IA. The posteriors are almost indistinguishable from each other. Figure adapted from B22b.

with IA. Additionally, we tested on a realistic KiDS-1000 data vector, which we accomplished by using shear signals with shape noise. Since the outer 2 deg^2 are not fully covered by the filter, we removed the outer 2 deg^2, so that by averaging over 20 light-cones an effective area of the KiDS-1000 data was achieved. The resulting shear profiles and the mean aperture number values for the highest and lowest two quantiles are shown in Fig. 6.5, where we excluded the middle quantile with the lowest cosmological signal to avoid the singular covariance matrix.

In order to quantify all these effects, we performed MCMC analyses using the data shown in Fig. 6.5. For the MCMC analyses we used the method of Percival et al. (2022) described in Sect. 2.3.2, with a t-distribution as the likelihood function. The resulting posterior for two IA amplitudes are shown in Fig. 6.6, where we added the galaxy bias b parameter and α parameter introduced in Sect. 5.3 as free parameters to the pipeline. The first important observation is that the IA amplitude does not, as expected, affect the posterior at all, so the modelling of it is obsolete and can be ignored in the later real data analysis. We do not expect the IA amplitude to influence our data vector because the $n(z)$ of the lens galaxies and source galaxies are separated. Therefore, the II term described in Eq. (2.93) vanishes. Second, and very importantly, the analyses could recover the input cosmology for all parameters within the $1\,\sigma$, even for the KiDS-bright redshift distribution with more non-linear effects and the additional information of the aperture number. The σ_8 and the galaxy bias b parameter correlate with the model vector amplitude, which is in concordance with Eq. (2.42), such that $\sigma_8 \propto b^{-1}$. Although this anti-correlation between σ_8 and b could potentially affect the robustness of estimating the parameters, they are essential for our model and therefore cannot be ignored.

6.3 Validation on baryonic feedback

As the last validation, we investigated the impact of baryons on the DSS with the *Magneticum* simulations described in Sect. 3.2.6. Four combinations emerged by combining the mocks with DM-only and Hydro (DM + Baryons) for the lenses and source: DM-DM, DM-Hydro, Hydro-DM and Hydro-Hydro. Figure 6.7 visualise the differences of $\langle N_{\rm ap} \rangle$ between the DM-only and Hydro lens mocks. Figure 6.8 visualise the differences between all four data vectors (DM-DM, DM-Hydro, Hydro-DM and Hydro-Hydro) compared to the dark matter-only vector (DM-DM). The deviations are well inside the expected KiDS-1000 uncertainty measured with the FLASK. The biggest differences are seen if baryonic feedback processes are included in the lens mocks, which is conceivable because pixels close to the $N_{\rm ap}$ threshold between two quantiles are moved to another quantile. Other studies of baryonic feedback like Heydenreich et al. (2022a) or Harnois-Déraps et al. (2021) found that the inclusion of baryons does impact their statistic. For the DSS, however, baryons have only a minor impact but becoming more relevant at small scales. Given this, we could safely neglect the effects of baryons in our real data analysis.

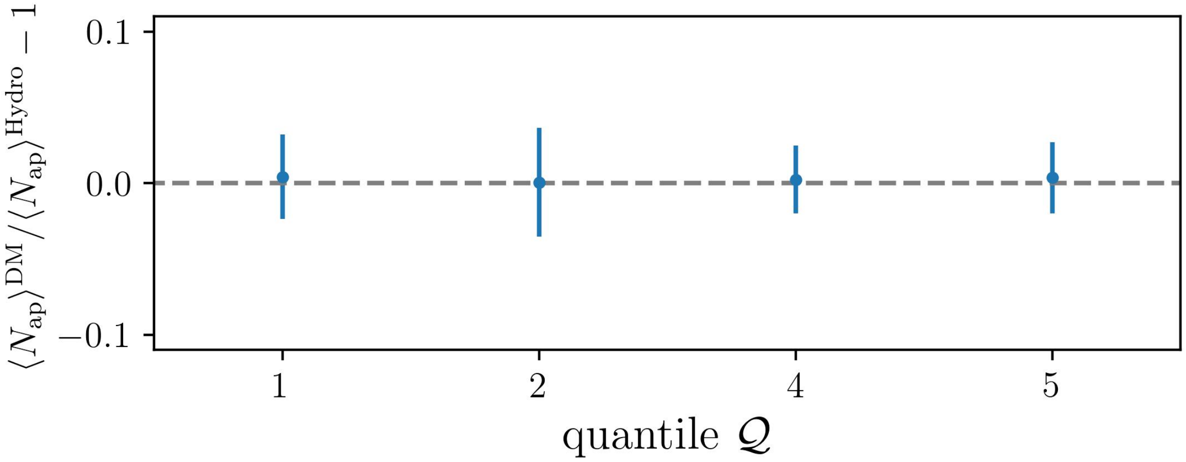

Figure 6.7: Comparison of the aperture number measurements from the hydro and dark matter-only *Magneticum* simulations. The error bars indicate the expected statistical uncertainty of KiDS-1000. Figure adapted from B22b.

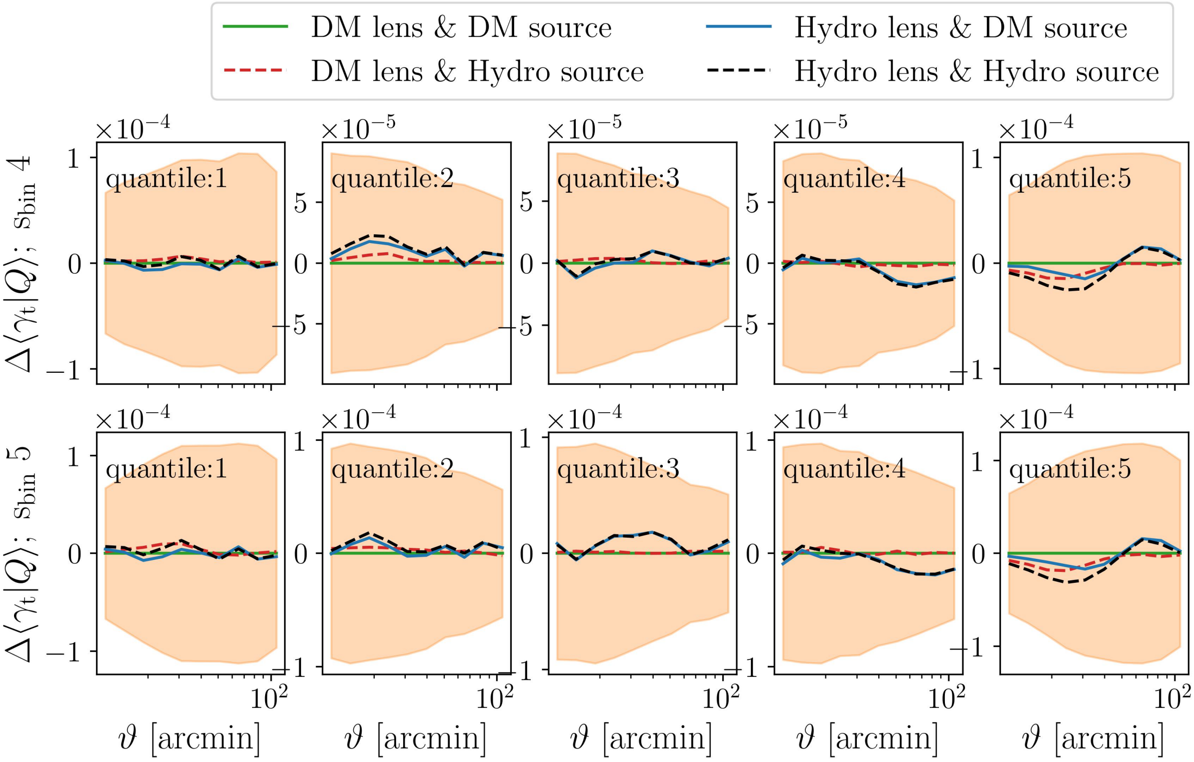

Figure 6.8: Absolute differences between the mean shear profiles for all quantiles using one of the four combinations DM-DM, DM-Hydro, Hydro-DM, and Hydro-Hydro relative mean shear profiles using the dark matter-only mocks (DM-DM). The error bands indicate the expected statistical uncertainty of KiDS-1000. Figure adapted from B22b.

7

Results and discussion of KiDS-1000 analysis

This chapter repeats the results of the real DSS analysis presented in B22b, where we used the KiDS-bright as lenses and the fourth and fifth tomographic bin of KiDS-1000 as sources. Although I was not involved in the infrastructure to create these catalogues, during the DSS analysis, I discovered that a subset of the KiDS-1000 tiles had an offset between the galaxy tile centroids and their corresponding mask centroids. This discovery resulted in a new data release (DR 4.1), which was used for the DSS analysis (and all subsequent KiDS-1000 analyses). I use the scientific formulation "we" for the rest of this chapter, since these results emerged from discussions with the co-authors, highlighting Marika Asgari and Hendrik Hildebrandt in addition to the first authors. The other authors mentioned are either infrastructure contributors of KiDS or provided simulations for the validation in the preceding chapter.

For all analyses in this chapter, we varied the two cosmological parameters Ω_m and σ_8 and the two astrophysical parameters b and α, and marginalised over the uncertainty of the mean redshift $\delta\langle z\rangle$ and the shear correction m-bias uncertainty. The prior ranges are summarised in Table 7.1.

Table 7.1: Uniformly $\mathcal{U}$ and normally distributed $\mathcal{N}$ priors on the parameters used in our cosmological inferences. The $\delta\langle z\rangle$ for the sources follow a joint normal distribution with covariance matrix $C_{\delta\langle z\rangle}$ shown in figure 6 of Hildebrandt et al. (2021). Table adapted from B22b.

parameter	prior
Ω_m	$\mathcal{U}(0.20, 0.50)$
σ_8	$\mathcal{U}(0.45, 1.00)$
bias b	$\mathcal{U}(0.5, 2.5)$
α	$\mathcal{U}(0.1, 8)$
$\delta\langle z\rangle$ full KiDS-bright sample	$\mathcal{N}(0.0, 0.01)$
$\delta\langle z\rangle$ red KiDS-bright sample	$\mathcal{N}(0.0, 0.01)$
$\delta\langle z\rangle$ blue KiDS-bright sample	$\mathcal{N}(0.0, 0.01)$
$\delta\langle z\rangle$ source bin 4,5	$\mathcal{N}([0.011, -0.006], C_{\delta\langle z\rangle})$
m-bias source bin 4	$\mathcal{N}(0.002, 0.012)$
m-bias source bin 5	$\mathcal{N}(0.007, 0.010)$

The resulting shear profiles and mean aperture number are shown in Figs. 7.1 and 7.2, where the displayed model is computed at the MAP value, listed in the first column of Table 7.2, using the best-estimated $n_{\mathrm{be}}(z)$ shown as the black solid line in Fig. 3.1. In this table, we also report the goodness-of-fit in terms of the reduced χ^2/d.o.f. and p-values (see Sect. 2.3.2), which show that the data are well fitted by the model. For the analyses shown in this chapter, we use the method of Percival et al. (2022) described in Sect. 2.3.2, with a t-distribution as the likelihood function.

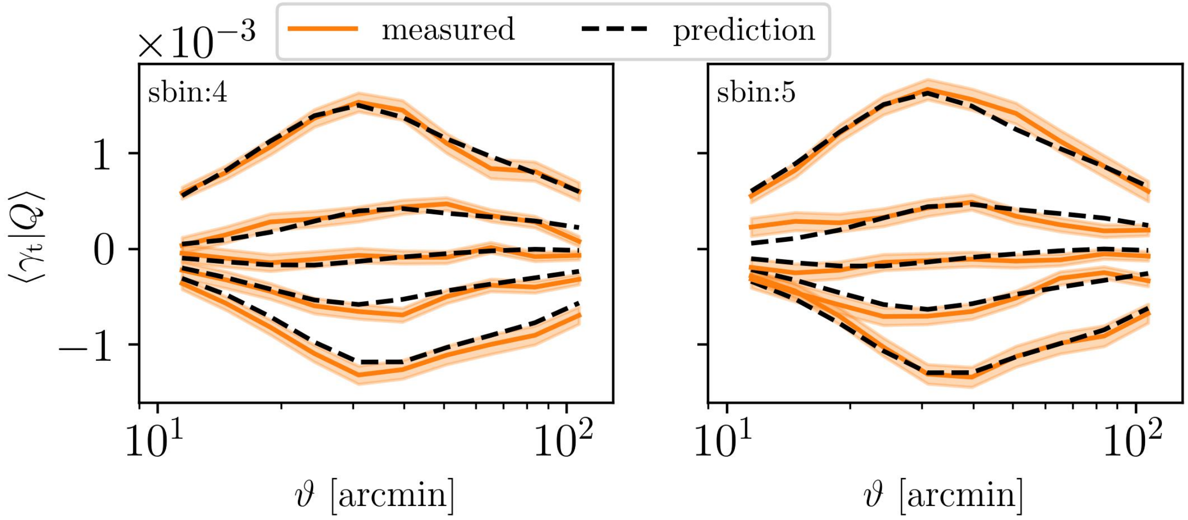

Figure 7.1: Shear profiles measured in the observed data, compared to the MAP values listed in the left colums of Table 7.2. The shaded region shows the statistical uncertainty estimated from 1000 FLASK realisations. Figure adapted from B22b.

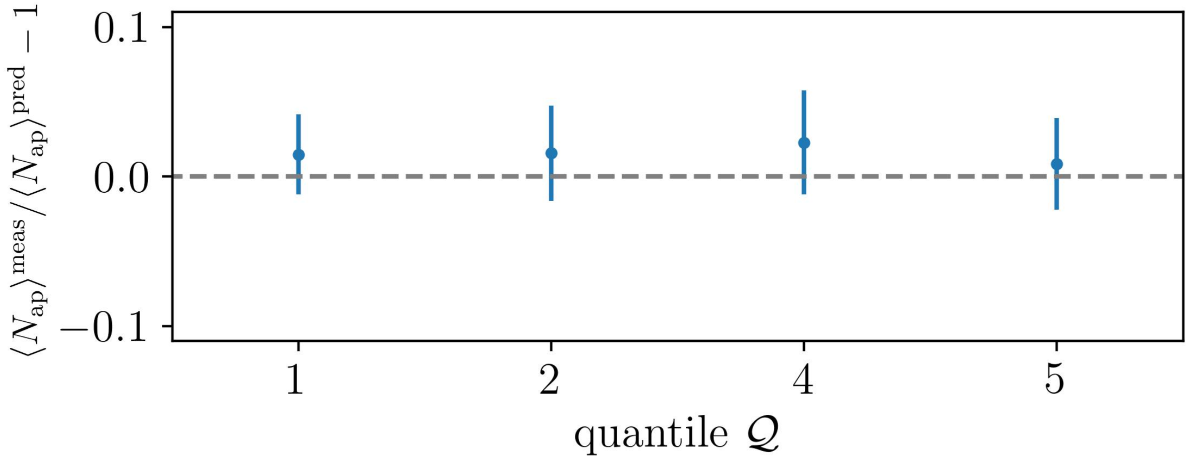

Figure 7.2: Comparing $\langle N_{\mathrm{ap}} \rangle$ measurements from the KiDS-bright sample to our model, evaluated at the MAP values shown in the left column of Table 7.2. Figure adapted from B22b

The posterior of the DSS using the entire data vector, meaning shear and aperture number information, and a data vector using only the shear information are presented in Fig. 7.3. We used the best-estimated lens $n_{\mathrm{be}}(z)$ for both analyses and compared them to posteriors of the KiDS-1000 cosmic shear constraints (COSEBIs) from Asgari et al. (2021) and to the CMB results from Planck Collaboration: Aghanim et al. (2020). The DSS has a slightly lower constraining power on S_8 compared to the COSEBIs analysis but is more constraining in Ω_{m} and σ_8 for both data vectors because clustering information was either included directly with the mean aperture number or indirectly as the shear profiles are measured according to the aperture number distribution. The sharp cut resulted from excluding all $\Omega_{\mathrm{m}} < 0.2$, where the model and the cosmo-SLICS disagreed. As both DSS analyses are entirely consistent with the cosmic shear results and have similar constraining power, we measured a similar tension to the CMB results. However, if a linear galaxy bias model is insufficient, the inferred S_8 might be smaller than the truth, as discussed in appendix A of B22b. Nonetheless, this is unlikely as the consistency between the shear-only DSS analysis and the complete DSS analysis supports the robustness of our inferred parameters concerning the galaxy bias model. Finally, we noted that the MAP of the full DSS

$$S_8^{\mathrm{DSS}} = 0.74^{+0.03}_{-0.02}\,, \tag{7.1}$$

compared to the KiDS-1000 cosmic shear constraints

$$S_8^{\mathrm{COSEBIs}} = 0.76^{+0.02}_{-0.02}\,. \tag{7.2}$$

revealed competitive S/N while using only tomographic bins four and five. The benefit of the COSEBIs is that they marginalised over more cosmological parameters and sampled the parameter space differently.

In the next section, we investigate the robustness of our results concerning the lens redshift distribution $n(z)$ and varying the covariance matrix. We further present our galaxy colour-split analysis, where we also discuss the galaxy bias b and α results in more detail.

Table 7.2: Marginalised MAP values and their 68% confidence intervals. Here Ω_{m}, σ_8, α, and the linear galaxy bias parameter b are varied, where $h = 0.6898$, $w_0 = -1$ and $n_{\mathrm{s}} = 0.969$ are fixed. However, we marginalised over the $\delta\langle z\rangle$ and m-bias uncertainties. Table adapted from B22b.

	$n_{\mathrm{be}}(z)$	$n_{\mathrm{ph}}(z)$	$n_{\mathrm{sp}}(z)$
Ω_{m}	$0.27^{+0.02}_{-0.02}$	$0.30^{+0.03}_{-0.02}$	$0.32^{+0.03}_{-0.03}$
σ_8	$0.78^{+0.04}_{-0.04}$	$0.76^{+0.04}_{-0.05}$	$0.74^{+0.05}_{-0.05}$
S_8	$0.74^{+0.03}_{-0.02}$	$0.76^{+0.03}_{-0.02}$	$0.77^{+0.03}_{-0.03}$
b	$1.32^{+0.12}_{-0.11}$	$1.31^{+0.11}_{-0.12}$	$1.28^{+0.14}_{-0.12}$
α	$1.34^{+0.74}_{-0.99}$	$1.41^{+0.92}_{-0.82}$	$1.87^{+0.97}_{-0.90}$
χ^2/d.o.f.	0.79	0.81	0.82
p-value	0.91	0.89	0.88

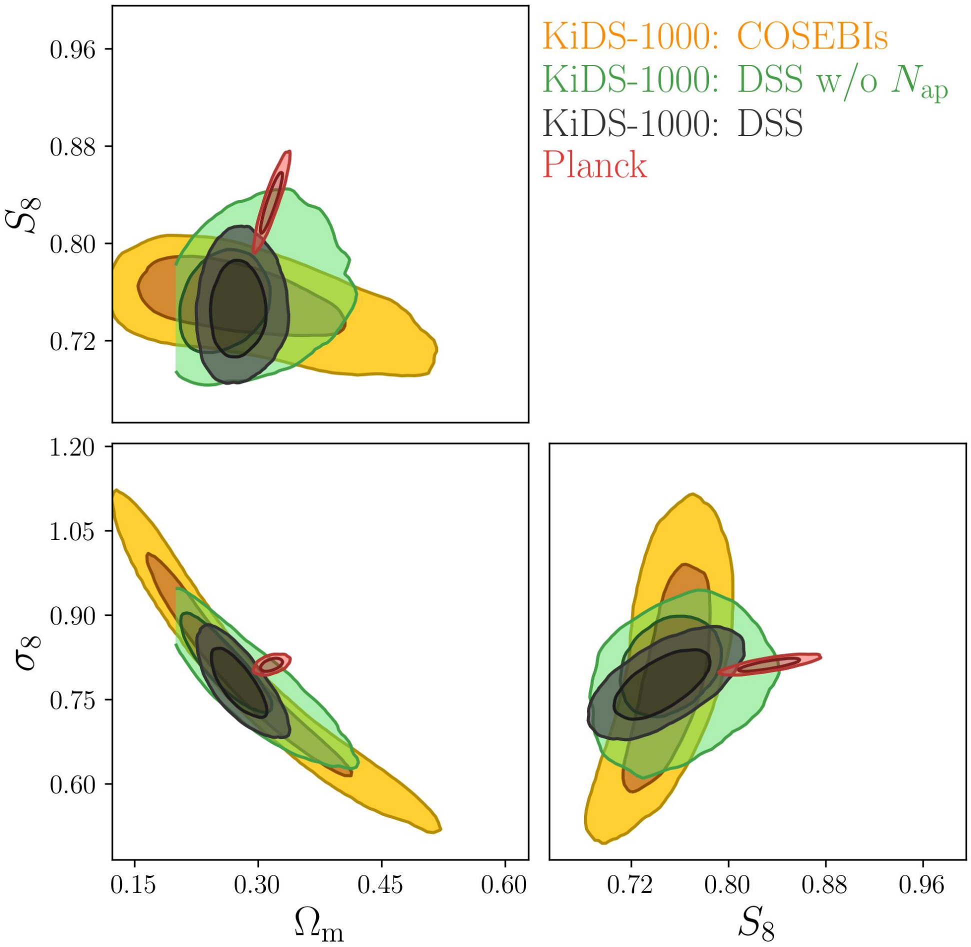

Figure 7.3: Cosmological posteriors of the DSS analysis with the adapted filter for the best-estimated $n_{\rm be}(z)$ using the full data vector (black) and shear-only (green) compared to the COSEBIs posteriors (orange) presented in Asgari et al. (2021) and CMB results of Planck Collaboration: Aghanim et al. (2020) in red. Due to the mismatch of the model with the cosmo-SLICS for cosmologies with $\Omega_{\rm m} < 0.2$, we cut the posteriors at $\Omega_{\rm m} = 0.2$. The consistency between the shear-only DSS analysis to the full analysis supports the assumption of using a linear galaxy bias model. Figure adapted from B22b.

7.1 Impact of the lens redshift distribution

The impact of the shape of the lens galaxy redshift distribution $n(z)$, shown in Fig. 3.1, is visualised in Fig. 7.4. For this, we used the best-estimated $n_{\rm be}(z)$, the photometric redshift distribution $n_{\rm ph}(z)$ itself without any smoothing, and the spectroscopic redshift $n_{\rm sp}(z)$ from those GAMA galaxies that are also in the KiDS-bright sample. As the $n_{\rm sp}(z)$ is not fully representative for the full KiDS-1000 survey, the posterior resulting from $n_{\rm sp}(z)$ should be taken with caution. The different posteriors are shifted along the $\Omega_{\rm m}$-σ_8 degeneracy axis, since the different $n(z)$ affect the predicted amplitude and slope of the shear profiles, which are in turn highly sensitive to $\Omega_{\rm m}$ and σ_8. We summarise the resulting MAP values in Table 7.2. As the true $n(z)$ is certainly not identical but very close to these tested $n(z)$, using the difference of the resulting MAP as additional uncertainties is probably a fair estimate.

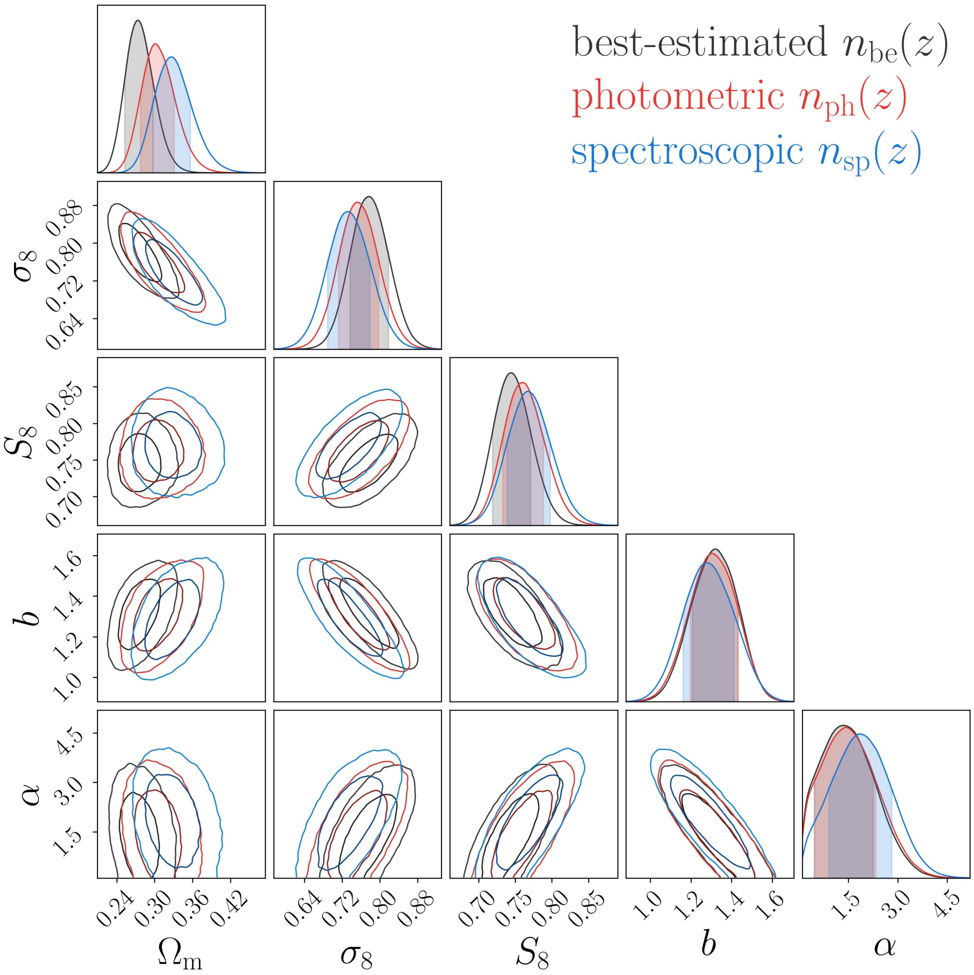

Figure 7.4: Posteriors resulting from the real KiDS-1000 data vector and model vector determined from using the different lens $n(z)$ shown in Fig. 3.1. The black contour is identical to black contour shown in Fig.7.3. Figure adapted from B22b.

We additionally tested the impact of the photometric redshift cut at $z_{\mathrm{ph}} = 0.1$ by measuring the posterior for the real KiDS-1000 data if we apply the photometric redshift cuts at $z_{\mathrm{ph}} > 0.15$ and $z_{\mathrm{ph}} > 0.2$. The posteriors shifted by less than the 68% credibility region, indicating the robustness of our measurement to this galaxy selection.

7.2 Cosmology scaling of the covariance matrix

The covariance matrices used so far are always determined at a specific point in the parameter space, which is usually not identical to the MAP. However, it is the subject of current analyses if the cosmology should be kept fixed in the covariance matrix (van Uitert et al., 2018) or measured at each parameter that the MCMC evaluates, as suggested in Eifler et al. (2009). The latter could result in over-constraints, as discussed in Carron (2013), so we explore both methods here to check if our analysis is affected.

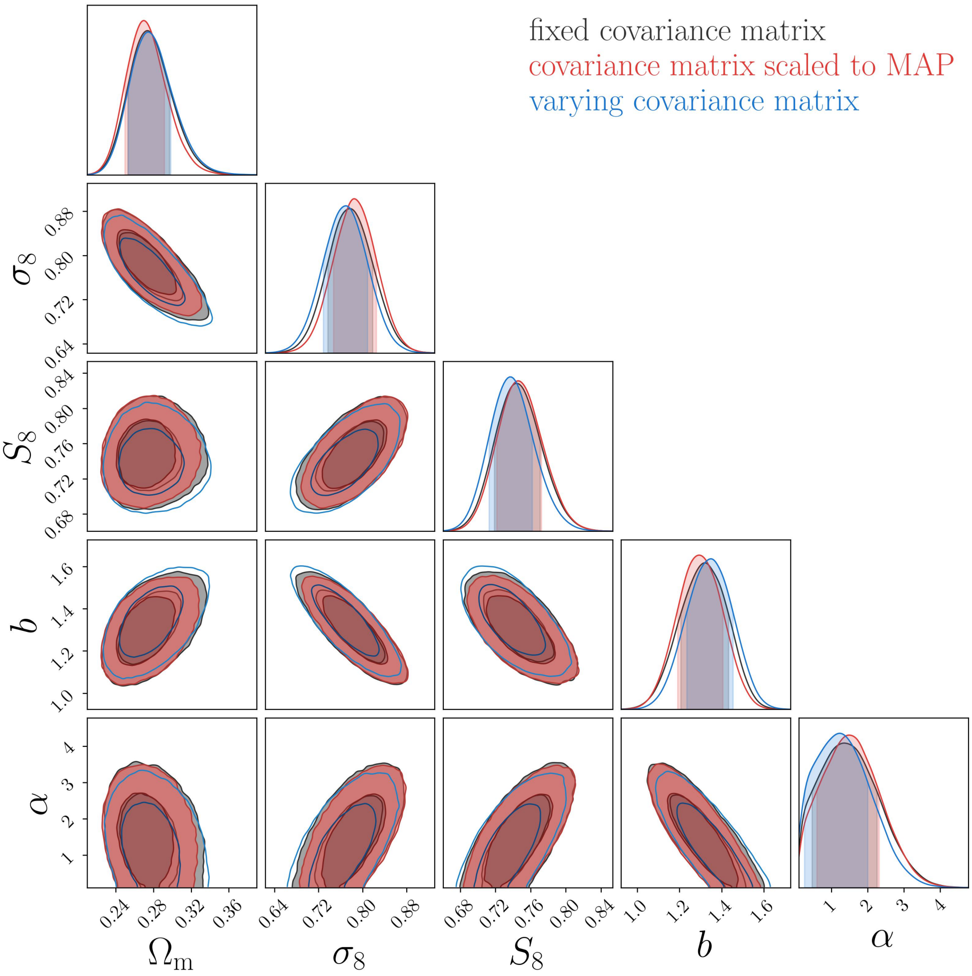

Figure 7.5: Comparison of posteriors resulting from the real KiDS-1000 data vector and model vector determined with the $n_\mathrm{be}(z)$, if the covariance matrices is scaled by Eq. (7.4). The differences are negligible. Figure adapted from B22b.

We do not have an analytical description of the DSS covariance matrix yet, so in principle, this requires measuring a covariance matrix at each step using simulations. As this is not feasible, we assume that the covariance matrix scales quadratically with the signal, which wrongly rescales the shape-noise components. Nevertheless, the quadratic scaling is expected to be a good approximation to check if a varying covariance matrix affects the posteriors of the DSS analysis. The scaling was done by calculating at a new cosmology $\boldsymbol{\Theta}$ the ratio between the predicted model $\boldsymbol{m}(\boldsymbol{\Theta})$ and the model predicted at the original cosmology of the covariance matrix $\boldsymbol{m}\left(\boldsymbol{\Theta}^{\mathrm{F}}\right)$,

$$r_i(\boldsymbol{\Theta}) = \frac{m_i(\boldsymbol{\Theta})}{m_i\left(\boldsymbol{\Theta}^{\mathrm{F}}\right)}\,, \tag{7.3}$$

where i is the i-th index of the model vector. So we infused the cosmological dependence by scaling the components ij of the covariance matrix as

$$C_{ij}(\boldsymbol{\Theta}) = C^{\mathrm{F}}_{ij}\, r_i(\boldsymbol{\Theta})\, r_j(\boldsymbol{\Theta})\,. \tag{7.4}$$

The determinant of the covariance matrix changes with cosmology, too, and therefore, needs to be recalculated at each step during the MCMC process.

In Fig. 7.5 we show three posteriors using the best-estimated $n_{\mathrm{be}}(z)$ and marginalise over all nuisance parameters as before. The black contours are the posterior with the original FLASK covariance matrix and are identical to the results shown in Fig. 7.4. The red contours are measured with a covariance matrix scaled to the MAP value. As a scaled covariance matrix might change the MAP, we found them in an iterative process. Lastly, we show the posteriors that result if the covariance matrix is scaled to each step during the MCMC process in blue. As all posteriors are well within $1\,\sigma$, we were not concerned about the robustness of our inferred parameters regarding a covariance matrix that varies with cosmological parameters.

Table 7.3: The MAP values and 68% confidence intervals resulting from MCMC chains shown in Fig. 7.6. The first column is the same as in Table 7.2. We fixed $h = 0.6898$, $w_0 = -1$ and $n_{\mathrm{s}} = 0.969$ but marginalised over the $\delta\langle z\rangle$ and m-bias uncertainties. If limits are not given, they are dominated by priors. Table taken from B22b.

<table>
<tr><th></th><th>full</th><th colspan="2">red + blue</th></tr>
<tr><td>Ω_{m}</td><td>$0.27^{+0.02}_{-0.02}$</td><td colspan="2">$0.28^{+0.02}_{-0.02}$</td></tr>
<tr><td>σ_8</td><td>$0.78^{+0.04}_{-0.04}$</td><td colspan="2">$0.78^{+0.04}_{-0.02}$</td></tr>
<tr><td>S_8</td><td>$0.74^{+0.03}_{-0.02}$</td><td colspan="2">$0.76^{+0.03}_{-0.02}$</td></tr>
<tr><td>b</td><td>$1.32^{+0.12}_{-0.11}$</td><td>$1.85^{+0.07}_{-0.16}$</td><td>$1.03^{+0.04}_{-0.11}$</td></tr>
<tr><td>α</td><td>$1.34^{+0.74}_{-0.99}$</td><td>$0.10^{+0.69}$</td><td>$2.29^{+0.34}_{-0.12}$</td></tr>
<tr><td>χ^2/d.o.f.</td><td>0.79</td><td colspan="2">1.01</td></tr>
<tr><td>p-value</td><td>0.91</td><td colspan="2">0.46</td></tr>
</table>

7.3 Red and blue split

To learn more about the behaviour of different galaxy types and as a cosmological robustness check, we present here a joint analysis of the red and blue galaxies of the KiDS-bright sample. We used the best-estimated $n_{\mathrm{be}}(z)$ for this analysis and combined the individual measured red and blue data vector in a joint analysis that doubles the elements of the model and data vector. The MAP values with corresponding reduced χ^2/d.o.f. and p-values stated in Table 7.3 indicate an accurate fit. The resulting posteriors are shown in Fig. 7.6.

First, it is noticeable that the posterior of the full KiDS-bright sample and that of the joint red and blue analysis are consistent and within $0.35\,\sigma$, which supports the robustness of the DSS analysis. Furthermore, we see that the blue sample prefers a smaller linear galaxy bias b than the red sample. This concurs with our discussion in Sect. 2.1.4, where red galaxies are known to be more strongly clustered than blue galaxies resulting in a larger galaxy bias. Finally, the α parameter reveals that blue galaxies follow a super-Poisson distribution and red galaxies a sub-Poisson distribution, since for the blue galaxies $\alpha \gg 1$ and the red galaxies have $\alpha < 1$. Friedrich et al. (2022) found that a higher satellite fraction leads to a higher α value, so the blue sample seems to have more satellites.

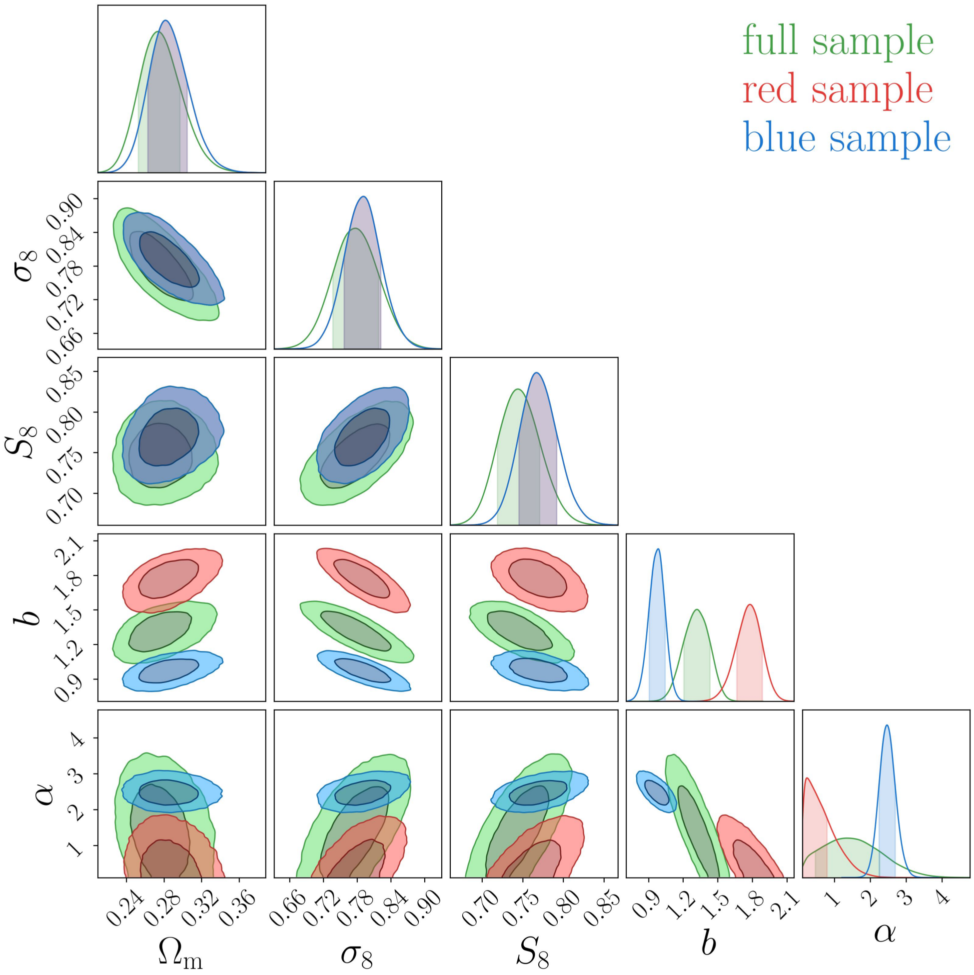

Figure 7.6: This figure shows in green the posteriors of the full sample using the real KiDS-1000 data vector and model vector determined with the $n_{\mathrm{be}}(z)$, and are identical to the black posteriors shown in Fig. 7.4. The joint analysis of red+blue has by construction the same cosmology, which results in the dark blue contours, but has individual galaxy bias b and α parameters. Figure adapted from B22b.

8

Conclusion

'Das Wichtigste ist, daß man nicht aufhört zu fragen. - The most important thing is that you don't stop asking.'

– Albert Einstein, speaking courage to a young student.

In this thesis, we modified the density split statistic (DSS) to general filter functions, which allows selecting optimised filter functions, U, in terms of signal-to-noise ratio (S/N). The overall idea of the DSS is to measure the mean tangential shear, γ_t, for some specific sub-areas of the survey. These sub-areas or quantiles, Q, are determined according to the aperture number, N_ap, which in turn is the galaxy number density smoothed with a filter function U. By correlating all pixels belonging to one quantile with the shear of the background galaxies, the tangential shear for a given quantile, $\langle\gamma_\mathrm{t}|Q\rangle$, follows. The DSS was introduced in Gruen et al. (2016), and the first cosmological parameter analysis with the DSS was done in Gruen et al. (2018, hereafter G18). They demonstrated that the DSS is a powerful cosmological tool by constraining cosmological parameters from the Dark Energy Survey (DES) First Year and Sloan Digital Sky Survey (SDSS) data, using the DSS model derived in Friedrich et al. (2018, hereafter F18).

This final chapter summarises our work and concludes with an outlook.

8.1 Summary

In the first series of papers, Burger et al. (2020), reviewed here in chapter 4, we developed a pair of adapted filter functions for the DSS, which is matched between the aperture mass and galaxy number statistics. This means that the filter functions smooth with the same angular weighting the lensing convergence and the galaxy number density. A key result of this work was that the adapted filter functions yield better correlations between galaxy number density and shear signal than the previously used top-hat filter, regardless of the galaxy bias model. Another significant result is that the S/N with the adapted filter was higher for all quantiles compared to a top-hat filter with approximately the same shear peak positions, indicating that the adapted filter's signals can be measured better in observed data. Lastly, we showed in this work that the adapted filter is more sensitive to different cosmological parameters, resulting in tighter parameter constraints.

All these advantages motivated us to modify the already existing model of the DSS described in F18 from solely top-hat filter functions to general filter functions. The results of this work are published in Burger et al. (2022a, hereafter B22a) and reviewed in this work in chapter 5. By recalculating the probability density function (PDF) of the projected matter density contrast smoothed with the filter function U, $p(\delta_{\mathrm{m},U})$, the conditional expectation values of the convergence inside a radius ϑ for a fixed smoothed matter density contrast, $\langle\kappa_{<\vartheta}|\delta_{\mathrm{m},U}\rangle$, and the conditional PDF of N_{ap} given the smoothed matter density contrast, $p(N_{\mathrm{ap}}|\delta_{\mathrm{m},U})$, the model was modified to general filter functions. While for $\langle\kappa_{<\vartheta}|\delta_{\mathrm{m},U}\rangle$ and $p(\delta_{\mathrm{m},U})$ we used the approaches of F18 with modified calculations of the moments, we introduced a fully new approach to calculate $p(N_{\mathrm{ap}}|\delta_{\mathrm{m},U})$ by using its characteristic function (CF). With the corresponding expression of the CF, $p(N_{\mathrm{ap}}|\delta_{\mathrm{m},U})$ is either calculated by inverse Fourier transformation or by a log-normal PDF approximation, where the first three moments follow from derivatives of the CF. For exclusively positive filters, like a top-hat or Gaussian filter, the description of $\delta_{\mathrm{m},U}$ by a log-normal PDF is very accurate. However, we used a bi-variate log-normal ansatz for compensated filters, which improved the accuracy significantly. Since compensated filter functions have a positive and a negative part, the idea was to consider both parts as exclusively positive filters and then combine both by using a convolution.

The model's validation was done in the second half of B22a and the first part of Burger et al. (2022b, hereafter B22b), and is summarised in chapter 6. We compared each model ingredient to simulations of Takahashi et al. (2017, hereafter T17), where no significant difference for non-negative filters was detected for the PDFs and the tangential shear profiles. For compensated filters, however, discrepancies resulted in a biased inference, although still inside $1\,\sigma$ of the expected fourth data release of the Kilo-Degree Survey (KiDS-1000) uncertainty. To correct this, we calibrated the model vector to match the T17. We verified that the bias was gone by performing another inference on the independent fiducial cosmology of cosmo-SLICS (Harnois-Déraps et al., 2019). Another advantage of the calibration is that it allows using even smaller scales, as suggested by F18, which increases the constraining power and potentially enables the study of baryonic effects that interfere at small scales. We further investigated the impact of baryons and intrinsic alignment (IA) on the DSS. But for the used scales, none of these affected our DSS analysis. Whereas baryonic effects might become more important for smaller scales, IA can be ignored as long as the redshift distributions of the lenses and sources do not overlap significantly. By investigating IA we also verified that the calibrated model yields unbiased results even if the means of the aperture number of the individual quantiles are included, and the shear profiles are measured from realistic source ellipticities.

In the remaining part of B22b, described here in chapter 7, we performed the first cosmological parameter estimation of the unblinded KiDS-1000 data using the DSS. For this analysis, the bright sample of the KiDS-1000 release (KiDS-bright) sample, described in Bilicki et al. (2018), serves to construct the foreground density map, while the shear information was taken from the fourth and fifth tomographic redshift bins of the KiDS-1000 data, described in Hildebrandt et al. (2021). One of this analysis's main uncertainties is the lenses' redshift distribution, which we investigated using $n(z)$ with different shapes. Since the posteriors varied by $\sim 0.5\,\sigma$, with the highest affect on Ω_{m}, we assigned an extra error term on our results, such that $S_8 = 0.74^{+0.03}_{-0.02}\pm 0.01$ after marginalising over systematic effects. The constraints on S_8 are competitive too and consistent with the KiDS-1000 cosmic shear constraints from Asgari et al. (2021), while using only a subset of all available shear data but varied over fewer parameters. Since the DSS analysis with the current set-up is not able to constrain parameters like the Hubble parameter h or the dark energy equation-of-state w_0 parameter, the posterior distribution would increase if h and w_0 are varied too. However, the DSS analysis with the current set-up is not sensitive to parameters like the IA amplitude or the primordial power spectrum power law index n_s, so varying these parameters would not change the resulting posteriors. Finally, as a cosmology robustness check and to better understand the behaviour of different galaxy types, we split the full KiDS-bright sample into red and blue galaxies and analysed them jointly in a combined data vector and a joint covariance matrix. The first important observation was that the posteriors of the cosmological parameters agree for the full and joint red+blue analyses within 0.35 standard deviations. The second observation was that linear galaxy bias behaves as expected, with blue galaxies being less and red galaxies more biased than the full sample. Lastly, we found that blue galaxies are super-Poisson distributed, and red galaxies are sub-Poisson distributed. This reveals that blue galaxies have a larger fraction of satellite galaxies according to Friedrich et al. (2020).

To conclude this work, we find that although higher-order statistics are complicated to model and so usually rely on cosmological simulations, the DSS model is a powerful cosmological tool with a significant advantage in breaking the Ω_m-σ_8 degeneracy. Furthermore, it enables the measurement of the galaxy bias on linear scales and the Poissanity of different galaxy types.

8.2 Outlook

In future analyses that deal with the DSS, it would be interesting to investigate the impact of the number of quantiles. Adding, for instance, the information of the highest 5% quantile would increase the information content of the highest density peaks, which potentially results in huge gain of constraining power.

Furthermore, we adjusted the size of our filter function such that the model is applicable to the KiDS-1000 analysis. However, smaller scales are promising to increase the constraining power and learn more about baryonic feedback processes. For this to be feasible, either the model needs to be improved, or it has to be checked if the calibration removes the model's inaccuracies at smaller scales.

Although using lens and sources redshift distributions that overlap significantly introduces effects like the boost factor described in G18, using overlapping lens-source combinations in future analyses could help to constrain IA parameters.

Lastly, for stage IV surveys like Euclid (Laureijs et al., 2011), with several tomographic bins, extraordinary resolution and billions of galaxies measured on an area of approximately 15 000 $\deg^2$, or the Vera Rubin Observatory Legacy Survey of Space and Time (Ivezic et al., 2008) with even 18 000 $\deg^2$ expected sky coverage, an inference of the dark energy equation-of-state w_0 will be an interesting new application of the DSS. Furthermore, as the constraining power of these stage IV surveys is massively increased, the assumption of a constant galaxy bias is potentially no longer satisfied. However, with the simulations already in place like the Scinet Light Cone Simulations (SLICS) with halo occupation distribution (HOD) mocks or soon to be available, these can be tested so that nothing can prevent an accurate and powerful DSS analysis of a Stage IV survey. In that context, it might also be interesting to see if stage IV surveys have enough constraining power to assign a different galaxy bias to each quantile, as galaxies are probably biased differently in matter density peaks and voids.

Bibliography

Abbott, B. P., Abbott, R., Abbott, T. D., et al., 2016. *Observation of gravitational waves from a binary black hole merger.* Phys. Rev. Lett., 116:061102. doi: 10.1103/PhysRevLett.116.061102. URL `https://link.aps.org/doi/10.1103/PhysRevLett.116.061102`

Abbott, T. M. C., Abdalla, F. B., Alarcon, A., et al., 2018. *Dark Energy Survey year 1 results: Cosmological constraints from galaxy clustering and weak lensing.* Physical Review D, 98, 4:043526. doi: 10.1103/PhysRevD.98.043526

Abramowitz, M. and Stegun, I. A. (eds.), *Handbook of mathematical functions with formulas, graphs, and mathematical tables*, volume 55 of *Applied mathematics series* (US Government Printing Office, Washington, DC, 1972), 10th print. with corrections edition. ISBN 9780318117300. URL `https://www.cs.bham.ac.uk/~aps/research/projects/as/`

Amon, A., Gruen, D., Troxel, M. A., et al., 2022. *Dark Energy Survey Year 3 results: Cosmology from cosmic shear and robustness to data calibration.* Physical Review D, 105, 2:023514. doi: 10.1103/PhysRevD.105.023514

Anderson, T. W., *An introduction to multivariate statistical analysis* (Wiley-Interscience, 2003). ISBN 9780471360919

Arfken, G. and Weber, H. J., *Mathematical methods for physicists* (Elsevier Academic Press, Amsterdam, Heidelberg, 2008), 6. ed., 5. [print., international ed.] edition. ISBN 978-0120598762

Asgari, M., Lin, C.-A., Joachimi, B., et al., 2021. *KiDS-1000 cosmology: Cosmic shear constraints and comparison between two point statistics.* Astronomy & Astrophysics, 645:A104. doi: 10.1051/0004-6361/202039070

Bartelmann, M., 2010. *Gravitational lensing.* Classical and Quantum Gravity, 27, 23:233001. doi: 10.1088/0264-9381/27/23/233001

Bartelmann, M. and Schneider, P., 2001. *Weak gravitational lensing.* Physics Reports, 340:291. doi: 10.1016/S0370-1573(00)00082-X

Barthelemy, A., Codis, S., and Bernardeau, F., 2021. *Probability distribution function of the aperture mass field with large deviation theory.* Monthly Notices of the Royal Astronomical Society, 503, 4:5204. doi: 10.1093/mnras/stab818

Bayes, T., 1763. *Lii. an essay towards solving a problem in the doctrine of chances. by the late rev. mr. bayes, f. r. s. communicated by mr. price, in a letter to john canton, a. m. f. r. s.* Philosophical Transactions of the Royal Society of London:370

Bergé, J., Amara, A., and Réfrégier, A., 2010. *Optimal Capture of Non-Gaussianity in Weak-Lensing Surveys: Power Spectrum, Bispectrum, and Halo Counts.* Astrophysical Journal, 712, 2:992. doi: 10.1088/0004-637X/712/2/992

Bernardeau, F., Colombi, S., Gaztañaga, E., and Scoccimarro, R., 2002. *Large-scale structure of the Universe and cosmological perturbation theory.* Physics Reports, 367, 1-3:1. doi: 10.1016/S0370-1573(02)00135-7

Bilicki, M., Dvornik, A., Hoekstra, H., et al., 2021. *Bright galaxy sample in the Kilo-Degree Survey Data Release 4. Selection, photometric redshifts, and physical properties.* Astronomy & Astrophysics, 653:A82. doi: 10.1051/0004-6361/202140352

Bilicki, M., Hoekstra, H., Brown, M. J. I., et al., 2018. *Photometric redshifts for the Kilo-Degree Survey. Machine-learning analysis with artificial neural networks.* Astronomy & Astrophysics, 616:A69. doi: 10.1051/0004-6361/201731942

Bridle, S. and King, L., 2007. *Dark energy constraints from cosmic shear power spectra: impact of intrinsic alignments on photometric redshift requirements.* New Journal of Physics, 9, 12:444. doi: 10.1088/1367-2630/9/12/444

Brouwer, M. M., Demchenko, V., Harnois-Déraps, J., et al., 2018. *Studying galaxy troughs and ridges using weak gravitational lensing with the Kilo-Degree Survey.* Monthly Notices of the Royal Astronomical Society, 481, 4:5189. doi: 10.1093/mnras/sty2589

Brown, M. L., Taylor, A. N., Hambly, N. C., and Dye, S., 2002. *Measurement of intrinsic alignments in galaxy ellipticities.* Monthly Notices of the Royal Astronomical Society, 333, 3:501. doi: 10.1046/j.1365-8711.2002.05354.x

Burger, P., Friedrich, O., Harnois-Déraps, J., and Schneider, P., 2022a. *A revised density split statistic model for general filters.* Astronomy & Astrophysics, 661:A137. doi: 10.1051/0004-6361/202141628

Burger, P., Schneider, P., Demchenko, V., et al., 2020. *An adapted filter function for density split statistics in weak lensing.* Astronomy & Astrophysics, 642:A161. doi: 10.1051/0004-6361/202038694

Burger, P. A., Friedrich, O., Harnois-Déraps, J., et al., 2022b. *KiDS-1000 Cosmology: Constraints from density split statistics* . arXiv:2208.02171

Carron, J., 2013. *On the assumption of Gaussianity for cosmological two-point statistics and parameter dependent covariance matrices.* Astronomy & Astrophysics, 551:A88. doi: 10.1051/0004-6361/201220538

Castro, T., Borgani, S., Dolag, K., et al., 2021. *On the impact of baryons on the halo mass function, bias, and cluster cosmology.* Monthly Notices of the Royal Astronomical Society, 500, 2:2316. doi: 10.1093/mnras/staa3473

Chisari, N., Codis, S., Laigle, C., et al., 2015. *Intrinsic alignments of galaxies in the Horizon-AGN cosmological hydrodynamical simulation.* Monthly Notices of the Royal Astronomical Society, 454, 3:2736. doi: 10.1093/mnras/stv2154

Cole, S., Lacey, C. G., Baugh, C. M., and Frenk, C. S., 2000. *Hierarchical galaxy formation.* Monthly Notices of the Royal Astronomical Society, 319, 1:168. doi: 10.1046/j.1365-8711.2000.03879.x

Cole, S., Percival, W. J., Peacock, J. A., et al., 2005. *The 2dF Galaxy Redshift Survey: power-spectrum analysis of the final data set and cosmological implications.* Monthly Notices of the Royal Astronomical Society, 362, 2:505. doi: 10.1111/j.1365-2966.2005.09318.x

Coles, P. and Lucchin, F., *Cosmology: The Origin and Evolution of Cosmic Structure, Second Edition* (Wiley, 2002). ISBN 9780471489093

Cuesta-Lazaro, C., Quera-Bofarull, A., Reischke, R., and Schäfer, B. M., 2018. *Gravitational corrections to light propagation in a perturbed FLRW universe and corresponding weak-lensing spectra.* Monthly Notices of the Royal Astronomical Society, 477, 1:741. ISSN 0035-8711. doi: 10.1093/mnras/sty672. URL `https://doi.org/10.1093/mnras/sty672`

de Jong, J. T. A., Verdoes Kleijn, G. A., Boxhoorn, D. R., et al., 2015. *The first and second data releases of the Kilo-Degree Survey.* Astronomy & Astrophysics, 582:A62. doi: 10.1051/0004-6361/201526601

de Jong, J. T. A., Verdoes Kleijn, G. A., Erben, T., et al., 2017. *The third data release of the Kilo-Degree Survey and associated data products.* Astronomy & Astrophysics, 604:A134. doi: 10.1051/0004-6361/201730747

De Lucia, G. and Blaizot, J., 2007. *The hierarchical formation of the brightest cluster galaxies.* Monthly Notices of the Royal Astronomical Society, 375, 1:2. doi: 10.1111/j.1365-2966.2006.11287.x

DES Collaboration: Abbott, T. M. C., Aguena, M., Alarcon, A., et al., 2022. *Dark Energy Survey Year 3 results: Cosmological constraints from galaxy clustering and weak lensing.* Physical Review D, 105, 2:023520. doi: 10.1103/PhysRevD.105.023520

Di Valentino, E., Anchordoqui, L. A., Akarsu, Ö., et al., 2021a. *Cosmology Intertwined II: The hubble constant tension.* Astroparticle Physics, 131:102605. doi: 10.1016/j.astropartphys.2021.102605

Di Valentino, E., Anchordoqui, L. A., Akarsu, Ö., et al., 2021b. *Cosmology Intertwined III:* $f\sigma_8$ *and* S_8. Astroparticle Physics, 131:102604. doi: 10.1016/j.astropartphys.2021.102604

Dicke, R. H., Peebles, P. J. E., Roll, P. G., and Wilkinson, D. T., 1965. *Cosmic Black-Body Radiation.* Astrophysical Journal, 142:414. doi: 10.1086/148306

Driver, S. P., Hill, D. T., Kelvin, L. S., et al., 2011. *Galaxy and Mass Assembly (GAMA): survey diagnostics and core data release.* Monthly Notices of the Royal Astronomical Society, 413, 2:971. ISSN 0035-8711. doi: 10.1111/j.1365-2966.2010.18188.x. URL `https://doi.org/10.1111/j.1365-2966.2010.18188.x`

Dyson, F. W., Eddington, A. S., and Davidson, C., 1920. *A Determination of the Deflection of Light by the Sun's Gravitational Field, from Observations Made at the Total Eclipse of May 29, 1919.* Philosophical Transactions of the Royal Society of London Series A, 220:291. doi: 10.1098/rsta.1920.0009

Edge, A., Sutherland, W., Kuijken, K., et al., 2013. *The VISTA Kilo-degree Infrared Galaxy (VIKING) Survey: Bridging the Gap between Low and High Redshift.* The Messenger, 154:32

Eifler, T., Schneider, P., and Hartlap, J., 2009. *Dependence of cosmic shear covariances on cosmology. Impact on parameter estimation.* Astronomy & Astrophysics, 502, 3:721. doi: 10.1051/0004-6361/200811276

Einstein, A., 1915. *Die Feldgleichungen der Gravitation.* Sitzungsberichte der Königlich Preußischen Akademie der Wissenschaften (Berlin), 2:844

Einstein, A., 1936. *Lens-Like Action of a Star by the Deviation of Light in the Gravitational Field.* Science, 84, 2188:506. doi: 10.1126/science.84.2188.506

Eisenstein, D. J., Weinberg, D. H., Agol, E., et al., 2011. *SDSS-III: Massive Spectroscopic Surveys of the Distant Universe, the Milky Way, and Extra-Solar Planetary Systems.* Astronomical Journal, 142, 3:72. doi: 10.1088/0004-6256/142/3/72

Eisenstein, D. J., Zehavi, I., Hogg, D. W., et al., 2005. *Detection of the Baryon Acoustic Peak in the Large-Scale Correlation Function of SDSS Luminous Red Galaxies.* Astrophysical Journal, 633, 2:560. doi: 10.1086/466512

Event Horizon Telescope Collaboration: Akiyama, K., Alberdi, A., Alef, W., et al., 2019. *First M87 Event Horizon Telescope Results. I. The Shadow of the Supermassive Black Hole.* Astrophysical Journal Letters, 875, 1:L1. doi: 10.3847/2041-8213/ab0ec7

Falco, E. E., Gorenstein, M. V., and Shapiro, I. I., 1985. *On model-dependent bounds on H 0 from gravitational images : application to Q 0957+561 A, B.* Astrophysical Journal Letters, 289:L1. doi: 10.1086/184422

Farouki, R. and Shapiro, S. L., 1981. *Computer simulations of environmental influences on galaxy evolution in dense clusters. II - Rapid tidal encounters.* Astrophysical Journal, 243:32. doi: 10.1086/158563

Friedmann, A., 1922. *Über die Krümmung des Raumes.* Zeitschrift fur Physik, 10:377. doi: 10.1007/BF01332580

Friedrich, O., Gruen, D., DeRose, J., et al., 2018. *Density split statistics: Joint model of counts and lensing in cells.* Physical Review D, 98, 2:023508. doi: 10.1103/PhysRevD.98.023508

Friedrich, O., Halder, A., Boyle, A., et al., 2022. *The PDF perspective on the tracer-matter connection: Lagrangian bias and non-Poissonian shot noise.* Monthly Notices of the Royal Astronomical Society, 510, 4:5069. doi: 10.1093/mnras/stab3703

Friedrich, O., Uhlemann, C., Villaescusa-Navarro, F., et al., 2020. *Primordial non-Gaussianity without tails - how to measure f_{NL} with the bulk of the density PDF.* Monthly Notices of the Royal Astronomical Society, 498, 1:464. doi: 10.1093/mnras/staa2160

Fu, L., Kilbinger, M., Erben, T., et al., 2014. *CFHTLenS: cosmological constraints from a combination of cosmic shear two-point and three-point correlations.* Monthly Notices of the Royal Astronomical Society, 441, 3:2725. doi: 10.1093/mnras/stu754

Giblin, B., Heymans, C., Asgari, M., et al., 2021. *KiDS-1000 catalogue: Weak gravitational lensing shear measurements.* Astronomy & Astrophysics, 645:A105. doi: 10.1051/0004-6361/202038850

Gillessen, S., Eisenhauer, F., Trippe, S., et al., 2009. *Monitoring Stellar Orbits Around the Massive Black Hole in the Galactic Center.* Astrophysical Journal, 692, 2:1075. doi: 10.1088/0004-637X/692/2/1075

Gosset, W. S., 1908. *The probable error of a mean.* Biometrika:1

Gruen, D., Friedrich, O., Amara, A., et al., 2016. *Weak lensing by galaxy troughs in DES Science Verification data.* Monthly Notices of the Royal Astronomical Society, 455, 3:3367. doi: 10.1093/mnras/stv2506

Gruen, D., Friedrich, O., Krause, E., et al., 2018. *Density split statistics: Cosmological constraints from counts and lensing in cells in DES Y1 and SDSS data.* Physical Review D, 98, 2:023507. doi: 10.1103/PhysRevD.98.023507

Gunn, J. E. and Gott, I., J. Richard, 1972. *On the Infall of Matter Into Clusters of Galaxies and Some Effects on Their Evolution.* Astrophysical Journal, 176:1. doi: 10.1086/151605

Haight, F. A., *Handbook of the Poisson distribution [by] Frank A. Haight* (Wiley New York, 1967)

Halder, A., Friedrich, O., Seitz, S., and Varga, T. N., 2021. *The integrated three-point correlation function of cosmic shear.* Monthly Notices of the Royal Astronomical Society, 506, 2:2780. doi: 10.1093/mnras/stab1801

Hamana, T., Shirasaki, M., Miyazaki, S., et al., 2020. *Cosmological constraints from cosmic shear two-point correlation functions with HSC survey first-year data.* PASJ, 72, 1:16. doi: 10.1093/pasj/psz138

Hamilton, A. J. S. and Tegmark, M., 2002. *The real-space power spectrum of the PSCz survey from 0.01 to 300h Mpc^{-1}.* Monthly Notices of the Royal Astronomical Society, 330, 3:506. doi: 10.1046/j.1365-8711.2002.05033.x

Harnois-Déraps, J., Amon, A., Choi, A., et al., 2018. *Cosmological simulations for combined-probe analyses: covariance and neighbour-exclusion bias.* Monthly Notices of the Royal Astronomical Society, 481, 1:1337. doi: 10.1093/mnras/sty2319

Harnois-Déraps, J., Giblin, B., and Joachimi, B., 2019. *Cosmic shear covariance matrix in wCDM: Cosmology matters.* Astronomy & Astrophysics, 631:A160. doi: 10.1051/0004-6361/201935912

Harnois-Déraps, J., Martinet, N., Castro, T., et al., 2021. *Cosmic shear cosmology beyond two-point statistics: a combined peak count and correlation function analysis of DES-Y1.* Monthly Notices of the Royal Astronomical Society, 506, 2:1623. doi: 10.1093/mnras/stab1623

Harnois-Déraps, J., Martinet, N., and Reischke, R., 2022. *Cosmic shear beyond 2-point statistics: Accounting for galaxy intrinsic alignment with projected tidal fields.* Monthly Notices of the Royal Astronomical Society, 509, 3:3868. doi: 10.1093/mnras/stab3222

Hartlap, J., Simon, P., and Schneider, P., 2007. *Why your model parameter confidences might be too optimistic. Unbiased estimation of the inverse covariance matrix.* Astronomy & Astrophysics, 464, 1:399. doi: 10.1051/0004-6361:20066170

Henriques, B. M. B., White, S. D. M., Thomas, P. A., et al., 2015. *Galaxy formation in the Planck cosmology - I. Matching the observed evolution of star formation rates, colours and stellar masses.* Monthly Notices of the Royal Astronomical Society, 451:2663. doi: 10.1093/mnras/stv705

Heydenreich, S., Brück, B., Burger, P., et al., 2022a. *Persistent homology in cosmic shear II: A tomographic analysis of DES-Y1.* arXiv:2204.11831

Heydenreich, S., Brück, B., and Harnois-Déraps, J., 2021. *Persistent homology in cosmic shear: Constraining parameters with topological data analysis.* Astronomy & Astrophysics, 648:A74. doi: 10.1051/0004-6361/202039048

Heydenreich, S., Linke, L., Burger, P., and Schneider, P., 2022b. *A roadmap to cosmological parameter analysis with third-order shear statistics I: Modelling and validation*. arXiv:2208.11686

Heymans, C., Tröster, T., Asgari, M., et al., 2021. *KiDS-1000 Cosmology: Multi-probe weak gravitational lensing and spectroscopic galaxy clustering constraints.* Astronomy & Astrophysics, 646:A140. doi: 10.1051/0004-6361/202039063

Hilbert, S., Hartlap, J., and Schneider, P., 2011. *Cosmic shear covariance: the log-normal approximation.* Astronomy & Astrophysics, 536:A85. doi: 10.1051/0004-6361/201117294

Hilbert, S., Hartlap, J., White, S. D. M., and Schneider, P., 2009. *Ray-tracing through the Millennium Simulation: Born corrections and lens-lens coupling in cosmic shear and galaxy-galaxy lensing.* Astronomy & Astrophysics, 499, 1:31. doi: 10.1051/0004-6361/200811054

Hildebrandt, H., Köhlinger, F., van den Busch, J. L., et al., 2020. *KiDS+VIKING-450: Cosmic shear tomography with optical and infrared data.* Astronomy & Astrophysics, 633:A69. doi: 10.1051/0004-6361/201834878

Hildebrandt, H., van den Busch, J. L., Wright, A. H., et al., 2021. *KiDS-1000 catalogue: Redshift distributions and their calibration.* Astronomy & Astrophysics, 647:A124. doi: 10.1051/0004-6361/202039018

Hildebrandt, H., Viola, M., Heymans, C., et al., 2017. *KiDS-450: cosmological parameter constraints from tomographic weak gravitational lensing.* Monthly Notices of the Royal Astronomical Society, 465, 2:1454. doi: 10.1093/mnras/stw2805

Hinshaw, G., Larson, D., Komatsu, E., et al., 2013. *Nine-year Wilkinson Microwave Anisotropy Probe (WMAP) Observations: Cosmological Parameter Results.* Astrophysical Journal Supplement, 208, 2:19. doi: 10.1088/0067-0049/208/2/19

Hirschmann, M., Dolag, K., Saro, A., et al., 2014. *Cosmological simulations of black hole growth: AGN luminosities and downsizing.* Monthly Notices of the Royal Astronomical Society, 442, 3:2304. doi: 10.1093/mnras/stu1023

Huang, H.-J., Eifler, T., Mandelbaum, R., and Dodelson, S., 2019. *Modelling baryonic physics in future weak lensing surveys.* Monthly Notices of the Royal Astronomical Society, 488, 2:1652. doi: 10.1093/mnras/stz1714

Hubble, E., 1929. *A Relation between Distance and Radial Velocity among Extra-Galactic Nebulae.* Contributions from the Mount Wilson Observatory, 3

Ivezic, Z., Axelrod, T., Brandt, W. N., et al., 2008. *Large Synoptic Survey Telescope: From Science Drivers To Reference Design.* Serbian Astronomical Journal, 176:1. doi: 10.2298/SAJ0876001I

Jarvis, M., Bernstein, G., and Jain, B., 2004. *The skewness of the aperture mass statistic.* Monthly Notices of the Royal Astronomical Society, 352, 1:338. doi: 10.1111/j.1365-2966.2004.07926.x

Joachimi, B., Cacciato, M., Kitching, T. D., et al., 2015. *Galaxy Alignments: An Overview.* Space Sci. Rev., 193, 1-4:1. doi: 10.1007/s11214-015-0177-4

Joudaki, S., Blake, C., Johnson, A., et al., 2018. *KiDS-450 + 2dFLenS: Cosmological parameter constraints from weak gravitational lensing tomography and overlapping redshift-space galaxy clustering.* Monthly Notices of the Royal Astronomical Society, 474, 4:4894. doi: 10.1093/mnras/stx2820

Joudaki, S., Hildebrandt, H., Traykova, D., et al., 2020. *KiDS+VIKING-450 and DES-Y1 combined: Cosmology with cosmic shear.* Astronomy & Astrophysics, 638:L1. doi: 10.1051/0004-6361/201936154

Kaiser, N., 1992. *Weak Gravitational Lensing of Distant Galaxies.* Astrophysical Journal, 388:272. doi: 10.1086/171151

Kauffmann, G., White, S. D. M., Heckman, T. M., et al., 2004. *The environmental dependence of the relations between stellar mass, structure, star formation and nuclear activity in galaxies.* Monthly Notices of the Royal Astronomical Society, 353, 3:713. doi: 10.1111/j.1365-2966.2004.08117.x

Kilbinger, M., Heymans, C., Asgari, M., et al., 2017. *Precision calculations of the cosmic shear power spectrum projection.* Monthly Notices of the Royal Astronomical Society, 472, 2:2126. doi: 10.1093/mnras/stx2082

Kilbinger, M. and Schneider, P., 2005. *Cosmological parameters from combined second- and third-order aperture mass statistics of cosmic shear.* Astronomy & Astrophysics, 442, 1:69. doi: 10.1051/0004-6361:20053531

Kuijken, K., Heymans, C., Dvornik, A., et al., 2019. *The fourth data release of the Kilo-Degree Survey: ugri imaging and nine-band optical-IR photometry over 1000 square degrees.* Astronomy & Astrophysics, 625:A2. doi: 10.1051/0004-6361/201834918

Kuijken, K., Heymans, C., Hildebrandt, H., et al., 2015. *Gravitational lensing analysis of the Kilo-Degree Survey.* Monthly Notices of the Royal Astronomical Society, 454, 4:3500. doi: 10.1093/mnras/stv2140

Laureijs, R., Amiaux, J., Arduini, S., et al., 2011. *Euclid Definition Study Report.* arXiv:1110.3193

Lewis, A., Challinor, A., and Lasenby, A., 2000. *Efficient Computation of Cosmic Microwave Background Anisotropies in Closed Friedmann-Robertson-Walker Models.* Astrophysical Journal, 538, 2:473. doi: 10.1086/309179

Ma, C.-P. and Fry, J. N., 2000. *Deriving the Nonlinear Cosmological Power Spectrum and Bispectrum from Analytic Dark Matter Halo Profiles and Mass Functions.* Astrophysical Journal, 543, 2:503. doi: 10.1086/317146

Martinet, N., Harnois-Déraps, J., Jullo, E., and Schneider, P., 2021. *Probing dark energy with tomographic weak-lensing aperture mass statistics.* Astronomy & Astrophysics, 646:A62. doi: 10.1051/0004-6361/202039679

Mathews, W. G. and Brighenti, F., 2003. *Stellar Orbits and the Interstellar Gas Temperature in Elliptical Galaxies.* Astrophysical Journal, 599, 2:992. doi: 10.1086/379537

Mead, A. J., Peacock, J. A., Heymans, C., Joudaki, S., and Heavens, A. F., 2015. *An accurate halo model for fitting non-linear cosmological power spectra and baryonic feedback models.* Monthly Notices of the Royal Astronomical Society, 454, 2:1958. doi: 10.1093/mnras/stv2036

Meszaros, P., 1974. *The behaviour of point masses in an expanding cosmological substratum.* Astronomy & Astrophysics, 37, 2:225

Mo, H. J., van den Bosch, F., and White, S. D. M., *Galaxy Formation and Evolution* (Cambridge University Press, 2010). ISBN 9780521857932

Newton, I., 1966. *Philosophiae naturalis principia mathematica, london 1687.* English translation: Sir Isaac Newton's Mathematical Principles, Univ. of Calif. Press, Berkeley

Padmanabhan, N., Schlegel, D. J., Seljak, U., et al., 2007. *The clustering of luminous red galaxies in the Sloan Digital Sky Survey imaging data.* Monthly Notices of the Royal Astronomical Society, 378, 3:852. doi: 10.1111/j.1365-2966.2007.11593.x

Papoulis, A. and Pillai, S. U., *Probability, random variables, and stochastic processes* (McGraw-Hill, Boston, 1991), 3rd ed. edition. ISBN 0-07-048477-5

Peacock, J. A. and Bilicki, M., 2018. *Wide-area tomography of CMB lensing and the growth of cosmological density fluctuations.* Monthly Notices of the Royal Astronomical Society, 481, 1:1133. doi: 10.1093/mnras/sty2314

Peacock, J. A. and Smith, R. E., 2000. *Halo occupation numbers and galaxy bias.* Monthly Notices of the Royal Astronomical Society, 318, 4:1144. doi: 10.1046/j.1365-8711.2000.03779.x

Peebles, P. J. and Ratra, B., 2003. *The cosmological constant and dark energy.* Reviews of Modern Physics, 75, 2:559. doi: 10.1103/RevModPhys.75.559

Peebles, P. J. E., 1966. *Primordial Helium Abundance and the Primordial Fireball. II.* Astrophysical Journal, 146:542. doi: 10.1086/148918

Peebles, P. J. E., *The large-scale structure of the universe* (Princeton University Press, 1980). ISBN 9780691082400

Penzias, A. A. and Wilson, R. W., 1965. *A Measurement of Excess Antenna Temperature at 4080 Mc/s.* Astrophysical Journal, 142:419. doi: 10.1086/148307

Percival, W. J., Friedrich, O., Sellentin, E., and Heavens, A., 2022. *Matching Bayesian and frequentist coverage probabilities when using an approximate data covariance matrix.* Monthly Notices of the Royal Astronomical Society, 510, 3:3207. doi: 10.1093/mnras/stab3540

Perlmutter, S., Aldering, G., Goldhaber, G., et al., 1999. *Measurements of* Ω *and* Λ *from 42 High-Redshift Supernovae.* Astrophysical Journal, 517, 2:565. doi: 10.1086/307221

Pires, S., Leonard, A., and Starck, J.-L., 2012. *Cosmological constraints from the capture of non-Gaussianity in weak lensing data.* Monthly Notices of the Royal Astronomical Society, 423, 1:983. doi: 10.1111/j.1365-2966.2012.20940.x

Planck Collaboration: Aghanim, N., Akrami, Y., Ashdown, M., et al., 2020. *Planck 2018 results. V. CMB power spectra and likelihoods.* Astronomy & Astrophysics, 641:A5. doi: 10.1051/0004-6361/201936386

Pontoppidan, K., Blome, C., Braun, H., et al., 2022. *The JWST Early Release Observations.* arXiv:2207.13067

Pyne, S. and Joachimi, B., 2021. *Self-calibration of weak lensing systematic effects using combined two- and three-point statistics.* Monthly Notices of the Royal Astronomical Society, 503, 2:2300. doi: 10.1093/mnras/stab413

Ragagnin, A., Dolag, K., Biffi, V., et al., 2017. *A web portal for hydrodynamical, cosmological simulations.* Astronomy and Computing, 20:52. doi: 10.1016/j.ascom.2017.05.001

Reimberg, P. and Bernardeau, F., 2018. *Large deviation principle at work: Computation of the statistical properties of the exact one-point aperture mass.* Physical Review D, 97, 2:023524. doi: 10.1103/PhysRevD.97.023524

Riess, A. G., Filippenko, A. V., Challis, P., et al., 1998. *Observational Evidence from Supernovae for an Accelerating Universe and a Cosmological Constant.* Astronomical Journal, 116, 3:1009. doi: 10.1086/300499

Riess, A. G., Yuan, W., Macri, L. M., et al., 2022. *A Comprehensive Measurement of the Local Value of the Hubble Constant with 1 km* s^{-1} *Mpc*$^{-1}$ *Uncertainty from the Hubble Space Telescope and the SH0ES Team.* Astrophysical Journal Letters, 934, 1:L7. doi: 10.3847/2041-8213/ac5c5b

Rindler, W., 1956. *Visual horizons in world models.* Monthly Notices of the Royal Astronomical Society, 116:662. doi: 10.1093/mnras/116.6.662

Roberts, M. S., Hogg, D. E., Bregman, J. N., Forman, W. R., and Jones, C., 1991. *Interstellar Matter in Early-Type Galaxies. I. The Catalog.* Astrophysical Journal Supplement, 75:751. doi: 10.1086/191548

Robertson, H. P., 1935. *Kinematics and World-Structure.* Astrophysical Journal, 82:284. doi: 10.1086/143681

Rubin, V. C., Ford, J., W. K., and Thonnard, N., 1980. *Rotational properties of 21 SC galaxies with a large range of luminosities and radii, from NGC 4605 (R=4kpc) to UGC 2885 (R=122kpc).* Astrophysical Journal, 238:471. doi: 10.1086/158003

Schneider, P., 1996. *Detection of (dark) matter concentrations via weak gravitational lensing.* Monthly Notices of the Royal Astronomical Society, 283, 3:837. doi: 10.1093/mnras/283.3.837

Schneider, P., 1998. *Cosmic Shear and Biasing.* Astrophysical Journal, 498, 1:43. doi: 10.1086/305559

Schneider, P., Eifler, T., and Krause, E., 2010. *COSEBIs: Extracting the full E-/B-mode information from cosmic shear correlation functions.* Astronomy & Astrophysics, 520:A116. doi: 10.1051/0004-6361/201014235

Schwarzschild, K., 1916. *Über das Gravitationsfeld eines Massenpunktes nach der Einsteinschen Theorie.* Sitzungsberichte der Königlich Preußischen Akademie der Wissenschaften (Berlin:189

Seljak, U., 2000. *Analytic model for galaxy and dark matter clustering.* Monthly Notices of the Royal Astronomical Society, 318, 1:203. doi: 10.1046/j.1365-8711.2000.03715.x

Sellentin, E. and Heavens, A. F., 2016. *Parameter inference with estimated covariance matrices.* Monthly Notices of the Royal Astronomical Society, 456, 1:L132. doi: 10.1093/mnrasl/slv190

Shanks, T., Hogarth, L. M., and Metcalfe, N., 2019. *Gaia Cepheid parallaxes and 'Local Hole' relieve* H_0 *tension.* Monthly Notices of the Royal Astronomical Society, 484, 1:L64. doi: 10.1093/mnrasl/sly239

Shirasaki, M. and Yoshida, N., 2014. *Statistical and Systematic Errors in the Measurement of Weak-Lensing Minkowski Functionals: Application to the Canada-France-Hawaii Lensing Survey.* Astrophysical Journal, 786, 1:43. doi: 10.1088/0004-637X/786/1/43

Smith, A., Cole, S., Baugh, C., et al., 2017. *A lightcone catalogue from the Millennium-XXL simulation.* Monthly Notices of the Royal Astronomical Society, 470, 4:4646. doi: 10.1093/mnras/stx1432

Smith, R. E., Peacock, J. A., Jenkins, A., et al., 2003. *Stable clustering, the halo model and non-linear cosmological power spectra.* Monthly Notices of the Royal Astronomical Society, 341, 4:1311. doi: 10.1046/j.1365-8711.2003.06503.x

Springel, V., 2005. *The cosmological simulation code GADGET-2.* Monthly Notices of the Royal Astronomical Society, 364, 4:1105. doi: 10.1111/j.1365-2966.2005.09655.x

Springel, V., Pakmor, R., Zier, O., and Reinecke, M., 2021. *Simulating cosmic structure formation with the gadget-4 code.* Monthly Notices of the Royal Astronomical Society, 506, 2:2871. ISSN 0035-8711. doi: 10.1093/mnras/stab1855. URL `https://doi.org/10.1093/mnras/stab1855`

Springel, V., White, S. D. M., Jenkins, A., et al., 2005. *Simulations of the formation, evolution and clustering of galaxies and quasars.* Nature, 435, 7042:629. doi: 10.1038/nature03597

Springel, V., Yoshida, N., and White, S. D. M., 2001. *GADGET: a code for collisionless and gasdynamical cosmological simulations.* New A, 6, 2:79. doi: 10.1016/S1384-1076(01)00042-2

Spurio Mancini, A., Piras, D., Alsing, J., Joachimi, B., and Hobson, M. P., 2022. *COSMOPOWER: emulating cosmological power spectra for accelerated Bayesian inference from next-generation surveys.* Monthly Notices of the Royal Astronomical Society, 511, 2:1771. doi: 10.1093/mnras/stac064

Takahashi, R., Hamana, T., Shirasaki, M., et al., 2017. *Full-sky Gravitational Lensing Simulation for Large-area Galaxy Surveys and Cosmic Microwave Background Experiments.* Astrophysical Journal, 850, 1:24. doi: 10.3847/1538-4357/aa943d

Takahashi, R., Sato, M., Nishimichi, T., Taruya, A., and Oguri, M., 2012. *Revising the Halofit Model for the Nonlinear Matter Power Spectrum.* Astrophysical Journal, 761, 2:152. doi: 10.1088/0004-637X/761/2/152

Vakili, M., Bilicki, M., Hoekstra, H., et al., 2019. *Luminous red galaxies in the Kilo-Degree Survey: selection with broad-band photometry and weak lensing measurements.* Monthly Notices of the Royal Astronomical Society, 487, 3:3715. doi: 10.1093/mnras/stz1249

van Daalen, M. P., Schaye, J., Booth, C. M., and Dalla Vecchia, C., 2011. *The effects of galaxy formation on the matter power spectrum: a challenge for precision cosmology.* Monthly Notices of the Royal Astronomical Society, 415, 4:3649. doi: 10.1111/j.1365-2966.2011.18981.x

van den Busch, J. L., Wright, A. H., Hildebrandt, H., et al., 2022. *KiDS-1000: Cosmic shear with enhanced redshift calibration.* Astronomy & Astrophysics, 664:A170. doi: 10.1051/0004-6361/202142083

van Uitert, E., Joachimi, B., Joudaki, S., et al., 2018. *KiDS+GAMA: cosmology constraints from a joint analysis of cosmic shear, galaxy-galaxy lensing, and angular clustering.* Monthly Notices of the Royal Astronomical Society, 476, 4:4662. doi: 10.1093/mnras/sty551

Varadhan, S. R. S., 2008. *Large deviations.* The Annals of Probability, 36, 2:397 . doi: 10.1214/07-AOP348. URL `https://doi.org/10.1214/07-AOP348`

Virtanen, P., Gommers, R., Oliphant, T. E., et al., 2020. *SciPy 1.0: Fundamental Algorithms for Scientific Computing in Python.* Nature Methods, 17:261. doi: 10.1038/s41592-019-0686-2

Wagoner, R. V., Fowler, W. A., and Hoyle, F., 1967. *On the Synthesis of Elements at Very High Temperatures.* Astrophysical Journal, 148:3. doi: 10.1086/149126

Walker, A. G., 1937. *On Milne's Theory of World-Structure.* Proceedings of the London Mathematical Society, 42:90. doi: 10.1112/plms/s2-42.1.90

Wong, K. C., Suyu, S. H., Chen, G. C. F., et al., 2020. *H0LiCOW - XIII. A 2.4 per cent measurement of* H_0 *from lensed quasars:* 5.3σ *tension between early- and late-Universe probes.* Monthly Notices of the Royal Astronomical Society, 498, 1:1420. doi: 10.1093/mnras/stz3094

Wright, A. H., Hildebrandt, H., van den Busch, J. L., et al., 2020. *KiDS+VIKING-450: Improved cosmological parameter constraints from redshift calibration with self-organising maps.* Astronomy & Astrophysics, 640:L14. doi: 10.1051/0004-6361/202038389

Xavier, H. S., Abdalla, F. B., and Joachimi, B., 2016. *Improving lognormal models for cosmological fields.* Monthly Notices of the Royal Astronomical Society, 459, 4:3693. doi: 10.1093/mnras/stw874

Zuntz, J., Paterno, M., Jennings, E., et al., 2015. *CosmoSIS: Modular cosmological parameter estimation.* Astronomy and Computing, 12:45. doi: 10.1016/j.ascom.2015.05.005

Zürcher, D., Fluri, J., Sgier, R., et al., 2022. *Dark energy survey year 3 results: Cosmology with peaks using an emulator approach.* Monthly Notices of the Royal Astronomical Society, 511, 2:2075. doi: 10.1093/mnras/stac078

Zwicky, F., 1933. *Die Rotverschiebung von extragalaktischen Nebeln.* Helvetica Physica Acta, 6:110

Zwicky, F., 1937a. *Nebulae as Gravitational Lenses.* Physical Review, 51, 4:290. doi: 10.1103/PhysRev.51.290

Zwicky, F., 1937b. *On the Probability of Detecting Nebulae Which Act as Gravitational Lenses.* Physical Review, 51, 8:679. doi: 10.1103/PhysRev.51.679

List of Figures

List of Tables

List of Acronyms

AGN Active Galactic Nuclei

BAOs baryonic acoustic oscillations

CF characteristic function

CMB cosmic microwave background

CNN convolutional neural networks

COSEBIs complete orthogonal sets of E/B-integrals

DES Dark Energy Survey

DSS density split statistic

d.o.f. degrees of freedom

EHT Event Horizon Telescope

FLASK Full-sky Log-normal Astro-fields Simulation Kit

F18 Friedrich et al. (2018)

GAMA Galaxy And Mass Assembly survey

GPU graphics processing unit

GPR Gaussian process regression

GR general relativity

G18 Gruen et al. (2018)

HOD halo occupation distribution

IA intrinsic alignment

KiDS Kilo-Degree Survey

KiDS-bright bright sample of the KiDS-1000 release

KiDS-1000 fourth data release of the Kilo-Degree Survey

KV450 third data release of the Kilo-Degree Survey

LDT large deviation theory

LRG luminous red galaxies

LSS cosmic large-scale structure

MAP maximum a-posterior

MCMC Markov chain Monte Carlo

MF moment generating functions

MS Millenium simulation

MSD mass-sheet degeneracy

PDF probability density function

SDSS Sloan Digital Sky Survey

SOMs self-organising maps

S/N signal-to-noise ratio

SNIa supernovae type Ia

SLICS Scinet Light Cone Simulations

T17 Takahashi et al. (2017)

2PCF two-point correlation functions

Appendix

B20

Burger, P., Schneider, P., Demchenko, V., Harnois-Deraps, J., Heymans, C., Hildebrandt, H., and Unruh, S., 2020. An adapted filter function for density split statistics in weak lensing. Astronomy & Astrophysics, 642:A161. doi:10.1051/0004-6361/202038694.

The author's contributions are as follows: I led the paper analysis and wrote all parts of it. Peter Schneider supported the development of the methods. Joachim Harnois-Deraps provided many of the used simulations and helped with the paper's analysis and writing. Hendrik Hildebrandt also helped with the paper's analysis and also to access real data observations. Sandra Unruh provided me with the ground structure of c++ code, which helped to measure the DSS from the Millenium simulation (MS). Vasiliy Demchenko and Catherine Heymans previously worked on DSS and helped with advices during the analysis. The paper can be found on page 101 onwards.

B22a

Burger, P., Friedrich, O., Harnois-Déraps, J., and Schneider, P., 2022a. A revised density split statistic model for general filters. Astronomy & Astrophysics, 661:A137. doi:10.1051/0004-6361/202141628.

The author's contributions are as follows: I led the paper analysis and wrote all parts of it. Oliver Friedrich and Peter Schneider helped significantly in the development of the analytical model. Joachim Harnois-Déraps provided us with all necessary simulations that were not public and also helped with the analysis. The paper can be found on page 113 onwards.

B22b

Burger, P., Friedrich, O., and Harnois-Déraps, J., Schneider, P., Asgari, M., Bilicki, M., Hildebrandt, H., Wright, A., Castro, T., Dolag, K., Heymans, C., Joachimi, B., Martinet, N., Shan, H., and Tröster, T., 2022b. KiDS-1000 Cosmology: Constraints from density split statistics. Submitted to Astronomy & Astrophysics. arXiv:2208.02171.

The author's contributions are as follows: I led the paper, Joachim Harnois-Déraps provided all necessary simulations, Oliver Friedrich and Peter Schneider contributed to the modelling, and all four helped in the development of the analysis. The remaining authors are either Kilo-Degree Survey (KiDS) infrastructure members or provided us with the Magneticum simulations. Marika Asgari, Hendrik Hildebrandt and Maciek Bilicki should be highlighted here as they gave valuable comments that improved the analysis. The paper can be found on page 133 onwards.

A&A 642, A161 (2020)
https://doi.org/10.1051/0004-6361/202038694
© ESO 2020

Astronomy & Astrophysics

An adapted filter function for density split statistics in weak lensing

Pierre Burger[1], Peter Schneider[1], Vasiliy Demchenko[2], Joachim Harnois-Deraps[2,3], Catherine Heymans[2,4],
Hendrik Hildebrandt[4], and Sandra Unruh[1]

[1] Argelander-Institut für Astronomie, Auf dem Hügel 71, 53121 Bonn, Germany
e-mail: `pburger@astro.uni-bonn.de`
[2] Institute for Astronomy, University of Edinburgh, Royal Observatory, Blackford Hill, Edinburgh EH9 3HJ, UK
[3] Astrophysics Research Institute, Liverpool John Moores University, 146 Brownlow Hill, Liverpool L3 5RF, UK
[4] Astronomisches Institut, Ruhr-Universität Bochum, German Centre for Cosmological Lensing, Universitätsstr. 150,
44801 Bochum, Germany

Received 18 June 2020 / Accepted 25 August 2020

ABSTRACT

Context. The density split statistics in weak gravitational lensing analyses probes the correlation between regions of different (foreground) galaxy number densities and their weak lensing signal, which is measured by the shape distortion of background galaxies.
Aims. In this paper, we reconsider density split statistics, by constructing a new angular filter function that is adapted to the expected relation between the galaxy number density and shear pattern, in a way that the filter weighting the galaxy number density is matched to the filter that is used to quantify the shear signal.
Methods. We used the results of numerical ray-tracing simulations, specifically through the Millennium Simulation supplemented by a galaxy distribution based on a semi-analytic model, to construct a matched pair of adapted filter functions for the galaxy density and the tangential shear signal. We compared the performance of our new filter to the previously used top-hat filter, applying both to a different and independent set of numerical simulations (SLICS, cosmo-SLICS).
Results. We show that the adapted filter yields a better correlation between the total matter and the galaxy distribution. Furthermore, the adapted filter provides a larger signal-to-noise ratio to constrain the bias between the total matter and the galaxy distribution, and we show that it is, in general, a more sensitive discriminator between different cosmologies, with the exception of cosmologies with very large σ_8 values. All analyses lead to the conclusion that our adapted filter should be favoured in future density split statistic works.

Key words. gravitational lensing: weak – methods: statistical – surveys – Galaxy: abundances – large-scale structure of Universe

1. Introduction

The large-scale structure (LSS) of the Universe is thought to originate from initially Gaussian density perturbations, a view supported by the apparent absence of non-Gaussian features in the cosmic microwave background (see Planck Collaboration V 2020). Correspondingly, at early times, these Gaussian perturbations result in a total symmetry in the abundance and amplitude of over- and under-dense regions. As structures evolve, this symmetry breaks so over-densities can grow to very large amplitudes. However, the fractional density contrast of under-densities is bounded from below.

Studying the matter distribution of the present LSS reveals a wealth of information about the evolution of the Universe. In particular, its distorting effect on the propagation of light from distant galaxies, dubbed cosmic shear, can be captured by analysing weak lensing surveys. By comparing the results of cosmological models with the observed signal, one can constrain cosmological parameters (see Hildebrandt et al. 2017; DES Collaboration 2020; Hamana et al. 2020).

The preferred methods to infer statistical properties of the matter and galaxy distribution are second- and higher-order statistics. Two-point correlation functions, or power spectra, measure the variance of density fluctuations as a function of scale. More generally, an n-point correlation function describes how probable it is to find a constellation of n connected objects. The advantage of analysing three-point statistics, which are more computationally time-consuming than second-order statistics, is its connection to the skewness of the density distribution resulting from the asymmetric behaviour of over- and under-dense regions. Another advantage of third-order statistics is that they scale differently with cosmological parameters. Hence, by simultaneously investigating second- and higher-order statistics, the power to constrain cosmological parameters increases (Pires et al. 2012; Fu et al. 2014).

First in Gruen et al. (2016), and later in Gruen et al. (2018) and Friedrich et al. (2018), a new weak lensing approach to analyse the LSS was introduced, the density split statistics (hereafter DSS), which differs from the usual n-point correlation analyses. The idea is to divide the sky into sub-areas of an equal size, according to the foreground (or lens) galaxy density (counts-in-cells, or CiC), and to measure the mean tangential shear, γ_t, around all points within a given sub-area. These sub-areas are defined by quantiles of the galaxy number density field. One expects that around points with a high density of (foreground) galaxies, that is, for the upper quantiles of the CiC, the tangential shear is larger, given that a high galaxy number density should correspond to a large matter over-density on average. In order to extract cosmological information from this DSS, Friedrich et al. (2018) derived a lognormal model which predicts the shear profiles and the probability density of CiC by using the redshift distribution of sources, lenses, and the mean CiC as inputs. In

Article published by EDP Sciences

Gruen et al. (2018), the model was used to constrain cosmological parameters from DSS measurements from the Dark Energy Survey (DES) First Year and Sloan Digital Sky Survey (SDSS) data, where they included in their analysis the tangential shear profiles for scales greater than the top-hat filter size $\theta_{\rm th}$. Their analysis yields constraints on the matter density $\Omega_m = 0.26^{+0.04}_{-0.03}$ that agree with the DES analysis of galaxy and shear two-point functions (see Abbott et al. 2018).

Brouwer et al. (2018) applied the DSS to the Kilo-Degree Survey (KiDS; Kuijken et al. 2015) data, using the catalogue of Bilicki et al. (2018) for the foreground (lens) galaxies, whereas the source galaxies used for estimating the shear were taken from the third data release of KiDS (see de Jong et al. 2017). In order to parameterised their measured shear signals, they fitted, for every quantile in the foreground galaxy CiC, a relation of the form $\gamma_t = A/\sqrt{\theta}$ to their tangential shear profile, for $\theta > \theta_{\rm min}$, where $\theta_{\rm min}$ is approximately the radius of the peak of the shear profile. By using this relation, they defined their signal-to-noise ratio $S/N = A/\sigma_A$, where σ_A is the 1σ error on the best-fit amplitude based on the full analytical covariance matrix of the shear profiles. With a top-hat of size $5'$, they found for the regions with the highest 20% values of the aperture number a $S/N = 21.7$ and for the lowest 20% a $S/N = 16.9$. We use this fit relation later in this analysis to compare the S/N of our adapted filter to that of the top-hat filter.

The prime motivation for this work is based on the fact that the two components of the DSS – the CiC of galaxies inside a radius θ, and the tangential shear profile $\gamma_t(\vartheta)$ for $\vartheta > \theta$ – are poorly matched. For example, the shear at radius $\vartheta > \theta$ around a given point is affected by the matter distribution at all radii $<\vartheta$, not just by that inside θ. Hence, even if the (foreground) galaxy density $n(\boldsymbol{\theta})$ had the same shape as the lensing convergence field $\kappa(\boldsymbol{\theta})$, the two aforementioned quantities would not be perfectly correlated. Instead, we consider here a pair of statistics for the foreground galaxy distribution and the shear profile that are "matched", in the sense that in the hypothetical case $n(\boldsymbol{\theta}) \propto \kappa(\boldsymbol{\theta})$, there would be a one-to-one relation between them. This is achieved by using the aperture statistics (see Schneider 1996, 1998), that is, aperture mass and aperture number counts. Although the case $n(\boldsymbol{\theta}) \propto \kappa(\boldsymbol{\theta})$ is not a realistic assumption, due to different redshift weighting in the projected galaxy number density on the sky and the projected matter density between us and the lensed source population to obtain the convergence, we nevertheless expect a strong correspondence on the same angular scales, described by the galaxy-dark matter bias b and correlation coefficient r (Pen 1998). Instead of using the CiC, we now split the sky into areas of different quantiles of the aperture number counts, and consider the mean shear profile for each quantile; the latter is then quantified by the aperture mass. For the purpose of selecting a suitable filter function for the aperture statistics, we employ results from the ray-tracing through the Millennium Simulation (hereafter MS; Springel et al. 2005; Hilbert et al. 2009), supplemented by a galaxy distribution obtained from a semi-analytic model (Henriques et al. 2015). Hence, our filter function is adapted to expectations from cosmological simulations.

This work is structured as follows. In Sect. 2 we review the basics of the aperture statistics. In Sect. 3 we describe the simulation data used in this paper. Beside the MS, we use the Scinet Light Cone Simulations (SLICS; see Harnois-Déraps et al. 2018, hereafter HD18) to compare the performance of our new statistics to that of the previously employed DSS. For studying the sensitivity to cosmological parameters, we use the cosmo-SLICS simulations (see Harnois-Déraps et al. 2019), which are a suite of simulations for 26 different cosmologies. The derivation of the adapted filter is described in Sect. 4, and the comparison of the original DSS with our new method is performed in Sect. 5. In Sect. 6 we investigate the different relationships between the total matter and galaxy distribution for a non-linear and linear galaxy bias model. This is achieved by calculating aperture masses and aperture numbers with our new method and the method used in the previous DSS. In Sect. 7 we compare both filters in their power to distinguish different cosmologies by use of cosmo-SLICS. In Sect. 8 we conclude and summarise our work. Furthermore, we give an outlook of possible future work and applications of our adapted filter.

2. Aperture statistics

Given a convergence (or dimensionless surface mass density) field $\kappa(\boldsymbol{\theta})$, the aperture mass is defined as

$$M_{\rm ap}(\boldsymbol{\theta}) := \int \kappa(\boldsymbol{\theta} + \boldsymbol{\theta}')\, U(|\boldsymbol{\theta}'|)\, {\rm d}2\theta', \qquad (1)$$

where $U(|\boldsymbol{\theta}|)$ is a compensated filter function, such that $\int \theta\, U(\theta)\, {\rm d}\theta = 0$. As shown in Schneider (1996), $M_{\rm ap}$ can also be expressed in terms of the tangential shear γ_t and a related filter function Q as

$$M_{\rm ap}(\boldsymbol{\theta}) = \int \gamma_t(\boldsymbol{\theta} + \boldsymbol{\theta}')\, Q(|\boldsymbol{\theta}'|)\, {\rm d}2\theta', \qquad (2)$$

where

$$Q(\theta) = \frac{2}{\theta^2} \int\limits_0^{\theta} \theta' U(\theta')\, {\rm d}' - U(\theta), \qquad (3)$$

which can be inverted, yielding

$$U(\theta) = 2 \int\limits_{\theta}^{\infty} \frac{Q(\theta')}{\theta'}\, {\rm d}' - Q(\theta). \qquad (4)$$

In analogy to $M_{\rm ap}$, we define the aperture number counts (Schneider 1998), or aperture number, as

$$N_{\rm ap}(\boldsymbol{\theta}) := \int n(\boldsymbol{\theta} + \boldsymbol{\theta}')\, U(|\boldsymbol{\theta}'|)\, {\rm d}2\theta', \qquad (5)$$

where $U(\boldsymbol{\theta})$ is the same filter function as in Eq. (1) and $n(\boldsymbol{\theta})$ is the galaxy number density on the sky. Our proposed modified DSS consists of splitting the sky into quantiles of $N_{\rm ap}$, and stacking the azimuthal-averaged tangential shear profile around all points of the given quantile. By setting $Q(\theta) = \gamma_t(\theta)$, we then define a new U filter for $N_{\rm ap}$ with Eq. (4), and iteratively repeat the process until we reach convergence (see Sect. 4 for details). This differs from Gruen et al. (2016) who determine the CiC from Eq. (5) with a top-hat filter where

$$U_{\rm th}(\theta) = \mathcal{H}(\theta_{\rm th} - \theta), \qquad (6)$$

with $\theta_{\rm th}$ is the size of the top-hat and $\mathcal{H}$ is the Heaviside step function. Since the top-hat filter $U_{\rm th}$ is not compensated, we can not use Eq. (3) to calculate a corresponding filter $Q_{\rm th}$. Instead, we set

$$Q_{\rm th}(\theta) \sim \begin{cases} 1/\sqrt{\theta}, & \text{if } 1.2\,\theta_{\rm th} < \theta < \theta_{\rm max} \\ 0, & \text{otherwise} \end{cases} \qquad (7)$$

following the work of Brouwer et al. (2018), where they used a $1/\sqrt{\theta}$ profile to parameterise their shear signals. The radius $\theta_{\rm max}$ is the size up to which we measure the shear profiles.

To efficiently calculate the aperture number we make use of the convolution theorem

$$N_{\rm ap}(\boldsymbol{\theta}) = \mathcal{F}^{-1}\left[\mathcal{F}\{n(\boldsymbol{\theta})\}\mathcal{F}\{U(|\boldsymbol{\theta}|)\}\right], \tag{8}$$

where $\mathcal{F}$ denotes the Fourier transformation and $\mathcal{F}^{-1}$ the inverse Fourier transformation (see Frigo & Johnson 2005, hereafter FFT).

3. Mock KiDS data

In this work, we use three different simulation suites, which we modify to be KiDS-like. As KiDS is not so dissimilar from DES (see Drlica-Wagner et al. 2018) and Hyper Suprime-Cam (see Aihara et al. 2019), we expect our conclusion to also hold for these weak lensing surveys. We use the well tested MS to develop our adapted filter, and test our filter with an independent set of simulation, SLICS, to avoid recurring systematic effects. We also use the cosmo-SLICS to compare the adapted and top-hat DSS filters in their power to discriminate different cosmologies.

3.1. Millennium Simulation (MS)

The MS, described in Springel et al. (2005), follows the evolution of 2160^3 dark matter particles of mass $8 \times 10^8\,M_\odot\,h^{-1}$ enclosed in a cube of size $(500\,{\rm Mpc}\,h^{-1})^3$. Galaxies are added to the simulation afterwards using a semi-analytical galaxy-formation model, where Saghiha et al. (2017) showed that the best match with the observed galaxy-galaxy lensing and galaxy-galaxy-galaxy lensing signals from the Canada-France-Hawaii Telescope Lensing Survey data (see Heymans et al. 2012) is obtained from the model of Henriques et al. (2015). Hilbert et al. (2009) described ray-tracing simulations through the MS. They constructed a suite of 64 pseudo-independent light cones of size $4 \times 4\,{\rm deg}^2$. For each of them, they calculated the lensing Jacobi matrix $\mathcal{A}$ on a 4096×4096 pixel grid, for a set of source redshifts, using a multiple lens plane algorithm. The Cartesian components of the shear for each grid point and each source redshift z_c are then obtained from the corresponding Jacobi matrix $\mathcal{A}$. We note that the same set of simulations has been used in several previous studies, for example, in Sadeh et al. (2016), Simon et al. (2019), and Unruh et al. (2019, 2020).

3.1.1. Constructing foreground galaxy number densities

To create the galaxy number density field $n(\boldsymbol{\theta})$ for each light cone, we project all galaxies with an SDSS r-band magnitude $m_r < 20.25$ mag[1] onto pixels of size $(4\,{\rm deg}/4096)^2$. The magnitude cut is chosen such that the galaxy number density in the MS matches the one in Bilicki et al. (2018). The resulting redshift distribution of the galaxies over all 64 light cones is displayed in Fig. 1 in orange, together with the redshift distribution of Bilicki et al. (2018) shown in blue. We note that our lens redshift distributions is broader compared to Gruen et al. (2018); especially at small redshifts our lenses extend down to $z \approx 0$.

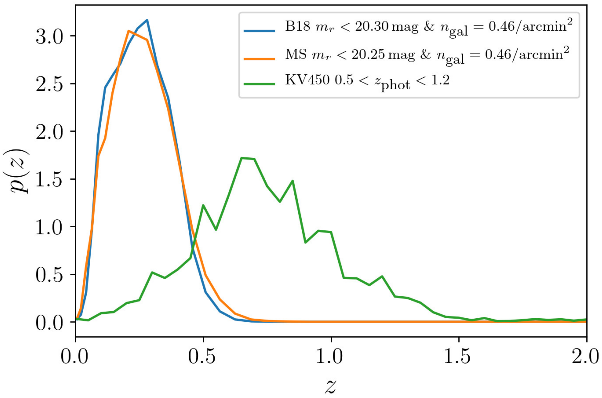

Fig. 1. Redshift distribution $p(z)$ of galaxies with $m_r < 20.25$ in the 64 MS light cones, compared to the estimated redshift distribution of KiDS galaxies with $m_r < 20.30$ (Bilicki et al. 2018, in the plot B18). Shown in green is the weighted source redshift PDF of the highest three tomographic bins; from Hildebrandt et al. (2020).

3.1.2. Constructing the source galaxy distribution

In order to mimic the KiDS shear estimates, we create for each grid point in a light cone a weighted mean of the shear over all source redshifts. We use the redshift distribution of the combined data set from the optical KiDS (see de Jong et al. 2013) and the near-infrared VISTA Kilo degree Infrared Galaxy survey (see Edge et al. 2013). In this combined data set (hereafter KV450), redshifts are estimated through photometric redshifts, $z_{\rm phot}$, and calibrated with spectroscopic redshifts (Hildebrandt et al. 2020). We consider only sources with $0.5 < z_{\rm phot} < 1.2$, such that our sources are mostly behind our low-redshift lenses, and adopted the redshift distribution $n(z)$ from Hildebrandt et al. (2020) to model these sources (shown in green in Fig. 1). From this distribution the weights for the redshift slices z_c (see Sect. 3.1) of the simulation are calculated to

$$w(z_c) = \int\limits_{z_{\rm low}(z_c)}^{z_{\rm up}(z_c)} p(z')\,{\rm d}', \tag{9}$$

where $z_{\rm low,up}(z_c)$ are the boundaries of the consecutive redshift slices in the MS with central redshift z_c. With these weights, the shear at each grid point $\gamma(\boldsymbol{\theta})$ is given as

$$\gamma(\boldsymbol{\theta}) = \frac{\sum_i w(z_{c,i})\,\gamma(\boldsymbol{\theta}, z_{c,i})}{\sum_i w(z_{c,i})}, \tag{10}$$

where $\gamma(\boldsymbol{\theta}, z_{c,i})$ is the shear value at position $\boldsymbol{\theta}$ from the ith redshift slice calculated with the corresponding Jacobi matrix $\mathcal{A}$. Since the MS are exclusively used to construct our new filters, it is best to ignore shape noise, hence we work directly with the noise-free shear values provided with Eq. (10).

3.2. Scinet Light Cone Simulations (SLICS)

In order to compare the performance of our adapted filter to that of the Gruen et al. (2016) top-hat filter, and to find the appropriate size of the top-hat filter such that the comparison is reasonable, we use the SLICS. This simulation suite is independent of the MS and is described in HD18. The SLICS are a set

---

[1] These magnitudes are provided by the semi-analytical galaxy-formation model.

of over 800 realisations, where each run follows 1536^3 particles inside a cube of comoving side length $L_{\mathrm{box}} = 505\,h^{-1}$Mpc and $n_c = 3072$ grid cells on the side. By use of the Zel'dovich approximation (see White 2014) each run starts with slightly different initial conditions at $z = 120$, computes the non-linear evolution of these collision-less particles to $z = 0$, and produces on-the-fly the halo catalogues and mass sheets required for a full light cone construction at 18 different source redshifts from $z = 0$ to $z = 3$. The underlying cosmological parameters for each run are $\Omega_m = 0.2905$, $\Omega_\Lambda = 0.7095$, $\Omega_b = 0.0473$, $h = 0.6898$, $\sigma_8 = 0.826$ and $n_s = 0.969$ (see Hinshaw et al. 2013). Given a particle mass of $2.88 \times 10^9\,h^{-1}\,M_\odot$, dark matter haloes with masses above $10^{11}\,h^{-1}\,M_\odot$ and structure formation deep into the non-linear regime are resolved. Furthermore, it has been shown in HD18 that for Fourier modes $k < 2.0\,h\,\mathrm{Mpc}^{-1}$, the three-dimensional dark matter power spectrum $P(k)$ agrees within 2% with the predictions from the Extended Cosmic Emulator (see Heitmann et al. 2014), followed by a progressive deviation for higher k-modes.

3.2.1. KV450 SLICS mocks

We use the KV450 SLICS as source galaxies[2]. These mock galaxies are placed at random angular coordinates on $100\,\mathrm{deg}^2$ light cones, with the KV450 number density $n_{\mathrm{gal}} = 6.93$ arcmin^{-2} and the best-estimated redshift distributions from Hildebrandt et al. (2020, see the DIR method therein). The galaxies are assigned their shear information γ from the lensing maps, following the linear interpolation algorithm described in Sect. 2 in HD18; and the observed ellipticities ϵ^{obs} are obtained as

$$\epsilon^{\mathrm{obs}} = \frac{\epsilon^{\mathrm{int}} + \gamma}{1 + \epsilon^{\mathrm{int}}\gamma^*} + \eta \approx \frac{\epsilon^n + \gamma}{1 + \epsilon^n\gamma^*}, \tag{11}$$

where ϵ^{obs}, ϵ^{int}, ϵ^n, η, and γ are complex numbers; the asterisk $*$ indicates complex conjugation. This equation relates the observed ellipticity ϵ^{obs} to the intrinsic shape ϵ^{int} and the shear γ, and adds measurement noise η to it. In order to combine intrinsic and measurement shape noise, both are incorporated into one pre-sheared noisy ellipticity ϵ^n. This ellipticity ϵ^n is generated by drawing random numbers from a Gaussian distribution with width $\sigma = 0.29$, which is consistent with the weighted observed ellipticity distribution of the KiDS data. Furthermore, we apply a selection cut on the photometric redshift of $0.5 < z_{\mathrm{phot}} < 1.2$, resulting in a galaxy number density of $n_{\mathrm{gal}} = 5.17\,\mathrm{arcmin}^{-2}$.

3.2.2. Galaxy And Mass Assembly (GAMA) SLICS mocks

For the lens sample we use the publicly available Galaxy And Mass Assembly (GAMA, see Driver et al. 2011) SLICS mocks, which are based on the halo occupation distribution (HOD) prescription of Smith et al. (2017, see HD18 for details on its implementation). The motivation to use these mocks is that they are an excellent source of lenses for a DSS analysis with KiDS data as sources, as demonstrated by Brouwer et al. (2018). The galaxy number density is $n_{\mathrm{gal}} \sim 0.25\,\mathrm{arcmin}^{-2}$, which is smaller compared to Bilicki et al. (2018) due to the smaller limiting magnitude of $m_r < 19.8$ mag and the smaller redshift range of $0 < z < 0.5$, but since we use both data sets in two independent analyses it does not matter. Theses different values of n_{gal} propagate into the aperture number, N_{ap} via Eq. (5), where we count these GAMA lens galaxies in squares of size $1\,\mathrm{arcmin}^2$ and assign the resulting galaxy number density $n(\boldsymbol{\theta})$ to the associated pixel. Finally, it was demonstrated in HD18 that on large scales these mock GAMA galaxies have a linear bias of about 1.2, and that the non-linear bias observed at smaller scales is similar to that seen in the GAMA data. This match was not guaranteed given that the galaxy bias in the simulations emerge from the HOD, and not from an input model.

3.3. Cosmo-SLICS

We use the cosmo-SLICS simulations described in Harnois-Déraps et al. (2019), to investigate the sensitivity of the top-hat filter and the adapted filter to cosmological parameters. These are a suite of simulations sampling 26 wCDM cosmologies distributed in a Latin hypercube, ray-traced multiple times to produce 50 pseudo-independent realisations for every cosmology, each producing light cones of size $100\,\mathrm{deg}^2$. The corresponding cosmologies are listed in Table A.1. In these simulations, the matter density Ω_m, the dimensionless Hubble parameter h, the normalisation of the matter power spectrum σ_8 and the time-independent dark energy equation-of-state w_0 are varied over a range that is large enough to complement the analysis of current weak lensing data (see Hildebrandt et al. 2020).

For each realisation, the algorithm to creates KV450-like catalogues follows the same pipeline as for the SLICS mocks, notably it reproduces the same galaxy number density and redshift distribution $n(z)$, but the different underlying cosmologies modify the lensing properties.

In contrast to the SLICS simulations, the cosmo-SLICS dark matter haloes are not fully post-processed into light cones at the moment of writing this paper, and therefore HOD-based mocks are not yet available. This does not prevent us from using the cosmo-SLICS to generate GAMA-like mocks, however these are instead based on a linear bias model (see Appendix A2 of HD18). Given the GAMA $n(z)$, this construction required four mass sheets[3]. Following the redshift distribution shown in Fig. 8 in HD18 each of these sheets was populated with a bias of unity, and accordingly to Sect. 3.2.2 the resulting number density for all four sheets together is $n_{\mathrm{gal}} = 0.25\,\mathrm{arcmin}^{-2}$. To be consistent with Sect. 3.2.2, we sum the galaxies in squares of size $1\,\mathrm{arcmin}^2$ and assign the galaxy number density $n(\boldsymbol{\theta})$ to the respective pixels.

4. The derivation of the adapted filter function

In order to investigate the projected galaxy number density $n(\boldsymbol{\theta})$ and lensing convergence $\kappa(\boldsymbol{\theta})$ on the same angular scales, we generate a compensated filter for $\theta < 30'$ using an iterative procedure with the MS as an input. Schematically the iterative process is structured as follows: The first step is to calculate the aperture number N_{ap} with a compensated filter U_i defined for $\theta < 10'$. Next, we extract the pixels which have the highest 10% aperture number values, and measure the tangential shear profile $\gamma_t(\theta)$ around these pixels up to $10'$. With setting $Q(\theta) \propto \gamma_t(\theta)$ and Eq. (4) we create a revised compensated filter U_{i+1}. The last step is to repeat all prevoius steps with the revised filter U_{i+1}. This iteration continues as long as the change in relative signal-to-noise $\Delta(S/N)/(S/N)_1 > 10^{-3}$ between consecutive iterations.

---

[2] These SLICS KV450 mocks are made publicly available on the SLICS portal at `https://slics.roe.ac.uk/`

[3] For the fiducial cosmology these mass sheets are at redshifts $z_i = 0.130, 0.221, 0.317, 0.410$.

We note that this value is chosen arbitrarily, but it is sufficient, because the deviation of the resulting shear profiles in Sect. 5, determined with a filter of a later iteration, would be less than the uncertainties of the shear profiles. Once we achieve convergence in this iterative process, we extrapolate the U and Q filters to 30′ to use the strong tangential shear signal beyond 10′.

After presenting the general approach of our derivation, we next explain the individual steps in more detail. The initial filter U_1 of the pipeline is defined as a compensated top-hat

$$U_1(|\boldsymbol{\theta}|) := \begin{cases} 1\,\mathrm{arcmin}^{-2}, & \text{if } \theta < 1' \\ -\frac{1}{99}\,\mathrm{arcmin}^{-2}, & \text{if } 1' \le \theta < 10' \\ 0\,\mathrm{arcmin}^{-2}, & \text{if } \theta > 10' \end{cases}, \tag{12}$$

where the chosen inner radius of 1′ is not crucial, because the iterative process finds the final shape of the filter independent of this boundary. The upper bound of 10′ is motivated by the fact that we expect the shear profiles with our filter to peak at roughly 2/3 of the filter size, which would then coincide with the shear profiles generated with a top-hat filter of size 5′ in Brouwer et al. (2018) which had the best S/N. The value $-1/99\,\mathrm{arcmin}^{-2}$ arises from the compensated nature of U. To calculate the aperture number with Eq. (5), we convolve the galaxy number density $n(\boldsymbol{\theta})$ with the filter U_1 by means of the convolution theorem Eq. (8). The resulting aperture number for one light cone is shown in the upper panel of Fig. 2, where over-dense regions are shown in red and under-dense regions in blue. Following the pipeline, we extract those pixels that have the highest 10% values of the aperture number and display them in the lower panel of Fig. 2. The outer 30′ edges are not considered since the FFT, which we use to efficiently apply the convolution theorem, assumes periodic boundary conditions. The reason to cut at 30′ instead of 10′ is that we want to use the same area of the light cones for the extended shear profile as for the ones measured in the iterative process.

Using the shear grids described in Sect. 3.1, an averaged shear grid around the extracted pixels is calculated as

$$\bar{\gamma}(\boldsymbol{\theta}) = \frac{1}{N_{\mathrm{peaks}}} \sum_{i=1}^{N_{\mathrm{peaks}}} \gamma(\boldsymbol{\theta} + \boldsymbol{\theta}_i), \tag{13}$$

where N_{peaks} is the number of extracted pixels with positions $\boldsymbol{\theta}_i$, which have the 10% highest values of N_{ap}. Next, we construct the grids of tangential and cross shear $\gamma_{t,\times}(\boldsymbol{\theta})$, with

$$\gamma_t(\boldsymbol{\theta}) = -\Re\mathrm{e}\left[\bar{\gamma}(\boldsymbol{\theta})e^{-2i\phi}\right]; \quad \gamma_\times(\boldsymbol{\theta}) = -\Im\mathrm{m}\left[\bar{\gamma}(\boldsymbol{\theta})e^{-2i\phi}\right], \tag{14}$$

where ϕ is the polar angle of $\boldsymbol{\theta}$. For all shear profiles we subtract the shear signal around random pixel positions per light cone to reduce the noise in the measurements (Singh et al. 2017).

The shear profiles for one light cone result from azimuthally averaging the $\gamma_{t,\times}(\boldsymbol{\theta})$ grids in 40 linearly spaced annuli for $0' < \theta < 10'$. By further averaging the signals over all 64 light cones, we extract the shear profiles indicated with the blue dots in Fig. 3, where the error bars are the uncertainties on the mean, obtained from the sample variance of all 64 light cones. In the lower panel the $\gamma_\times$ profile is displayed, and although a 40 × 40 covariance cannot be reliably calculated from only 64 realisations, the cross shear profiles appear to be consistent with zero. The shape of the γ_t profiles are as expected for a DSS analysis and similar to those of previous DSS works (Brouwer et al. 2018; Gruen et al. 2018; Friedrich et al. 2018).

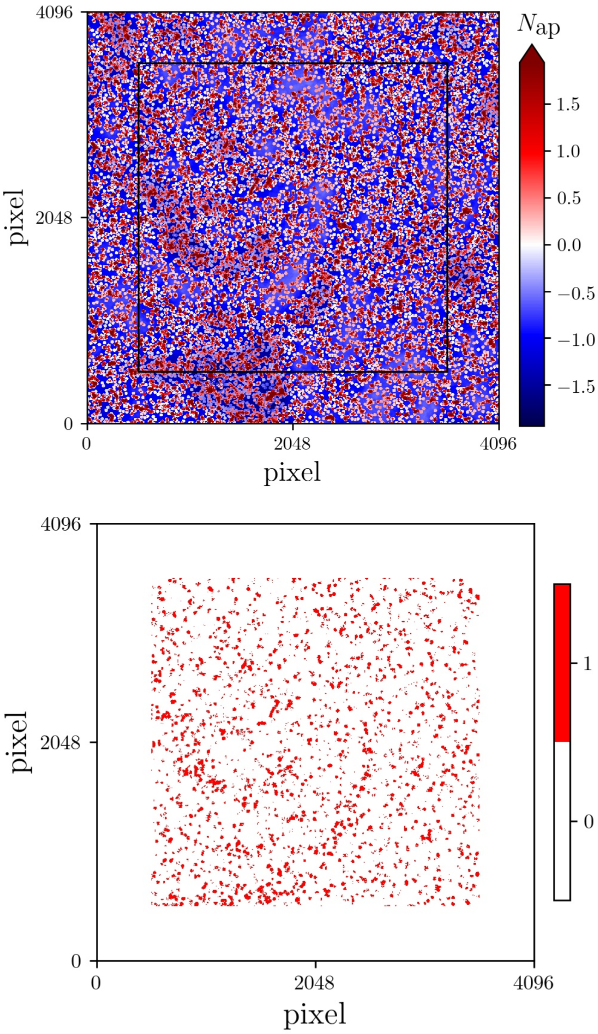

Fig. 2. *Upper panel*: aperture number N_{ap} on a $4 \times 4\,\mathrm{deg}^2$ grid of the MS light cone 37 as an example light cone. *Lower panel*: extracted pixels which have the highest 10% number values of N_{ap}. The outer 30′ margins are not considered since the FFT assumes periodic boundary conditions. Therefore, the outer margins in the N_{ap} field are disregarded and marked with the black square in the *upper panel*.

For determining the filter function U, we quantify the information content about these shear profiles through M_{ap}, by defining a signal-to-noise ratio (Schneider 1996),

$$\frac{S}{N} = \frac{\sqrt{2}}{\sigma_\epsilon} \frac{\sum_i \gamma_t(\theta_i)\, Q(\theta_i)}{\sqrt{\sum_i Q^2(\theta_i)}}, \tag{15}$$

where the noise here is taken to be pure shape noise due to intrinsic source ellipticity, with a dispersion of $\sigma_\epsilon = 0.3$.

The next step of the pipeline is motivated by Eq. (15), which following the Cauchy–Schwarz inequality, is maximised if the filter Q is proportional to the shear γ_t. We therefore set the Q_2 filter function to

$$Q_2(\theta) \propto \begin{cases} \gamma_t(\theta), & \text{if } 0' < \theta < 10' \\ 0, & \text{otherwise} \end{cases}. \tag{16}$$

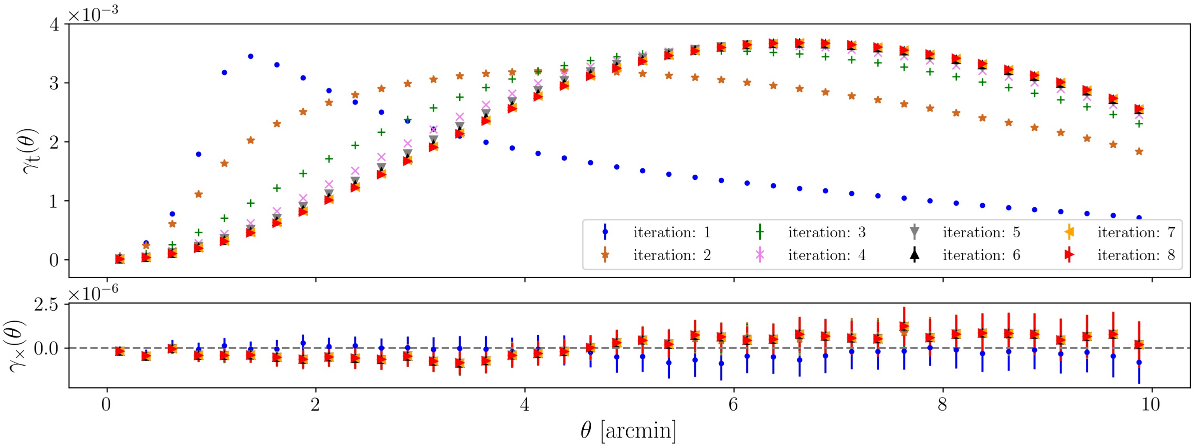

Fig. 3. *Upper panel*: tangential shear profiles, γ_t, for the first eight iterations, showing how the peak moves to larger radii. *Lower panel*: $\gamma_\times$ profiles are consistent with zero. The uncertainties are the standard deviation on the mean determined with the 64 MS realisations.

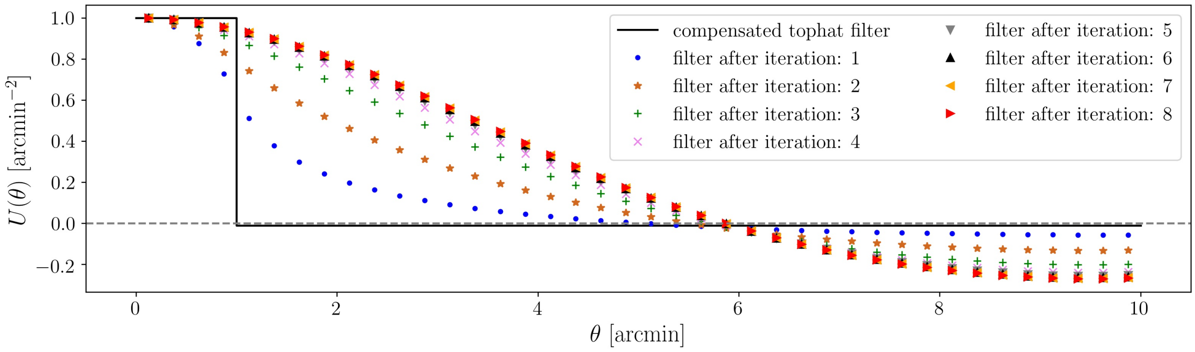

Fig. 4. Resulting filter U , from Eq. (4), after each iteration. With each iteration the filter gets wider until it converges after ~7 iterations. The filters are scaled such that the value of the first θ-bin is unity, which eases comparison with the compensated top-hat filter.

With this filter Q_2 and Eq. (4), we obtain filter U_2, displayed with the blue colour in Fig. 4.

Now the iterative process starts, where we rerun the pipeline with the new filters U_{i+1}. As seen in Fig. 3 the peak of the tangential shear moves to larger radii after each iteration, as the filter U_{i+1} gets wider with each iteration. This effect is not surprising, because we are calculating the filters U_{i+1} from the shear signals, and therefore, the changes are strongly related. After some iterations this broadening starts to converge; in order to measure this convergence, we make use of the S/N calculated with Eq. (15). As a reference S/N value for the first iteration, we calculate an initial filter Q_1 from Eq. (3) as

$$Q_1(\theta) = \frac{1}{\theta^2}\left(1 + \frac{1}{99}\right)\mathcal{H}(\theta - 1')\mathcal{H}(10' - \theta). \tag{17}$$

The resulting S/N values relative to the S/N of the first iteration are stated in Table 1. The S/N does not change after the 7th iteration by more than 10^{-3}, and therefore indicates convergence.

Table 1. S/N relative to the S/N of the first iteration step.

Step	1	2	3	4
$(S/N)/(S/N)_1$	1.	1.819	2.189	2.257
Step	5	6	7	8
$(S/N)/(S/N)_1$	2.271	2.274	2.275	2.275

Once we have converged on a final filter U_7, we expand the range up to a radius of 30′ to make use of the strong tangential shear signal beyond 10′. This size is restricted to 30′ to minimise the rejected margins due to the boundary effects of the FFT, as seen in the lower panel of Fig. 2. The resulting shear profile, and thus the shape of the final adapted filter Q, is shown in Fig. 5. The corresponding adapted filter U, from Eq. (4) using the extended adapted filter Q, is displayed in Fig. 6. Compared to the filters in Fig. 4 the zero crossing of the adapted filter U is at larger θ. This is due to the positive extended tail of the tangential shear profile (adapted filter Q in Fig. 5), which is used to determine the adapted filter U. After this point we do not change this filter anymore, and all filter functions mentioned from now on refer to this pair of adapted filters. We note that the used angular scales for the derivation of the filter function (1′, 10′ and 30′) may not be optimal, but for the purpose of this work in comparing it to an analysis with a top-hat filter function (Sects. 5–7) the optimised sizes are not crucial. Nevertheless, they will be reviewed in future analyses. Since the comparisons of the adapted and the top-hat filter in the following sections is exclusively done with the SLICS and cosmo-SLICS, the MS is from this point on no longer used.

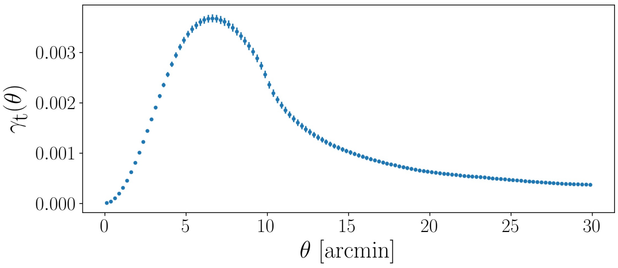

Fig. 5. Tangential shear profile, γ_t, around the highest 10% pixel values of $N_{\rm ap}$ determined with the filter U_7 for $\theta < 10'$ and measured up to radii of 30′ to use the strong tangential shear signal beyond 10′. For the rest of this analysis, this is the shape of the adapted filter Q. The uncertainties are the standard deviation on the mean determined with the 64 MS realisations.

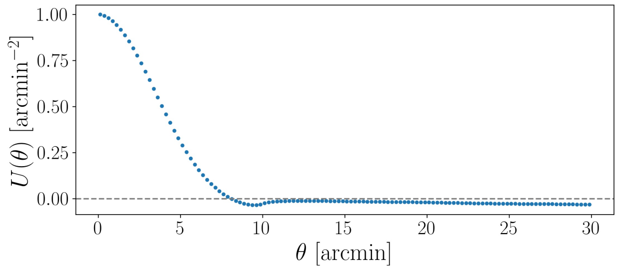

Fig. 6. Adapted compensated filter $U(\theta)$ calculated from the shear profile of Fig. 5 and Eq. (4). The filter is normalised such that the first value is 1 arcmin^{-2}. This final $U(\theta)$ filter is adopted for the rest of the analysis.

5. Suitable top-hat size and S/N comparison

In order to compare the DSS measured using the adapted filter U to the Gruen et al. (2016) top-hat filter function $U_{\rm th}(\theta)$ we must determine the size of the top-hat filter $\theta_{\rm th}$ such that the averaged shear peak positions around the highest and the lowest quantiles of the aperture number field are comparable between both filters. For that, we use 64 realisations of SLICS, with KV450 sources and GAMA lenses.

Following the work of Gruen et al. (2018), we divide the sky according to the aperture number, $N_{\rm ap}$, into five sub-areas of equal size and call them quantiles of the aperture number field. The aperture number is calculated either with the adapted filter function U or with three different top-hat filters of size $\theta_{\rm th} = 5'$, 6′, and 7′. For each quantile, we calculate the tangential shear profiles in 25 logarithmic θ annuli with the software TREECORR (see Jarvis et al. 2004); this is different to the approach in Sect. 4, since for the SLICS and cosmo-SLICS the shear estimates are not given on a grid but from mock catalogues. The resulting shear profiles are displayed for the different filter functions in Fig. 7. We neglect shape noise here to find the optimal top-hat size.

In order to determine the most comparable top-hat filter, we calculate for each filter the angular position of the measured peak of the γ_t profile of the highest and lowest quantile and report in the legend of Fig. 7 the average of these two. The averaged peak position $\theta = 9.3'$ of the shear profiles generated with a top-hat filter of size $\theta_{\rm th} = 6'$ matches the averaged peak position $\theta = 9.3'$ of the shear profiles generated with the adapted filter. Therefore, we set the size of the top-hat filter for all following analyses to $\theta_{\rm th} = 6'$.

Our first performance comparison is based on a respective S/N. The signal S is the averaged aperture mass for axis-symmetric tangential shear profiles $\gamma_t(\boldsymbol{\theta}) = \gamma_t(\theta)$, such that Eq. (2) simplifies to

$$M_{\rm ap}^i = 2\pi \int \gamma_t^i(\theta')\, Q(\theta')\, \theta' {\rm d}', \tag{18}$$

where i denotes the quantile around which the tangential shear profile $\gamma_t^i(\theta)$ is azimuthal-averaged. To calculate the aperture mass with the tangential shear profiles of the DSS with the top-hat filter, we use Eq. (7) for the $Q = Q_{\rm th}$ filter with $\theta_{\rm max} = 30'$. We reiterate that $Q_{\rm th}$ is not adapted to $U_{\rm th}$, but we use it here to provide a comparison to the earlier work of Brouwer et al. (2018). In order to have a S/N, which measures the significance of a nonzero detection, we estimate the noise N as the standard deviation of $M_{\rm ap}^{\rm rand}$ determined by tangential shear profiles around $N_{\rm pix}$ random pixel positions from the 64 realisations, where $N_{\rm pix}$ is the number of pixels in one quantile. Together this gives the signal-to-noise ratio of the i-quantile to

$$\left(\frac{S}{N}\right)^i = \frac{\langle M_{\rm ap}^i \rangle}{\sqrt{\langle (M_{\rm ap}^{\rm rand} - \langle M_{\rm ap}^{\rm rand}\rangle)^2 \rangle}}, \tag{19}$$

where $\langle \ldots \rangle$ refers to the ensemble average over all 64 realisations. For this S/N comparison we use the TREECORR γ_t estimates obtained from ellipticities with shapes noise, so that the noise here describes the sampling variance as well as the shape noise in the data. The resulting S/N for each quantile i, shown in Fig. 8, reveals that the adapted filter performs better, which is consistent with the higher amplitude of the shear profiles seen in Fig. 7.

6. $N_{\rm ap}$ versus $M_{\rm ap}$

After deriving the adapted filter and specifying the top-hat filter size, we want to test our expectation that the adapted filter yields a better correlation between the galaxy and total matter distribution. For this analysis, we make use of 25 light cones from SLICS with a non-linear bias model and 25 light cones from the fiducial cosmology of cosmo-SLICS with a linear bias model, where we expect that for the latter the correlation is stronger since $n(\boldsymbol{\theta}) \propto \kappa(\boldsymbol{\theta})$ here. For both models we calculate the aperture number with Eq. (5) and the aperture mass with Eq. (2) for all pixels with the corresponding adapted filters and top-hat filters, where $\theta_{\rm th} = 6'$ and $\theta_{\rm max} = 30'$. For the aperture number we sum, as before, the foreground (lens) galaxies in squares of size 1 arcmin^2, and for the aperture mass we average the ellipticities of background (source) galaxies in squares of size 1 arcmin^2. Although we would expect similar relative correlation coefficients if we included shape noise in the shear estimates, we opted for the noise-free estimate to be closer to the true correlation coefficient. The results for both filter pairs are shown in Fig. 9, where the upper panels corresponds to the non-linear bias model (SLICS) and the lower panels to the linear bias model (fiducial cosmology from cosmo-SLICS). The correlation coefficient specified in the upper left corner of each panel is determined as

$$\rho = \frac{\left\langle \left(M_{\rm ap}(\boldsymbol{\theta}) - \langle M_{\rm ap}\rangle\right)\left(N_{\rm ap}(\boldsymbol{\theta}) - \langle N_{\rm ap}\rangle\right)\right\rangle}{\sqrt{\left\langle \left(M_{\rm ap}(\boldsymbol{\theta}) - \langle M_{\rm ap}\rangle\right)^2 \right\rangle \left\langle \left(N_{\rm ap}(\boldsymbol{\theta}) - \langle N_{\rm ap}\rangle\right)^2 \right\rangle}}, \tag{20}$$

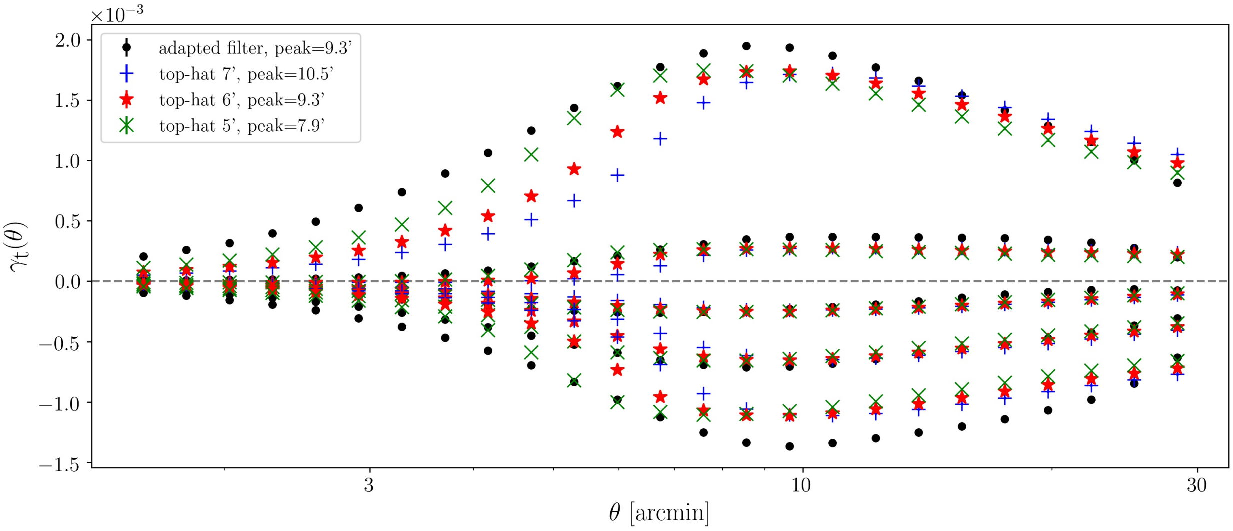

Fig. 7. Tangential shear profiles, γ_t, from SLICS generated with the adapted filter and three top-hat filters of different sizes. The measurements using a top-hat of size 6′ have roughly the same peak position as the adapted filter results. The uncertainties are the standard deviation on the mean determined with the 64 SLICS realisations, and since shape noise is not included, the error bars are almost unseen.

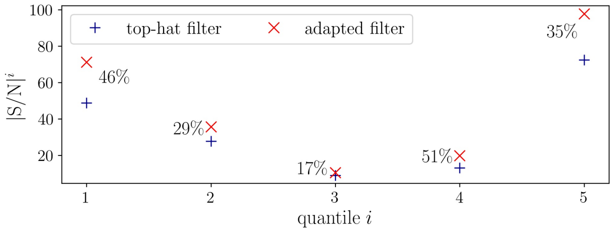

Fig. 8. Comparison of the $|S/N|^i$ between the adapted filter and a top-hat filter of size $\theta_{\rm th} = 6'$ calculated with Eq. (19) for the quantiles i. The uncertainties of the S/N are calculated with a jackknife estimator resampling the S/N data 64 times, removing at each draw one of the γ_t measurement and are below 2%. The values next to the points in the plot are the relative differences.

where $\langle\ldots\rangle$ refers to the ensemble average over all pixel positions $\boldsymbol{\theta}$ of the 25 light cones[4]. The higher the correlation factor ρ is, the better the galaxy number density field traces the underlying matter field. As expected, the adapted filter yields a better correlation as seen in the correlation coefficient ρ, which is ~20% higher for the adapted filter. Furthermore, it is seen that for the linear-bias model ρ is ~10% higher.

7. Sensitivity to constrain cosmological parameters

In this section, we investigate the sensitivity of the adapted and top-hat filters to varying cosmological parameters by use of the cosmo-SLICS, based on the aperture mass of Eq. (18). As seen in Fig. 10 for the highest and lowest quantile, $M_{\rm ap}$ and S_8 have a strong correlation, which indicates that $M_{\rm ap}$ is suitable as a metric for the comparison of different cosmologies.

For each of the 50 realisations per cosmology we first compute the aperture number with the two different filters and the TREECORR γ_t profiles with shape noise of the five quantiles[5]. Afterwards, we calculated an aperture mass $M^i_{\rm ap}$ by use of Eq. (18) with the shear profiles of each realisation n. With these

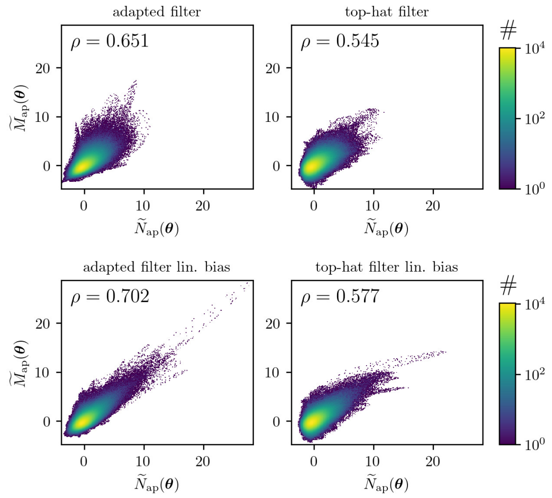

Fig. 9. Pixel-by-pixel $M_{\rm ap}(\boldsymbol{\theta})$ vs. $N_{\rm ap}(\boldsymbol{\theta})$ comparison for a non-linear bias model (*upper panels*) and linear bias model (*lower panels*). The aperture mass and number are calculated except for the outer margins for each individual pixel, which is different to Sect. 5 where $M^i_{\rm ap}$ is calculated from shear profiles of specific quantiles. To ease the comparison between $M_{\rm ap}(\boldsymbol{\theta})$ and $N_{\rm ap}(\boldsymbol{\theta})$ we re-scaled $M_{\rm ap}(\boldsymbol{\theta}) \rightarrow \widetilde{M}_{\rm ap}(\boldsymbol{\theta}) := (M_{\rm ap}(\boldsymbol{\theta}) - \langle M_{\rm ap}\rangle)/\sqrt{\langle(M_{\rm ap}(\boldsymbol{\theta}) - \langle M_{\rm ap}\rangle)^2\rangle}$, correspondingly $N_{\rm ap}(\boldsymbol{\theta}) \rightarrow \widetilde{N}_{\rm ap}(\boldsymbol{\theta})$, where $\langle\ldots\rangle$ is the ensemble average over all pixel positions $\boldsymbol{\theta}$. This re-scaling does not affect the correlation coefficient ρ shown in the upper left corner of each panel. The panels on the left-hand side correspond to the adapted filter, and those on right-hand side to the top-hat filter. For both bias models, the adapted filter yields a stronger correlation, computed with Eq. (20).

---

[4] Due to the periodic boundary effects of the FFT we do not consider the outer 30′ margins.

[5] Each quantile corresponds to one of the five sub-areas of the aperture number as in Sect. 5.

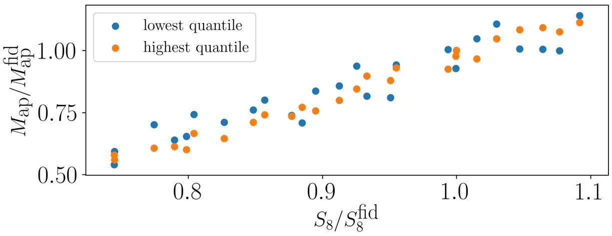

Fig. 10. Comparison between $M_{\rm ap}$ and S_8 for the highest and lowest quantile from $N_{\rm ap}$ with the adapted filter of all cosmologies given in cosmo-SLICS. These two quantities are strongly correlated which indicates that $M_{\rm ap}$ is a useful cosmological probe. For the fiducial case of $S_8 = 0.8231$ the blue and the orange dot are both at $M_{\rm ap}/M_{\rm ap}^{\rm fid} = 1$, so that you see only one orange dot since they are on top of each other.

aperture masses we determine for each quantile in each cosmology an averaged aperture mass $\langle M_{\rm ap}^i \rangle$, where we average over the 50 realisation of each cosmology. Additionally we calculate one 5×5 covariance matrix for each filter (adapted and top-hat) from the shear profiles of the 50 fields for the fiducial cosmology, which captures the correlation between the individual quantiles as

$$C_{\rm fid}^{ij} = \frac{1}{50-1} \sum_{n=1}^{50} (M_{{\rm ap},n}^i - \langle M_{\rm ap}^i \rangle)(M_{{\rm ap},n}^j - \langle M_{\rm ap}^j \rangle), \tag{21}$$

where i and j indicate the individual quantile and subscript "fid" indicates the fiducial cosmology. Using these quantities, we calculate for each cosmology with cosmological parameters $\mathbf{x}$ a χ^2 as a measure of the deviation from the fiducial cosmology as

$$\chi^2(\mathbf{x}|\mathbf{M}_{\rm ap}^{\rm fid}, C_{\rm fid}) = \left[\mathbf{M}_{\rm ap}^{\rm fid} - \mathbf{M}_{\rm ap}(\mathbf{x})\right]^\top C_{\rm fid}^{-1} \left[\mathbf{M}_{\rm ap}^{\rm fid} - \mathbf{M}_{\rm ap}(\mathbf{x})\right], \tag{22}$$

where $\mathbf{M}_{\rm ap}$ is the vector of the averaged amplitudes $\langle M_{\rm ap}^i \rangle$ of the five quantiles of the respective cosmology, with large χ^2 values corresponding to deviations that are easier to detect.

The resulting χ^2-values for the 25 cosmologies are displayed in Fig. 11, in which the χ^2 for both filters are compared to each other. It can be seen that the top-hat filter performs slightly better for some cosmologies with a low χ^2. But for most cases, the adapted filter performs better in distinguishing between different cosmologies.

In order to investigate the sensitivity of the DSS to cosmological parameters in more detail, we display the two-dimensional parameter space in Fig. 12a, where the colour represents the χ^2 of the analysis with the adapted filter. We see that the DSS is particularly powerful to distinguish between different values of $S_8 = \sigma_8 \sqrt{\Omega_m/0.3}$. Unfortunately, the cosmo-SLICS set does not cover values of $S_8 > 0.9$, but we expect that the χ^2 would further increase. In contrast, there is hardly any correlation between χ^2 and w_0, so that this parameter cannot be well constrained by DSS without a tomographic analysis.

Returning to the comparison between the adapted and the top-hat filter, we show in Fig. 12c the two-dimensional parameter space, but encoding in colour $\Delta\chi^2 = \chi^2_{\rm ad} - \chi^2_{\rm th}$. For most cosmologies, the adapted filter performs better, or no significant difference is seen, which is consistent with Fig. 11. Whereas for most parameter pairs no clear trend with $\Delta\chi^2$ is seen, a clear correlation is present for S_8: for small S_8 values, the adapted filter performs better, but for large S_8 and small Ω_m values (i.e. large σ_8), the top-hat filter is more sensitive. High σ_8 values imply strong clustering of the matter distribution. As a consequence, the analysis with the top-hat filter has difficulties to correctly assign regions of the sky within the lowest four quantiles, resulting in shear profiles with quite similar amplitudes, as seen in the lower right panel of Fig. 13. The adapted filter is less affected by this effect, and therefore, χ^2, which is a measure of the deviation to the fiducial cosmology, is larger for the top-hat filter than for the adapted filter (see Fig. A.1 for a visualisation of the $\Delta\chi^2$ in a $\sigma_8 - \Omega_m$ parameter space). Nevertheless, for all other cosmologies, the adapted filter is the better choice to distinguish different cosmologies.

Gaussian process regression emulator (GPRE)

As all four cosmological parameters vary between the different cosmo-SLICS models, a comparison between the different cosmologies is non-trivial. To investigate the performance of the DSS with the two different filters on a continuous two-dimensional projected parameter space, we make use of a flexible GPRE described in Appendix A1 in Harnois-Déraps et al. (2019) to emulate averaged tangential shears γ_t for various cosmologies. The training of the emulator for each individual quantile and for both filters is carried out with the 26 cosmo-SLICS cosmologies. In order to test the accuracy of the GPRE we apply the "leave-one-out" cross-validation method and show the results in Fig. A.2. The shear profiles of the highest and lowest two quantiles can be predicted with an accuracy of generally better than 10%. The shear profiles of the fourth and third quantile have a relative accuracy far worse than that, but this is not surprising since these quantiles have a very low shear signal. However, we checked that our results are robust with respect to including or excluding these two quantiles.

In order to produce smooth two-dimensional constraints on the four cosmological parameters, we vary two of the four parameters in 41 steps in the same range as the parameters were given in cosmo-SLICS and fixed the other two remaining parameters to the fiducial cosmology. Next, we calculate for each grid point the aperture masses $M_{\rm ap}^i$ from Eq. (18) and χ^2 from Eq. (22) as measures of the deviation of the predicted shear profiles from the predicted fiducial shear profiles. We emulate directly the averaged shear profiles, so that $\mathbf{M}_{\rm ap}$ in Eq. (22) is the vector of $M_{\rm ap}^i$ calculated with the emulated shear profiles. The covariance matrix employed is the one calculated with the 50 realisations from the fiducial cosmology of cosmo-SLICS by use of Eq. (21). The results for the individual parameter pairs are displayed in Fig. 12b. As expected, the further we deviate from the fiducial cosmology the higher is the χ^2. By inspecting the individual panels, we see that the S_8 and Ω_m parameters are well constrained. Furthermore, it is clearly visible that these two parameters are dominating the change in the shear profiles for all parameter pairs. This can be seen especially in the case when S_8 and Ω_m are fixed and h or w_0 are varied, where the χ^2 has a very weak gradient.

We also investigated the difference between the adapted and top-hat filters, seen in Fig. 12d. Around the fiducial cosmology, the χ^2 values of both filters are indistinguishable, but as the trend of the 25 cosmo-SLICS nodes (Fig. 12c) already suggests, the analysis with top-hat is more sensitive for large σ_8 values, whereas the adapted filter is better for the remaining parameter regions.

Summarising this section, we find that the top-hat and adapted filters perform similarly around the fiducial cosmology to differentiate cosmologies, but moving away from the fiducial cosmology the adapted filter is more constraining than the top-hat filter, with the exception of large σ_8 values.

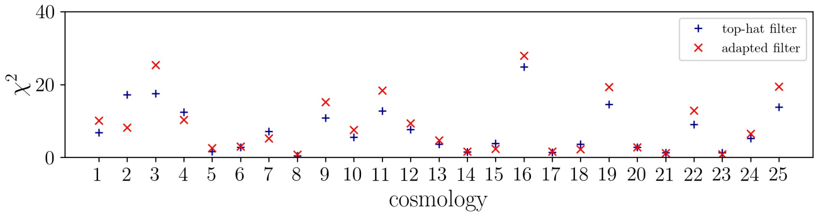

Fig. 11. Comparison of the χ^2 for all 25 cosmologies between the two filters, where the blue plus signs represent the top-hat filter and the red crosses correspond to the adapted filter. The parameters of the 25 cosmological model are shown in Table A.1.

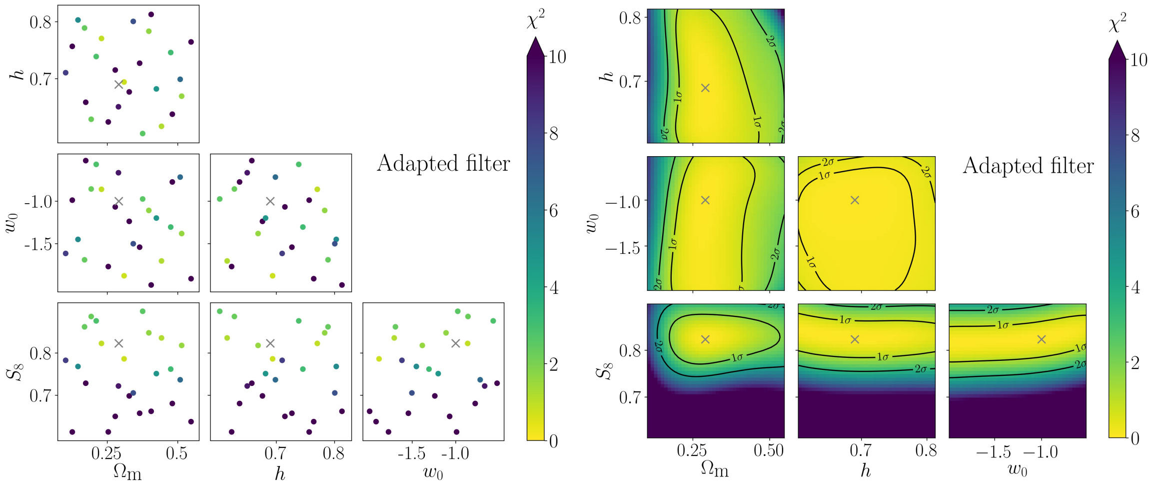

(a) Cosmo-SLICS: adapted filter

(b) GPRE: adapted filter

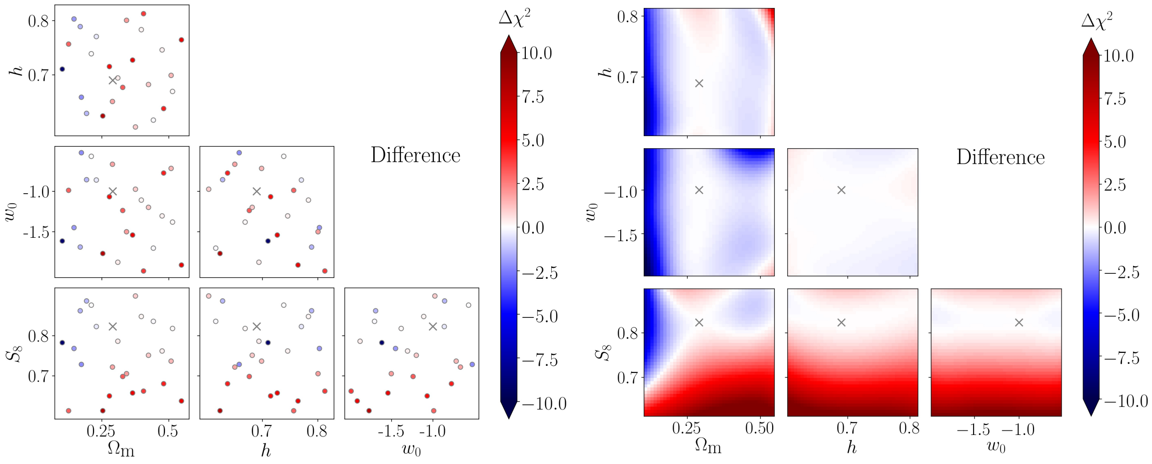

(c) Cosmo-SLICS: difference

(d) GPRE: difference

Fig. 12. Cosmological parameter space, where the colour in the *upper panels* indicates the χ^2 corresponding to the adapted filter and in the *lower panels* to $\Delta\chi^2 = \chi^2_\mathrm{ad} - \chi^2_\mathrm{th}$. The χ^2 of the *left-hand side* are determined with the cosmo-SLICS data and on the *right-hand side* with the flexible Gaussian process regression emulator. The grey cross marks the fiducial cosmology. One should not compare the right-hand side with the left-hand side directly, since in each node on the left, all four cosmological parameters are varied, whereas on the right, only two of the parameters are varied and the other two are fixed to the fiducial cosmology.

8. Summary and conclusion

In this work, we constructed a pair of adapted filter functions for the DSS, using ray tracing and a semi-analytic model galaxy population in the MS in an iterative process. Our new pair of filters is matched with respect to the aperture mass and galaxy number statistics. In other words, the adapted pair of filters measures the lensing convergence and the galaxy number density with the same angular weighting. Based on numerical weak lensing simulations, we confirmed our expectation that the correlation between galaxy number density and shear signal is higher with our adapted filter than for the top-hat filter. We verified that this result holds both for a linear and a non-linear galaxy bias model, using mock GAMA×KV450 data constructed from the SLICS and the cosmo-SLICS weak lensing simulations.

Furthermore, we showed that the adapted filter is indeed a useful improvement for the DSS, by comparing it with the previously used top-hat filter of appropriate scale, using their

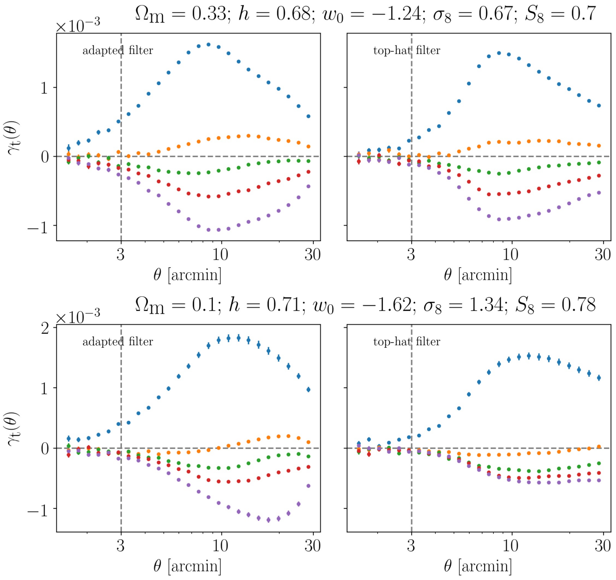

Fig. 13. Tangential shear profiles, γ_t, for two different cosmologies for the adapted filter on the *left-hand side* and the top-hat filter on the *right-hand side*. The uncertainties are the standard deviation on the mean determined with the 50 realisations.

resulting S/N in different sub-areas of the sky and their sensitivity to discriminate between different sets of cosmological parameters as metrics. These sub-areas are called quantiles of the aperture number field. For the S/N comparison, we made use of the wCDM SLICS simulation and showed that the adapted filter has a higher S/N for most quantiles. For comparing the sensitivity of both filters to different cosmologies, we employed the cosmo-SLICS, which is a suite of 26 different cosmologies with 50 realisations each. From the 50 realisations in each cosmology, we calculated a χ^2 as a measure for the deviation from the fiducial cosmology. It turned out that both filters behave similarly near the fiducial cosmology, but that the adapted filter is more constraining in most regions of parameter space probed by cosmo-SLICS, except for very high values of σ_8 where the top-hat filter yielded higher deviation from the fiducial cosmology. In order to investigate the performance of the DSS with the two different filters on a continuous two-dimensional projected parameter space, we also made use of a flexible GPRE, which is a promising tool for future cosmological analyses. Both the S/N and the cosmological analyses lead to the conclusion that the adapted filter yields tighter cosmological constraints than the top-hat filter and should be employed in future DSS analyses.

As an outlook, it would be interesting to investigate the arbitrariness of dividing the aperture number field into five quantiles. For instance, one could optimally combine the shear profiles or find a way to not bin the sky at all, as binning decreases the information content. Furthermore, the filter size used here has not been optimised and should also be varied. Our first attempt here to look into the usefulness of the new DSS to constrain cosmological parameters relied fully on numerical simulations, we aim to modify the analytical model derived by Friedrich et al. (2018) to account for the adapted filter, allowing for an alternative modelling option in an up-coming cosmological study, similar to the approach of Gruen et al. (2018).

Acknowledgements. We thank the anonymous referee for very constructive and fruitful comments. Furhter, we would like to thank Oliver Friedrich, Patrick Simon, Jan Luca von den Busch and Sven Heydenreich for useful discussions, and Mike Jarvis for maintaining TREECORR. The results in this paper are based on observations made with ESO Telescopes at the La Silla Paranal Observatory under programme IDs 177.A-3016, 177.A-3017, 177.A-3018 and 179.A-2004, and on data products produced by the KiDS consortium. The KiDS production team acknowledges support from: Deutsche Forschungsgemeinschaft, ERC, NOVA and NWO-M Grants; Target; the University of Padova, and the University Federico II (Naples). We acknowledge support from the European Research Council under Grant numbers 770935 (H. H.) and 647112 (C. H, J. H. D.). P. B. acknowledges supported by the Deutsche Forschungsgemeinschaft, project SCHN342-13. H. Hildebrandt is supported by a Heisenberg grant of the Deutsche Forschungsgemeinschaft (Hi 1495/5-1). J. H. D. is supported by a STFC Ernest Rutherford Fellowship (project reference ST/S004858/1). S. U. is partly supported by the German Deutsche Forschungsgemeinschaft, DFG project numbers SL 172/1-1 and SCHN 342/13-1. V. D. acknowledges the Higgs Centre Nimmo Scholarship and the Edinburgh Global Research Scholarship. C. H. acknowledges support from the Max Planck Society and the Alexander von Humboldt Foundation in the framework of the Max Planck-Humboldt Research Award endowed by the Federal Ministry of Education and Research. Author contributions: all authors contributed to the development and writing of this paper. The authorship list is given in two groups: the lead authors (P. B., P. S.), followed by an alphabetical group, which provided data central to this work, or contributed to the analysis.

References

Abbott, T. M. C., Abdalla, F. B., Alarcon, A., et al. 2018, Phys. Rev. D, 98, 043526
Aihara, H., AlSayyad, Y., Ando, M., et al. 2019, PASJ, 71, 114
Bilicki, M., Hoekstra, H., Brown, M. J. I., et al. 2018, A&A, 616, A69
Brouwer, M. M., Demchenko, V., Harnois-Déraps, J., et al. 2018, MNRAS, 481, 5189
de Jong, J. T. A., Verdoes Kleijn, G. A., Kuijken, K. H., & Valentijn, E. A. 2013, Exp. Astron., 35, 25
de Jong, J. T. A., Verdoes Kleijn, G. A., Erben, T., et al. 2017, A&A, 604, A134
DES Collaboration (Abbott, T., et al.) 2020, Phys. Rev. D, 102, 023509
Driver, S. P., Hill, D. T., Kelvin, L. S., et al. 2011, MNRAS, 413, 971
Drlica-Wagner, A., Sevilla-Noarbe, I., Rykoff, E. S., et al. 2018, ApJS, 235, 33
Edge, A., Sutherland, W., Kuijken, K., et al. 2013, Messenger, 154, 32
Friedrich, O., Gruen, D., DeRose, J., et al. 2018, Phys. Rev. D, 98, 023508
Frigo, M., & Johnson, S. G. 2005, IEEE Proc., 93, 216
Fu, L., Kilbinger, M., Erben, T., et al. 2014, MNRAS, 441, 2725
Gruen, D., Friedrich, O., Amara, A., et al. 2016, MNRAS, 455, 3367
Gruen, D., Friedrich, O., Krause, E., et al. 2018, Phys. Rev. D, 98, 023507
Hamana, T., Shirasaki, M., Miyazaki, S., et al. 2020, PASJ, 72, 16
Harnois-Déraps, J., Amon, A., Choi, A., et al. 2018, MNRAS, 481, 1337
Harnois-Déraps, J., Giblin, B., & Joachimi, B. 2019, A&A, 631, A160
Heitmann, K., Lawrence, E., Kwan, J., Habib, S., & Higdon, D. 2014, ApJ, 780, 111
Henriques, B. M. B., White, S. D. M., Thomas, P. A., et al. 2015, MNRAS, 451, 2663
Heymans, C., Van Waerbeke, L., Miller, L., et al. 2012, MNRAS, 427, 146
Hilbert, S., Hartlap, J., White, S. D. M., & Schneider, P. 2009, A&A, 499, 31
Hildebrandt, H., Viola, M., Heymans, C., et al. 2017, MNRAS, 465, 1454
Hildebrandt, H., Köhlinger, F., van den Busch, J. L., et al. 2020, A&A, 633, A69
Hinshaw, G., Larson, D., Komatsu, E., et al. 2013, ApJS, 208, 19
Jarvis, M., Bernstein, G., & Jain, B. 2004, MNRAS, 352, 338
Kuijken, K., Heymans, C., Hildebrandt, H., et al. 2015, MNRAS, 454, 3500
Pen, U.-L. 1998, ApJ, 504, 601
Pires, S., Leonard, A., & Starck, J.-L. 2012, MNRAS, 423, 983
Planck Collaboration V. 2020, A&A, 641, A5
Sadeh, I., Abdalla, F. B., & Lahav, O. 2016, PASP, 128, 104502
Saghiha, H., Simon, P., Schneider, P., & Hilbert, S. 2017, A&A, 601, A98
Schneider, P. 1996, MNRAS, 283, 837
Schneider, P. 1998, ApJ, 498, 43
Simon, P., Saghiha, H., Hilbert, S., et al. 2019, A&A, 622, A104
Singh, S., Mandelbaum, R., Seljak, U., Slosar, A., & Vazquez Gonzalez, J. 2017, MNRAS, 471, 3827
Smith, A., Cole, S., Baugh, C., et al. 2017, MNRAS, 470, 4646
Springel, V., White, S. D. M., Jenkins, A., et al. 2005, Nature, 435, 629
Unruh, S., Schneider, P., & Hilbert, S. 2019, A&A, 623, A94
Unruh, S., Schneider, P., Hilbert, S., et al. 2020, A&A, 638, A96
White, M. 2014, MNRAS, 439, 3630

Appendix A: Additional material

Table A.1. Overview of all the different cosmological parameters for the 26 cosmo-SLICS models, which are used in Sect. 7 for the cosmological analysis.

	Ω_m	h	w_0	σ_8	S_8
fid	0.2905	0.6898	−1.0000	0.8364	0.8231
1	0.3282	0.6766	−1.2376	0.6677	0.6984
2	0.1019	0.7104	−1.6154	1.3428	0.7826
3	0.2536	0.6238	−1.7698	0.6670	0.6133
4	0.1734	0.6584	−0.5223	0.9581	0.7284
5	0.3759	0.6034	−0.9741	0.8028	0.8986
6	0.4758	0.7459	−1.3046	0.6049	0.7618
7	0.1458	0.8031	−1.4498	1.1017	0.7680
8	0.3099	0.6940	−1.8784	0.7734	0.7861
9	0.4815	0.6374	−0.7737	0.5371	0.6804
10	0.3425	0.8006	−1.5010	0.6602	0.7054
11	0.5482	0.7645	−1.9127	0.4716	0.6375
12	0.2898	0.6505	−0.6649	0.7344	0.7218
13	0.4247	0.6819	−1.1986	0.6313	0.7511
14	0.3979	0.7833	−1.1088	0.7360	0.8476
15	0.1691	0.7890	−1.6903	1.1479	0.8618
16	0.1255	0.7567	−0.9878	0.9479	0.6131
17	0.5148	0.6691	−1.3812	0.6243	0.8178
18	0.1928	0.6285	−0.8564	1.1055	0.8862
19	0.2784	0.7151	−1.0673	0.6747	0.6500
20	0.2106	0.7388	−0.5667	1.0454	0.8759
21	0.4430	0.6161	−1.7037	0.6876	0.8356
22	0.4062	0.8129	−1.9866	0.5689	0.6620
23	0.2294	0.7706	−0.8602	0.9407	0.8226
24	0.5095	0.6988	−0.7164	0.5652	0.7366
25	0.3652	0.7271	−1.5414	0.5958	0.6574

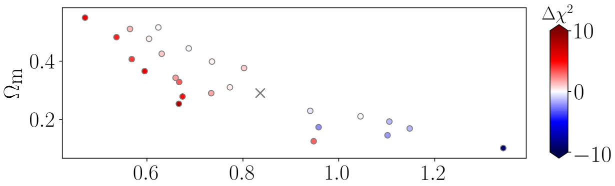

Fig. A.1. Cosmological parameter space $\sigma_8-\Omega_m$, where the colour indicates $\Delta\chi^2 = \chi^2_{\rm ad} - \chi^2_{\rm th}$ of the 25 nodes of cosmo-SLICS determined in Sect. 7. It is clearly seen that for large σ_8 the analysis with the top-hat filter yields higher χ^2. The grey cross indicates the fiducial cosmology.

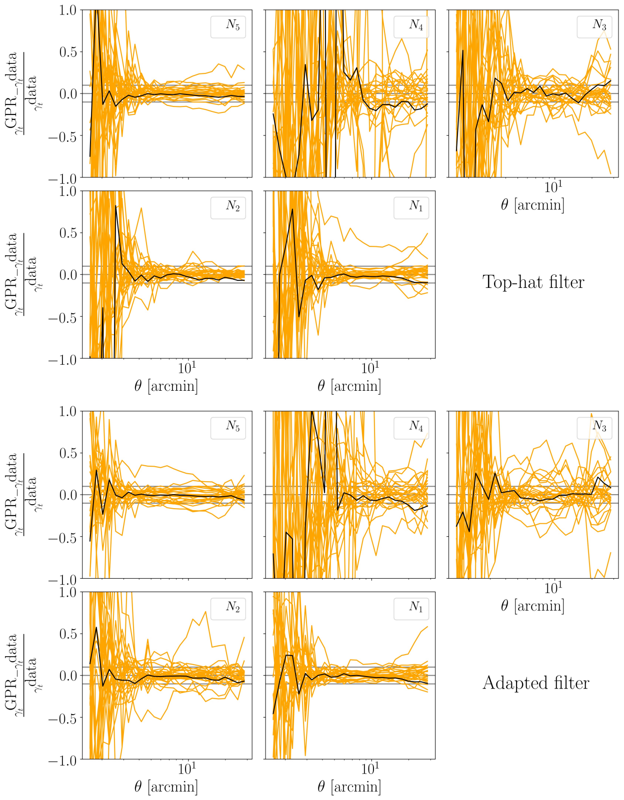

Fig. A.2. "Leave-one-out" cross-validation to test performance of accuracy of the GPRE, which is used in Sect. 7 to investigate the performance of the DSS with the two different filters on a continuous two-dimensional projected parameter space. On the y-axis the relative difference between the predicted shear profile of one cosmology if the emulator is trained exclusively by the remaining cosmologies and the corresponding shear profile which the emulator tries to emulate. The black lines here are correspond to the fiducial case. The quantiles N_4 and N_3 are quite inaccurate, but the other quantiles are of the 10% level accurate, which are indicated with horizontal grey lines.

A&A 661, A137 (2022)
https://doi.org/10.1051/0004-6361/202141628

Astronomy & Astrophysics

A revised density split statistic model for general filters

Pierre Burger[1], Oliver Friedrich[2,3], Joachim Harnois-Déraps[4,5], and Peter Schneider[1]

[1] Argelander-Institut für Astronomie, Auf dem Hügel 71, 53121 Bonn, Germany
e-mail: `pburger@astro.uni-bonn.de`
[2] Kavli Institute for Cosmology, University of Cambridge, Cambridge CB3 0HA, UK
[3] Churchill College, University of Cambridge, Cambridge CB3 0DS, UK
[4] School of Mathematics, Statistics and Physics, Newcastle University, Newcastle Upon Tyne NE1 7RU, UK
[5] Astrophysics Research Institute, Liverpool John Moores University, 146 Brownlow Hill, Liverpool L3 5RF, UK

Received 24 June 2021/ Accepted 2 March 2022

ABSTRACT

Context. Studying the statistical properties of the large-scale structure in the Universe with weak gravitational lensing is a prime goal of several current and forthcoming galaxy surveys. The power that weak lensing has to constrain cosmological parameters can be enhanced by considering statistics beyond second-order shear correlation functions or power spectra. One such higher-order probe that has proven successful in observational data is density split statistics (DSS), in which one analyses the mean shear profiles around points that are classified according to their foreground galaxy density.

Aims. In this paper, we generalise the most accurate DSS model to allow for a broad class of angular filter functions used for the classification of the different local density regions. This approach is motivated by earlier findings showing that an optimised filter can provide tighter constraints on model parameters compared to the standard top-hat case.

Methods. As in the previous DSS model we built on large deviation theory approaches and approximations thereof to model the matter density probability distribution function, and on perturbative calculations of higher-order moments of the density field. The novel addition relies on the generalisation of these previously employed calculations to allow for general filter functions and is validated on several sets of numerical simulations.

Results. It is shown that the revised model fits the simulation measurements well for many filter choices, with a residual systematic offset that is small compared to the statistical accuracy of current weak lensing surveys. However, by use of a simple calibration method and a Markov chain Monte Carlo analysis, we studied the expected sensitivity of the DSS to cosmological parameters and find unbiased results and constraints comparable to the commonly used two-point cosmic shear measures. Hence, our DSS model can be used in competitive analyses of current cosmic shear data, while it may need refinements for forthcoming lensing surveys.

Key words. gravitational lensing: weak – large-scale structure of Universe – methods: statistical – galaxies: abundances – surveys

1. Introduction

Studying the matter distribution of the present large-scale structure reveals a wealth of information about the evolution of the Universe. In particular, its distorting effect on the propagation of light from distant galaxies, known as cosmic shear, can be captured by analysing weak lensing surveys. By comparing the results of cosmological models with the observed signal, one can constrain cosmological parameters (see e.g. Asgari et al. 2021; Abbott et al. 2022; Hamana et al. 2020).

The preferred methods used to infer statistical properties of the matter and galaxy distribution concentrate on second-order statistics, such as the two-point correlation functions or their Fourier counterparts, the power spectra. Although these statistics have an impressive accuracy to describe for instance primordial perturbations visible in the cosmic microwave background (CMB; e.g. Planck Collaboration V 2020) they probe only the Gaussian information present in the density fluctuations. However, these initial conditions developed significant non-Gaussian features by means of non-linear gravitational instability, which can only be investigated with higher-order statistics. Although they are typically more time consuming to model and measure, these higher-order statistics scale differently with cosmological parameters, and are not affected in the same way by residual systematics. Hence, by jointly investigating second- and higher-order statistics, the constraining power on cosmological parameters increases (see e.g. Bergé et al. 2010; Pyne & Joachimi 2021; Pires et al. 2012; Fu et al. 2014; Kilbinger & Schneider 2005).

A large number of analytical models for the two-point statistics exists in the literature (Takahashi et al. 2012; Heitmann et al. 2014; Euclid Collaboration 2021; Mead et al. 2020; Nishimichi et al. 2021); however, the analysis of higher-order statistics is usually based on simulations. Analytical models for higher-order lensing statistics are rare, although they are important not only for scientists to understand physical processes, but also to cross-check simulations, which are usually only tested against Gaussian statistics. For example, Reimberg & Bernardeau (2018) and Barthelemy et al. (2021) used large deviation theory (LDT) to compute the reduced-shear correction to the aperture mass probability distribution function (PDF); Munshi et al. (2020) and Halder et al. (2021) analytically modelled the integrated shear three-point function; the lensing peak count function was modelled in Fan et al. (2010), Lin & Kilbinger (2015) and Shan et al. (2018), while the lensing PDF is modelled in Boyle et al. (2021).

The examples mentioned above all pertain to the analysis of cosmic shear data. However, it has been established in recent analyses that the addition of foreground clustering data, and their

Article published by EDP Sciences

cross-correlation with the background source galaxies, yield significantly better constraints (Abbott et al. 2018; Heymans et al. 2021). While the central analyses focused again on two-point statistics, Friedrich et al. (2018, hereafter F18) developed a competitive model based on density split statistics (hereafter DSS). The idea is to measure the mean tangential shear around small sub-areas of the survey, and to stack the signal according to the foreground galaxy density in these sub-areas. We expect the tangential shear to be larger around points with a high density of foreground galaxies, given they correspond to a large matter overdensity on average. The model derived in F18 is based on non-perturbative calculations of the matter density PDF, which predicts the shear profiles and the probability density of galaxy counts in the sub-areas, for a given cosmological model, a redshift distribution for the source and lens galaxy populations, and a mean galaxy density. In Gruen et al. (2018, hereafter G18), the F18 model is used to constrain cosmological parameters from DSS measurements from the Dark Energy Survey (DES) First Year and Sloan Digital Sky Survey (SDSS) data, which yields constraints on the matter density $\Omega_\mathrm{m} = 0.26^{+0.04}_{-0.03}$ that agree and are competitive with the DES analysis of galaxy and shear two-point functions (see Abbott et al. 2018).

One of the motivations of this work is based on Burger et al. (2020, hereafter B20), who use a suite of numerical simulations to show that using matched filter functions for searching peaks and troughs in the galaxy and matter density contrast has clear advantages compared to the top-hat filter used in the F18 model, both in terms of the overall signal S/N and in recovering accurately the galaxy bias term. Another motivation of using compensated filters is that these filters are more confined in Fourier space and are therefore better at smoothing out large ℓ-modes where baryonic effects play an important role (Asgari et al. 2020). Therefore, it is of interest to generalise the DSS to a broader set of filter functions. Smoothing cosmic density fields with filters other than top-hat ones significantly complicates the LDT-like calculations used by F18 and G18 (cf. Barthelemy et al. 2021) because for top-hat filters the Lagrangian to Eulerian mapping inherent in LDT is particularly simple. However, we find here that density split statistics with non-top-hat filters that are sufficiently concentrated around their centres can still be accurately modelled with computationally feasible extensions of approximations made by F18. This paper describes our modifications to the F18 model that will allow us to optimise filtering strategies when applying density split statistics to Stage III weak lensing surveys such as KiDS. Throughout this paper, if not otherwise stated, we assume a spatially flat universe.

This work is structured as follows. In Sect. 2 we review the basics of the aperture statistics; we then detail our changes to the F18 model in Sect. 3. In Sect. 4 we describe the simulations, and the construction of our mock data used to validate the revised model. In Sect. 5 we compare the model predictions with simulations, and establish the model's limitations. We summarise our work in Sect. 6.

2. Aperture statistics

The lensing convergence κ and shear γ are related via the lensing potential ψ (Schneider et al. 1992) as

$$\kappa(\boldsymbol{\theta}) = \frac{1}{2}\left(\partial_1^2 + \partial_2^2\right)\psi(\boldsymbol{\theta})\,, \quad \gamma(\boldsymbol{\theta}) = \frac{1}{2}\left(\partial_1^2 - \partial_2^2 + 2\mathrm{i}\partial_1\partial_2\right)\psi(\boldsymbol{\theta}), \qquad (1)$$

with $\partial_i = \frac{\partial}{\partial\theta_i}$ and $\boldsymbol{\theta}$ the angular position on the sky; we employ the flat-sky approximation. Given a reference point in a Cartesian coordinate system on the sky and a second point whose separation to the first is oriented at an angle ϕ with respect to that coordinate system, we can express the shear at the second point in terms of the tangential and cross-shear with respect to the first point as

$$\gamma_\mathrm{t} = -\mathrm{Re}\left(\gamma\,\mathrm{e}^{-2\mathrm{i}\phi}\right), \quad \gamma_\times = -\mathrm{Im}\left(\gamma\,\mathrm{e}^{-2\mathrm{i}\phi}\right), \qquad (2)$$

where the factor 2 in the exponent is due to the polar nature of the shear. Given a convergence field $\kappa(\boldsymbol{\theta})$, the aperture mass at position $\boldsymbol{\theta}$ is defined as

$$M_\mathrm{ap}(\boldsymbol{\theta}) := \int \mathrm{d}^2\theta'\,\kappa(\boldsymbol{\theta}+\boldsymbol{\theta}')\,U\left(\left|\boldsymbol{\theta}'\right|\right), \qquad (3)$$

where $U(\vartheta)$ is a compensated axisymmetric filter function, such that $\int \vartheta\, U(\vartheta)\,\mathrm{d}\vartheta = 0$. As shown in Schneider (1996), if U is compensated, M_ap can also be expressed in terms of the tangential shear γ_t and a related filter function Q as

$$M_\mathrm{ap}(\boldsymbol{\theta}) = \int \mathrm{d}^2\theta'\,\gamma_\mathrm{t}(\boldsymbol{\theta}+\boldsymbol{\theta}')\,Q\left(\left|\boldsymbol{\theta}'\right|\right), \qquad (4)$$

where

$$Q(\vartheta) = \frac{2}{\vartheta^2}\int_0^\vartheta \mathrm{d}\vartheta'\,\vartheta'\,U(\vartheta') - U(\vartheta), \qquad (5)$$

which can be inverted, yielding

$$U(\vartheta) = 2\int_\vartheta^\infty \mathrm{d}\vartheta'\,\frac{Q(\vartheta')}{\vartheta'} - Q(\vartheta). \qquad (6)$$

In analogy to M_ap, we define, as done in B20, the aperture number counts (Schneider 1998), or aperture number, as

$$N_\mathrm{ap}(\boldsymbol{\theta}) := \int \mathrm{d}^2\theta'\,n(\boldsymbol{\theta}+\boldsymbol{\theta}')\,U\left(\left|\boldsymbol{\theta}'\right|\right), \qquad (7)$$

where $U(\boldsymbol{\vartheta})$ is the same filter function as in Eq. (3) and $n(\boldsymbol{\vartheta})$ is the (foreground) galaxy number density on the sky. This definition of the aperture number is equivalent to the "Counts-in-Cell" (CiC) from Gruen et al. (2016) if a top-hat filter of the form

$$U_\mathrm{th}(\vartheta) = \frac{1}{A}\mathcal{H}(\vartheta_\mathrm{th} - \vartheta), \qquad (8)$$

is used, where $\mathcal{H}$ is the Heaviside step function and A is the area of the filter. However, B20 demonstrated that top-hat filters are not optimal, and that a better performance is achieved by an adapted filter in terms of signal-to-noise-ratio (S/N) and in recovering accurately the galaxy bias term. In this paper we compute aperture mass statistics with Eq. (4) using simulated weak lensing catalogues of background source galaxies, notably regarding positions and ellipticities, and aperture number statistics with Eq. (7) from the position of simulated foreground lens galaxies (see Sect. 4).

3. Revised model

In this section we describe our modifications of the original F18 model. Although the derivations shown here are self-contained, we recommend the interested reader to consult the original

F18 paper. In particular, it is shown there that the full non-perturbative calculation of the PDF within large deviation theory (LDT) can be well approximated with a log-normal PDF that matches variance and skewness of the LDT result. This allowed F18 and G18 to replace the expensive LDT computation with a faster one, hence making the calculation of full Markov chain Monte Carlo (MCMC) functions feasible. The reason why this approximation works well is that, for top-hat filters, the scaling of variance and higher-order cumulants in LDT is similar to that found in log-normal distributions. This cannot be expected a priori for other filter functions. However, through comparison with N-body simulations we find here (cf. Sect. 5) that either a simple log-normal or a combination of two log-normal distributions still accurately describes the density PDFs required to analyse density split statistics with more general classes of filters. The following section describes these calculations. In order to reduce the mathematical calculations in this section, some derivations are detailed in Appendix A.

We start by defining the line-of-sight projection of the 3D matter density contrast $\delta_{\mathrm{m,3D}}$, weighted by a foreground (lens) galaxy redshift probability distribution $n_{\mathrm{f}}(z)$ as

$$\delta_{\mathrm{m,2D}}(\boldsymbol{\theta}) = \int \mathrm{d}\chi \, q_{\mathrm{f}}(\chi) \, \delta_{\mathrm{m,3D}}\left(\chi\boldsymbol{\theta}, \chi\right), \tag{9}$$

where χ is the co-moving distance and the projection kernel $q_{\mathrm{f}}(\chi)$ is

$$q_{\mathrm{f}}(\chi) = n_{\mathrm{f}}\left(z\left[\chi\right]\right) \frac{\mathrm{d}z[\chi]}{\mathrm{d}\chi}. \tag{10}$$

This 2D matter density contrast can then be used together with a linear bias term to represent a tracer density contrast (see Sect. 3.3 or Sect. 4). Following F18, the next step consists of smoothing the results with a filter U of size Θ:

$$\delta_{\mathrm{m},U}(\boldsymbol{\theta}) \equiv \int_{|\boldsymbol{\theta}'|<\Theta} \mathrm{d}^2\theta' \; \delta_{\mathrm{m,2D}}\left(\boldsymbol{\theta} + \boldsymbol{\theta}'\right) \; U\left(\left|\boldsymbol{\theta}'\right|\right). \tag{11}$$

This simplifies in the case of a top-hat filter of size Θ to

$$\delta^{\Theta}_{\mathrm{m,th}}(\boldsymbol{\theta}) = \frac{1}{A} \int_{|\boldsymbol{\theta}'|<\Theta} \mathrm{d}^2\theta' \; \delta_{\mathrm{m,2D}}\left(\boldsymbol{\theta} + \boldsymbol{\theta}'\right). \tag{12}$$

Similar to the 2D density contrast, the convergence, which is needed to describe the DSS signal, is given by

$$\kappa(\boldsymbol{\theta}) = \int \mathrm{d}\chi \, W_{\mathrm{s}}(\chi) \, \delta_{\mathrm{m,3D}}\left(\chi\boldsymbol{\theta}, \chi\right), \tag{13}$$

where $W_{\mathrm{s}}(\chi)$ is the lensing efficiency defined as

$$W_{\mathrm{s}}(\chi) = \frac{3\Omega_{\mathrm{m}} H_0^2}{2c^2} \int_{\chi}^{\infty} \mathrm{d}\chi' \, \frac{\chi\left(\chi' - \chi\right)}{\chi' a(\chi)} \, q_{\mathrm{s}}\left(\chi'\right), \tag{14}$$

with $q_{\mathrm{s}}(\chi) = n_{\mathrm{s}}\left(z\left[\chi\right]\right) \frac{\mathrm{d}z[\chi]}{\mathrm{d}\chi}$ being the line-of-sight probability density of the sources, Ω_{m} the matter density parameter, H_0 the Hubble parameter, and c the speed of light. The mean convergence inside an angular separation ϑ, $\kappa_{<\vartheta}$, follows then in analogy to Eq. (12) by substituting $\delta_{\mathrm{m,2D}}(\boldsymbol{\theta})$ with $\kappa(\boldsymbol{\theta})$.

The aim of our model is to predict the tangential shear profiles γ_{t} given a quantile Q of the foreground aperture number N_{ap}, $\langle\gamma_{\mathrm{t}}|Q\rangle$, where for instance the highest quantile is the set of lines of sight of the sky that have the highest values of N_{ap}. Therefore, to determine $\langle\gamma_{\mathrm{t}}|Q\rangle$ the model calculates $\left\langle\gamma_{\mathrm{t}}|N_{\mathrm{ap}}\right\rangle$ and sums up all that belong to the corresponding quantile Q. The expectation value of $\left\langle\gamma_{\mathrm{t}}|N_{\mathrm{ap}}\right\rangle$ is computed from the convergence profile as

$$\left\langle\gamma_{\mathrm{t}}(\vartheta)|N_{\mathrm{ap}}\right\rangle = \left\langle\kappa_{<\vartheta}|N_{\mathrm{ap}}\right\rangle - \left\langle\kappa_{\vartheta}|N_{\mathrm{ap}}\right\rangle = -\frac{\vartheta}{2}\frac{\mathrm{d}}{\mathrm{d}\vartheta}\left\langle\kappa_{<\vartheta}|N_{\mathrm{ap}}\right\rangle, \tag{15}$$

where κ_{ϑ} is the azimuthally averaged convergence at angular separation ϑ from the centre of the filter, and $\kappa_{<\vartheta}$ is the average convergence inside that radius. The latter quantity, conditioned on a given N_{ap}, can be specified by

$$\left\langle\kappa_{<\vartheta}|N_{\mathrm{ap}}\right\rangle = \int \mathrm{d}\delta_{\mathrm{m},U} \; \left\langle\kappa_{<\vartheta}|\delta_{\mathrm{m},U}, N_{\mathrm{ap}}\right\rangle p\left(\delta_{\mathrm{m},U}|N_{\mathrm{ap}}\right) \tag{16}$$

$$\approx \int \mathrm{d}\delta_{\mathrm{m},U} \; \left\langle\kappa_{<\vartheta}|\delta_{\mathrm{m},U}\right\rangle \; p\left(\delta_{\mathrm{m},U}|N_{\mathrm{ap}}\right), \tag{17}$$

where in the second step we assumed that the expected convergence within ϑ only depends on the projected matter density contrast $\delta_{\mathrm{m},U}$ and not on the particular realisation of shot-noise in N_{ap} found within that fixed matter density contrast[1].

By use of Bayes' theorem, we can express the conditional PDF as

$$p\left(\delta_{\mathrm{m},U}|N_{\mathrm{ap}}\right) = \frac{p\left(N_{\mathrm{ap}}|\delta_{\mathrm{m},U}\right) p\left(\delta_{\mathrm{m},U}\right)}{p\left(N_{\mathrm{ap}}\right)}, \tag{18}$$

where $p\left(N_{\mathrm{ap}}|\delta_{\mathrm{m},U}\right)$ is the probability of finding N_{ap} given the smoothed density contrast $\delta_{\mathrm{m},U}$. The normalisation in the denominator of Eq. (18) follows by integrating over the numerator,

$$p\left(N_{\mathrm{ap}}\right) = \int \mathrm{d}\delta_{\mathrm{m},U} \; p\left(\delta_{\mathrm{m},U}\right) \; p\left(N_{\mathrm{ap}}|\delta_{\mathrm{m},U}\right). \tag{19}$$

As seen in the derivation above, we are left with three ingredients in order to calculate the tangential shear profiles given a quantile Q of the aperture number $\left\langle\gamma_{\mathrm{t}}(\vartheta)|N_{\mathrm{ap}}\right\rangle$:

(I) the PDF of the matter density contrast smoothed with the filter function U (used in Eqs. (18), (19))

$$p\left(\delta_{\mathrm{m},U}\right); \tag{20}$$

(II) the expectation value of the convergence inside a radius ϑ given the smoothed density contrast (used in Eq. (17))

$$\left\langle\kappa_{<\vartheta}|\delta_{\mathrm{m},U}\right\rangle; \tag{21}$$

(III) the distribution of N_{ap} for the given filter function U given the smoothed density contrast (used in Eqs. (18), (19))

$$p\left(N_{\mathrm{ap}}|\delta_{\mathrm{m},U}\right). \tag{22}$$

Since all three ingredients are sensitive to the filter U, we need to adjust all of them coherently with respect to the top-hat case.

---

[1] This assumption is not evident per se, since via mode coupling the large-scale profile of a given density perturbation may well be correlated to the shot-noise (i.e. small-scale fluctuations) of galaxy formation in the centre of that perturbation. F18 have found the approximation $\left\langle\kappa_{<\vartheta}|\delta_{\mathrm{m},U}, N_{\mathrm{ap}}\right\rangle \approx \left\langle\kappa_{<\vartheta}|\delta_{\mathrm{m},U}\right\rangle$ to be accurate in the Buzzard N-body simulations (DeRose et al. 2019), but a more stringent investigation of this assumption is left for future work.

3.1. $(I) : p\,(\delta_m, U)$

As shown by F18 the full LDT computation of the matter density PDF can accurately approximated by a shifted log-normal distribution with vanishing mean (Hilbert et al. 2011), which is fully characterised by two parameters, σ and δ_0, as

$$p\left(\delta_{\mathrm{m},U}\right) = \frac{1}{\sqrt{2\pi}\sigma\left(\delta_{\mathrm{m},U} + \delta_0\right)} \exp\left(-\frac{\left[\ln\left(\delta_{\mathrm{m},U}/\delta_0 + 1\right) + \sigma^2/2\right]^2}{2\sigma^2}\right). \tag{23}$$

The two free parameters can be determined by specifying the variance $\left\langle\delta^2_{\mathrm{m},U}\right\rangle$ and skewness $\left\langle\delta^3_{\mathrm{m},U}\right\rangle$ of the PDF as (Hilbert et al. 2011)

$$\left\langle\delta^2_{\mathrm{m},U}\right\rangle = \delta_0^2\left[\exp\left(\sigma^2\right) - 1\right], \tag{24}$$

$$\left\langle\delta^3_{\mathrm{m},U}\right\rangle = \frac{3}{\delta_0}\left\langle\delta^2_{\mathrm{m},U}\right\rangle^2 + \frac{1}{\delta_0^3}\left\langle\delta^2_{\mathrm{m},U}\right\rangle^3; \tag{25}$$

we derive the expression of $\left\langle\delta^2_{\mathrm{m},U}\right\rangle$ and $\left\langle\delta^3_{\mathrm{m},U}\right\rangle$ in Appendix A (see Eq. (A.28)).

As we show later, this approximation works well for non-negative filter functions like top-hat or Gaussian filters. However, the log-normal PDF approximation becomes less accurate for compensated filters that include negative weights. In these cases we instead divide U into $U_>(\vartheta) = U(\vartheta)\mathcal{H}(\vartheta_{\mathrm{ts}} - \vartheta)$ and $U_<(\vartheta) = -U(\vartheta)\mathcal{H}(\vartheta - \vartheta_{\mathrm{ts}})$, where ϑ_{ts} is the transition scale from positive to negative filter weights. As a consequence, we obtain two correlated log-normal random variables, $\delta_{\mathrm{m},U_>}$ and $\delta_{\mathrm{m},U_<}$, whose joint distribution can be represented by a bi-variate log-normal distribution as

$$p\left(\delta_{\mathrm{m},U_>}, \delta_{\mathrm{m},U_<}\right) = \frac{1}{2\pi\sigma_>\left(\delta_{\mathrm{m},U_>} + \delta_{0,>}\right)\sigma_<\left(\delta_{\mathrm{m},U_<} + \delta_{0,<}\right)\sqrt{1-\rho^2}} \times \exp\left(-\frac{1}{2(1-\rho^2)}\left[\Delta_>^2 + \Delta_<^2 - 2\rho\Delta_>\Delta_<\right]\right), \tag{26}$$

where we defined

$$\Delta_> = \frac{\ln\left(\delta_{\mathrm{m},U_>}/\delta_{0,>} + 1\right) + \sigma_>^2/2}{\sigma_>} \tag{27}$$

and similarly for $\Delta_<$. The correlation coefficient ρ is determined by

$$\rho = \ln\left(\frac{\left\langle\delta_{\mathrm{m},U_>}\delta_{\mathrm{m},U_<}\right\rangle}{\delta_{0,>}\delta_{0,<}} + 1\right)\frac{1}{\sigma_>\sigma_<}, \tag{28}$$

and in order to calculate the difference of two independent random variables $\delta_{\mathrm{m},U} = \delta_{\mathrm{m},U_>} - \delta_{\mathrm{m},U_<}$ we can use the convolution theorem (Arfken & Weber 2008) to get

$$p\left(\delta_{\mathrm{m},U}\right) = \int_{-\infty}^{\infty} \mathrm{d}\delta_{\mathrm{m},U_>}\, p\left(\delta_{\mathrm{m},U_>}, \delta_{\mathrm{m},U_>} - \delta_{\mathrm{m},U}\right). \tag{29}$$

3.2. $(II) : \langle\kappa_{<\vartheta}|\delta_{m,U}\rangle$

In order to calculate the expectation value of the mean convergence inside an angular radius ϑ, $\kappa_{<\vartheta}$, given the matter density contrast $\delta_{\mathrm{m},U}$, we assume that both follow a joint log-normal distribution (see e.g. the discussion in Appendix B of G18). In this case, the expectation value can be written as

$$\frac{\left\langle\kappa_{<\vartheta}|\delta_{\mathrm{m},U}\right\rangle}{\kappa_0} = \exp\left(\frac{C\,\left[2\ln\left(\delta_{\mathrm{m},U}/\delta_0 + 1\right) + V - C\right]}{2V}\right) - 1, \tag{30}$$

where δ_0 is determined with Eq. (25) and the three variables C, V, and κ_0 can be calculated from the moments $\left\langle\delta^2_{\mathrm{m},U}\right\rangle$, $\left\langle\kappa_{<\vartheta}\,\delta_{\mathrm{m},U}\right\rangle$, and $\left\langle\kappa_{<\vartheta}\,\delta^2_{\mathrm{m},U}\right\rangle$, which follow from the derivation in Appendix A (see Eq. (A.29)):

$$V = \ln\left(1 + \frac{\left\langle\delta^2_{\mathrm{m},U}\right\rangle}{\delta_0^2}\right), \tag{31}$$

$$C = \ln\left(1 + \frac{\left\langle\kappa_{<\vartheta}\,\delta_{\mathrm{m},U}\right\rangle}{\delta_0\kappa_0}\right), \tag{32}$$

$$\kappa_0 = \frac{\left\langle\kappa_{<\vartheta}\,\delta_{\mathrm{m},U}\right\rangle^2 \mathrm{e}^V}{\left\langle\kappa_{<\vartheta}\,\delta^2_{\mathrm{m},U}\right\rangle - 2\left\langle\kappa_{<\vartheta}\,\delta_{\mathrm{m},U}\right\rangle\left\langle\delta^2_{\mathrm{m},U}\right\rangle/\delta_0}. \tag{33}$$

We note that the assumption that $\delta_{\mathrm{m},U}$ is log-normal distributed is not well justified for filters with negative weights as we mentioned in the previous section. A possible improvement could be done for instance by assuming again that $\delta_{\mathrm{m},U}$ is made up of two log-normal random variables, and we would need to calculate conditional moments like $\langle\kappa_{<\vartheta}|\delta_{\mathrm{m},U_>} - \delta_{\mathrm{m},U_<}\rangle$. This would significantly increase the amount of joint moments needed in our calculation and would render fast modelling unfeasible. However, an improved modelling is also unnecessary at present, given the statistical uncertainties we expect for Stage III weak lensing surveys such as KiDS-1000. We demonstrate this empirically in Sect. 5 by comparison to N-body simulated data, but we also want to give a brief theoretical motivation. The average value of $\kappa_{<\vartheta}$, given that $\delta_{\mathrm{m},U}$ lies within the range $[\delta_{\min}, \delta_{\max}]$, is given by

$$\left\langle\kappa_{<\vartheta}|\delta_{\mathrm{m},U} \in [\delta_{\min}, \delta_{\max}]\right\rangle = \frac{\int_{\delta_{\min}}^{\delta_{\max}} \mathrm{d}\delta_{\mathrm{m},U}\; p\left(\delta_{\mathrm{m},U}\right)\left\langle\kappa_{<\vartheta}|\delta_{\mathrm{m},U}\right\rangle}{\int_{\delta_{\min}}^{\delta_{\max}} \mathrm{d}\delta_{\mathrm{m},U}\; p\left(\delta_{\mathrm{m},U}\right)}. \tag{34}$$

If $\kappa_{<\vartheta}$ and $\delta_{\mathrm{m},U}$ were joint Gaussian random variables, then $p\left(\delta_{\mathrm{m},U}\right)$ would be a Gaussian PDF and we would have $\left\langle\kappa_{<\vartheta}|\delta_{\mathrm{m},U}\right\rangle = \delta_{\mathrm{m},U}\;\left\langle\delta_{\mathrm{m},U}\kappa_{<\vartheta}\right\rangle / \left\langle\delta^2_{\mathrm{m},U}\right\rangle$. We now argue that the leading-order correction to this Gaussian approximation consists of replacing $p\left(\delta_{\mathrm{m},U}\right)$ by our full non-Gaussian model, without changing $\left\langle\kappa_{<\vartheta}|\delta_{\mathrm{m},U}\right\rangle$, since this would be exactly correct in the limit of strong correlation between the two variables. Our log-normal approximation to $\left\langle\kappa_{<\vartheta}|\delta_{\mathrm{m},U}\right\rangle$ is then already a next-to-leading-order correction and a bi-variate log-normal approximation for $\left\langle\kappa_{<\vartheta}|\delta_{\mathrm{m},U}\right\rangle$ would be of even higher order. While this reasoning is admittedly only heuristic, it is proven correct by the accuracy of our model predictions for the lensing signals in Sect. 5.

3.3. $(III) : p\left(N_{\mathrm{ap}}|\delta_{m,U}\right)$

The third basic ingredient is the PDF of N_{ap} given the projected matter density contrast smoothed with the filter U. Assuming a Poisson distribution for N_{ap}, which is the most straightforward ansatz, is unfortunately not possible because negative values are expected with a compensated filter (i.e. in some of the $U_<$ contributions). We use instead a completely new approach compared to

F18, and derive an expression for $p\left(N_{\mathrm{ap}}|\delta_{\mathrm{m},U}\right)$ by use of the characteristic function (Papoulis & Pillai 1991, hereafter CF), which is an alternative representation of a probability distribution, similar to the moment generating functions, but based on the Fourier transform of the PDF. Of interest to us, the n th derivative of the CFs can be used to calculate the n th moment of the PDF. The CF corresponding to $p\left(N_{\mathrm{ap}}|\delta_{\mathrm{m},U}\right)$ is defined as

$$\Psi(t) = \left\langle \mathrm{e}^{\mathrm{i}tN_{\mathrm{ap}}} \right\rangle_{\delta_{\mathrm{m},U}} = \int_{\mathbb{R}} \mathrm{d}N_{\mathrm{ap}}\, p\left(N_{\mathrm{ap}}|\delta_{\mathrm{m},U}\right) \mathrm{e}^{\mathrm{i}tN_{\mathrm{ap}}}, \tag{35}$$

where in our particular case, we derive in Appendix A.4 a closed expression as

$$\Psi(t) = \exp\left(2\pi n_0 \int_0^\infty \mathrm{d}\vartheta\; \vartheta\; \left(1 + b\,\langle w_\vartheta|\delta_{\mathrm{m},U}\rangle\right) \left[\mathrm{e}^{\mathrm{i}tU(\vartheta)} - 1\right]\right) \tag{36}$$

with n_0 being the mean number density of foreground galaxies on the sky. The assumption of linear galaxy bias enters here by the term $b\,\langle w_\vartheta|\delta_{\mathrm{m},U}\rangle$, with

$$w_\vartheta = \frac{1}{2\pi}\int_0^{2\pi} \mathrm{d}\phi\; \delta_{\mathrm{m,2D}}(\vartheta,\phi). \tag{37}$$

Hence, $n_0\left(1 + b\,\langle w_\vartheta|\delta_{\mathrm{m},U}\rangle\right)$ is the effective number density at ϑ given $\delta_{\mathrm{m},U}$. The conditional expectation value $\langle w_\vartheta|\delta_{\mathrm{m},U}\rangle$ is given in analogy to Eq. (30), but replacing $\left\langle \kappa_{<\vartheta}\,\delta^k_{\mathrm{m},U}\right\rangle \to \left\langle w_{<\vartheta}\,\delta^k_{\mathrm{m},U}\right\rangle$ in Eqs. (31)–(33) for $k = 1, 2$ and using that

$$\langle w_\vartheta|\delta_{\mathrm{m},U}\rangle = \langle w_{<\vartheta}|\delta_{\mathrm{m},U}\rangle + \frac{\vartheta}{2}\frac{\mathrm{d}}{\mathrm{d}\vartheta}\langle w_{<\vartheta}|\delta_{\mathrm{m},U}\rangle, \tag{38}$$

where the joint moments $\left\langle w_{<\vartheta}\,\delta^k_{\mathrm{m},U}\right\rangle$ are also derived in Eq. (A.30). Next, we re-express Eq. (36) as the product of two terms,

$$\Psi(t) = \exp[p(t)]\,\exp[\mathrm{i}q(t)], \tag{39}$$

where

$$p(t) = 2\pi n_0 \int_0^{R_{\max}} \mathrm{d}\vartheta\; \vartheta\; \left(1 + b\,\langle w_\vartheta|\delta_{\mathrm{m},U}\rangle\right)\left(\cos[tU(\vartheta)] - 1\right), \tag{40}$$

$$q(t) = 2\pi n_0 \int_0^{R_{\max}} \mathrm{d}\vartheta\; \vartheta\; \left(1 + b\,\langle w_\vartheta|\delta_{\mathrm{m},U}\rangle\right)\sin\left[tU(\vartheta)\right], \tag{41}$$

and $R_{\max}$ is the angular radius beyond which U vanishes. We note that G18 and F18 found super-Poisson shot-noise in their work. They interpret these deviations from Poisson noise as having a number $\neq 1$ of galaxies per Poisson halo. This would suggest that we could incorporate non-Poissonian behaviour by replacing n_0 with an effective density of Poisson halos and making this a free parameter of our model. However, more recent investigations (e.g. Friedrich et al., in prep.) cast doubt on the simplified interpretation of F18 and G18. A proper investigation of the problem of non-Poissonian shot-noise is beyond the scope of this work, and we will address it in future investigations.

Finally, the probability density function $p\left(N_{\mathrm{ap}}|\delta_{\mathrm{m},U}\right)$ follows from the inverse Fourier transform of the CF

$$\begin{aligned} p\left(N_{\mathrm{ap}}|\delta_{\mathrm{m},U}\right) &= \frac{1}{2\pi}\int_{\mathbb{R}} \mathrm{d}t\,\exp(-\mathrm{i}tN_{\mathrm{ap}})\Psi(t) \\ &= \frac{1}{2\pi}\int_{\mathbb{R}} \mathrm{d}t\,\cos\left(q(t) - tN_{\mathrm{ap}}\right)\exp[p(t)], \end{aligned} \tag{42}$$

where the second step follows from the fact that the imaginary part cancels out.

In Appendix A.4 we discuss a similar approach, where we assume that $p\left(N_{\mathrm{ap}}|\delta_{\mathrm{m},U}\right)$ is log-normal distributed. In that case, to specify the PDF, only the first three moments are needed, which follow from derivatives of the CF. As shown in Appendix A.4 both methods yield almost identical results, and since the log-normal approach is significantly faster, we use it hereafter, unless otherwise stated.

To summarise, the major changes compared to the F18 model are the following:

1. To determine $p\left(\delta_{\mathrm{m},U}\right)$ we
   - updated the calculation of the variance $\left\langle \delta^2_{\mathrm{m},U}\right\rangle$ and of the skewness $\left\langle \delta^3_{\mathrm{m},U}\right\rangle$ in Appendix A to general filter functions;
   - combine in Eqs. (26)–(29) two log-normal random variables for the positive and negative parts for compensated filters to obtain the final expression for any filter shape.
2. To determine $p\left(N_{\mathrm{ap}}|\delta_{\mathrm{m},U}\right)$ we
   - calculate the characteristic function of galaxy shot-noise around a given matter density profile via Eq. (35);
   - use log-normal approximation or inverse Fourier transform Eq. (42) to obtain the PDF of shot-noise from its characteristic function.
3. To determine $\langle \kappa_{<\vartheta}|\delta_{\mathrm{m},U}\rangle$ we
   - updated the calculations of $\langle \kappa_{<\vartheta}\,\delta_{\mathrm{m},U}\rangle$ and $\left\langle \kappa_{<\vartheta}\,\delta^2_{\mathrm{m},U}\right\rangle$ to general filter functions (see Appendix A).

4. Simulation data

Before using our revised model in data analyses, it is mandatory to quantify its precision and range of validity. We use for this validation exercise three simulations suites:

- the full-sky gravitational lensing simulations described in Takahashi et al. (2017, hereafter T17), with which we carry out a detailed investigation of the model in a simple survey configuration;
- the cosmo-SLICS simulations, described in Harnois-Déraps et al. (2019), with which we validate our model on a independent simulation suite;
- the SLICS simulations, described in Harnois-Déraps et al. (2018), with which we construct a KiDS-1000 like covariance matrix.

4.1. T17 simulations

The T17 simulations are constructed from a series of nested cubic boxes with side lengths of $L, 2L, 3L, \ldots$ placed around a fixed vertex representing the observer's position, with $L = 450\,\mathrm{Mpc}\,h^{-1}$. Each box is replicated eight times and placed around the observer using periodic boundary conditions. The number of particles per box is fixed to 2048^3, which results in higher mass and spatial resolutions at lower redshifts. Within each box three spherical lens shells are constructed, each with a width of $150\,\mathrm{Mpc}\,h^{-1}$, which are then used by the public code GRayTrix[2] to trace the light-ray trajectories from the

---

[2] http://th.nao.ac.jp/MEMBER/hamanatk/GRayTrix/

observer to the last scattering surface[3]. With the N-body code GADGET2 (Springel et al. 2001) the gravitational evolution of dark matter particles without baryonic processes are followed from the initial conditions, which in turn are determined by use of second-order Lagrangian perturbation theory. The initial linear power spectrum followed from the Code for Anisotropies in the Microwave Background (CAMB; Lewis et al. 2000) with $\Omega_\mathrm{m} = 1 - \Omega_\Lambda = 0.279$, $\Omega_\mathrm{b} = 0.046$, $h = 0.7$, $\sigma_8 = 0.82$, and $n_\mathrm{s} = 0.97$. The matter power spectrum agrees with theoretical predictions of the revised Halofit (Takahashi et al. 2012) within 5%(10%) for $k < 5(6)\,h\,\mathrm{Mpc}^{-1}$ at $z < 1$. In order to account for the finite shell thickness and angular resolution, T17 provide correction formulae, which we repeat in Appendix B. Although various resolution options are available, for our purpose the realisations with a resolution of NSIDE = 4096 are sufficient.

We use the publicly available matter density contrast maps to create a realistic lens galaxy catalogue that mimics the second and third redshift bins of the luminous red galaxies sample constructed from the KiDS-1000 data (Vakili et al. 2019), as shown by the solid lines in Fig. 1. The reason to mock the LRG sample is that the galaxy bias for this kind of galaxies can be roughly described with a constant linear bias, which is needed for the analytical model. We excluded the lowest-redshift lens bin, first because of its low galaxy number density ($n_0 = 0.012\,\mathrm{gal\,arcmin}^{-2}$) in which the shot-noise level is significant, and second because the density field is more nonlinear, and hence we expect the log-normal approximation to break down. Since there is a significant overlap between the KiDS-1000 sources and the lenses in the fourth LRG redshift bin, we reject it as well. To create our lens galaxy samples we first project the T17 3D density maps $\delta_\mathrm{m,3D}$ following the $n(z)$ shown as the step functions in Fig. 1 to get two $\delta_\mathrm{m,2D}$ maps. For both maps we then distribute galaxies following a Poisson distribution with parameter $\lambda = n\,(1 + b\,\delta_\mathrm{m,2D})$, where b is a constant linear galaxy bias and n is chosen such that the galaxy number density is $n_0 = 0.028\,\mathrm{gal\,arcmin}^{-2}$ for the second bin (hereafter the low-redshift bin $z_\mathrm{l}^\mathrm{low}$) and $n_0 = 0.046\,\mathrm{gal\,arcmin}^{-2}$ for the third lens bin (hereafter the high-redshift bin $z_\mathrm{l}^\mathrm{high}$). Since our method requires a constant linear galaxy bias, we specify a bias of 1.72 for lens bin two and 1.74 for lens bin three, similar to those reported in Vakili et al. (2019). F18 found this linear bias assumption to be accurate enough for year 1 data of the Dark Energy Survey, which is similar in constraining power to our target KiDS data (but we note that an investigation of higher-order biasing is underway in Friedrich et al., in prep.).

In our validation test, we use a shear grid at a single source plane located at $z = 0.8664$, indicated by the black dashed line in Fig. 1. F18 showed that the model works for realistic redshift distributions, and this choice simplifies the generation of our source catalogues. Furthermore, in order to determine a realistic covariance matrix, we transform the shear field into an observed ellipticity field by adding shape noise to the shear grid as

$$\epsilon^\mathrm{obs} = \frac{\epsilon^\mathrm{s} + g}{1 + \epsilon^\mathrm{s} g^*}, \tag{43}$$

where ϵ^obs, ϵ^s, and γ are complex numbers, and the asterisk ($*$) indicates complex conjugation. The source ellipticities ϵ^s per pixel are generated by drawing random numbers from a Gaussian distribution with width

$$\sigma_\mathrm{pix} = \frac{\sigma_\epsilon}{\sqrt{n_\mathrm{gal} A_\mathrm{pix}}} \approx 0.29, \tag{44}$$

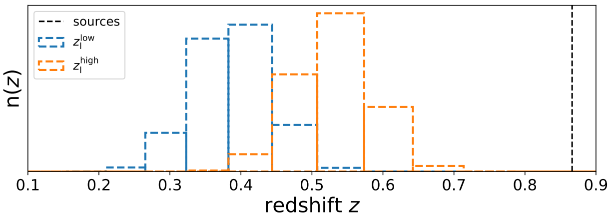

Fig. 1. Lens galaxy redshift distribution constructed from the T17 simulation given the true $n(z)$ of the second $z_\mathrm{l}^\mathrm{low}$ and third $z_\mathrm{l}^\mathrm{high}$ LRG bin (Vakili et al. 2019). The black dashed line shows the redshift of the source galaxies.

where A_pix is the pixel area of the shear grid, and the effective number density n_gal and σ_ϵ are chosen such that they are consistent with the KiDS data. While this transformation is valid in terms of the reduced shear $g = \gamma/(1 - \kappa)$, we use throughout this paper the approximation $\gamma \approx g$, as the typical values for the convergence are small, $|\kappa| \ll 1$. We neglect the intrinsic alignment of galaxies in this work.

4.2. Extracting the model components from the T17 simulations

In order to validate the different components of our model, we need to extract $p\,(\delta_{\mathrm{m},U})$, $p\left(N_\mathrm{ap}\right)$, and $\langle\gamma_\mathrm{t}|Q\rangle$ from the simulation. The first two follow directly by smoothing the maps of the projected density contrast and the lens galaxy with the corresponding filters. This smoothing can be performed in two different ways. The first is to use the HEALPY function QUERY_DISC, which finds all pixel centres that are located within a given radius, whereas the second approach uses the HEALPY function SMOOTHING, with a given beam window function created by the function BEAM2BL. The two approaches result in PDFs that differ slightly, since the QUERY_DISC does not reproduce an exact top-hat, while the SMOOTHING approach is only over a finite ℓ-range. Nevertheless, we found that both approaches are consistent for NSIDE = 4096 well within the uncertainty we estimate from 48 sub-patches (see discussion below), and hence we use the second approach which is significantly faster.

The tangential shear information $\langle\gamma_\mathrm{t}|Q\rangle$ is measured for each quantile Q by the software TREECORR (Jarvis et al. 2004) in 15 log-spaced bins with angular separation $\Theta/20 < \vartheta < \Theta$, where Θ is the size of the filter being used. For the top-hat filter we measured the shear profiles from $6' < \vartheta < 120'$, corresponding to a filter with a size of $120'$. We note here that for all measured shear profiles the shear around random points is always subtracted, which ensures that the shear averaged over all quantiles for one realisation vanishes by definition.

In order to have an uncertainty for all three model quantities, we divide the full-sky map into 48 sub-patches, such that each patch has a size of approximately $859.4\,\mathrm{deg}^2$. For $p\,(\delta_{\mathrm{m},U})$ and $p\left(N_\mathrm{ap}\right)$ we determined for each sub-patch one distribution, such that we were able to calculate a standard deviation from 48 values for each bin in the PDF. For the covariance matrix we use 10 out of the 108 realisations and divide each full-sky map in 48 sub-patches, which then results in a covariance matrix measured from 480 fields. Furthermore, both for the covariance and for the error bars in the plotted shear profiles we use Eq. (43) to create noisy shear profiles for each sub-patch, which are then rescaled to the effective KiDS-1000 area (see Giblin et al. 2021).

---

[3] These maps are freely available for download at `http://cosmo.phys.hirosaki-u.ac.jp/takahasi/allsky_raytracing/`

4.3. Cosmo-SLICS

We use the cosmo-SLICS simulations described in Harnois-Déraps et al. (2019) to determine the validity regime of our revised model for different cosmologies. These are a suite of weak lensing simulations sampling 26 points (listed in Table B.1) in a broad cold dark matter (CDM) parameter space, distributed in a Latin hypercube to minimise interpolation errors. Specifically, the matter density Ω_{m}, the dimensionless Hubble parameter h, the normalisation of the matter power spectrum σ_8, and the time-independent equation-of-state parameter of dark energy w_0 are varied over a range that is large enough to complement the analysis of current weak lensing data (see e.g. Harnois-Déraps et al. 2021). Each simulation follows 1536^3 particles inside a cube of co-moving side length $L_{\mathrm{box}} = 505\,h^{-1}\,\mathrm{Mpc}$ and $n_{\mathrm{c}} = 3072$ grid cells on the side, starting with initial conditions produced with the Zel'dovich approximation. Moreover, the cosmo-SLICS evolve a pair of simulations at each node, designed to suppress the sampling variance (see Harnois-Déraps et al. 2019, for more details). Each cosmological model is ray-traced multiple times to produce 50 pseudo-independent light cones of size $100\,\mathrm{deg}^2$.

For each realisation, we create KiDS-1000-like sources and KiDS-LRG-like lens catalogues, following the pipeline described in Harnois-Déraps et al. (2018); notably, we reproduce exactly the source galaxy number density and $n(z)$ that is used in Asgari et al. (2021), who report a total number density $n_{\mathrm{gal}} = 6.93\,\mathrm{arcmin}^{-2}$ and a redshift distribution estimated from self-organising maps (see Wright et al. 2020). These mock galaxies are then placed at random angular coordinates on $100\,\mathrm{deg}^2$ light cones. In contrast to the T17 mocks, we test our model with two source redshift bins, corresponding to the KiDS-1000 fourth and fifth tomographic bins (hereafter $z_{\mathrm{s}}^{\mathrm{low}}$ and $z_{\mathrm{s}}^{\mathrm{high}}$). The source galaxies are assigned a shear signal γ from a series of lensing maps, following the linear interpolation algorithm described in Sect. 2 in Harnois-Déraps et al. (2018). For our lens sample we opted to include the second and third tomographic bin of the LRG galaxies described in Vakili et al. (2019) ($z_{\mathrm{l}}^{\mathrm{low}}$ and $z_{\mathrm{l}}^{\mathrm{high}}$). Compared to the T17 values, the $n(z)$ of the cosmo-SLICS LRG mocks have a coarser redshift resolution of the simulations. Moreover, the $n(z)$ vary slightly for different underlying cosmologies, due to variations in the relation between co-moving distance and redshift. Following Vakili et al. (2019), we generate our LRG catalogues assuming a constant linear galaxy bias of 1.72 and 1.74, with a galaxy number density of $n_0 = 0.028\,\mathrm{gal\,arcmin}^{-2}$ and $n_0 = 0.046\,\mathrm{gal\,arcmin}^{-2}$.

4.4. SLICS

In total the SLICS[4] are a set of over 800 fully independent realisations similar to the fiducial ΛCDM cosmo-SLICS model. The underlying cosmological parameters for each run are the same, fixed to $\Omega_{\mathrm{m}} = 0.2905$, $\Omega_{\Lambda} = 0.7095$, $\Omega_{\mathrm{b}} = 0.0473$, $h = 0.6898$, $\sigma_8 = 0.826$ and $n_{\mathrm{s}} = 0.969$ (see Hinshaw et al. 2013). For Fourier modes $k < 2.0\,h\,\mathrm{Mpc}^{-1}$, the SLICS and cosmo-SLICS three-dimensional dark matter power spectrum $P(k)$ agrees within 2% with the predictions from the Extended Cosmic Emulator (see Heitmann et al. 2014), followed by a progressive deviation for higher k-modes (Harnois-Déraps et al. 2018). We use the SLICS to estimate a reliable covariance matrix, which, combined with the cosmo-SLICS, allows us to test our model for a simulation that is independent of T17. Similar to the T17 simulations, the signal of the SLICS is combined with the randomly oriented intrinsic shapes ϵ^{s} to create ellipticities, whereas ϵ^{s} is drawn from a Gaussian distribution with width σ_ϵ directly since the shear information are given here per galaxy. We added an additional layer of realism and used a redshift-dependent shape noise that better reproduces the data properties. Specifically, we used $\sigma_\epsilon = 0.25$ and 0.27 for the source bins, as reported in Giblin et al. (2021).

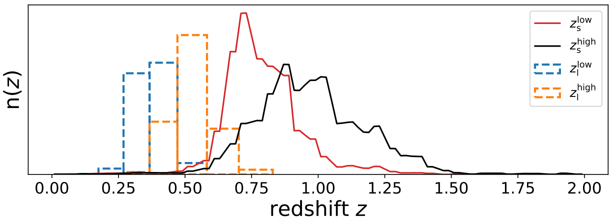

Fig. 2. Redshift distributions of the second and third LRG (lens) bins and the last two KiDS-1000 (source) bins of the SLICS simulations. The $n(z)$ are scaled such that a comparison is possible.

4.5. Extracting the SLICS and cosmo-SLICS data vector

The extraction of the data vector for the SLICS and cosmo-SLICS analyses is similar to the T17 case, where shape noise was not included for the cosmo-SLICS data vector to better capture the cosmological signal. Another slight difference is that the light cones are now square, which accentuates the edge effects when the aperture filter overlaps with the light-cone boundaries. In principle, it is possible to weight the outer rims for each N_{ap} map, so that the whole map can be used. Although this would increase our statistical power, it could also introduce a systematic offset. We opted instead to exclude the outer rim for each realisation resulting in an effective area of $(10-2\Theta)^2\,\mathrm{deg}^2$ with Θ the size of the corresponding filter. This procedure also ensures that roughly the same number of background galaxies are used to calculate the shear profile around each pixel.

5. Testing the revised model

We used the simulations described in Sect. 4 to test our revised model and its accuracy in predicting shear profiles. Following the results of F18 we chose a top-hat filter of 20′ as our starting point and we considered a number of more general filters with a similar angular extent, shown in Fig. 3. Our motivation for studying these filters is as follows: We use a Gaussian filter to test whether the model performs well for non-constant but positive filters; the "adapted" filter is the filter that results from B20; the "Mexican" filter removes the local minimum at $\vartheta \sim 40'$; the "broad Mexican" has a larger width; finally, the "wide Mexican" suppresses the negative tail. In order to lower the amplitude of the negative part while keeping a similar width, we adjusted the upper bound of the wide-Mexican filter to conserve the compensation to 150′, which makes it better suited to large contiguous survey areas.

Before comparing our model to the simulations, we note that we are using here the revised model even for the top-hat filter, for which we could instead use the F18 model directly. Notably, the derivations of $\left\langle\delta^2_{\mathrm{m},U}\right\rangle$ and $\left\langle\delta^3_{\mathrm{m},U}\right\rangle$ are identical in the revised model, and we show in the following plots for the top-hat filters that both models yield almost identical results in predicting the

---

[4] The SLICS are made publicly available on the SLICS portal at `https://slics.roe.ac.uk/`

shear profiles with a top-hat filter. Therefore, from here on, we only show results from the revised model. In the following three sections, we validate the key model ingredients introduced in Sects. 3.1–3.3.

5.1. Validating $p(\delta_{\mathrm{m},U})$

We show in Fig. 4 the PDF of the smoothed two-dimensional density contrast for all six filters, and for the two lens bins. We see by inspecting the different panels that the predictions agree with the simulations for the two lens bins within 1 σ cosmic variance expected for KiDS-1000. We note here that this PDF cannot be measured in real data, and that the real test for the accuracy of our model are the shear signals, with larger uncertainties due to shape noise. Nevertheless, for the top-hat and the Gaussian we have an agreement between model and simulation well within the 1 σ, which indicates that the log-normal approximation for theses filters is good. The other filters show stronger deviations when using a log-normal approximation, but these are weaker when the negative part of the filter approaches zero (wide Mexican) or when the width of the filter increases (broad Mexican), although the negative part of the broad Mexican is stronger than for the Mexican filter. This indicates that probing on larger scales either with a broader or wider filter the log-normal approximation is more accurate. Furthermore, when using the bi-variate log-normal approach discussed in Sect. 3.1, the residuals are even more suppressed, and thus we cannot recognise differences in the match between predicted and measured PDF for all compensated filters. Although the model for the compensated filters is not as good as for the non-negative filters (top-hat and Gaussian), the revised model remains consistent throughout with the T17 simulations.

5.2. Validating $p\left(N_{\mathrm{ap}}\right)$

We show in Fig. 5 how well the model can predict $p\left(N_{\mathrm{ap}}\right)$ given the galaxy distributions described in Sect. 4. As for $p(\delta_{\mathrm{m},U})$, the best matches are observed for the non-negative filters, where the simple log-normal PDF is used. For the compensated filters with the bi-variate log-normal $p(\delta_{\mathrm{m},U})$ we note a slight deviation in the skewness of $p\left(N_{\mathrm{ap}}\right)$. These discrepancies are not seen when placing galaxies at random positions regardless of any underlying matter density field as shown in Fig. A.1, which indicates that they must originate either from $p(\delta_{\mathrm{m},U})$ or from the $\langle w_\vartheta|\delta_{\mathrm{m},U}\rangle$ term (we set the latter to 0 for uniform random fields). It might be that the deviations seen in $p\left(N_{\mathrm{ap}}\right)$ are exclusively caused by the deviations in $p(\delta_{\mathrm{m},U})$, but since they are much smaller, we expect that the assumptions made in computing $\langle w_\vartheta|\delta_{\mathrm{m},U}\rangle$ induce additional inaccuracies. Nevertheless, we show next that these deviations result in shear signals whose residuals are well within the statistical uncertainties of Stage III weak lensing surveys such as KiDS-1000. However the accuracy of the $\langle w_\vartheta|\delta_{\mathrm{m},U}\rangle$ term will likely need to be improved for future surveys like *Euclid*, as discussed in Sect. 3.2.

5.3. Validating $\langle\gamma_t|Q\rangle$

Having quantified the accuracy of the basic ingredients of our model, we are now in a position to compare the predicted and measured shear profiles. This is a major result of our paper, which is shown in Fig. 6. Following G18, we used five quantiles and we measured the shear profiles up to 120′ (or 150′ for the wide Mexican case). For the top-hat, Gaussian, and wide Mexican filters we see no significant deviations between the model and the simulations. For the adapted and the smaller Mexicans the shear profiles show minor discrepancies in some quantiles and at large angular scales, but are always consistent within the KiDS-1000 accuracy. The shapes of the signals are affected by the choice of the filter. We can observe shifts in the peak positions and changes in the slope of the signals especially at small scales. This will allow us in the future to select filters that optimise the signal-to-noise ratio of the measurement, while being clean of systematics related to small-scale inaccuracies. Finally, we show in Fig. B.2 that for the compensated filter the difference in using the proposed bi-variate log-normal approach is slightly more accurate than using a plain log-normal. Although the difference does not change the final results noticeably, and although it introduces some inconsistency in the sense that we use a bi-variate approach for $p(\delta_{\mathrm{m,U}})$ but not for $\langle\kappa_{<\theta}|\delta_{\mathrm{m,U}}\rangle$[5], we decided to stay with the proposed ansatz because it is slightly more accurate, and we plan to use $p\left(N_{\mathrm{ap}}\right)$ in future analysis.

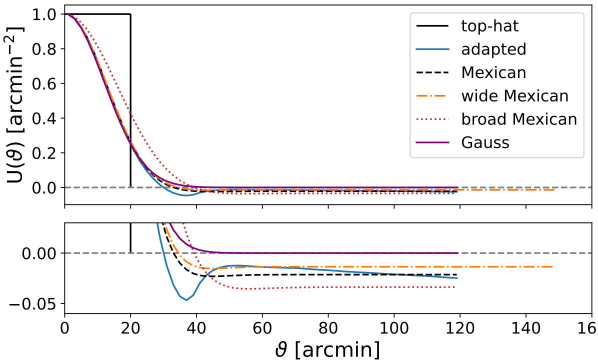

Fig. 3. Different filters U used in this work to verify the new model. For all filters we scaled the first bin value to 1/arcmin^{-2} for comparison. The corresponding Q-filters are shown in Fig. B.1. The wide Mexican filter extends up to 150′.

In order to check whether the discrepancies seen for some compensated filters yield biased results, we performed an MCMC analysis. As our data vector we used the T17 shear profiles shown in Fig. 6, where we made a conservative cut and included only scales above 14′, since as shown in F18 the model is not fully accurate for small angular scales. For the comparison we decided to use the adapted filter and the top-hat filter to have one analysis with and one without these discrepancies. Furthermore, since the mean aperture mass summed over all quantiles vanishes per definition, one of the five shear signals is fully determined by the others, and so we discarded for all cases the middle quantile with the lowest signal. Thus, we ended up with data and model vectors of size 88. As explained previously, we measured our covariance matrix from ten T17 simulations, each divided into 48 sub-patches, for a total of 480 sub-patches. We note here that the galaxy number density can slightly deviate between the different realisations due to the Poisson sampling. Given the amplitude of these small fluctuations, these can be safely neglected. Next we de-biased the inverse covariance

---

[5] Since the impact is already quite small when adjusting $p\left(N_{\mathrm{ap}}\right)$, we are confident that also using a bi-variate approach for $\langle\kappa_{<\theta}|\delta_{\mathrm{m,U}}\rangle$ would result in even smaller improvements as discussed in greater detail at the end of Sect. 3.2.

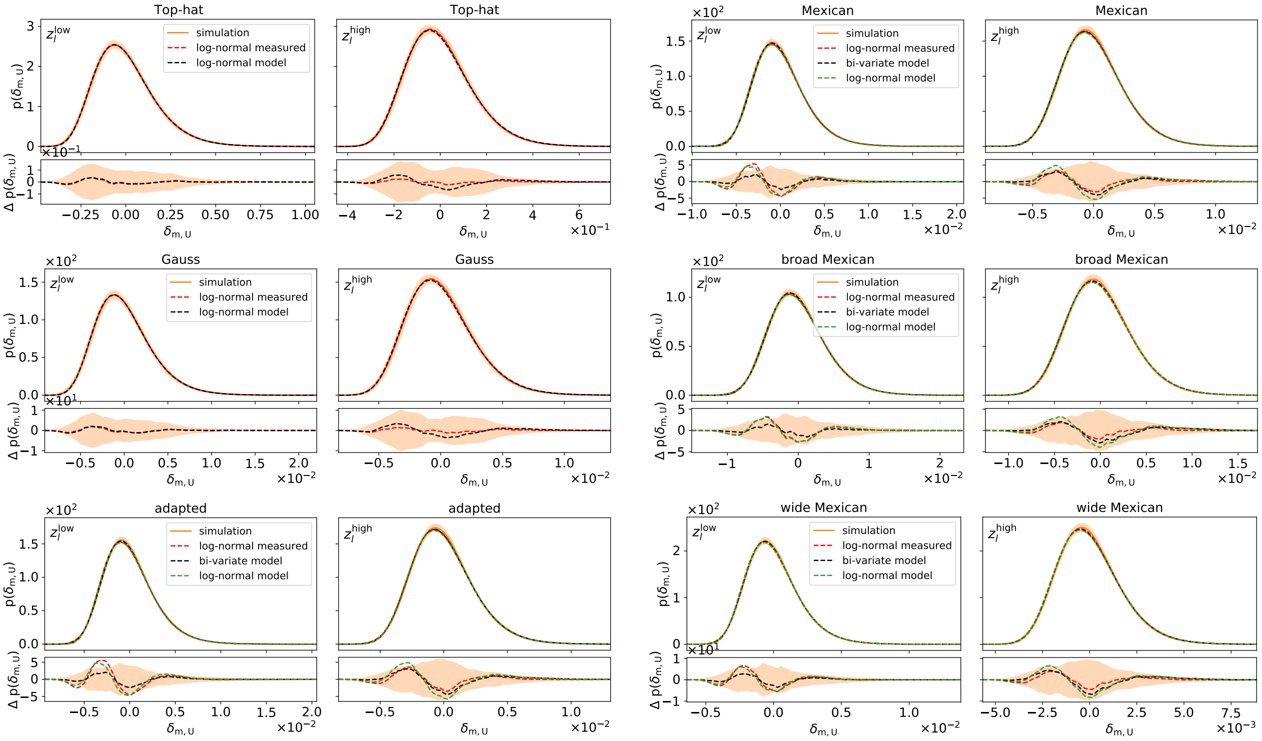

Fig. 4. PDF of $\delta_{\mathrm{m},U}$ smoothed with the filters shown in Fig. 3. The orange shaded region is the standard deviation of 48 sub-patches scaled by a 777.4/859.4, where 777.4 deg^2 is the effective survey area of KiDS-1000 (see Giblin et al. 2021) and 859.4 deg^2 is the area of one sub-patch. The red dashed curve corresponds to a log-normal PDF with the measured moments $\left\langle\delta^2_{\mathrm{m},U}\right\rangle$ and $\left\langle\delta^3_{\mathrm{m},U}\right\rangle$ from the smoothed T17 density maps, and indicates the accuracy using a log-normal PDF. The green and the black dashed lines are both from the model; the green corresponds to the PDF of $\delta_{\mathrm{m},U}$ when using log-normal and the black using the bi-variate approach described in Eq. (26). *Lower panels*: residuals $\Delta p\left(\delta_{\mathrm{m},U}\right)$ of all lines with respect to the simulations.

matrix C^{-1} following Hartlap et al. (2007),

$$C^{-1} = \frac{n-p-2}{n-1}\hat{C}^{-1}, \tag{45}$$

where n is the number of simulations (480) and p the size of the data vector (88). Finally, given our data $\mathbf{d}$ measured from only one noise-free T17 realisation, and our model vector $\mathbf{m}$, we measured the χ^2 statistics as

$$\chi^2 = \left[\mathbf{m}-\mathbf{d}\right]^T C^{-1}\left[\mathbf{m}-\mathbf{d}\right]. \tag{46}$$

Given this set-up we ran an MCMC varying the matter density parameter $\Omega_{\rm m}$ and normalisation of the power spectrum σ_8 for the adapted and the top-hat filters, where we marginalised over the biases of the lens samples. As shown in Fig. 7 the analysis with the adapted filter results in a biased inference for the $\Omega_{\rm m}$-σ_8-plane (although still within 1σ); this is not the case for the top-hat filter. We note here that this bias is due to the systematic offset in the slope of the highest quantile, which in turn is is highly sensitive to $\Omega_{\rm m}$. Since the amplitude of the shear profiles are correct and these are highly correlated with the $S_8 = \sigma_8\sqrt{\Omega_{\rm m}/0.3}$ parameter, the contours shift to smaller σ_8 values in order to compensate for the bigger $\Omega_{\rm m}$ value[6]. In the next section we calibrate the model to investigate whether this systematic bias can be corrected.

5.4. Calibrating the model

In this section we calibrate the remaining small inaccuracies of the analytical model seen in Fig. 6 which result in the systematic bias we had observed in the parameter constraints shown in Fig. 7. For this we decided to divide out for each quantile the residuals between the model, $\gamma_{\rm M_T}$, at the T17 cosmological parameters, $p_{\rm T17}$, and the noiseless shear profiles measured from the T17 simulations, $\gamma_{\rm T17}$, such that the calibrated model at parameters p is defined as

$$\gamma_{\rm M,cal}(p) = \gamma_{\rm M}(p)\frac{\gamma_{\rm T17}}{\gamma_{\rm M}(p_{\rm T17})}. \tag{47}$$

Since we used the $n(z)$ combinations of the fiducial cosmo-SLICS shown in Fig. 2 to validate the calibration, we decided to use the $n(z)$ shown in Fig. 1, and in order to have the source $n(z)$ as close as possible to the one of the cosmo-SLICS we averaged several T17 shear grids at different redshifts for the same realisation weighted by the source $n(z)$ shown in Fig. 2. In Fig. B.4 we show the calibration vectors for the highest and lowest quantile for the top-hat and adapted filter, where it can be seen that the different lens $n(z)$ is more important than the source $n(z)$.

Next, in order to investigate whether the calibration decreases the systematic biases we performed another MCMC analysis on independent simulations, where our data vector is the fiducial cosmology from the cosmo-SLICS shear profiles shown in Fig. 8, with the original model in red and the calibrated one in black. As before we used the adapted filter and

---

[6] The calibration of the residual in the highest quantile alone led to an unbiased result.

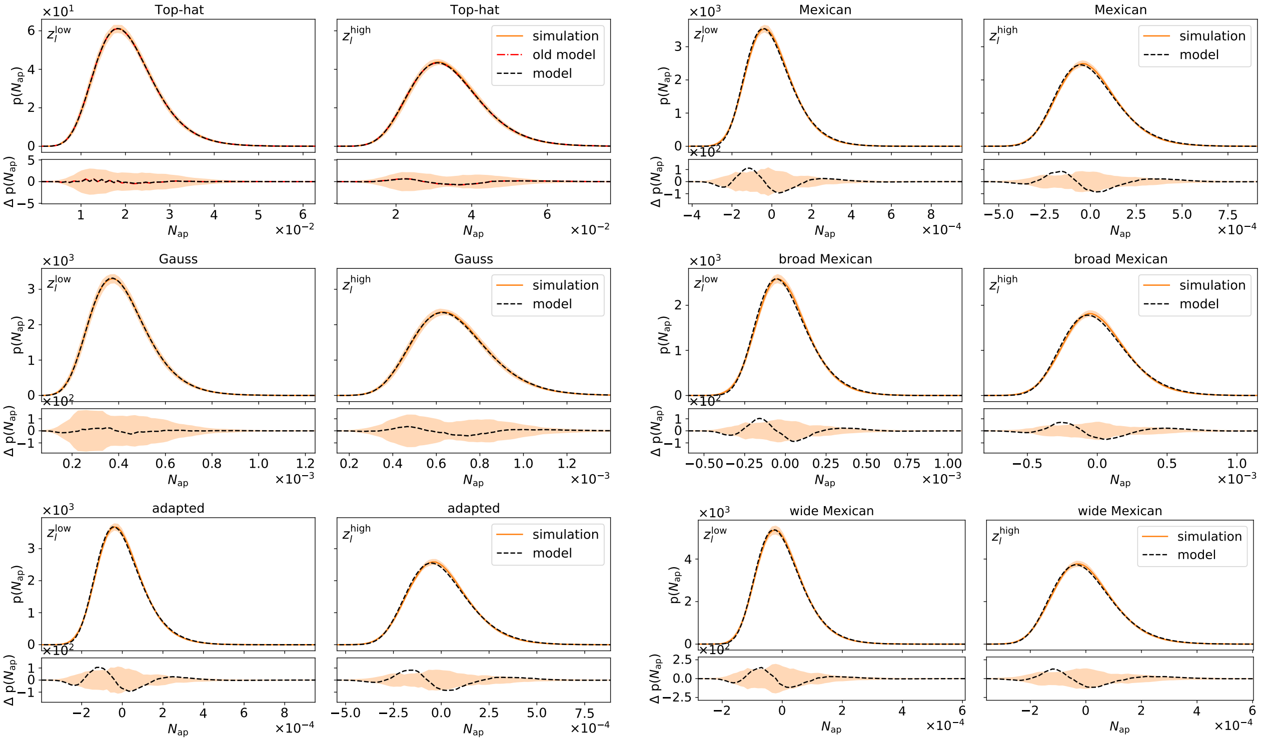

Fig. 5. PDF of $N_{\rm ap}$ calculated with the filters U in Fig. 3. The orange lines are determined with the simulations and the orange shaded region is the standard deviation from 48 sub-patches. The black dashed lines correspond to the results from the new model, and for comparison the red dashed line in the *upper left panel* is from the old model. *Lower panels:* residuals $\Delta p\left(N_{\rm ap}\right)$ of all lines with respect to the simulations.

the top-hat filter. The match between the predicted and measured shear profiles is slightly degraded compared to the T17 simulations, which could be caused by edge effects (contiguous full-sky vs. 100 $\deg^2$ patches), the smaller statistic (41 253 $\deg^2$ vs. 5000 $\deg^2$), or differences in the underlying matter power spectrum $P(k)$ that is used in the model. We use the Takahashi et al. (2012) HALOFIT function throughout this paper, which is calibrated on the same N-body code that is used to create the T17 simulations (Springel et al. 2001, GADGET2), and which is known to have an excess power of 5–8% in the mildly non-linear regime (Heitmann et al. 2014). The cosmo-SLICS, in contrast, are produced from CUBEP^{3}M (Harnois-Déraps et al. 2013), whose $P(k)$ agrees better with the Cosmic Emulator of Heitmann et al. (2014). We tested different choices of power spectra models calculated with the PYCCL package (Chisari et al. 2019), but found differences in the predicted shear profiles that are negligible compared to the expected KiDS-1000 uncertainties.

Discarding again the middle quantile with the lowest signal, using four different redshift combinations (Sect. 4.3) and the signal at all scales because the model is calibrated at all scales, we have data and model vectors of size 160. In this scenario we calculated our covariance matrix from 614 SLICS simulations[7] with shape noise that mimics the KiDS-1000 data. After de-biasing the inverse covariance matrix C^{-1} with Eq. (45) we calculated the χ^2 with Eq. (46). Given this set-up we ran multiple MCMC, where we used the original model and the calibrated model. As shown in Fig. 9 the calibrated model for the adapted filter results compared to the original model in less a biased inference. Interestingly, the results for the top-hat filter seen in Fig. B.3 are slightly more biased than the calibrated model for the adapted filter. Since this offset is still inside 1σ, it is likely to be only a statistical fluke due to the remaining residual between model and cosmo-SLICS simulations. The constraining power between top-hat and adapted filter are different because the smoothing scales of the two filters were not adjusted as in Burger et al. (2020), and are here sensitive to different physical scales. Nevertheless, we show in Table 1 the resulting constrains for both filters, where it is seen that the calibration moves the results, also for the top-hat filter, closer to the truth.

In order to compare our results with those of G18, who derived constraints of $\Omega_{\rm m} = 0.26^{+0.04}_{-0.03}$ and $S_8 = 0.90^{+0.10}_{-0.08}$ with their fiducial analysis, we need to multiply our uncertainty intervals by $\sqrt{777.4/1321}$ to account for the smaller area of KiDS-1000 (777.4 $\deg^2$) compared to the DES Y1 area (1321 $\deg^2$). Furthermore, we exclusively used information about the shear profiles, whereas G18 also used the mean aperture number in each quantile. For this work we were a bit sceptical about using the aperture number here for the compensated filters because we have significant residual discrepancies between model and simulation, which would affect our analysis. The match of the shear profiles in turn is very accurate in our simulations, which shows that they are robust against uncertainties in $P\left(N_{\rm ap}\right)$[8]. For instance, if one monotonically transforms the $N_{\rm ap}$ values, the predicted $P\left(N_{\rm ap}\right)$ changes, but the segmentation into

---

[7] For the remaining ~200 realisations we have no corresponding lens galaxy mocks.

[8] The predicted shear profiles do not change significantly even if the predicted $P\left(N_{\rm ap}\right)$ is substituted with the measured $P\left(N_{\rm ap}\right)$.

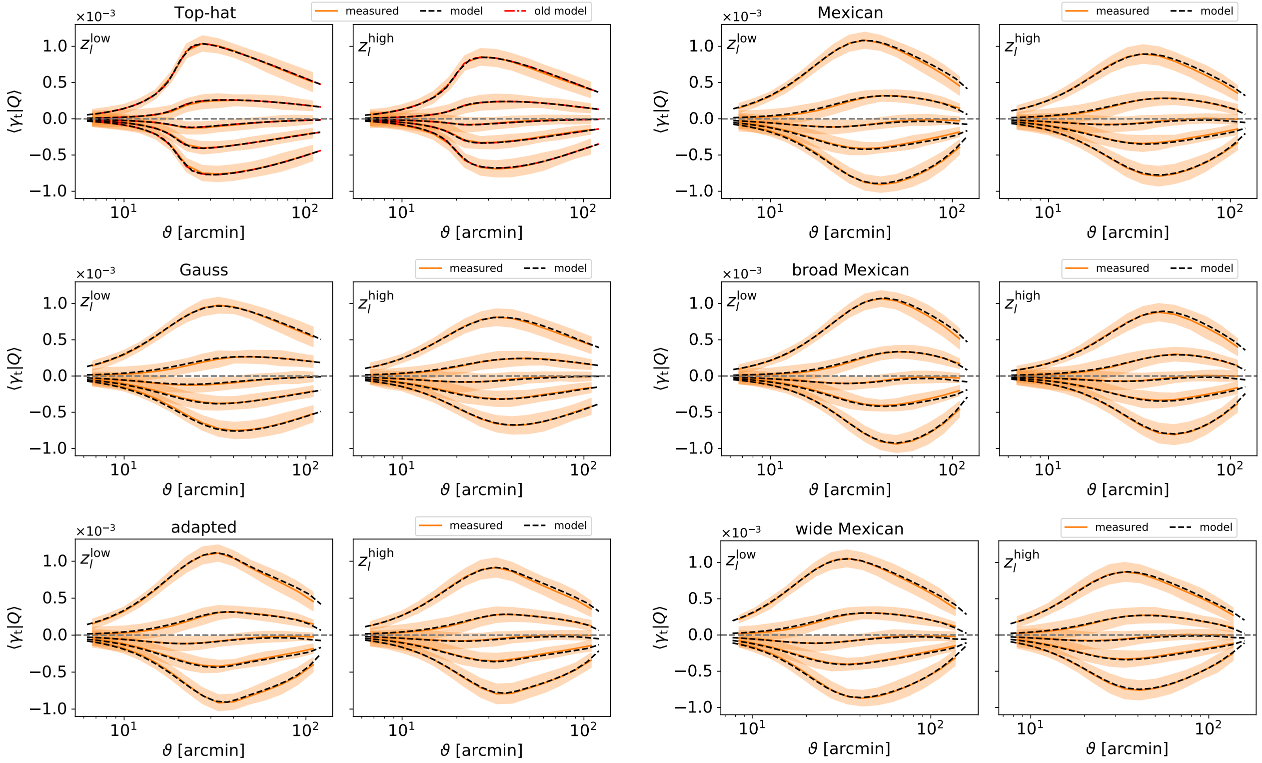

Fig. 6. Predicted shear profiles for the two lens samples (dashed black line) and measured shear profiles (in orange) for the new model with filter U. The orange shaded region is the standard deviation on the mean from 48 sub-patches, scaled to the KiDS-1000 area. The residuals between model and simulations were tested to determine whether they can be erased when the PDF of the aperture number is fixed to the measured value from T17, but the same discrepancies were present.

quantiles is not affected, hence the shear profiles would remain the same. In order to use $P\left(N_{\rm ap}\right)$ in future analysis we need to model shot noise in the galaxy distribution and investigate if the residuals between model and simulations result in systematic biases, but we will keep this for future work. Nevertheless, we see that our constraints from using only information about the shear profiles can be similar to the ones in G18. In addition, due to the calibration method used here, smaller smoothing scales are available than those recommended in F18, where even the top-hat filter has significant deviations. This could allow us to further improve the significance for future DSS analyses or to investigate effects such as baryonic feedback and intrinsic alignments, which are typically relevant on scales $<10\,{\rm Mpc}\,h^{-1}$.

6. Summary and conclusion

In our previous work (Burger et al. 2020) we showed that using compensated filters in the density split statistic (DSS) to quantify over- and underdense regions on the sky have advantages compared to the top-hat filter, both in terms of the overall S/N and of recovering accurately the galaxy bias term. Furthermore, we expect that compensated filters are less influenced by baryonic effect, since they are more confined in Fourier space and therefore are better in smoothing out large ℓ-modes where baryonic effects play an important role. This will be investigated in more detail in a follow-up paper, when we start dealing with real data. Gruen et al. (2016) demonstrated that the DSS is a powerful cosmological tool by constraining cosmological parameters with DSS measurements from the Dark Energy Survey (DES) First

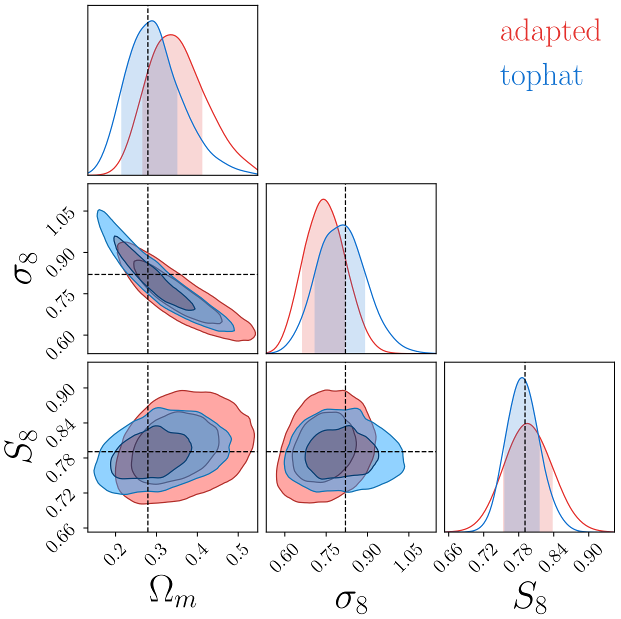

Fig. 7. MCMC results for the top-hat and adapted filter using the model and the T17 simulations as our data vector and a covariance matrix calculated from ten T17 realisations each divided into 48 sub-patches. For the adapted filter a systematic bias for σ_8 and $\Omega_{\rm m}$ is found, although it cancels out for the $S_8 = \sigma_8\sqrt{\Omega_{\rm m}/0.3}$ parameter. The contours here are marginalised over the lens galaxy bias parameters.

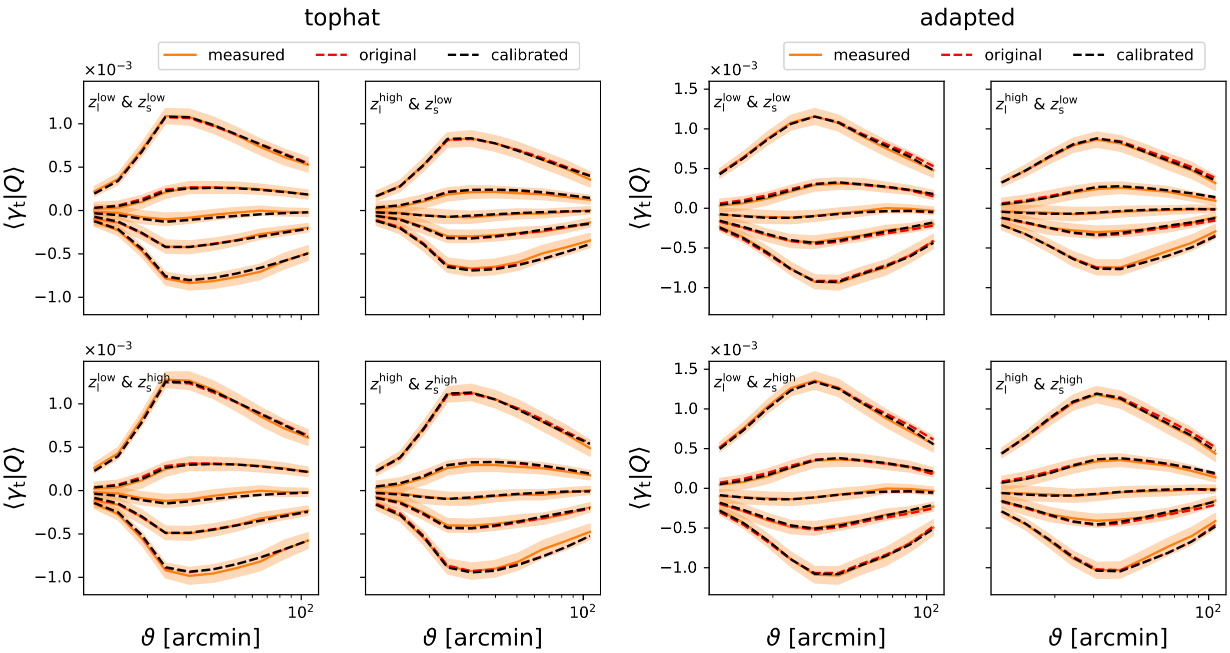

Fig. 8. Shear profiles for the top-hat filter (left) and for the adapted filter (right) for the fiducial cosmology of cosmo-SLICS. The orange lines are the mean shear profiles and the orange shaded region is the expected KiDS-1000 uncertainty. The red dashed line corresponds to the original model and the black to the calibrated model.

Year and Sloan Digital Sky Survey (SDSS) data, using the DSS model derived in Friedrich et al. (2018) which uses a top-hat filter. They found for the matter density parameter $\Omega_{\rm m} = 0.26^{+0.04}_{-0.03}$, a constraint that agrees with and is competitive with the DES analysis of galaxy and shear two-point functions (see Abbott et al. 2018).

Following these works, we modify the model of Friedrich et al. (2018) in such a way that it can predict the shear profiles $\langle\gamma_{\rm t}|Q\rangle$ for a given quantile Q of the aperture number $N_{\rm ap}$ for general filters (Gaussian and also compensated filters). This is achieved by recalculating the three basic ingredients, which are the PDF of the projected matter density contrast smoothed with the filter function, $p\,(\delta_{{\rm m},U})$; the expectation value of the convergence inside a radius ϑ for a fixed smoothed matter density contrast, $\langle\kappa_{<\vartheta}|\delta_{{\rm m},U}\rangle$; and the distribution of $N_{\rm ap}$ for the given filter function U given the smoothed matter density contrast, $p\left(N_{\rm ap}|\delta_{{\rm m},U}\right)$. For $\langle\kappa_{<\vartheta}|\delta_{{\rm m},U}\rangle$ we modified the calculation of the moments for general filters, while we introduced new approaches to calculate $p\left(N_{\rm ap}|\delta_{{\rm m},U}\right)$ and $p\,(\delta_{{\rm m},U})$ for compensated filters. For non-negative filters, $\delta_{{\rm m},U}$ is well described by a log-normal PDF, although we found significant deviations for compensated filters. To solve this issue we used a bi-variate log-normal ansatz, where we assumed that $\delta_{{\rm m},U}$ can be divided into two log-normal random variables with each separately following a log-normal distribution. For the calculation of $p\left(N_{\rm ap}|\delta_{{\rm m},U}\right)$ we derived an expression for the corresponding characteristic function, which can be used either directly to calculate $p\left(N_{\rm ap}|\delta_{{\rm m},U}\right)$ by inverse Fourier transformation or by calculating the first three moments, which then specify a log-normal distribution for $p\left(N_{\rm ap}|\delta_{{\rm m},U}\right)$. The differences between these two approaches are considerably smaller than the statistical uncertainty, and so we used the latter approach because of its smaller computational time.

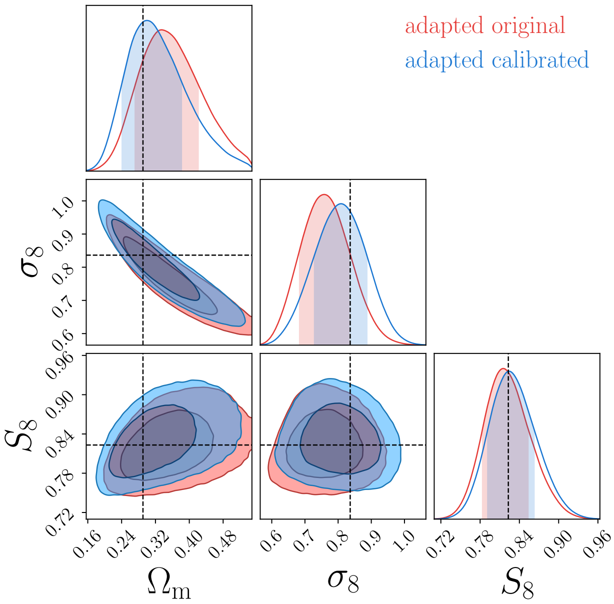

Fig. 9. MCMC results for the adapted filter using the original and calibrated model. The data vector is calculated from the fiducial cosmology of cosmo-SLICS and a covariance matrix from 614 SLICS realisations. It is clearly seen that the calibrated model is less biased than the original one. The contours are marginalised over the lens galaxy bias parameters.

In order to validate the revised model, we compared it to the Takahashi et al. (2017) simulations. For non-negative filters like a top-hat or a Gaussian, no significant difference between the model and simulations for the PDF or the tangential shear profiles were detected. For compensated filters, however, we found

Table 1. Overview of the maximum-posterior cosmologies with the constraining power that we obtain for the original and calibrated model.

	Ω_m	σ_8	S_8
ad. original	$0.332^{+0.089}_{-0.060}$	$0.760^{+0.072}_{-0.077}$	$0.814^{+0.039}_{-0.031}$
th. original	$0.320^{+0.068}_{-0.048}$	$0.774^{+0.069}_{-0.060}$	$0.812^{+0.028}_{-0.022}$
ad. calibrated	$0.298^{+0.084}_{-0.056}$	$0.809^{+0.078}_{-0.080}$	$0.824^{+0.038}_{-0.033}$
th. calibrated	$0.309^{+0.058}_{-0.051}$	$0.794^{+0.067}_{-0.062}$	$0.812^{+0.027}_{-0.021}$

Notes. For all results we marginalise over the biases b of the lenses. The input cosmology of the fiducial cosmo-SLICS is $\Omega_\mathrm{m} = 0.2905$, $\sigma_8 = 0.8364$ and thus $S_8 = \sigma_8\sqrt{\Omega_\mathrm{m}/0.3} = 0.8231$. We fixed the time-independent equation-of-state parameter of dark energy $w_0 = -1.0$ and Hubble parameter $h = 0.6868$ to their true values. We note that the parameter uncertainties increase slightly if we also vary parameters like w_0, h, or the scalar spectral index n_s.

some discrepancies in the predicted PDF of N_ap and shear signals, which results in a biased inference, although still inside 1σ. To correct this biased result, we calibrated the model to match the noiseless Takahashi et al. (2017) and tested the calibrated model with the independent fiducial cosmology of cosmo-SLICS (Harnois-Déraps et al. 2019). With the calibration applied, all systematic biases are removed, so we are confident that we can apply the model to Stage III surveys such as KiDS-1000. Although this calibration is less important for the top-hat and Gaussian filter, it is still an interesting approach because it allows even smaller scales to be used for both the shear profiles and the filter scales. The use of smaller scales, where the original models fail, makes it possible to increase the constraining power or to study baryonic effects that normally play an important role only at small scales.

After passing all these tests, we are confident that the revised model can be readily applied to Stage III lensing data. We note that a number of systematic effects related to weak lensing analyses will require external simulations, notably regarding the inclusion of secondary signal from the intrinsic alignments of galaxies, or from the impact of baryonic feedback on the matter distribution. However, our model is able to capture the uncertainty on the lens and source redshift distribution, the shape calibration bias, or the galaxy bias at a low computational cost, and is therefore ideally suited to perform competitive weak lensing analyses in the future.

Acknowledgements. We thank the anonymous referee for the very constructive and fruitful comments. This paper went through the whole KiDS review process, where we especially want to thank the KiDS-internal referee Benjamin Joachimi for his fruitful comments to improve this work. Further, we would like to thank Mike Jarvis for maintaining TREECORR and Ryuichi Takahashi for making his simulation suite publicly available. PB acknowledges support by the Deutsche Forschungsgemeinschaft, project SCHN342-13. OF gratefully acknowledges support by the Kavli Foundation and the International Newton Trust through a Newton-Kavli-Junior Fellowship and by Churchill College Cambridge through a postdoctoral By-Fellowship. JHD is supported by a STFC Ernest Rutherford Fellowship (project reference ST/S004858/1). Author contributions: all authors contributed to the development and writing of this paper.

References

Abbott, T. M. C., Abdalla, F. B., Alarcon, A., et al. 2018, Phys. Rev. D, 98, 043526

Abbott, T. M. C., Aguena, M., Alarcon, A., et al. 2022, Phys. Rev. D, 105, 023520

Abramowitz, M., & Stegun, I. A. 1972, in Handbook of Mathematical Functions with Formulas, Graphs, and Mathematical Tables, 10th edn. (Washington DC: US Government Printing Office), Applied Mathematics Series, 55

Arfken, G., & Weber, H. 2008, Mathematical Methods for Physicists, 6th edn. (Amsterdam, Heidelberg: Elsevier Academic Press)

Asgari, M., Tröster, T., Heymans, C., et al. 2020, A&A, 634, A127

Asgari, M., Lin, C.-A., Joachimi, B., et al. 2021, A&A, 645, A104

Barthelemy, A., Codis, S., & Bernardeau, F. 2021, MNRAS, 503, 5204

Bergé, J., Amara, A., & Réfrégier, A. 2010, ApJ, 712, 992

Bernardeau, F., & Valageas, P. 2000, A&A, 364, 1

Bernardeau, F., Colombi, S., Gaztañaga, E., & Scoccimarro, R. 2002, Phys. Rep., 367, 1

Boyle, A., Uhlemann, C., Friedrich, O., et al. 2021, MNRAS, 505, 2886

Burger, P., Schneider, P., Demchenko, V., et al. 2020, A&A, 642, A161

Chisari, N. E., Alonso, D., Krause, E., et al. 2019, ApJS, 242, 2

DeRose, J., Wechsler, R. H., Becker, M. R., et al. 2019, ArXiv e-prints [arXiv:`1901.02401`]

Eisenstein, D. J., & Hu, W. 1998, ApJ, 496, 605

Euclid Collaboration (Knabenhans, M., et al.) 2021, MNRAS, 505, 2840

Fan, Z., Shan, H., & Liu, J. 2010, ApJ, 719, 1408

Friedrich, O., Gruen, D., DeRose, J., et al. 2018, Phys. Rev. D, 98, 023508

Fu, L., Kilbinger, M., Erben, T., et al. 2014, MNRAS, 441, 2725

Giblin, B., Heymans, C., Asgari, M., et al. 2021, A&A, 645, A105

Gruen, D., Friedrich, O., Amara, A., et al. 2016, MNRAS, 455, 3367

Gruen, D., Friedrich, O., Krause, E., et al. 2018, Phys. Rev. D, 98, 023507

Halder, A., Friedrich, O., Seitz, S., & Varga, T. N. 2021, MNRAS, 506, 2780

Hamana, T., Shirasaki, M., Miyazaki, S., et al. 2020, PASJ, 72, 16

Harnois-Déraps, J., Pen, U.-L., Iliev, I. T., et al. 2013, MNRAS, 436, 540

Harnois-Déraps, J., Amon, A., Choi, A., et al. 2018, MNRAS, 481, 1337

Harnois-Déraps, J., Giblin, B., & Joachimi, B. 2019, A&A, 631, A160

Harnois-Déraps, J., Martinet, N., Castro, T., et al. 2021, MNRAS, 506, 1623

Hartlap, J., Simon, P., & Schneider, P. 2007, A&A, 464, 399

Heitmann, K., Lawrence, E., Kwan, J., Habib, S., & Higdon, D. 2014, ApJ, 780, 111

Heymans, C., Tröster, T., Asgari, M., et al. 2021, A&A, 646, A140

Hilbert, S., Hartlap, J., & Schneider, P. 2011, A&A, 536, A85

Hinshaw, G., Larson, D., Komatsu, E., et al. 2013, ApJS, 208, 19

Jarvis, M., Bernstein, G., & Jain, B. 2004, MNRAS, 352, 338

Kilbinger, M., & Schneider, P. 2005, A&A, 442, 69

Lewis, A., Challinor, A., & Lasenby, A. 2000, ApJ, 538, 473

Limber, D. N. 1953, ApJ, 117, 134

Lin, C.-A., & Kilbinger, M. 2015, A&A, 576, A24

Mead, A. J., Tröster, T., Heymans, C., Van Waerbeke, L., & McCarthy, I. G. 2020, A&A, 641, A130

Munshi, D., McEwen, J. D., Kitching, T., et al. 2020, J. Cosmol. Astropart. Phys., 2020, 043

Nishimichi, T., Takada, M., Takahashi, R., et al. 2021, ApJ, 884, 29

Papoulis, A., & Pillai, S. U. 1991, Probability, Random Variables, and Stochastic Processes, 3rd edn. (Boston: McGraw-Hill)

Pires, S., Leonard, A., & Starck, J.-L. 2012, MNRAS, 423, 983

Planck Collaboration V. 2020, A&A, 641, A5

Pyne, S., & Joachimi, B. 2021, MNRAS, 503, 2300

Reimberg, P., & Bernardeau, F. 2018, Phys. Rev. D, 97, 023524

Schneider, P. 1996, MNRAS, 283, 837

Schneider, P. 1998, ApJ, 498, 43

Schneider, P., Ehlers, J., & Falco, E. E. 1992, Gravitational Lenses, Astronomy and Astrophysics Library (Berlin and Heidelberg: Springer)

Shan, H., Liu, X., Hildebrandt, H., et al. 2018, MNRAS, 474, 1116

Springel, V., Yoshida, N., & White, S. D. M. 2001, New Astron, 6, 79

Takahashi, R., Sato, M., Nishimichi, T., Taruya, A., & Oguri, M. 2012, ApJ, 761, 152

Takahashi, R., Hamana, T., Shirasaki, M., et al. 2017, ApJ, 850, 24

Vakili, M., Bilicki, M., Hoekstra, H., et al. 2019, MNRAS, 487, 3715

Wright, A. H., Hildebrandt, H., van den Busch, J. L., et al. 2020, A&A, 640, L14

Appendix A: Detailed derivations for the new model

In this appendix we show more detailed derivations of the results than in the main text. We start with the calculation of the variances or covariances in the flat-sky approximation, continue with calculations of the third-order moments and finish with the derivation of the PDF of the aperture number given a smoothed density contrast by use of the characteristic function.

A.1. Variance and skewness for general filters at leading order in perturbation theory

Although analytical possible we decided against using the bi-spectrum to calculate third-order moments like the skewness. Instead we use a formalism where we calculate the second- and third-order moments of the smoothed density contrasts within cylinder of physical radius R and physical length L using the flat-sky approximation shown in Appendix B in F18 for a top-hat filter, and apply it to our case with a general filter U. Numerically, this approach is faster since, as we will see below, it is possible to express the third-order moments in terms of second-order moments. Another advantage is that the projection is only along one dimension (radius of the cylinder) compared to the bi-spectrum, where the projection is at least along a 2D grid. Following F18 we start by considering a cylinder of radius R and length L. In Fourier space the top-hat filter for such a cylinder is given by

$$W_{R,L}(\mathbf{k}) = \frac{1}{(2\pi)^3}\,\frac{\sin(Lk_\parallel/2)}{Lk_\parallel/2}\,\frac{2J_1(k_\perp R)}{k_\perp R} \equiv \frac{1}{(2\pi)^3}\,\frac{\sin(Lk_\parallel/2)}{Lk_\parallel/2}\,W_R^{\rm th}(k_\perp), \tag{A.1}$$

where J_1 is the first Bessel function, and $k_\parallel$ and $k_\perp$ are the components of $\mathbf{k}$ parallel and orthogonal to the cylinder, respectively. The variance of the matter contrast within such a cylinder is given at leading order by

$$\left\langle \delta^2_{R,L}\right\rangle(\chi) = D_+^2 \int \mathrm{d}k_\parallel\,\mathrm{d}^2k_\perp\,\frac{\sin^2(Lk_\parallel/2)}{(Lk_\parallel/2)^2}\left[W_R^{\rm th}(k_\perp)\right]^2 P_{\rm lin,0}(k_\perp) \approx \frac{2\pi D_+^2}{L}\int \mathrm{d}k\,k\left[W_R^{\rm th}(k)\right]^2 P_{\rm lin,0}(k), \tag{A.2}$$

where the last expression follows from $L \gg R$, and since the integration depends from now on only on $k_\perp$ we write the orthogonal component as k. The linear matter power spectrum of $P_{\rm lin,0}$ is calculated using Eisenstein & Hu (1998), and D_+ is the growth factor which depends on the conformal time. We note that the factor $1/L$ cancels out when projecting the moments in Eq. (A.28-A.30) using the Limber approximation (Limber 1953). According to this derivation for a top-hat filter we get for a general filter U that

$$W_{U_\chi}(k) = \int_0^{2\pi}\int_0^{\infty} \mathrm{d}r\,\mathrm{d}\vartheta\,U_\chi(r)\,\mathrm{e}^{-\mathrm{i}kr\cos\vartheta} = 2\pi\int_0^\infty \mathrm{d}r\,J_0(kr)\,r\,U_\chi(r), \tag{A.3}$$

where $U_\chi(r) = U(r/\chi) = U(\vartheta)/\chi^2$, with $U(\vartheta)$ being a filter measured in angular coordinates (see Fig. 3). Correspondingly, the variance of the matter density contrast for a general filter U in the flat-sky approximation is

$$\left\langle \delta^2_{U,L}\right\rangle(\chi) = \frac{2\pi D_+^2}{L}\int \mathrm{d}k\;k\;W^2_{U_\chi}(k), P_{\rm lin,0}(k). \tag{A.4}$$

Following lines similar to those of Appendix B.4 of F18, the leading-order contribution to the skewness of matter density contrast for the general filter U can be calculated as

$$\begin{aligned}\left\langle \delta^3_{U,L}\right\rangle(\chi) &= 3\hat{c}\pi^{-1}\int\!\!\int \mathrm{d}q_1\,\mathrm{d}q_2\,q_1\,q_2\,W_{U_\chi}(q_1)\,W_{U_\chi}(q_2)\,P_{\rm lin,0}(q_1)\,P_{\rm lin,0}(q_2)\int \mathrm{d}\phi\;W_{U_\chi}\left(\sqrt{q_1^2+q_2^2+2q_1q_2\cos\phi}\right)F_2(q_1,q_2,\phi)\\ &\equiv 3\hat{c}\pi^{-1}\int\!\!\int \mathrm{d}q_1\,\mathrm{d}q_2\,q_1\,q_2\,W_{U_\chi}(q_1)\,W_{U_\chi}(q_2)\,P_{\rm lin,0}(q_1)\,P_{\rm lin,0}(q_2)\,\Phi_{U_\chi}(q_1,q_2),\end{aligned} \tag{A.5}$$

where $\hat{c} = \frac{4\pi^2 D_+^4}{L^2}$. The function F_2 in a general ΛCDM universe is given by

$$F_2(q_1,q_2,\phi) = \frac{1}{2}\left(2 + \frac{q_1}{q_2}\cos\phi + \frac{q_2}{q_1}\cos\phi\right) + (1+\mu)\,(\cos^2\phi - 1) = 1 + \frac{1}{2}\cos\phi\left(\frac{q_1}{q_2}+\frac{q_2}{q_1}\right) - (1-\mu)\,\sin^2\phi, \tag{A.6}$$

where μ results from perturbation theory and is a function of the growth factor D_+ (see Appendix B.1 in F18 for more details)[9], and ϕ is the angle between the vectors with absolute values q_1 and q_2. Given the definition of W_{U_χ} in Eq. (A.3), Φ_{U_χ} can be written as

$$\Phi_{U_\chi}(q_1,q_2) = 2\pi\int_0^\infty \mathrm{d}r\,r\,U_\chi(r)\int \mathrm{d}\phi\;J_0\left(r\sqrt{q_1^2+q_2^2+2q_1q_2\cos\phi}\right)F_2(q_1,q_2,\phi). \tag{A.7}$$

Next, we use Graf's addition theorem (see e.g. Abramowitz & Stegun 1972), which states that

$$J_0\left(\sqrt{q_1^2+q_2^2+2q_1q_2\cos\phi}\right) = \sum_{m=-\infty}^{\infty}(-1)^m J_m(q_1)\,J_m(q_2)\,\mathrm{e}^{\mathrm{i}m\phi} = J_0(q_1)\,J_0(q_2) + 2\sum_{m=1}^{\infty}(-1)^m J_m(q_1)\,J_m(q_2)\,\cos(m\phi), \tag{A.8}$$

---

[9] For an Einstein-de Sitter universe $\mu = 5/7$.

such that $\Phi_{U_\chi}(q_1, q_2)$ becomes

$$
\begin{aligned}
&2\pi \int_0^\infty r\, U_\chi(r)\mathrm{d}r \int_0^{2\pi} \mathrm{d}\phi \left[J_0(rq_1)\, J_0(rq_2) + 2\sum_{m=1}^{\infty} (-1)^m J_m(rq_1)\, J_m(rq_2)\, \cos(m\phi) \right] \left[1 + \frac{1}{2}\cos(\phi)\left(\frac{q_1}{q_2} + \frac{q_2}{q_1} \right) - (1-\mu)\, \sin^2\phi \right] \\
&= \underbrace{2\pi^2(1+\mu) \int_0^\infty r\, U_\chi(r)\mathrm{d}r\, J_0(rq_1)\, J_0(rq_2)}_{A} \underbrace{- 2\pi^2 \int_0^\infty r\, U_\chi(r)\mathrm{d}r\, J_1(rq_1)\, J_1(rq_2) \left(\frac{q_1}{q_2} + \frac{q_2}{q_1} \right)}_{B} \underbrace{+ 2\pi^2(1-\mu) \int_0^\infty r\, U_\chi(r)\mathrm{d}r\, J_2(rq_1)\, J_2(rq_2)}_{C},
\end{aligned}
\tag{A.9}
$$

where we made use of the orthogonality of the trigonometric functions. Plugging $\Phi_{U_\chi}(q_1, q_2)$ back into Eq. (A.5) and considering each term separately we get

$$
\begin{aligned}
A:\quad & 3\hat{c}\pi^{-1} \int\!\!\int \mathrm{d}q_1\, \mathrm{d}q_2\, q_1\, q_2\, W_{U_\chi}(q_1)\, W_{U_\chi}(q_2)\, P_{\mathrm{lin},0}(q_1)\, P_{\mathrm{lin},0}(q_2)\, 2\pi \int_0^\infty \mathrm{d}r\, rU_\chi(r)\, \pi(1+\mu)\, J_0(rq_1)\, J_0(rq_2) \\
&= 6\pi\hat{c}(1+\mu) \int_0^\infty \mathrm{d}r\, rU_\chi(r) \left[\int \mathrm{d}q\, q\, W_{U_\chi}(q)\, P_{\mathrm{lin},0}(q)\, J_0(rq) \right]^2,
\end{aligned}
\tag{A.10}
$$

and by analogy

$$
\begin{aligned}
C:\quad & 3\hat{c}\pi^{-1} \int\!\!\int \mathrm{d}q_1 \mathrm{d}q_2\, q_1 q_2\, W_{U_\chi}(q_1) W_{U_\chi}(q_2)\, P_{\mathrm{lin},0}(q_1) P_{\mathrm{lin},0}(q_2)\, 2\pi \int_0^\infty \mathrm{d}r\, rU_\chi(r)\, \pi(1-\mu)\, J_2(rq_1) J_2(rq_2) \\
&= 6\pi\hat{c}(1-\mu) \int_0^\infty \mathrm{d}r\, rU_\chi(r) \left[\int \mathrm{d}q\, q\, W_{U_\chi}(q)\, P_{\mathrm{lin},0}(q)\, J_2(rq) \right]^2,
\end{aligned}
\tag{A.11}
$$

and finally

$$
\begin{aligned}
B:\quad & -3\hat{c}\pi^{-1} \int\!\!\int \mathrm{d}q_1\, \mathrm{d}q_2\, q_1\, q_2\, W_{U_\chi}(q_1)\, W_{U_\chi}(q_2)\, P_{\mathrm{lin},0}(q_1)\, P_{\mathrm{lin},0}(q_2)\, 2\pi \int_0^\infty \mathrm{d}r\, rU_\chi(r)\, \pi J_1(rq_1)\, J_1(rq_2) \left[\frac{q_1}{q_2} + \frac{q_2}{q_1} \right] \\
&= -12\pi\hat{c} \int_0^\infty \mathrm{d}r\, rU_\chi(r) \int \mathrm{d}q_1\, q_1^2\, W_{U_\chi}(q_1)\, P_{\mathrm{lin},0}(q_1)\, J_1(rq_1) \int \mathrm{d}q_2\, W_{U_\chi}(q_2)\, P_{\mathrm{lin},0}(q_2)\, J_1(rq_2).
\end{aligned}
\tag{A.12}
$$

The following transformations provide a more compressed expression for $\left\langle \delta^3_{U_\chi,L} \right\rangle(\chi)$, which can then be used to verify our derivation by comparing it with the result from F18 for a top-hat filter. For this, we rewrite the expression of Bessel functions in terms of $W_r^{\mathrm{th}}(q)$ as

$$
J_2(rq) = \frac{1}{rq} J_1(rq) - \frac{1}{q}\frac{\mathrm{d}}{\mathrm{d}r} J_1(rq) = \frac{1}{rq} J_1(rq) - \left[r\frac{\mathrm{d}}{\mathrm{d}r}\frac{J_1(rq)}{rq} + \frac{1}{rq} J_1(rq) \right] = -\frac{1}{2}\frac{\mathrm{d}}{\mathrm{d}\ln(r)} W_r^{\mathrm{th}}(q), \tag{A.13}
$$

$$
J_0(rq) = \frac{1}{rq} J_1(rq) + \frac{1}{q}\frac{\mathrm{d}}{\mathrm{d}r} J_1(rq) = \frac{1}{rq} J_1(rq) + \left[r\frac{\mathrm{d}}{\mathrm{d}r}\frac{J_1(rq)}{rq} + \frac{1}{rq} J_1(rq) \right] = W_r^{\mathrm{th}}(q) + \frac{1}{2}\frac{\mathrm{d}}{\mathrm{d}\ln(r)} W_r^{\mathrm{th}}(q), \tag{A.14}
$$

and with

$$
\frac{1}{rq}\frac{\mathrm{d}^2}{\mathrm{d}r^2} J_1(rq) = \frac{1}{2}\frac{\mathrm{d}^2}{\mathrm{d}r^2} W_r^{\mathrm{th}}(q) - \frac{2}{r^2}\left[\frac{1}{rq} J_1(rq) - \frac{1}{q}\frac{\mathrm{d}}{\mathrm{d}r} J_1(rq) \right] = \frac{1}{2}\frac{\mathrm{d}^2}{\mathrm{d}r^2} W_r^{\mathrm{th}}(q) + \frac{1}{r^2}\frac{\mathrm{d}}{\mathrm{d}\ln(r)} W_r^{\mathrm{th}}(q), \tag{A.15}
$$

we get

$$
rqJ_1(rq) = J_2(rq) - rq\frac{1}{q^2}\frac{\mathrm{d}^2}{\mathrm{d}r^2} J_1(rq) = J_2(rq) - r^2\frac{1}{rq}\frac{\mathrm{d}^2}{\mathrm{d}r^2} J_1(rq) = -\frac{3}{2}\frac{\mathrm{d}}{\mathrm{d}\ln(r)} W_r^{\mathrm{th}}(q) - \frac{r^2}{2}\frac{\mathrm{d}^2}{\mathrm{d}r^2} W_r^{\mathrm{th}}(q). \tag{A.16}
$$

Using these relations together with the following notation

$$
Q_1(r,\chi) = \frac{2\pi D_+^2}{L} \int \mathrm{d}k\, k\, W_{U_\chi}(k)\, W_r^{\mathrm{th}}(k)\, P_{\mathrm{lin},0}(k), \tag{A.17}
$$

$$Q_2(r,\chi) = \frac{2\pi D_+^2}{L} \int \mathrm{d}k\, k\, W_{U_\chi}(k)\, \frac{\mathrm{d}}{\mathrm{d}\ln(r)} W_r^{\mathrm{th}}(k)\, P_{\mathrm{lin},0}(k), \tag{A.18}$$

$$Q_3(r,\chi) = \frac{2\pi D_+^2}{L} \int \mathrm{d}k\, k\, W_{U_\chi}(k)\, \frac{\mathrm{d}^2}{\mathrm{d}r^2} W_r^{\mathrm{th}}(k)\, P_{\mathrm{lin},0}(k). \tag{A.19}$$

we find that

$$A: \quad 6\pi\hat{c}(1+\mu) \int_0^\infty \mathrm{d}r\, r\, U_\chi(r) \left[\int \mathrm{d}q\, q\, W_{U_\chi}(q)\, P_{\mathrm{lin},0}(q)\, J_0(rq) \right]^2 = 6\pi(1+\mu) \int_0^\infty \mathrm{d}r\, r\, U_\chi(r) \left[Q_1(r,\chi) + \frac{1}{2} Q_2(r,\chi) \right]^2, \tag{A.20}$$

$$C: \quad 6\pi\hat{c}(1-\mu) \int_0^\infty \mathrm{d}r\, r\, U_\chi(r) \left[\int \mathrm{d}q\, q\, W_{U_\chi}(q)\, P_{\mathrm{lin},0}(q)\, J_2(rq) \right]^2 = 6\pi(1-\mu) \int_0^\infty \mathrm{d}r\, r\, U_\chi(r) \left[-\frac{1}{2} Q_2(r,\chi) \right]^2, \tag{A.21}$$

and

$$\begin{aligned} B: \quad & -12\pi\hat{c} \int_0^\infty \mathrm{d}r\, r\, U_\chi(r) \int \mathrm{d}q_1\, q_1\, W_{U_\chi}(q_1)\, P_{\mathrm{lin},0}(q_1)\, rq_1 J_1(rq_1) \int \mathrm{d}q_2\, q_2\, W_{U_\chi}(q_2)\, P_{\mathrm{lin},0}(q_2)\, \frac{1}{rq_2} J_1(rq_2) \\ & = -12\pi \int_0^\infty \mathrm{d}r\, r\, U_\chi(r) \left[-\frac{3}{2} Q_2(r,\chi) - \frac{r^2}{2} Q_3(r,\chi) \right] \frac{1}{2} Q_1(r,\chi). \end{aligned} \tag{A.22}$$

Finally, combining A, B, and C, the skewness of $\delta_{U_\chi,L}$ simplifies to

$$\begin{aligned} \left\langle \delta_{U,L}^3 \right\rangle(\chi) &= 6\pi \int_0^\infty \mathrm{d}r\, r\, U_\chi(r) \Big((1+\mu) \left[Q_1(r,\chi) + \frac{1}{2} Q_2(r,\chi) \right]^2 + (1-\mu)\, \frac{1}{4} Q_2^2(r,\chi) + \frac{3}{2} Q_1(r,\chi) Q_2(r,\chi) + \frac{r^2}{2} Q_1(r,\chi)\, Q_3(r,\chi) \Big) \\ &= 3\pi \int_0^\infty \mathrm{d}r\, r\, U_\chi(r) \Big(2(1+\mu) \left[Q_1^2(r,\chi) + Q_1(r,\chi)\, Q_2(r,\chi) \right] + 3 Q_1(r,\chi)\, Q_2(r,\chi) + Q_2^2(r,\chi) + r^2 Q_1(r,\chi)\, Q_3(r,\chi) \Big) \\ &= 3\pi \int \mathrm{d}r\, U_\chi(r)\, \frac{\mathrm{d}}{\mathrm{d}r} \left(r^2 \left[(1+\mu)\, Q_1^2(r,\chi) + Q_1(r,\chi)\, Q_2(r,\chi) \right] \right), \end{aligned} \tag{A.23}$$

where it is seen that for a top-hat of size ϑ with $U_\chi(r) = \mathcal{H}(\vartheta - \chi r)$ the result in Eq. (B.35) immediately follows.

Although all necessary ingredients for specifying the PDF of $\delta_{\mathrm{m},U}$ are derived already, we still need moments like $\left\langle \delta_{\chi\vartheta,L}\, \delta_{U,L}^2 \right\rangle(\chi)$ to compute quantities like $\langle \kappa_{<\vartheta} | \delta_{\mathrm{m},U} \rangle$ or $\left\langle w_{<\vartheta}\, \delta_{\mathrm{m},U}^k \right\rangle$. With the definitions of two further integrals,

$$Q_4(r,\chi\vartheta) = \frac{2\pi D_+^2}{L} \int \mathrm{d}q\, q\, W_{\chi\vartheta}^{\mathrm{th}}(q)\, P_{\mathrm{lin}}(q)\, W_r^{\mathrm{th}}(q), \tag{A.24}$$

$$Q_5(r,\chi\vartheta) = \frac{2\pi D_+^2}{L} \int \mathrm{d}q\, q\, W_{\chi\vartheta}^{\mathrm{th}}(q)\, P_{\mathrm{lin}}(q)\, \frac{\mathrm{d}}{\mathrm{d}\ln r} W_r^{\mathrm{th}}(q), \tag{A.25}$$

and using the result of F18 that for a top-hat filter of size R

$$\Phi_R^{\mathrm{th}}(q_1, q_2) = \int \mathrm{d}\phi\, W_R^{\mathrm{th}} \left(\sqrt{q_1^2 + q_2^2 + 2 q_1 q_2 \cos\phi} \right) F_2(q_1, q_2, \phi) = \pi(1+\mu)\, W_R^{\mathrm{th}}(q_1)\, W_R^{\mathrm{th}}(q_2) + \frac{\pi}{2} \frac{\mathrm{d}}{\mathrm{d}\ln R} \left[W_R^{\mathrm{th}}(q_1)\, W_R^{\mathrm{th}}(q_2) \right], \tag{A.26}$$

the joint filter moments between the matter density contrast smoothed with the general filter and the matter density contrast smoothed with a top-hat of size ϑ follows analogously to the skewness, and is given by

$$\begin{aligned} \left\langle \delta_{\vartheta,L}\, \delta_{U,L}^2 \right\rangle(\chi) &= \frac{\hat{c}}{\pi} \int\!\!\int \mathrm{d}q_1\, \mathrm{d}q_2\, q_1\, q_2\, W_{U_\chi}(q_1)\, W_{U_\chi}(q_2)\, P_{\mathrm{lin},0}(q_1)\, P_{\mathrm{lin},0}(q_2)\, \Phi_{\chi\vartheta}^{\mathrm{th}}(q_1, q_2) \\ &\quad + \frac{2\hat{c}}{\pi} \int\!\!\int \mathrm{d}q_1\, \mathrm{d}q_2\, q_1\, q_2\, W_{U_\chi}(q_1)\, W_{\chi\vartheta}^{\mathrm{th}}(q_2)\, P_{\mathrm{lin},0}(q_1)\, P_{\mathrm{lin},0}(q_2)\, \Phi_{U_\chi}(q_1, q_2) \\ &= (1+\mu)\, Q_1^2(\chi\vartheta,\chi) + Q_1(\chi\vartheta,\chi)\, Q_2(\chi\vartheta,\chi) \\ &\quad + 2\pi \int \mathrm{d}r\, U_\chi(r) \frac{\mathrm{d}}{\mathrm{d}r} \left(r^2 (1+\mu)\, Q_1(r,\chi)\, Q_4(r,\chi\vartheta) + \frac{r^2}{2} \left[Q_1(r,\chi)\, Q_5(r,\chi\vartheta) + Q_2(r,\chi)\, Q_4(r,\chi\vartheta) \right] \right). \end{aligned} \tag{A.27}$$

A.2. Limber projection

Given the moments of the smoothed density contrasts at comoving distance χ derived in the previous section, the moments in Eqs. (24, 25) and Eqs. (31–33) for $k = 1, 2,$ or 3 follow (see e.g. Bernardeau & Valageas 2000),

$$\left\langle \delta^k_{\mathrm{m},U} \right\rangle = \int \mathrm{d}\chi \, q^k_{\mathrm{f}}(\chi) \, L^{k-1} \left\langle \delta^k_{U,L} \right\rangle (\chi), \tag{A.28}$$

$$\left\langle \kappa_{<\vartheta} \delta^k_{\mathrm{m},U} \right\rangle = \int \mathrm{d}\chi \, W_{\mathrm{s}}(\chi) \, q^k_{\mathrm{f}}(\chi) \, L^{k-1} \left\langle \delta_{\vartheta,L} \, \delta^k_{U,L} \right\rangle (\chi), \tag{A.29}$$

$$\left\langle w_{<\vartheta} \delta^k_{\mathrm{m},U} \right\rangle = \int \mathrm{d}\chi \, q^{k+1}_{\mathrm{f}}(\chi) \, L^{k-1} \left\langle \delta_{\vartheta,L} \, \delta^k_{U,L} \right\rangle (\chi), \tag{A.30}$$

where $q_{\mathrm{f}}(\chi)$ is the projection kernel defined in Eq. (10) and $W_{\mathrm{s}}(\chi)$ the lensing efficiency defined in Eq. (14). We note that these three equations employ a Limber approximation, which consists of $L \to \infty$ (Limber 1953), and that the physical radius r of filter U scales with χ as described below Eq. (A.3). We also note that these expectation values are independent of L.

A.3. Non-linear regime

In order to go to the non-linear regime for second-order moments, we replace the linear power spectrum in the above calculations with the non-linear power spectrum, which in turn is determined with the halofit model from Takahashi et al. (2012) using an analytic approximation for the transfer function (Eisenstein & Hu 1998).

For the third-order moments we use that for a top-hat filter of size R the filter simplifies to $U_\chi(r) = \frac{1}{\pi R^2} \mathcal{H}(R - r)$, such that

$$\begin{aligned} Q_1(R,\chi) &= \frac{2\pi D_+^2}{L} \int \mathrm{d}k \, k \, W_{U_\chi}(k) \, W^{\mathrm{th}}_R(k) \, P_{\mathrm{lin},0}(k) \\ &= \frac{2\pi D_+^2}{L} \int \mathrm{d}k \, k \, W^{\mathrm{th}}_R(k) \, W^{\mathrm{th}}_R(k) \, P_{\mathrm{lin},0}(k) \\ &= \left\langle \delta^2_{R,L} \right\rangle (\chi), \end{aligned} \tag{A.31}$$

and

$$\begin{aligned} Q_2(R,\chi) &= \frac{2\pi D_+^2}{L} \int \mathrm{d}k \, k \, W_{U_\chi}(k) \, \frac{\mathrm{d}}{\mathrm{d}\ln(r)} W^{\mathrm{th}}_R(k) \, P_{\mathrm{lin},0}(k) \\ &= \frac{2\pi D_+^2}{L} \int \mathrm{d}k \, k \, W^{\mathrm{th}}_R(k) \frac{\mathrm{d}}{\mathrm{d}\ln(R)} W^{\mathrm{th}}_R(k) P_{\mathrm{lin},0}(k) \\ &= \frac{1}{2} \frac{\mathrm{d}}{\mathrm{d}\ln(R)} \left\langle \delta^2_{R,L} \right\rangle (\chi). \end{aligned} \tag{A.32}$$

Furthermore, the skewness simplifies in the this case to:

$$\left\langle \delta^3_{R,L} \right\rangle (\chi) = 3(1 + \mu) \left\langle \delta^2_{R,L} \right\rangle^2 (\chi) + \frac{3}{2} \left\langle \delta^2_{R,L} \right\rangle (\chi) \frac{\mathrm{d} \left\langle \delta^2_{R,L} \right\rangle (\chi)}{\mathrm{d}\ln(R)}. \tag{A.33}$$

This then helps to define

$$S_3 \equiv \frac{\left\langle \delta^3_{R,L} \right\rangle (\chi)}{\left\langle \delta^2_{R,L} \right\rangle^2 (\chi)} = 3(1 + \mu) + \frac{3}{2} \frac{\mathrm{d}}{\mathrm{d}\ln(R)} \ln(\left\langle \delta^2_{R,L} \right\rangle), \tag{A.34}$$

which in the linear and the non-linear regime is approximately the same (Bernardeau et al. 2002), meaning that in order to get the skewness in the non-linear regime we approximate

$$\left\langle \delta^3_{R,L} \right\rangle_{\text{non-linear}} (\chi) \approx S_3 \left\langle \delta^2_{R,L} \right\rangle^2_{\text{non-linear}} (\chi). \tag{A.35}$$

For the general filter we use that the numerical integration of r in $\left\langle \delta^3_{U_\chi,L} \right\rangle (\chi)$ results basically in a sum of top-hat filters, such that we make use of S_3 to scale each term individual to the non-linear regime. For the joint filter moment $\left\langle \delta_{\chi\vartheta,L} \, \delta^2_{U_\chi,L} \right\rangle (\chi)$ we use a generalised version of S_3, which states that for two different top-hat filters of size R_1 and R_2

$$\left\langle \delta^2_{R_1,L} \delta_{R_2,L} \right\rangle (\chi) \propto \langle \delta_{R_1,L} \delta_{R_2,L} \rangle (\chi) \left\langle \delta^2_{R_1,L} \right\rangle (\chi). \tag{A.36}$$

Using again that the r-integration results in a sum of top-hat filters and factoring out the non-derivative terms similar to Eq. (A.34), we scale individually all the non-derivative terms to the non-linear regime.

A.4. Characteristic function

We consider a large circle of radius R, inside of which there are $N = n_0 \pi R^2$ galaxies, where n_0 is the galaxy number density. The probability of finding a galaxy at separation ϑ is

$$p(\vartheta; \delta_{\mathrm{m},U}) = \frac{2\vartheta}{R^2 \eta} (1 + b \, \langle w_\vartheta | \delta_{\mathrm{m},U} \rangle), \tag{A.37}$$

where $\langle w_\vartheta | \delta_{\mathrm{m},U} \rangle$ is the expectation of the mean 2D density contrast on a circle at ϑ (see Eq. (37)) given the smoothed density contrast defined in Eq. (38). The assumption of linear galaxy bias enters here by the term $b \, \langle w_\vartheta | \delta_{\mathrm{m},U} \rangle$. The normalisation is

$$\eta = \int_0^R \frac{2\vartheta}{R^2} (1 + b \, \langle w_\vartheta | \delta_{\mathrm{m},U} \rangle) \, \mathrm{d}\vartheta, \tag{A.38}$$

which goes to unity for $R \to \infty$. The characteristic function (CF) of the aperture number N_{ap}, given the smoothed 2D density contrast $\delta_{\mathrm{m},U}$, is given by

$$\begin{aligned} \Psi(t) &= \left\langle \mathrm{e}^{\mathrm{i}tN_{\mathrm{ap}}} \right\rangle_{\delta_{\mathrm{m},U}} = \int_{\mathbb{R}} \mathrm{d}N_{\mathrm{ap}} \, p\left(N_{\mathrm{ap}} | \delta_{\mathrm{m},U}\right) \mathrm{e}^{\mathrm{i}tN_{\mathrm{ap}}} \\ &= \left[\prod_{i=1}^{N} \int_0^R \mathrm{d}\vartheta_i \, p(\vartheta_i; \delta_{\mathrm{m},U}) \right] \mathrm{e}^{\mathrm{i}t \sum_j U(\vartheta_j)} \\ &= \left[\int_0^R \mathrm{d}\vartheta \, \frac{2\vartheta}{R^2 \eta} (1 + b \, \langle w_\vartheta | \delta_{\mathrm{m},U} \rangle) \mathrm{e}^{\mathrm{i}tU(\vartheta)} \right]^N \\ &= \left[\int_0^R \mathrm{d}\vartheta \, \frac{2\vartheta}{R^2 \eta} (1 + b \, \langle w_\vartheta | \delta_{\mathrm{m},U} \rangle) \left(\mathrm{e}^{\mathrm{i}tU(\vartheta)} - 1 + 1 \right) \right]^N \\ &= \left[1 + \frac{\pi n_0}{N \eta} \int_0^R \mathrm{d}\vartheta \, 2\vartheta \, (1 + b \, \langle w_\vartheta | \delta_{\mathrm{m},U} \rangle) \left(\mathrm{e}^{\mathrm{i}tU(\vartheta)} - 1 \right) \right]^N \\ &\underbrace{\longrightarrow}_{N,R\to\infty} \exp\left[2\pi n_0 \int_0^\infty \mathrm{d}\vartheta \, \vartheta \, (1 + b \, \langle w_\vartheta | \delta_{\mathrm{m},U} \rangle) \left(\mathrm{e}^{\mathrm{i}tU(\vartheta)} - 1 \right) \right], \end{aligned}$$

where we used in the second line that

$$N_{\mathrm{ap}} = \int_0^\infty \mathrm{d}^2\vartheta \, U\left(|\boldsymbol{\vartheta}|\right) \, n\left(\boldsymbol{\vartheta}\right) = \sum_j U\left(\vartheta_j\right),$$

with $n(\boldsymbol{\vartheta}) = \sum_j \delta_{\mathrm{D}}(\boldsymbol{\vartheta} - \boldsymbol{\vartheta}_j)$, and that the galaxy positions ϑ_i independently trace the density profile $\langle w_\vartheta | \delta_{\mathrm{m},U} \rangle$. As discussed in Sect. 3.3, the exact approach is to transform the CF to the probability density function $p\left(N_{\mathrm{ap}} | \delta_{\mathrm{m},U}\right)$ by use of the inverse Fourier transformation. Alternatively, we assume that the PDF is well approximated by a log-normal distribution as

$$p\left(N_{\rm ap}|\delta_{{\rm m},U}\right) = \frac{1}{\sqrt{2\pi}S\left(N_{\rm ap}+L\right)}\exp\left(\frac{-\left[\ln\left(N_{\rm ap}+L\right)-M\right]^2}{2S^2}\right), \tag{A.39}$$

where the parameters S, M, L are fixed with the first raw moment

$$\mu_1' = \left\langle N_{\rm ap}|\delta_{{\rm m},U}\right\rangle = \left\langle N_{\rm ap}\right\rangle_{\delta_{{\rm m},U}} = \exp\left(M+\frac{S^2}{2}\right)-L, \tag{A.40}$$

and the central moments

$$\mu_2 = \left\langle\left(N_{\rm ap}-\left\langle N_{\rm ap}\right\rangle\right)^2\right\rangle_{\delta_{{\rm m},U}} = \exp(2M+S^2)\left[{\rm e}^{S^2}-1\right], \tag{A.41}$$

$$\mu_3 = \left\langle\left(N_{\rm ap}-\left\langle N_{\rm ap}\right\rangle\right)^3\right\rangle_{\delta_{{\rm m},U}} = \exp\left(3M+\frac{3}{2}S^2\right)\left[{\rm e}^{S^2}-1\right]^2\left[{\rm e}^{S^2}+2\right]. \tag{A.42}$$

The raw moments can be calculated from the derivatives of the CF,

$$\mu_n' = \left.\frac{{\rm d}^n\Psi(t)}{{\rm d}({\rm i}t)^n}\right|_{t=0}. \tag{A.43}$$

With the definition

$$E_n = 2\pi n_0\int_0^\infty {\rm d}\vartheta\;\vartheta\;(1+b\left\langle w_\vartheta|\delta_{{\rm m},U}\right\rangle)U^n(\vartheta), \tag{A.44}$$

it follows that

$$\begin{aligned}
\mu_0' &= 1,\\
\mu_1' &= E_1, \qquad\qquad (A.45)\\
\mu_2' &= (E_1)^2+E_2,\\
\mu_3' &= (E_1)^3+3E_1E_2+E_3,
\end{aligned}$$

and so

$$\mu_2 = \mu_2' - (\mu_1')^2 = (E_1)^2+E_2-(E_1)^2 = E_2, \tag{A.46}$$

$$\mu_3 = \mu_3' - 3\mu_1'\mu_2' + 2(\mu_1')^2 = E_3. \tag{A.47}$$

To find the parameters of the log-normal distribution Eq. (A.39) by use of the raw and central moments in Eqs. (A.45–A.47) we define

$$\begin{aligned}
\gamma = \frac{\mu_3}{\mu_2^{3/2}} &= \sqrt{\exp(S^2)-1}\left[2+\exp(S^2)\right]\\
&= \sqrt{q-1}\,(2+q)\,,
\end{aligned} \tag{A.48}$$

where we defined in the last step $q = \exp(S^2)$. Modifying γ we get

$$0 = q^3+3q^2-4-\gamma^2, \tag{A.49}$$

which always has one real solution q_0, and so the parameters follow to

$$S = \sqrt{\ln(q_0)}, \tag{A.50}$$

$$M = \frac{1}{2}\ln\left(\frac{\mu_2}{q_0^2-q_0}\right), \tag{A.51}$$

$$L = \sqrt{\frac{\mu_2}{q_0-1}} - \mu_1'. \tag{A.52}$$

To check this derivation and compare it to the direct approach of using the inverse Fourier transform, we created an idealised case of a full-sky uniform random field $n_{\rm side} = 4096$ with a number density $n_0 \approx 0.034/{\rm arcmin}^2$. Next we calculated by use of the HEALPY internal SMOOTHING function $N_{\rm ap}$ for the top-hat filter of size 20′ and the for the adapted filter. In the determination of the predicted PDF we set, $\left\langle w_\vartheta|\delta_{{\rm m},U}\right\rangle = 0$ so $p\left(N_{\rm ap}\right)$ follows immediately with Eq. (A.39) or Eq. (42). It is clearly seen in Fig. A.1 that the model for both filters has an excellent fit with the measured PDF of the aperture number. Additionally, we show in Fig. A.2 a comparison between the predicted $p\left(N_{\rm ap}\right)$ using the full characteristic function Eq. (36) versus the log-normal approach Eq. (A.39) for the low-redshift bin $z_l^{\rm low}$ from the Takahashi set-up. In the lower panel the residual difference between the two methods is three orders of magnitude smaller than the signal itself, which shows that the two approaches are identical given the uncertainties we expect for Stage III surveys. Since the log-normal approach is faster to compute we can use this approach in future analyses where computational speed is essential.

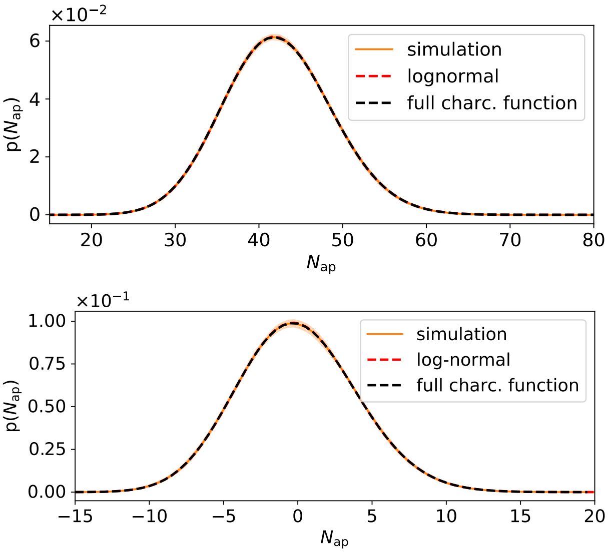

Fig. A.1. Probability distribution of the aperture number resulting in a uniform random field smoothed with the top-hat filter of size 20′ in the *upper panel* and for the adapted filter U of size 120′ in the *lower panel*. The orange shaded region is the standard deviation determined from 48 sub-patches.

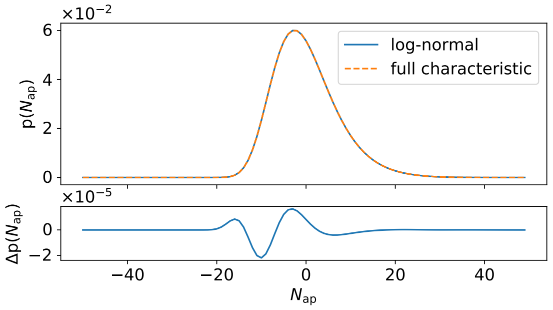

Fig. A.2. Comparison between the two approaches to calculate $p\left(N_{\rm ap}\right)$. It is clearly seen that both methods yield almost the same result.

Appendix B: Correction formulae for the power spectra of the T17 simulations

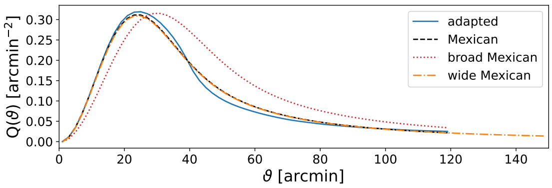

Fig. B.1. Different filters Q resulting from the corresponding U filters shown in Fig. 3 used in this work to verify the new model.

Table B.1. Overview of all the different cosmological parameters for the 26 cosmo-SLICS models, which are used in Sect. 5 for the cosmological analysis.

	Ω_{m}	h	w_0	σ_8	S_8
fid	0.2905	0.6898	−1.0000	0.8364	0.8231
1	0.3282	0.6766	−1.2376	0.6677	0.6984
2	0.1019	0.7104	−1.6154	1.3428	0.7826
3	0.2536	0.6238	−1.7698	0.6670	0.6133
4	0.1734	0.6584	−0.5223	0.9581	0.7284
5	0.3759	0.6034	−0.9741	0.8028	0.8986
6	0.4758	0.7459	−1.3046	0.6049	0.7618
7	0.1458	0.8031	−1.4498	1.1017	0.7680
8	0.3099	0.6940	−1.8784	0.7734	0.7861
9	0.4815	0.6374	−0.7737	0.5371	0.6804
10	0.3425	0.8006	−1.5010	0.6602	0.7054
11	0.5482	0.7645	−1.9127	0.4716	0.6375
12	0.2898	0.6505	−0.6649	0.7344	0.7218
13	0.4247	0.6819	−1.1986	0.6313	0.7511
14	0.3979	0.7833	−1.1088	0.7360	0.8476
15	0.1691	0.7890	−1.6903	1.1479	0.8618
16	0.1255	0.7567	−0.9878	0.9479	0.6131
17	0.5148	0.6691	−1.3812	0.6243	0.8178
18	0.1928	0.6285	−0.8564	1.1055	0.8862
19	0.2784	0.7151	−1.0673	0.6747	0.6500
20	0.2106	0.7388	−0.5667	1.0454	0.8759
21	0.4430	0.6161	−1.7037	0.6876	0.8356
22	0.4062	0.8129	−1.9866	0.5689	0.6620
23	0.2294	0.7706	−0.8602	0.9407	0.8226
24	0.5095	0.6988	−0.7164	0.5652	0.7366
25	0.3652	0.7271	−1.5414	0.5958	0.6574

To account for the finite angular resolution T17 suggested a simple damping factor at small scales as

$$C_\ell^\kappa \to \frac{C_\ell^\kappa}{1+(\ell/\ell_{\mathrm{res}})^2}, \tag{B.1}$$

where $\ell_{\mathrm{res}} = 1.6 \times N_{\mathrm{side}}$. Additionally, to take the shell thickness into account they conducted a simple fitting formula by which the matter power spectrum should be modified to

$$P_\delta(k) \to P_\delta^W(k) = \frac{(1+c_1 k^{-\alpha_1})^{\alpha_1}}{(1+c_2 k^{-\alpha_2})^{\alpha_3}} P_\delta(k), \tag{B.2}$$

where the parameters are simulation specific and are $c_1 = 9.5171 \times 10^{-4}$, $c_2 = 5.1543 \times 10^{-3}$, $\alpha_1 = 1.3063$, $\alpha_2 = 1.1475$, $\alpha_3 = 0.62793$, and the wavenumber k is in units of h/Mpc. We note that although we incorporated these corrections in the following, they have very little effect on the scales we are considering.

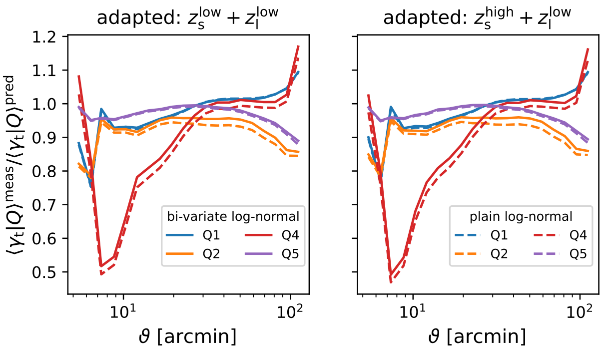

Fig. B.2. Comparison between the uncalibrated shear profiles for the adapted filter with and without using the bi-variate log-normal approach discussed in Sect. 3.1 The ratio is calculated between the measured shear profiles from T17 for the lower LRG source bin and for sources where several T17 shear grids were averaged, weighted by the $n(z)$ given in Fig. 2. The bi-variate log-normal shear profiles are more consistent with the measured shear profiles and thus (although the shear signals were calibrated) the more accurate model was chosen. Here only the highest and lowest two quantiles are shown because the middle one is to close to zero.

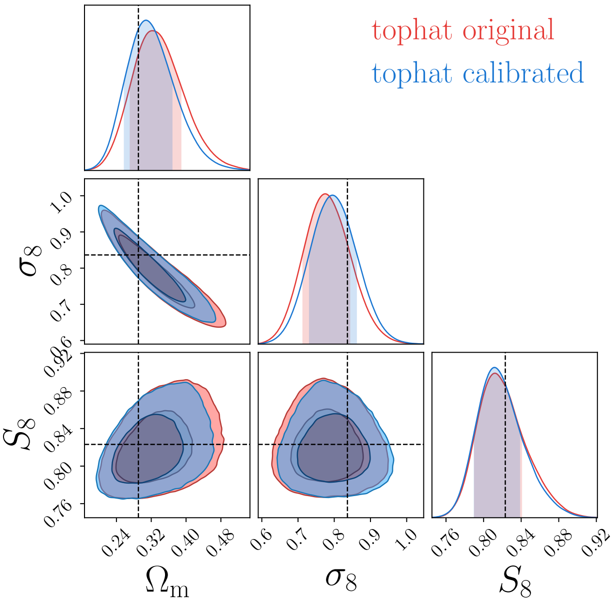

Fig. B.3. MCMC results for the top-hat filter using the original and calibrated model. The data vector is calculated from the fiducial cosmology of cosmo-SLICS and a covariance matrix from 614 SLICS realisations. The systematic biases are likely to be statistical flukes due to the noise in the data vector. The contours are marginalised over the lens galaxy bias parameters.

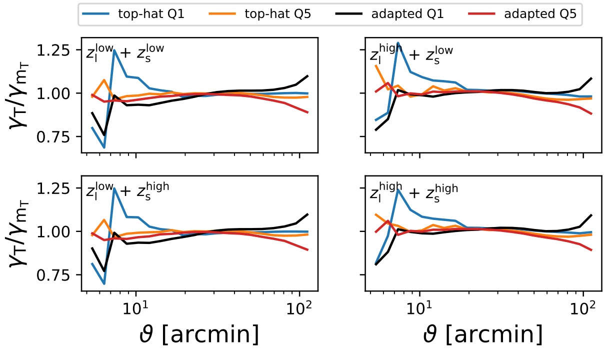

Fig. B.4. Calibration of the model $\gamma_{M_T}(p_T)$ by the T17 simulations $\gamma_T(p_T)$ explained in Eq. (47), shown for the highest and lowest quantile for the adapted and top-hat filter. The corresponding redshift distributions of the lenses are given in Fig. 1 and for the sources several T17 shear grids are averaged, weighted by the $n(z)$ given in Fig. 2.

Astronomy & Astrophysics manuscript no. output ©ESO 2022
August 8, 2022

KiDS-1000 Cosmology: Constraints from density split statistics

Pierre A. Burger[1], Oliver Friedrich[2], Joachim Harnois-Déraps[3], Peter Schneider[1], Marika Asgari[4], Maciej Bilicki[5], Hendrik Hildebrandt[6], Angus H. Wright[6], Tiago Castro[7, 8, 9], Klaus Dolag[2, 10], Catherine Heymans[6, 11], Benjamin Joachimi[12], Konrad Kuijken[13], Nicolas Martinet[14], HuanYuan Shan[15, 16], and Tilman Tröster[17]

[1] Argelander-Institut für Astronomie, Auf dem Hügel 71, 53121 Bonn, Germany
[2] Universitäts-Sternwarte, Fakultät für Physik, Ludwig-Maximilians-Universität München, Scheinerstr.1, 81679 München
[3] School of Mathematics, Statistics and Physics, Newcastle University, Newcastle upon Tyne, NE1 7RU, UK
[4] E.A Milne Centre, University of Hull, Cottingham Road, Hull, HU6 7RX, United Kingdom
[5] Center for Theoretical Physics, Polish Academy of Sciences, al. Lotników 32/46, 02-668 Warsaw, Poland
[6] Ruhr University Bochum, Faculty of Physics and Astronomy, Astronomical Institute (AIRUB), German Centre for Cosmological Lensing, 44780 Bochum, Germany
[7] INAF – Istituto Nazionale di Astrofisica, Osservatorio Astronomico di Trieste, via Tiepolo 11, 34143 Trieste, Italy
[8] INFN – Istituto Nazionale di Fisica Nucleare, Sezione di Trieste, via Valerio 2, 34127 Trieste, Italy
[9] Institute for Fundamental Physics of the Universe, Via Beirut 2, 34151 Trieste, Italy
[10] Germany Max-Planck-Institut für Astrophysik, Karl-Schwarzschild-Straße 1, 85741 Garching, Germany
[11] Institute for Astronomy, University of Edinburgh, Royal Observatory, Blackford Hill, Edinburgh, EH9 3HJ, UK
[12] Department of Physics and Astronomy, University College London, Gower Street, London WC1E 6BT, UK
[13] Leiden Observatory, Leiden University, P.O.Box 9513, 2300RA Leiden, The Netherlands
[14] Aix-Marseille Univ., CNRS, CNES, LAM, Marseille, France
[15] Shanghai Astronomical Observatory (SHAO), Nandan Road 80, Shanghai 200030, China
[16] University of Chinese Academy of Sciences, Beijing 100049, China
[17] Institute for Particle Physics and Astrophysics, ETH Zürich, Wolfgang-Pauli-Strasse 27, 8093 Zürich, Switzerland
e-mail: `pburger@astro.uni-bonn.de`

XXXXXXXX

ABSTRACT

Context. Weak lensing and clustering statistics beyond two-point functions can capture non-Gaussian information about the matter density field, thereby improving the constraints on cosmological parameters relative to the mainstream methods based on correlation functions and power spectra.
Aims. This paper presents a cosmological analysis of the fourth data release of the Kilo Degree Survey based on the density split statistics, which measures the mean shear profiles around regions classified according to foreground densities. The latter is constructed from a bright galaxy sample, which we further split into red and blue samples, allowing us to probe their respective connection to the underlying dark matter density.
Methods. We use the state-of-the-art model of the density splitting statistics and validate its robustness against mock data infused with known systematic effects such as intrinsic galaxy alignment and baryonic feedback.
Results. After marginalising over the photometric redshift uncertainty and the residual shear calibration bias, we measure for the full KiDS-bright sample a structure growth parameter of $S_8 \equiv \sigma_8 \sqrt{\Omega_\mathrm{m}/0.3} = 0.74^{+0.03}_{-0.02}$ that is competitive to and consistent with two-point cosmic shear results, a matter density of $\Omega_\mathrm{m} = 0.28 \pm 0.02$, and a constant galaxy bias of $b = 1.32^{+0.12}_{-0.10}$.

Key words. gravitational lensing: weak – (cosmology:) cosmological parameters – (cosmology:) large-scale structure of Universe

1. Introduction

Gravitational lensing, the theory which describes the deflection of light by massive objects, reveals a wealth of information about the evolution of matter structure in the Universe (see, e.g. Hamana et al. 2020; Asgari et al. 2021; Amon et al. 2022, for recent cosmic shear analyses). The most commonly used methods focus on two-point statistics, namely the two-point correlation functions and their Fourier counterparts, the power spectra, because of their accurate theoretical description and control over systematic inaccuracies. These statistics are excellent for capturing the Gaussian information contained in the data and are complete if the data is Gaussian-distributed, such as the cosmic microwave background (CMB; e.g. Planck Collaboration et al. 2020). In the late Universe, however, non-linear gravitational instabilities generate a significant amount of non-Gaussian features, whose information can only be accessed with higher-order statistics. Furthermore, since higher-order statistics scale differently with cosmology and are affected differently by residual systematic effects, the constraining power on cosmological parameters increases by jointly investigating second- and higher-order statistics (see, e.g. Kilbinger & Schneider 2005; Bergé et al. 2010; Pires et al. 2012; Fu et al. 2014; Pyne & Joachimi 2021).

As the current analysis of cosmological parameters estimation reaches the per-cent level, tensions arise between observations of the early and late or local Universe. A famous tension is the one for the Hubble parameter H_0 (Di Valentino et al. 2021a) but is not subject to this work. More interesting for us is the tension in the matter clustering parameter $S_8 = \sigma_8 \sqrt{\Omega_\mathrm{m}/0.3}$, where it seems that the local Universe is less clustered than observations of the CMB suggest (Hildebrandt et al. 2017; Joudaki et al. 2020; Heymans et al. 2021; Di Valentino et al. 2021b).

Recent development in analysis methods have enabled the joint investigation of weak lensing and galaxy clustering data (van Uitert et al. 2018; Joudaki et al. 2018; Abbott et al. 2018; DES Collaboration et al. 2021), yielding significantly better constraints, especially along the σ_8-Ω_m degeneracy axis. Even though foreground clustering data introduces largely uncertain astrophysical parameters, such as the galaxy bias, that complicate the analysis, these joint analyses inform us better about the correlation between galaxies and the underlying matter distribution (Sánchez et al. 2017). Here again, two-point statistics have been favoured so far for the reasons mentioned above, such that the combination of all measurements (cosmic shear, galaxy clustering and galaxy-galaxy lensing) are generally referred to as '3×2pts' statistics.

To access the additional information contained in the non-Gaussian features, a competitive statistics to the 3×2pts method was recently proposed in Gruen et al. (2016), coined the 'density-split statistics' (DSS hereafter). This technique measures the tangential shear on the full pixelated survey footprint and bins the resulting shear profiles as a function of the foreground mass density. For example, high galaxy density regions generally trace large matter over-density regions, in which the tangential shear is expected to be larger, which varies with cosmology. The DSS, therefore, captures information both from the shape and amplitude of the shear profiles and from the number of foreground galaxies in each density bin, with the latter helping significantly in measuring the galaxy bias.

The first ingredient needed is a prediction model to interpret the measurements and constrain cosmological and astrophysical parameters. This can be constructed either from simulations (see, e.g., Harnois-Déraps et al. 2021; Zürcher et al. 2022, for examples of simulation-based inference using lensing peak count) or from analytical calculations, where for instance Reimberg & Bernardeau (2018) and Barthelemy et al. (2021) made use of large deviation theory (LDT) to model the reduced-shear correction to the aperture mass probability distribution function (PDF). On the one hand, the simulation-based approach has advantages regarding the numerical incorporation of critical systematic effects such as the intrinsic alignment (IA) of galaxies (see, e.g. Harnois-Déraps et al. 2022, hereafter HD22) and baryonic processes extracted from hydrodynamical simulations. However, it typically requires large simulation suites that jointly vary all the parameters under consideration. On the other hand, analytical modelling of the DSS can better dissect the basic underlying properties of the LSS, and it can be sufficiently fast computed at any point in the cosmological parameter space. Such a model was derived in Friedrich et al. (2018, hereafter F18), based on non-perturbative modelling of the matter density PDF. For a given cosmology, mean foreground galaxy density, and redshift distributions of the foreground and background galaxies, the F18 model, predicts the mean tangential shear profiles and the PDF of the galaxy counts in each mass density bin. In Gruen et al. (2018, hereafter G18), the F18 model is used to constrain cosmological parameters from measurements of the Dark Energy Survey (DES) First Year and Sloan Digital Sky Survey (SDSS) data, yielding results competitive with the main DES 3×2 pt analysis (Abbott et al. 2018).

To date, no cosmological constraints from DSS exist except that of G18. However, the methods have been improved significantly. In particular, Brouwer et al. (2018) presented a contemporary measurement of the DSS extracted from the third data release of the Kilo-Degree Survey data (KiDS), wherein in the foreground galaxies are selected to mimic the spectroscopic Galaxy And Mass Assembly survey (hereafter GAMA; Driver et al. 2011). They developed an optimal methodology in their work, notably showing how the resulting signal-to-noise (S/N) depends on the smoothing scale for the density map of foreground galaxies.

Burger et al. (2022, hereafter B22) modified the analytical model by F18 for an application to galaxy density fields smoothed with general filters. As discussed in Burger et al. (2020), compensated filter functions outperform the previously used top-hat filter functions in terms of the overall S/N of the shear signals and in recovering the correlation between the galaxy and matter density contrast. B22 mention another advantage of compensated filter functions: they are more compact in Fourier space and, therefore, can better suppress large-ℓ modes where baryonic effects play an important role, as studied in Asgari et al. (2020). On the downside, compensated filters complicate the LDT-like calculations (Barthelemy et al. 2021). Nevertheless, B22 show that the density split statistics with compensated filters can still be accurately modelled in a computationally tractable manner after calibrating residual inaccuracies at large and small scales on the simulations of Takahashi et al. (2017).

The current paper presents the first cosmological inference based on a DSS analysis of the KiDS data. We exploit the model advances presented in B22, using the dense sample of bright galaxies presented in Bilicki et al. (2021) to construct our foreground density maps, and compute the tangential shear from the lensing catalogue constructed from the fourth KiDS data release. Our inference includes a marginalisation over several residual systematic uncertainties. We verify with numerical N-body and hydrodynamical simulations that our measurements are robust against IA of galaxies and baryonic feedback.

This work is structured as follows. In Sect. 2 we review the basics of the DSS and introduce small modifications of our model to the one from B22. In Sect. 3 we present the observed data used in our analysis, then describe in Sect. 4 the simulations needed for the validation of our inference pipeline that is described in Sect. 5. In Sect. 6 we perform our validation of the model together with an investigation on IA and baryonic physics that could potentially contaminate our results. In Sect. 7 we finally present our main results and conclude with a discussion and summary in Sect. 8.

2. Theoretical background

The DSS essentially measures the tangential shear around subareas of the sky that are assigned according to the galaxy foreground density. It is therefore closely related to aperture statistics, which we introduce here first. Given a convergence field $\kappa(\boldsymbol{\theta})$, the aperture mass map is defined as

$$M_\mathrm{ap}(\boldsymbol{\theta}) := \int \mathrm{d}^2\theta' \, \kappa(\boldsymbol{\theta}+\boldsymbol{\theta}')\, U(|\boldsymbol{\theta}'|)\,, \tag{1}$$

where $\boldsymbol{\theta}$ is the position on the flat sky, and $U(\vartheta)$ is a compensated, axisymmetric filter function, such that $\int \vartheta\, U(\vartheta)\, \mathrm{d}\vartheta = 0$. The aperture mass, M_ap, can also be expressed in terms of the tangential shear γ_t (Schneider 1996) and a second filter function

Q as

$$M_{\rm ap}(\boldsymbol{\theta}) = \int \mathrm{d}^2\theta' \, \gamma_{\rm t}(\boldsymbol{\theta} + \boldsymbol{\theta}') \, Q(|\boldsymbol{\theta}'|) \,, \tag{2}$$

where

$$Q(\vartheta) = \frac{2}{\vartheta^2} \int_0^{\vartheta} \mathrm{d}\vartheta' \, \vartheta' \, U(\vartheta') - U(\vartheta) \,. \tag{3}$$

The above relation between the two filters U and Q can be inverted,

$$U(\vartheta) = 2 \int_{\vartheta}^{\infty} \mathrm{d}\vartheta' \, \frac{Q(\vartheta')}{\vartheta'} - Q(\vartheta) \,, \tag{4}$$

allowing us to work either with convergence maps or shear catalogues. Replacing the convergence by the foreground galaxy number count $n(\boldsymbol{\theta})$ in Eq. (1), we define the aperture number counts, or simply aperture number, as (Schneider 1998)

$$N_{\rm ap}(\boldsymbol{\theta}) := \int \mathrm{d}^2\theta' \, n(\boldsymbol{\theta} + \boldsymbol{\theta}') \, U(|\boldsymbol{\theta}'|) \,. \tag{5}$$

This definition is equivalent to the 'Counts-in-Cell' (CiC) statistics mentioned in Gruen et al. (2016) if the filter U is defined as a top-hat. In that case, however, U is not compensated; hence, one cannot relate the filters U and Q.

The general idea of the DSS is to divide the survey area into quantiles Q according to the aperture number $N_{\rm ap}$ and then measure the mean tangential shear in the corresponding quantiles $\langle\gamma_{\rm t}|Q\rangle$. We detail in Sect. 2.1 how we achieve this in the data and in Sect. 2.2 how we predict it analytically.

2.1. Measuring the DSS vector

We follow several ordered pipeline steps to extract the DSS data vector for the cosmological inference.

1. Distribute the foreground (lens) galaxies onto a `HEALPix` (Górski et al. 2005) grid $n(\boldsymbol{\theta})$ of `nside` = 4096, which results in a pixel area of $A_{\rm HP} \approx 0.74\,\mathrm{arcmin}^2$.
2. Determine the aperture number field $N_{\rm ap}$ with a filter function U, with a finite filter radius Θ and maximal one transition from positive to negative values at $\theta_{\rm tr}$. This is achieved with the `healpy` function `smoothing`, with a beam window function that is the U-filter in the spherical harmonic space determined with `healpy` function `beam2bl`. Since Eq. 5 assumes full knowledge of $n(\boldsymbol{\theta})$ on the sky which has to be modified in the presence of a mask $m(\boldsymbol{\theta})$ as

$$\begin{aligned} N_{\rm ap}(\boldsymbol{\theta}) = {} & \frac{\int_0^{\theta_{\rm tr}} U(\boldsymbol{\theta}')\,\mathrm{d}^2\theta'}{\int_0^{\theta_{\rm tr}} m(\boldsymbol{\theta}+\boldsymbol{\theta}')U(\boldsymbol{\theta}')\,\mathrm{d}^2\theta'} \int_0^{\theta_{\rm tr}} n(\boldsymbol{\theta}+\boldsymbol{\theta}')U(\boldsymbol{\theta}')\,\mathrm{d}^2\theta' \\ & + \frac{\int_{\theta_{\rm tr}}^{\Theta} U(\boldsymbol{\theta}')\,\mathrm{d}^2\theta'}{\int_{\theta_{\rm tr}}^{\Theta} m(\boldsymbol{\theta}+\boldsymbol{\theta}')U(\boldsymbol{\theta}')\,\mathrm{d}^2\theta'} \int_{\theta_{\rm tr}}^{\Theta} n(\boldsymbol{\theta}+\boldsymbol{\theta}')U(\boldsymbol{\theta}')\,\mathrm{d}^2\theta' \,, \end{aligned} \tag{6}$$

   where in this work $m(\boldsymbol{\theta})$ is the KiDS-1000 mask. For example, the second part of this equation vanishes for a top-hat filter. We divide the filter in this way to prevent the masked area from entering the positive part to decrease $N_{\rm ap}$ systematically and artificially increase the aperture number when entering the negative filter region. By separating the compensated filter into its positive and negative parts, we can correct both individually. Furthermore, since this correction becomes less accurate in heavily masked regions, we include only those pixels where the number of unmasked pixels within the given filter radius (effective area) is greater than 50% of the total number of pixels inside the same circle (maximal area), which we treat as our 'good' pixels. We note that this can change from pixel to pixel because our `HEALPix` map originates from a flat sky mask. To avoid that a pixel is considered good, but more than 50% pixels are missing in the negative part, we included for compensated filters only those pixels where the effective area for the positive and the negative part is greater than 50% of their individual maximal area. With our choice of the 50% threshold, we attempt to achieve a compromise between statistical power and falsely measured $N_{\rm ap}$ values. G18 considered only regions with at least 80% coverage, but since the KiDS footprint is very narrow, we had to relax that threshold to avoid shot noise-dominated data vectors. Therefore, we decided to use the highest threshold that yields shear profiles that do not deviate significantly from shear profiles with smaller threshold values. The result is shown in Fig. A.1, where it is seen that the shear profiles with threshold values of 50% or smaller are quite similar and start to deviate for higher threshold values.
3. Next, we allocate those good pixels to five quantiles Q according to their $N_{\rm ap}$ value. The pixels from each quantile are then correlated with the tangential shear information from the source catalogues using the `treecorr` (Jarvis et al. 2004) software in 10 log-spaced bins with angular separation $10\,\mathrm{arcmin} < \vartheta < 120\,\mathrm{arcmin}$. This results in measurements of the five tangential shear profiles $\langle\gamma_{\rm t}|Q\rangle$, i.e., one per quantile. We note here that for all measured profiles, the shear around random points is subtracted, which ensures that the average over all quantiles vanishes by definition.
4. Finally, we construct our data vector, which consists of the shear profiles from the highest two and lowest two quantiles, plus the mean of the aperture number values in the same four quantiles. We must exclude the information of one quantile Q since the other four quantiles fully determine it by construction, for the reason explained above. The same is true for mean aperture number values in those quantiles, whose average is fixed by the total galaxy number density measured in the data. This results with 10 θ bins, four quantiles and two source bins in a data vector of $80 + 4 = 84$ elements. We exclude the middle quantile for the whole analysis since it has the least cosmological information.

2.2. Modelling the DSS vector

Our modelling of the DSS signal is inspired by the LDT approach and builds from the original F18 model and the subsequent improvements presented in B22. We refer the reader to these two references for the complete details on the model calculations and highlight here only the broad principles and the minor modifications we have made. Briefly, the model consists of three key ingredients: (i) the PDF of the matter density contrast, smoothed with the filter function U, labelled $\delta_{{\rm m},U}$; (ii) the expectation value of the convergence inside a radius ϑ given the smoothed matter density contrast defined above; (iii) the distribution of $N_{\rm ap}$ values given $\delta_{{\rm m},U}$. B22 shows how these are computed for arbitrary filter functions and quantile counts. We, however, focus here on the 'adapted compensated' filter case, introduced in B20 and shown in figure 3 in B22, and five quantiles.

As in B22, the model is calibrated using the full-sky simulations described in Takahashi et al. (2017) to suppress the residual differences of the modelled and measured data vector. The KiDS-1000 lens distribution used in the current paper peaks at a lower redshift than that in B22, and we know that the DSS model is slightly less accurate in that case, but we will show that the calibration is accurate enough to yield unbiased results.

Since real galaxies are not expected to be perfectly Poisson-distributed, we modify the distribution of the aperture number computed in the B22 model in a way that allows for super-Poissonian shot noise. Inspired by F18, we achieve this by scaling the galaxy number density n_0 with a free parameter $\alpha > 0$, such that $n_0\,\alpha^{-1}$ can be interpreted as an effective number density of Poissonian tracers. This implies that the quantity $p(N_{\rm ap}\,\alpha^{-1}|\delta_{{\rm m},U})$ follows a log-normal distribution, instead of $p(N_{\rm ap}|\delta_{{\rm m},U})$ as in B22. Consequently, the characteristic function Ψ, determining the parameters of the log-normal distribution, must be modified to (see equation 36 of B22)

$$\Psi(t) = \exp\left(2\pi\frac{n_0}{\alpha}\int_0^\infty {\rm d}\vartheta\;\vartheta\;\left(1 + b\,\langle w_\vartheta|\delta_{{\rm m},U}\rangle\right)\left[{\rm e}^{{\rm i}tU(\vartheta)} - 1\right]\right)\,, \quad (7)$$

where w_ϑ is the mean 2D density contrast on a circle at ϑ (see Eq. 37 in B22), and b is the linear galaxy bias. Moreover, to ensure that the mean aperture number remains constant, we further modify the calculation of $p\left(N_{\rm ap}|\delta_{{\rm m},U}\right)$ as (see equation A39 of B22):

$$p\left(N_{\rm ap}|\delta_{{\rm m},U}\right) \to \frac{1}{\alpha}p\left(N_{\rm ap}\alpha^{-1}|\delta_{{\rm m},U}\right)\,. \quad (8)$$

Since the expectation value $\langle N_{\rm ap}|\delta_{{\rm m},U}\rangle \propto \alpha$ and the variance $\langle (N_{\rm ap} - \langle N_{\rm ap}|\delta_{{\rm m},U}\rangle)^2|\delta_{{\rm m},U}\rangle \propto \alpha^2$ we see that the ratio of variance to expectation value is proportional to α as required to describe deviations from Poissonian samples. Similar to Friedrich et al. (2018), we require $\alpha > 0.1$ in our parameter sampling for numerical reasons. We also compared our definition of this α parameter to the one implemented in Friedrich et al. (2018) and found no differences in the predictions.

Compared with numerical simulations, this model has been shown in B22 to be accurate, with residual inaccuracies to be everywhere significantly smaller than the statistical noise of the KiDS-1000 data. We, therefore, do not need to include a modelling error in our uncertainty budget. Furthermore, we also tested a non-linear galaxy bias model, where we exchanged the constant galaxy bias b with $b = b_1 + b_2\delta_{{\rm m},U} > 0$. However, b_2 was highly correlated with other parameters like $\Omega_{\rm m}$ which prevented our parameter estimation from converging and therefore had to be excluded for this analysis. We also test if the assumption of a linear galaxy bias is satisfied (see Fig. A.2 and its description), and the results of that test can be summarised as follows: a linear galaxy bias model is sufficient if an analysis using shear and $N_{\rm ap}$ information gives similar cosmological results as using only shear information since the shear profiles are basically insensitive to the galaxy bias model.

3. Observational data

In our analysis, we exploit the fourth data release of the KiDS (Kuijken et al. 2015, 2019; de Jong et al. 2015, 2017), which is a public survey carried out at the European Southern Observatory[1]. KiDS was designed for weak lensing applications, producing high-quality images with VST-OmegaCAM camera. Thanks to the infrared data from its overlapping partner survey VIKING (VISTA Kilo-degree Infrared Galaxy survey, Edge et al. 2013), galaxies are observed in nine optical and near-infrared bands, $u, g, r, i, Z, Y, J, H, K_s$, allowing for better control over redshift uncertainties (Hildebrandt et al. 2021, hereafter H21) to earlier releases. The weak lensing data in KiDS DR4 are collectively called 'KiDS-1000' as they cover $\sim$ 1000 deg^2 of images; this reduces to 777.4 deg^2 of the effective area after masking. These galaxies are further split into lens and source samples, which we discuss in more detail in the following sections, with properties summarised in Table 1.

3.1. Lens catalogues

Our primary lens catalogue is the 'KiDS-bright' sample described in Bilicki et al. (2021, hereafter Bi21), a flux-limited galaxy catalogue with accurate and precise photometric redshifts, $z_{\rm ph}$, derived using the nine photometric bands available in the KiDS-1000 data. This highly pure and complete[2] galaxy dataset was selected to match the properties of the partly overlapping Galaxy And Mass Assembly (GAMA, Driver et al. 2011) spectroscopic dataset. KiDS-bright is limited to $r < 20$ mag, covers $\sim$ 1000 deg^2 and contains about one million galaxies after artifact masking. To obtain photometric redshift estimates, Bi21 took advantage of the large amount of spectroscopic calibration data measured by GAMA and trained a supervised machine-learning neural network algorithm implemented in the ANNz2 software (Sadeh et al. 2016) to map an input space of 9-band magnitudes to an output redshift. The ANNz2 training sample consists of matched KiDS galaxies with spectroscopic redshifts from the GAMA equatorial fields, where that survey is the most complete and provides representative training data. The trained model was subsequently applied to the entire inference dataset, the photometrically-selected KiDS galaxies with the same $r < 20$ cut and magnitudes detected in the same nine bands. This sample spans the redshift range of $0 < z \lesssim 0.6$; however, since our analytical DSS model is less accurate for very small redshifts, we further exclude all galaxies with $z_{\rm ph} < 0.1$. This cut only slightly lowers the number of lenses and results in a projected number density of 0.325 arcmin^{-2}, as summarised in the first row of Table 1.

The main properties of interest to us are the galaxy bias, which has not been measured before for the KiDS-bright sample, the galaxy number density, and the redshift distribution, which is needed in the modelling. As shown in Bi21, the photometric redshift distribution of the full KiDS-bright sample is measured with high precision: jackknife subsampling reveals negligible mean bias, with a small overall scatter of $\sigma_z \approx 0.018(1+z)$. However, for our theoretical model, we need to estimate our newly selected foreground sample's true $n(z)$ distribution. We take advantage of the very good match between the GAMA spectroscopic sample and the KiDS-bright dataset, allowing us to build an accurate model of the photometric redshift error distribution, as discussed in Bi21. Following the description in Peacock & Bilicki (2018), an estimate of the true $n(z)$ can be obtained from a convolution between the normalised photometric redshift distribution of all the galaxies in our selected sample, $p(z_{\rm ph})$, and a photo-z error model $p_{\delta z}(\Delta z)$,

$$n(z) = \int p(z_{\rm ph})\,p_{\delta z}(\Delta z)\,{\rm d}z_{\rm ph}\,. \quad (9)$$

---

[1] The KiDS data products are public and available through `http://kids.strw.leidenuniv.nl/DR4`

[2] By purity, we mean very low fractions of stars and quasars (point sources) or artefacts. Completeness is evaluated with respect to GAMA.

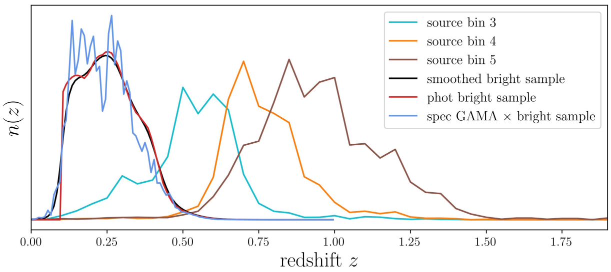

Fig. 1: Redshift distributions, $n(z)$, of the galaxy samples. The lens sample is obtained from the KiDS-bright galaxies described in Bi21. The blue line shows $n(z_{\rm spec})$, i.e. the redshift distribution of KiDS galaxies for which we have spectra from the GAMA survey. The red line shows $n(z_{\rm ph})$, the distribution of the full KiDS-bright sample as estimated by ANNz2 with a photometric redshift cut of $z_{\rm ph} < 0.1$. The black line shows our fiducial $n(z)$: a smoothed version of $n(z_{\rm ph})$ that better accounts for photometric redshift errors. The cyan, orange, and brown lines show the third, fourth and fifth redshift bins of the KiDS-1000 data, as estimated in H21. As the third bin strongly overlaps the sources, it is excluded from the analysis.

Following (Bilicki et al. 2014), we adopt a 'modified Lorentzian',

$$p_{\delta z}(\Delta z) \propto \left(1 + \frac{\Delta z^2}{2as^2}\right)^{-a} , \tag{10}$$

which was shown in Bi21 to reproduce the photo-z errors better than a Gaussian error model. In the above expression, $\Delta z = (z_{\rm ph} - z_{\rm spec})/(1 + z_{\rm spec})$, while the parameters a and s are fitted directly from the KiDS-bright galaxies that also have GAMA spectroscopic redshifts. The best-fit a and s values for our selection are provided in the top row of Table 1, and the resulting $n(z)$ is shown in black in Fig. 1.

In order to estimate the uncertainty on our $n(z)$ estimate, we notice that Eq. (9) has two ingredients: the photometric redshift distribution $n(z_{\rm ph})$, which is 'exact' in the sense that they are directly measured, and the photo-z error model $p_{\delta z}$. Putting aside possible systematic effects related to adopting this machine learning approach in this framework, we only need to quantify the uncertainty associated with our choice of the error model. To account for this, we measured how much the output $n(z)$ changes when the a and s parameters are determined from different sub-samples on the sky. For this, we split the KiDS-bright × GAMA matched sample into 10 sub-samples along the right ascension, where each sub-sample has the same number of objects. We fit a and s to each sub-sample with Eq. (10) and convolve the resulting $p_{\delta z}$ with the full $p(z_{\rm ph})$ of the KiDS-bright sample. The resulting 10 $n(z)$ distributions are almost indistinguishable from our best estimate, as displayed in Fig. A.3. We, therefore, conclude that we can safely neglect the error coming from the Lorentzian fit.

It is difficult to estimate all uncertainties accurately on the $n(z)$ estimate since, for this, we would need to test the ANN2z algorithm on another spectroscopic survey with the same selection. We investigate this further and study the impact of changing the shape and the mean of the $n(z)$. Therefore, beside the best estimated $n(z)$, we also consider to use the $n(z_{\rm ph})$ directly, as well as the spectroscopic redshift distribution $n(z_{\rm spec})$ itself, coming from the matched KiDS-bright × GAMA galaxies; both also shown in Fig. 1. We further allow the $n(z)$ to shift along the redshift direction to give the analysis some flexibility, where the shift value $\delta\langle z\rangle$ is drawn from a Gaussian with a standard deviation of 0.01 and vanishing mean, motivated by the uncertainty on the mean of the source redshift distribution.

In addition to the full lens sample described above, we take advantage of the colour information contained in the KiDS-bright data to construct colour-selected subsamples. This allows us to constrain the bias of blue and red galaxy populations separately from the DSS signal. Following Bi21, we use an empirical split between red and blue galaxies based on their location on the absolute r-band magnitude M_r and the rest-frame $u-g$ colour diagram. The rest-frame quantities are based on LePhare (Arnouts et al. 1999) with the derivations presented in Bi21. We apply a cut through the green valley in the colour-magnitude diagram, which results in a line that delimits the red and blue samples that satisfy

$$u - g = 0.825 - 0.025\,M_r\,. \tag{11}$$

We identify those galaxies that are at least 0.05 mag above (below) the cut line as red (blue) galaxies. We estimate their underlying redshift distributions following the same approach as for the full sample, and the resulting $n(z)$ are shown in Fig. B.1. The effective number densities and best-fit parameters of the modified Lorentzian redshift error model are also listed in the second and third rows of Table 1. We finally note that, while these colour-selected sub-samples are particularly interesting from a galaxy formation perspective, our main cosmological results are obtained from the full lens sample, which has the highest signal-to-noise.

3.2. Source catalogues

The fiducial KiDS-1000 cosmic shear catalogue consists of five tomographic bins, whose redshifts are calibrated using the self-organising map (SOM) method[3] of Wright et al. (2020) and presented in Hildebrandt et al. (2021). Although the five bins can be exploited in a cosmic shear analysis as in Asgari et al. (2021), for the DSS analyses, one must also be cautious about source-lens coupling, which arises if sources and lenses belong to the same gravitational potential. This can significantly affect our signal and bias our cosmological inference if left unmodeled. A significant redshift overlap between the source and lens distribution can result in further contamination by the IA of source galaxies that are tidally connected with the foreground lenses. We measure this effect in Sect. 4.2 from IA-infused weak lensing simulations and show that, given the KiDS-bright $n(z)$, this can be avoided by excluding the first three tomographic bins of the KiDS-1000 sources from the analysis. An additional lens-source coupling complication is the so-called boost factor, which arises due to the clustering of sources with over-dense and the anti-correlation of sources with under-dense regions. This can be taken into account by modifying the source $n(z)$ depending on clustering properties (Gruen et al. 2018). Since we exclude the third bin, we do not need to consider this further complication. The fourth and fifth redshift bins, shown as the orange and brown lines in Fig. 1, are separate enough from the lens $n(z)$ to avoid any appreciable lens-source coupling and are therefore used in our cosmological analysis. The uncertainty on the redshift distribution and the residual systematic offsets are very small, as listed in the last two rows of Table 1.

---

[3] The SOM method organises galaxies into groups based on their nine-band photometry and finds matches within spectroscopic samples. Galaxies for which no matches are found are removed from the catalogue.

Table 1: Overview of the observational KiDS-1000 data, describing the lens and source catalogues in this table's upper and lower parts, respectively. The a and s parameters enter the Lorentzian fitting function (see Eq. 10) and capture the uncertainty on the redshift of our lens sample. The uncertainties on the mean redshift, $\Delta\langle z\rangle$, for the lenses is motivated by the uncertainty from the sources, although it is probably an upper limit of the error. We show the mean and uncertainty on the redshift bias for the source samples, taken from H21 and used in Asgari et al. (2021). The rightmost columns displays the measured ellipticity dispersion per component, σ_ϵ measured in Giblin et al. (2021), and the shear multiplicative m-bias correction updated in van den Busch et al. (2022).

name	$n_{\rm eff}[\rm arcmin^{-2}]$	$\delta\langle z\rangle$	a	s
Full KiDS-bright sample	0.325	0.0 ± 0.01	2.613	0.0149
Red KiDS-bright sample	0.131	0.0 ± 0.01	3.099	0.0133
Blue KiDS-bright sample	0.165	0.0 ± 0.01	2.845	0.0166
name	$n_{\rm eff}[\rm arcmin^{-2}]$	$\delta\langle z\rangle$	σ_ϵ	m-bias $\times 10^3$
Source sample bin 4	1.26	0.011 ± 0.0087	0.25	8 ± 12
Source sample bin 5	1.31	-0.006 ± 0.0097	0.27	12 ± 10

The galaxy shear estimates are provided by the lensfit tool (Miller et al. 2013; Fenech Conti et al. 2017) and are described in more detail in Giblin et al. (2021), where it is shown that shear-related systematic effects do not cause more than a 0.1σ shift in $S_8 \equiv \sigma_8(\Omega_{\rm m}/0.3)^{0.5}$ when measured by cosmic shear two-point functions.

4. Simulated data

Besides the real KiDS-1000 data, we validate our inference pipeline on several simulated data sets, study the impact of key systematic uncertainties and carry out the cosmological inference. Namely, we use:

- The publicly available `FLASK` tool (Full-sky Log-normal Astro-fields Simulation Kit) described in Xavier et al. (2016) to estimate the covariance of errors in the DSS data vector of the KiDS-1000;
- the cosmo-SLICS+IA simulations, described in HD22, to quantify the impact of IA on our measurements and to validate the new $N_{\rm ap}$ segment in our pipeline (see the end of Sect. 2) that was not present in the B22 model;
- the *Magneticum* lensing simulations, first introduced in Hirschmann et al. (2014), to investigate the impact of stellar and AGN feedback.

More details are provided in the following sections.

4.1. FLASK log-normal simulations

Our cosmological inference analysis requires an estimate of the error covariance of the DSS data vector. Since an analytical covariance matrix for the DSS is challenging to compute, we make use instead of an ensemble of log-normal simulations produced with the publicly available `FLASK` tool[4] (Xavier et al. 2016). In Hilbert et al. (2011) it is shown that log-normal random fields are a good approximation to the 1-point PDF of the weak lensing convergence and shear field, and Friedrich et al. (2020) show that they are in fact accurate enough to estimate the covariance matrix for higher-order statistics in Stage-III lensing surveys (see their figure 4).[5] Compared to full N-body simulations, `FLASK` log-normal random fields are computationally cheap to create. The fact that `FLASK` outputs full-sky maps has the advantage that it can easily be masked to match the footprint of the data, making area re-scaling unnecessary. For the creation of our mock catalogues, we use the cosmological parameters that approximately match current cosmological analyses and fixed the matter density parameter to $\Omega_{\rm m} = 0.3$, the normalisation of the matter power spectrum to $\sigma_8 = 0.74$, the dimensionless Hubble parameter to $h = 0.7$, the dark energy equation-of-state parameter to $w_0 = -1$ and the power spectrum power law index to $n_s = 0.97$. Furthermore, we provide `FLASK` with the angular power spectrum of the projected matter density field, the convergence power spectrum for both source bins, and the two matter-lensing cross-spectra. By assuming a flat universe throughout this paper, given the $n(z)$ shown in Fig. 1, and using the PYCCL software package[6] (Chisari et al. 2019) to get the 3D matter density contrast power spectrum $P_\delta(\ell/\chi, \chi)$, we calculate the angular power spectrum by use of the Limber-approximated projection (Kaiser 1992) as

$$C_{i,j}(\ell) = \int_0^\infty \mathrm{d}\chi \, \frac{W_i(\chi)W_j(\chi)}{\chi^2} \, P_\delta(\ell/\chi, \chi)\,, \tag{12}$$

where i, j are placeholder for either the galaxy or convergence projection, such that $W_g(\chi) = n_{\rm l}(z[\chi])\frac{\mathrm{d}z(\chi)}{\mathrm{d}\chi}$ for the lenses with redshift distribution $n_{\rm l}$, while for the source with redshift distribution $n_{\rm s}$ we have instead

$$W_{\rm s}(\chi) = \frac{3\Omega_{\rm m}H_0^2}{2c^2}\int_\chi^\infty \mathrm{d}\chi' \, \frac{\chi(\chi'-\chi)}{\chi' a(\chi)} \, n_{\rm s}(z[\chi'])\frac{\mathrm{d}z[\chi']}{\mathrm{d}\chi'}\,. \tag{13}$$

Besides these angular power spectra, `FLASK` needs the log-normal shift parameters κ_0 and δ_0, where $-\kappa_0$ and $-\delta_0$ defining the lower limits of the log-normal random variable of the convergence and matter density fields, respectively. Whereas the shift parameter $\kappa_0 = \{0.02, 0.03\}$ for the convergence power spectra for the two source bins can be determined directly from the fitting formula equation (38) in Hilbert et al. (2011), we estimated the shift parameter $\delta_0 = \{0.57, 0.59, 0.56\}$ for the three lens samples (full, red, blue), as described in Gruen et al. (2016), by assuming that it can be approximated by the shift parameter of the smoothed density contrast, which in turn is calculated

---

[4] `FLASK`: `http://www.astro.iag.usp.br/~flask/`

[5] We tested that an area-rescaled covariance matrix coming from over 600 fully independent N-body simulations (see Harnois-Déraps et al. 2018, for a description of the SLICS simulation suite) results in similar constraints.

[6] Currently available here: `https://github.com/LSSTDESC/CCL`

from our model for a top-hat filter function (see equation 23 in B22). Given this setup, `FLASK` returns a foreground density map $\delta_{\rm m,2D}(\boldsymbol{\theta})$ and two sets of correlated shear and convergence grids $\gamma_{1,2}(\boldsymbol{\theta}), \kappa(\boldsymbol{\theta})$, one per tomographic source bin. We populate our mock KiDS-bright galaxies on the density map by sampling, for each pixel $\boldsymbol{\theta}$, a Poisson distribution with mean parameter $\lambda = n_{\rm eff}[1 + b\,\delta_{\rm m,2D}(\boldsymbol{\theta})]$, where $b = 1.4$ is the (constant) linear galaxy bias estimated from preliminary analyses with only some realisations[7] and $n_{\rm eff} = 0.325\,{\rm arcmin}^{-2}$ is the mean galaxy density of the KiDS-bright sample. Similarly, we populate the two source planes by Poisson-sampling for each pixel a number of source galaxies $n_{\rm pix}$ with parameter $\lambda = n_{\rm eff}A_{\rm pix}$, where $A_{\rm pix}$ is the area of the pixel under consideration[8], and the effective number density $n_{\rm eff}$ is taken from Table 1. We finally combine the two shear components of each object with their convergence to construct reduced shear components $g_{1,2}$, and further combine these with a shape noise contribution $\epsilon^{\rm s}$ taken from sampling a Gaussian distribution with vanishing mean and deviation σ_ϵ also taken from Table 1. This results in catalogues containing observed ellipticities $\boldsymbol{\epsilon}^{\rm obs}$ transformed as (Seitz & Schneider 1997)

$$\epsilon^{\rm obs} = \frac{\boldsymbol{\epsilon}^{\rm s} + \boldsymbol{g}}{1 + \boldsymbol{\epsilon}^{{\rm s},*}\boldsymbol{g}}\,. \tag{14}$$

Note that the quantities in bold here are all complex numbers, and the asterisk '$*$' indicates complex conjugation. This procedure ensures that we match the number of foreground and background galaxies in the data and the associated shape noise level.

4.2. cosmo-SLICS+IA

As mentioned earlier, the second suite of simulations is used to validate the inference pipeline and study the impact of IA on our DSS measurements. We use for this the fiducial suite of the cosmo-SLICS presented in Harnois-Déraps et al. (2019), which consists of a set of 50 simulated light-cones of 100 deg^2 each, run in a ΛCDM universe with $\Omega_{\rm m} = 0.2905$, $\Omega_\Lambda = 0.7095$, $\Omega_{\rm b} = 0.0473$, $h = 0.6898$, $\sigma_8 = 0.836$ and $n_{\rm s} = 0.969$. The mocks follow the non-linear evolution of 1536^3 particles up to $z = 0$, computed by the CUBEP^{3}M N-body code (Harnois-Déraps et al. 2013). For Fourier modes of comoving wave number $k < 2.0\,h\,{\rm Mpc}^{-1}$, the cosmo-SLICS three-dimensional dark matter power spectrum $P(k)$ agrees within 2% with the predictions from the Extended Cosmic Emulator (Heitmann et al. 2014), followed by a progressive deviation for higher k-modes (Harnois-Déraps et al. 2019), offering a sufficient resolution to model Stage-III galaxy surveys. The particle data were assigned onto mass sheets at 18 redshifts and then post-processed into 10×10 deg^2 light-cones. Lensing maps were produced at 18 source redshift planes for each cosmo-SLICS light cone and used to interpolate lensing information onto galaxy catalogues.

Like B22, we construct cosmo-SLICS mock source samples that reproduce a number of key data properties, including the tomographic $n(z)$, the galaxy number density $n_{\rm eff}$ and the shape noise levels. As for the `FLASK` simulations, we use Eq. (14) to add shape noise to the reduced shear signal. Source galaxies are placed at random positions on the light cones, and the shear quantities $(\gamma_{1/2}, \kappa)$ are interpolated at these positions from the enclosing lensing maps.

We also construct mock KiDS-bright samples by populating the light-cone mass maps with galaxies that trace the underlying dark matter field linearly, following the method presented in Harnois-Déraps et al. (2018). We here again fix the galaxy bias to 1.4 and an effective number density of $n_{\rm eff} = 0.325\,{\rm arcmin}^{-2}$.

4.2.1. IA infusion

The impact of galaxy IA is a known secondary signal to the cosmic shear measurements that have been neglected in past DSS studies. In this paper, we verify the validity of this assumption by measuring our statistics in simulated source data that are infused with IA. We will find that IA influences our data vector only if the lenses' $n(z)$ overlap with that of the sources. Following the methods described in HD22, the IA properties of these galaxies are computed as

$$\epsilon_1^{\rm IA} = -\frac{A_{\rm IA}\bar{C}_1\bar{\rho}(z)}{D(z)}(s_{xx} - s_{yy})\,, \quad \epsilon_2^{\rm IA} = -\frac{2A_{\rm IA}\bar{C}_1\bar{\rho}(z)}{D(z)}s_{xy}\,, \tag{15}$$

where $s_{ij} = \partial_{ij}\phi$ are the Cartesian components of the projected tidal field tensors interpolated at their positions, with ϕ being the gravitational potential. In the above expression, $A_{\rm IA}$ captures the strength of the coupling between the ellipticities and the tidal field, $\bar{\rho}(z)$ is the matter density, $D(z)$ is the linear growth factor, $\bar{C}_1 = 5 \times 10^{-14} M_\odot^{-1} h^{-2}\,{\rm Mpc}^3$, as calibrated in Brown et al. (2002). These intrinsic ellipticity components $\epsilon_{1/2}^{\rm IA}$ are then combined with the cosmic shear signal by Eq. (14), resulting in an IA-contaminated weak lensing sample that is consistent with the NLA model of Bridle & King (2007). We refer the reader to HD22 for full details about the IA infusion method. We test several values of $A_{\rm IA}$, more precisely, we infused $A_{\rm IA} = \{1, 1.5, 2\}$, and inspect in each case the impact on the DSS data vector.

4.3. Magneticum

Baryon feedback is also known to affect the distribution of the large-scale structure significantly, as the sustained outflows of energy arising from stellar winds, supernovae and AGN reduce the clustering on intra-cluster scales by up to tens of per cent (van Daalen et al. 2011). The exact strength of this suppression is still largely uncertain, with different hydro-dynamical simulations predicting different redshift and scale dependencies (see, e.g. Chisari et al. 2015, for a review of recent results). Without consensus, we opted to measure the DSS in one of these hydro-dynamical simulations for which the impact is quite high and inspect how an extreme baryon impact would affect our data vector.

The *Magneticum* lensing simulations were first introduced in Hirschmann et al. (2014) and used to mock up KiDS-450 and Stage-IV cosmic shear data (Martinet et al. 2021), and subsequently in Harnois-Déraps et al. (2021) to study the impact of baryons in the peak count analysis of the Dark Energy Survey Y1 data. The underlying matter field is constructed from the *Magneticum Pathfinder* simulations,[9] more specifically by the *Run-2* and *Run-2b* data described in Hirschmann et al. (2014) and Ragagnin et al. (2017). These are based on the GADGET3 smoothed particle hydrodynamical code (Springel 2005) and are able to reproduce a large number of observations (see Castro et al. 2021, for more details). These both co-evolve dark matter particles of

---

[7] Also different values would not affect the posteriors as we discuss in Sect.7.2.

[8] Note that the public KiDS-1000 mask is provided on a flat sky with a resolution of 0.01 arcmin^2. This will result in a `HEALPix` mask that varies from pixel to pixel given the fact that the pixelation is different and have a size of 0.74 arcmin^2.

[9] `www.magneticum.org`

mass $6.9{\times}10^8 h^{-1} M_\odot$ and gas particles with mass $1.4{\times}10^8 h^{-1} M_\odot$, in comoving volumes of side 352 and 640 h^{-1} Mpc, respectively. Included key mechanisms are radiative cooling, star formation, supernovae, AGN, and their associated feedback on the matter density field. From sequences of projected mass planes, we use the procedure outlined above for the cosmo-SLICS simulations to generate KiDS-1000 sources and KiDS-bright lenses for 10 pseudo-independent light-cones, each covering 100 deg^2. We repeat the same procedure on dark matter-only light-cones, such that any difference is caused by the presence of baryons.

We note that the cosmo-SLICS+IA and *Magneticum* light-cones are square-shaped, a geometry that accentuates the edge effects when the aperture filter overlaps with the light-cone boundaries. One could, in principle, weight the outer rims for each $N_{\rm ap}$ map, such that the whole map can be used; although this would increase our statistical power, it could also introduce a systematic offset. We opted instead to exclude the outer rim for each realization, resulting in an effective area of 36 deg^2, where a 2 deg band has been removed, matching the size of the adapted filter. This procedure also ensures that roughly the same number of background galaxies are used to calculate the shear profile around each pixel.

5. Cosmological parameter inference

Before performing several Markov chain Monte Carlo (MCMC) samplings in the following two sections, we describe here the pipeline of our Monte-Carlo sampler. In our different MCMC runs, the model vector, the data vector and the covariance matrix are varied, but the overall pipeline stays the same.

Table 2: Uniformly $\mathcal{U}$ and normally distributed $\mathcal{N}$ priors on the parameters used in our cosmological inferences. The normally distributed priors on the multiplicative shear m-bias and photometric redshift errors $\delta\langle z\rangle$ are used only for the real data analysis, not for the simulations where we set them to zero. The $\delta\langle z\rangle$ for the sources follow a joint normal distribution with covariance matrix $C_{\delta\langle z\rangle}$ shown in figure 6 of H21.

parameter	prior
$\Omega_{\rm m}$	$\mathcal{U}(0.20, 0.50)$
σ_8	$\mathcal{U}(0.45, 1.00)$
bias b	$\mathcal{U}(0.5, 2.5)$
α	$\mathcal{U}(0.1, 8)$
$\delta\langle z\rangle$ full KiDS-bright sample	$\mathcal{N}(0.0, 0.01)$
$\delta\langle z\rangle$ red KiDS-bright sample	$\mathcal{N}(0.0, 0.01)$
$\delta\langle z\rangle$ blue KiDS-bright sample	$\mathcal{N}(0.0, 0.01)$
$\delta\langle z\rangle$ source bin 4,5	$\mathcal{N}([0.011, -0.006], C_{\delta\langle z\rangle})$
m-bias source bin 4	$\mathcal{N}(0.002, 0.012)$
m-bias source bin 5	$\mathcal{N}(0.007, 0.010)$

Our statistical analysis has two free cosmological parameters that we fit for: the matter density parameter $\Omega_{\rm m}$ and the normalisation of the power spectrum σ_8. We additionally vary the galaxy bias term b and the super-Poissonnian shot-noise parameter α (see Eq. 7). We detail the prior ranges of all parameters in Table 2, where we also show the Gaussian priors for the nuisance parameters used in the data analysis (but not in the simulation-based validation runs).

For the estimated covariance matrix $\tilde{C}$, which itself is a random variable, Percival et al. (2022) suggested a procedure that uses a more general joint prior of the mean and covariance matrix as the Jeffreys prior proposed in equation 6 in Sellentin & Heavens (2016). The method by Percival et al. (2022) leads to credible intervals that can also be interpreted as confidence intervals with approximately the same coverage probability. From a data vector $\mathbf{d}$ and a covariance matrix $\tilde{C}$ measured from $n_{\rm r}$ simulated survey realisations, the posterior distribution of a model vector $\mathbf{m}$ that depends on n_θ parameters $\mathbf{\Theta}$ is

$$\boldsymbol{P}\left(\mathbf{m}(\mathbf{\Theta})|\mathbf{d},\tilde{C}\right) \propto |\tilde{C}|^{-\frac{1}{2}}\left(1+\frac{\chi^2}{n_{\rm r}-1}\right)^{-m/2} , \tag{16}$$

where

$$\chi^2 = [\mathbf{m}(\mathbf{\Theta})-\mathbf{d}]^{\rm T}\,\tilde{C}^{-1}\,[\mathbf{m}(\mathbf{\Theta})-\mathbf{d}] \, . \tag{17}$$

The power law index m is

$$m = n_\theta + 2 + \frac{n_{\rm r}-1+B(n_{\rm d}-n_\theta)}{1+B(n_{\rm d}-n_\theta)} \tag{18}$$

with $n_{\rm d}$ being the number of data points and

$$B = \frac{n_{\rm r}-n_{\rm d}-2}{(n_{\rm r}-n_{\rm d}-1)(n_{\rm r}-n_{\rm d}-4)} \, . \tag{19}$$

By setting $m = n_{\rm r}$ the formalism of Sellentin & Heavens (2016) is recovered.

Finally, since the model prediction is too slow for our MCMC, we use the emulation tool contained in `CosmoPower` (Spurio Mancini et al. 2022), which was first developed to emulate power spectra but can easily be adapted for arbitrary vectors. We trained the emulator on 2000 model points in the parameter space $\{\Omega_{\rm m}, \sigma_8, b, \alpha\}$ distributed in a Latin hypercube, where we also included $\delta\langle z\rangle$ Gaussian distributed values with the mean as shown in Table 2 but twice the standard deviation. To quantify the accuracy of the emulator, we calculated the model at 500 independent points in the same parameter space, as determined with the emulator or directly with the model and show the model vector accuracy in Fig. A.4. The fractional error is better than 2% (95% confidence level).

5.1. Reporting parameter constraints and goodness-of-fit

In this work, we followed the approach of Joachimi et al. (2021) to report our parameter constraints. In particular, we seek to report the global best fit to the data, i.e. the set of parameter values that provide the maximum a posteriori (MAP) distribution, computed as

$$\mathbf{\Theta}_{\rm MAP} = \underset{\mathbf{\Theta}}{\operatorname{argmax}}\left[\boldsymbol{P}(\mathbf{m}(\mathbf{\Theta})|\mathbf{d},\tilde{C})\right] . \tag{20}$$

where we found the maximum by running several minimisation processes. To estimate the resulting uncertainties around the MAP, we use the suggested projected-joint-highest-posterior-density (PJ-HPD) method, which calculates the parameter ranges that encompass the 68% and 95% credible intervals.

Furthermore, with the degrees of freedom (d.o.f.), we also report the reduced χ^2/d.o.f. to quantify the goodness-of-fit, where the χ^2 results from the point in the high-dimensional parameter space that has the highest posterior probability. To unbias the covariance matrix $\tilde{C}$, which is used to estimate the χ^2-values, we instead of inverting $\tilde{C}\,$h with the known Hartlap factor (Hartlap et al. 2007) defined as h $= (n_{\rm r}-1)/(n_{\rm r}-n_{\rm d}-2)$, but rather use

$$\tilde{C}' = \frac{(n_{\rm r}-1)\,[1+B(n_{\rm d}-n_\theta)]}{n_{\rm r}-n_{\rm d}+n_\theta-1}\tilde{C} \, . \tag{21}$$

To estimate the d.o.f. we measure for 1000 mock data vectors the best χ^2 and fit a χ^2 distribution to it. The 1000 mock data vectors are drawn from a multivariate Gaussian distribution, where the mean is the model prediction at the MAP values, and the covariance is the corresponding covariance matrix for that particular model. As we have only four free parameters and the rest are fixed by prior knowledge, we expect that the resulting d.o.f. is only slightly less than the raw number of elements in the data vector.

Lastly, we report the p-value in each case, which provides the probability of finding a χ^2 that is more extreme for the given d.o.f., and therefore indicates the goodness of fit. For our analysis, we choose a significance level of 0.01 to be a reliable fit.

We note here that we have verified with some selected cosmo-SLICS nodes that the theoretical model for the KiDS-bright sample is valid and accurate for $\sigma_8 < 1.0$, with indications that it loses accuracy for larger values of σ_8. This does not affect our results, given that the preferred values of σ_8 are well below this limit.

6. Validating the model on simulations

In this section, we validate our model on simulated measurements, several of which are infused with known and controlled systematic effects. The first (fiducial) test establishes that our model is unbiased in the simplest setup, where lens galaxies linearly trace the pure dark matter density maps, while source galaxies are given by the noise-free pure gravitational shear. The second test verifies that our results are unchanged in the presence of IA, as described in Sect. 4.2, while, lastly, we investigate the impact of baryonic physics on our statistics. The fiducial and the IA tests use 20 light cones, which have an unmasked area close to that of the KiDS-1000 footprint[10]. The measurements on the *Magneticum* mocks use the 10 available light-cones. Furthermore, we measured the shear profiles from KiDS-like mocks with shape noise to validate our model on a realistic data vector.

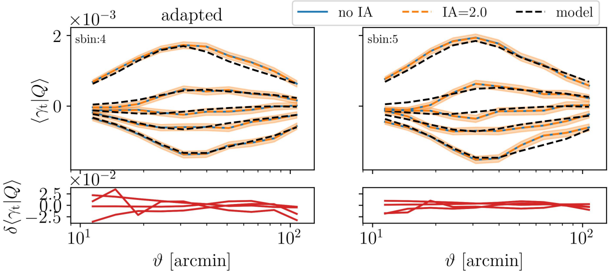

Fig. 2: Shear profiles measured with the adapted filter for the KiDS-bright-like lenses and sources from the cosmo-SLICS+IA simulations for two different IA amplitudes (see the legend). The orange regions are estimated from the covariance matrix, while the black dashed lines are obtained from our IA-free analytical predictions at the input cosmology and using the $n(z)$ shown in Fig. 1. As the differences between the shear profiles with varying IA amplitude can barely be seen, we display the relative difference between them in the bottom panels for the highest and lowest two quantiles.

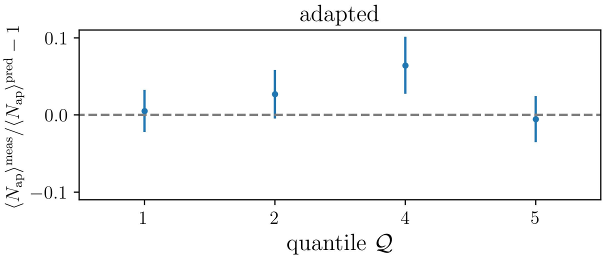

Fig. 3: Relative difference between the mean $\langle N_{\rm ap} \rangle$ measured in the cosmo-SLICS+IA bright mocks for four quantiles, and the value of $\langle N_{\rm ap} \rangle$ predicted by the model at the same cosmology. The blue error bars show the KiDS-1000 statistical uncertainty measured from `FLASK`.

6.1. Validation on intrinsic alignment

To quantify the influence of IA on our results, we performed an MCMC analysis on the mock infused with a strong IA amplitude ($A_{\rm IA} = 2.0$) and compared it to our fiducial model ($A_{\rm IA} = 0$). For this, we used the mocks described in Sect. 4.2, excluding the third source tomographic bin due to the lens-source coupling. The resulting profiles and mean relative number counts that are used for our pipeline validation are shown in Figs. 2 and 3, respectively. Although the aperture number is not affected by IA, it has a slight effect on the profiles, and hence we verify how it impacts the full data analysis. We performed this validation test for the adapted and top-hat filters but show the resulting shear signals, and the corresponding mean aperture number values only for the adapted filter since those of the top-hat filter are very similar and would not yield more insights.

To quantify our decision to discard the third source tomographic bin from our analysis, we show in Fig. A.5 the same shear profiles as in Fig. 2 but also the ones resulting from the third redshift bin, where we clearly see the third tomographic bin is heavily affected by IA, due to a significant overlap in redshift between the lens and source populations, and therefore would need additional modelling of IA, which we disregard for this work, and thus we exclude the third bin.

The MCMC results for the two IA amplitudes (no IA and IA = 2.0) are shown in Fig. 4. First, it is clearly shown that changing the IA amplitude does not affect the posterior at all. Second, and very importantly, the input cosmology is recovered. We observe a small offset on the parameter α, but the other parameters are all recovered within the 1 σ region. This confirms that the < 6% deviations seen on the aperture number count presented in Fig. 4 do not impact our cosmological inference. Finally, we observe an anti-correlation between the S_8 or σ_8 parameter and the galaxy bias b parameter, which is expected since all three parameters are directly correlated with the amplitude of the shear signal. This correlation and the correlation of S_8 and σ_8 to the α parameter could potentially impair the robustness of the later constrained parameters. However, these parameters are particularly important for our model and, therefore, can not be ignored. The same validation is done for the top-hat filter in Appendix C.

6.2. Validation on baryonic feedback

As a last important verification, we investigate for the first time the impact of baryons on the DSS with the *Magneticum* simulations described in Sect. 4.3. By combining the different DM-only and Hydro mock data for the lenses and sources, we end up with

---

[10] After removing the outer strip, each light-cone has an effective area of 36 deg^2, which roughly matches the unmasked area of the KiDS-1000 data if 20 light cones are added.

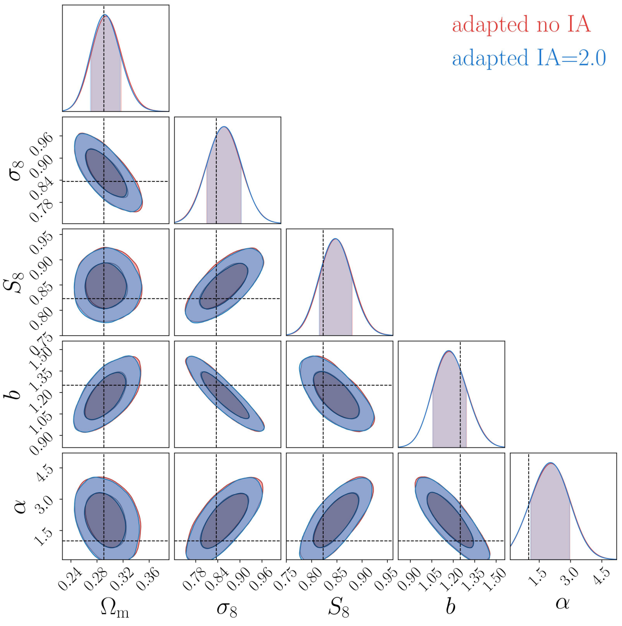

Fig. 4: Pipeline validation: Cosmological inference with the adapted filter using the cosmo-SLICS simulations with and without IA infusion, analysed with our model that ignores IA. The posteriors are almost indistinguishable from each other.

four scenarios (lens-source = DM-DM, DM-Hydro, Hydro-DM and Hydro-Hydro). Figure 5 shows the residuals between the shear profiles measured from dark matter-only mocks (DM-DM) to the other three combinations for each quantile. Clearly, the deviations are well inside the expected KiDS-1000 uncertainty. The biggest differences are seen if baryonic feedback processes are included in the lens mocks: some pixels, close to the $N_{\rm ap}$ threshold between two quantiles, are shifted to another quantile by the presence of baryons. This is in concordance with the mean aperture numbers reported in Fig. 6, which shows that the mean aperture numbers with baryons are slightly lower. Different to our studies of baryonic feedback like Heydenreich et al. (2022) or Harnois-Déraps et al. (2021), the inclusion of baryons in the sources has only a minor impact on the DSS, but as expected, becoming more important at small scales. In light of this, we can safely neglect the impact of baryons in our real data analysis.

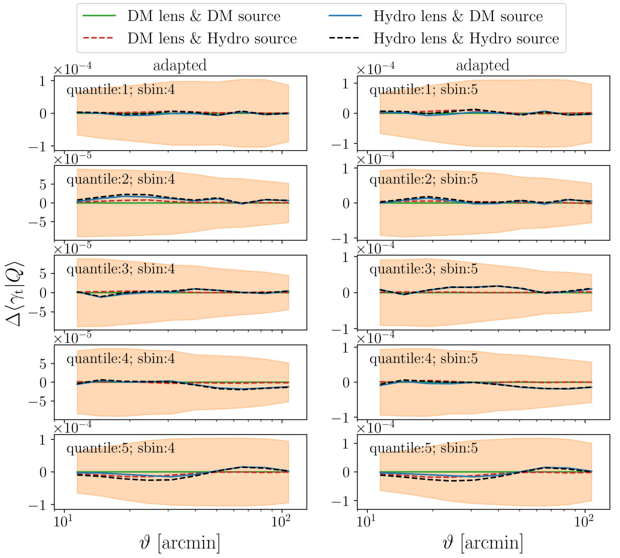

Fig. 5: Absolute differences between the mean shear profiles for all quantiles using either dark matter-only or full hydrodynamical *Magneticum* simulations. The residuals are with respect to the dark matter-only mocks for the lenses and sources and are always within the expected statistical uncertainty shown as the orange bands.

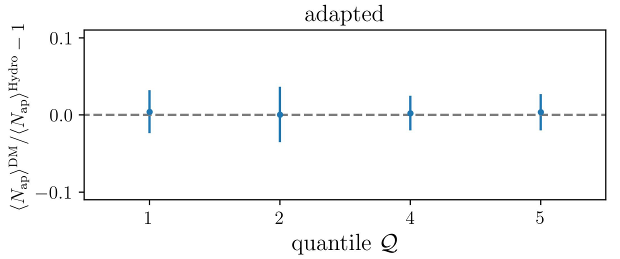

Fig. 6: Same as Fig. 3, but here comparing measurements from the hydro and dark matter-only *Magneticum* simulations. The relative difference is always well inside the expected statistical uncertainty of KiDS-1000.

7. Results and discussion

After validating our model to simulations in B22 and our additional testing on the impact of IA and baryonic physics, we are well equipped to analyse real lensing data accurately. As described in Sect. 3, we use the KiDS-bright sample as our foreground lenses and the fourth and fifth KiDS-1000 tomographic bins as our cosmic shear data. To recap, in our fiducial analysis, we used the $n(z)$ shown as the black solid line in Fig.1, we varied the two cosmological parameters $\Omega_{\rm m}$ and σ_8 as well as the two astrophysical parameters b and α. We marginalised over the systematic effects parameters describing the $\delta\langle z\rangle$ and m-bias uncertainty. In Figs. 7 and 8 we display the resulting shear profiles and mean aperture number. The model shown on these figures is computed at the best-fit MAP values, listed in the first column of Table 3. In that table, the p-values indicate that the data are well fitted by the model, being all well above our threshold value fixed at $p = 0.01$. The d.o.f. are estimated as described in Sect. 5.1, where we show in Fig. A.6 the distribution of χ^2 values and for which a χ^2-distribution with 81 d.o.f. fits well. As expected, the resulting d.o.f is slightly lower than the raw number of elements. The reduced χ^2 values are slightly below the expectation of 1.0, potentially indicating that the uncertainties could be slightly overestimated, although they are well inside the expected reduced χ^2 scatter of $\pm\sqrt{2}$, hence do not warrant further investigation.

Using the approach described in Sect. 5.1 to estimate the uncertainty around the MAP, we find

$$S_8^{\rm DSS} = 0.743^{+0.030}_{-0.024}\,, \tag{22}$$

which is consistent with and competitive to the KiDS-1000 cosmic shear constraints from Asgari et al. (2021),

$$S_8^{\rm COSEBIs} = 0.759^{+0.021}_{-0.024}\,. \tag{23}$$

We present the posterior of these two analyses in the left panel of Fig. 9, where the consistency between the two probes is obvious. The DSS has a slightly lower constraining power on S_8;

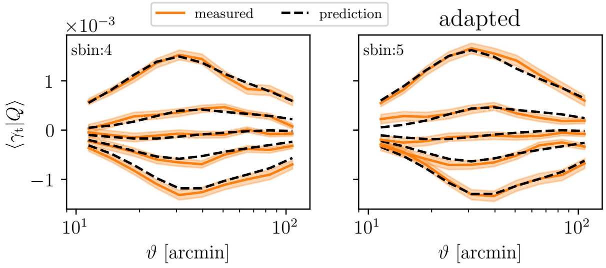

Fig. 7: Shear profiles measured in the data, compared to the best-fit predictions (MAP) obtained with values listed in Table 3, for the adapted filter. The shaded region shows the statistical uncertainty estimated from 1000 `FLASK` realisations.

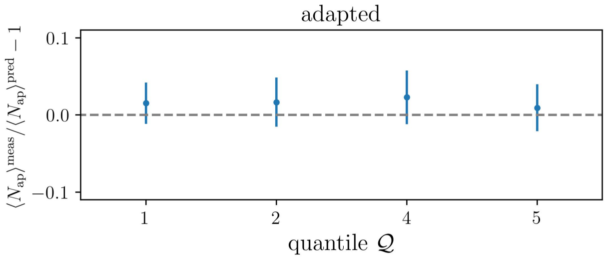

Fig. 8: Same as Fig. 3, but here comparing measurements from the KiDS-bright sample and our model, evaluated at the MAP values shown in Table 3. The measured $\langle N_{\rm ap}\rangle$ are all greater than the predicted $\langle N_{\rm ap}\rangle$ at MAP just indicating that the measured $p(N_{\rm ap})$ is broader than the predicted one.

however, the $\Omega_{\rm m}$-σ_8 degeneracy is broken, thanks to the additional information provided by the foreground data. But even for the shear-only case shown in green in Fig. 9, the DSS has better constraining power for the $\Omega_{\rm m}$ and σ_8 parameters, although the lower bound should be taken with caution as we excluded all $\Omega_{\rm m} < 0.2$, as the model does not agree with the cosmo-SLICS for smaller $\Omega_{\rm m}$ values. Furthermore, although the results of Fig. A.2 show that the inferred S_8 might be smaller compared to the truth if a linear galaxy bias model is not sufficient, the consistency between the shear-only DSS analysis to the complete DSS analysis supports the robustness of our inferred parameters with respect to the galaxy bias model (see the discussion at the end of Sect. 2.2). The comparison to the COSEBIs analysis reveals competitive S/N for the S_8 parameter while using only a fraction of the lensing sources (tomographic bins four and five). Caution should be taken when comparing their respective constraining power, as the COSEBIs analysis marginalises over more cosmological parameters and samples the parameter space differently. Nevertheless, it seems that a joint COSEBIs-DSS analysis could further improve the constraints, which we leave for future work. Lastly, as the DSS estimates of S_8 are slightly lower but with higher uncertainty, we measure a similar tension to the CMB results as the COSEBIs analysis.

In the next section, we investigate the robustness of our results with respect to the lens redshift distribution $n(z)$, of varying the covariance matrix. We further present our galaxy colour-split analysis and additionally discuss the galaxy bias b and α results.

7.1. Impact of lens redshift distribution

To estimate the impact of the shape of the lens galaxy redshift distribution (on top of shifting the mean by $\delta\langle z\rangle$ in the sampling), we repeat the analysis for the three $n(z)$ shown in Fig. 1. These are the smoothed version of the photometric redshift distribution $n(z)$, the photometric redshift distribution $n(z_{\rm phot})$ itself without any smoothing, and the spectroscopic redshift $n(z_{\rm spec})$ from those GAMA galaxies that are also in the KiDS-bright sample. Although Bi21 showed that GAMA is representative and that mismatches should be rare, the results from the GAMA spectroscopic $n(z_{\rm spec})$ should be taken with caution because the equatorial fields have a relatively small sky coverage, leading to features in the $n(z)$ that are caused by the large-scale structure present in these fields. For this investigation, we use the same setup as for the fiducial analysis, varying the two cosmological parameters $\Omega_{\rm m}$ and σ_8 together with the α and the linear galaxy bias b parameter. We also marginalised over the nuisance parameters shown bottom half of Table 2. In the right panel of Fig. 9 we display the different posteriors following from the three alternative $n(z)$. It is clearly seen that the posteriors are shifted along the $\Omega_{\rm m}$-σ_8 degeneracy axis, whereas these shifts partially cancel out for S_8. Due to the different lens $n(z)$, the amplitude and the slope of the shear signal predictions are slightly different. In particular, higher amplitude and steeper slope of the shear profiles result in larger σ_8 and smaller $\Omega_{\rm m}$, and vice-versa. Furthermore, we notice that the linear galaxy bias b and the noise α are stable against changes in the $n(z)$.

Lastly, in order to investigate the impact of our photometric redshift cut at $z_{\rm ph} = 0.1$ (see Sect. 3.1), we perform two additional analyses, this time modifying the photometric redshift threshold to $z_{\rm ph} > 0.15$ and $z_{\rm ph} > 0.2$. We find that the posteriors shifts are smaller than the 68% credibility region, indicating that removing low-redshift galaxies does not result in systematically different $\Omega_{\rm m}$ or σ_8.

Table 3: Overview of the marginalised MAP values and 68% confidence intervals resulting from MCMC chains where $\Omega_{\rm m}$, σ_8, α, and the linear galaxy bias parameter are varied. We fixed $h = 0.6898$, $w_0 = -1$ and $n_{\rm s} = 0.969$ but marginalised over the $\delta\langle z\rangle$ and m-bias uncertainties.

adapted	$n(z)$	$n(z_{\rm ph})$	$n(z_{\rm spec})$
$\Omega_{\rm m}$	$0.28^{+0.02}_{-0.02}$	$0.30^{+0.03}_{-0.02}$	$0.32^{+0.03}_{-0.03}$
σ_8	$0.78^{+0.04}_{-0.04}$	$0.76^{+0.04}_{-0.05}$	$0.74^{+0.04}_{-0.05}$
S_8	$0.74^{+0.03}_{-0.02}$	$0.76^{+0.03}_{-0.03}$	$0.77^{+0.04}_{-0.03}$
b	$1.32^{+0.12}_{-0.10}$	$1.31^{+0.14}_{-0.10}$	$1.28^{+0.13}_{-0.13}$
α	$1.35^{+0.79}_{-0.91}$	$1.42^{+0.82}_{-0.94}$	$1.86^{+0.92}_{-0.89}$
χ^2/d.o.f.	0.80	0.81	0.81
p-value	0.91	0.90	0.90

7.2. Cosmology scaling of the covariance matrix

The covariance matrix used in the main analysis is determined at a specific point in the parameter space (see Sect. 4.1), which is not identical to the MAP. However, assuming the MAP values are the true parameters, the most robust likelihood analysis would be achieved with a data covariance matrix estimated at the MAP values. This section, therefore, explores the impact of considering a cosmology-dependent covariance matrix.

In the related literature, there are two common approaches on whether the cosmology should be kept fixed in the covariance

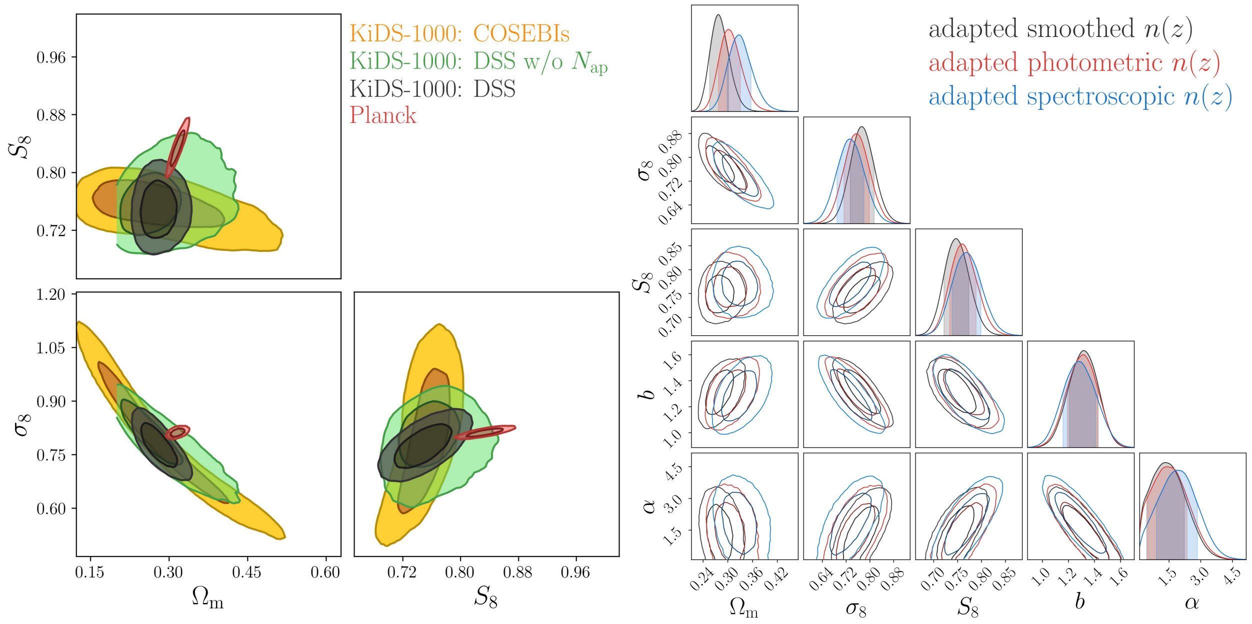

Fig. 9: On the left: Cosmological posteriors for the adapted filter for the best estimated $n(z)$ in black using the full data vector and in green using only shear information compared to the COSEBIs posteriors in orange presented in Asgari et al. (2021) and to the (TT, TE, EE+lowE) results of Planck Collaboration et al. (2020) in red. The sharp cut of the green posterior is due to the conservative prior of $\Omega_{\rm m} > 0.2$, as the model does not agree with the cosmo-SLICS for smaller $\Omega_{\rm m}$ values. The shear-only posterior is shown in this figure to support the assumption of using a linear galaxy bias model. On the right: Posteriors of the full DSS vector resulting from using the different lens $n(z)$ shown in Fig. 1. The $n(z_{\rm phot})$ and $n(z)$ have, by construction, the same mean redshift, while the mean redshift of the spectroscopic redshift estimate is ~ 0.015 lower. The main DSS results include a marginalisation over our uncertainty in the mean redshifts of both the lens and source samples, which partially compensates for some of these differences. The posterior obtained using the GAMA spectroscopic $n(z)$, shown in blue, should be taken with caution as it is estimated from a smaller sky coverage and, as such, contains larger statistical fluctuations.

matrix (van Uitert et al. 2018) or varied at each point sampled by the MCMC, as in Eifler et al. (2009). It is argued in Carron (2013) that the latter could result in over-constraints, whereas Kodwani et al. (2019) argues that the effect is small. We, therefore, explore both methods here.

We achieve our cosmology rescaling by assuming that the covariance matrix scales quadratically with the signal. This is only strictly true in the Gaussian regime; nevertheless, it is a good first approximation, even though the impact on the non-linear mode coupling is neglected in this approach.

To achieve the rescaling, we compute at a new cosmology $\boldsymbol{\Theta}$ the ratio between the predicted model $\boldsymbol{m}(\boldsymbol{\Theta})$ and the model predicted at the `FLASK` cosmology $\boldsymbol{m}\left(\boldsymbol{\Theta}^{\rm F}\right)$,

$$r_i(\boldsymbol{\Theta}) = \frac{\boldsymbol{m}_i(\boldsymbol{\Theta})}{\boldsymbol{m}_i\left(\boldsymbol{\Theta}^{\rm F}\right)}\,. \tag{24}$$

We then multiply each element of the fiducial covariance matrix, $C^{\rm F}_{ij}$, by the scaling factors,

$$C_{ij}(\boldsymbol{\Theta}) = C^{\rm F}_{ij}\, r_i(\boldsymbol{\Theta})\, r_j(\boldsymbol{\Theta})\,, \tag{25}$$

and obtain a cosmology-rescaled covariance matrix.

As explained in Eifler et al. (2009), this method is only valid for a noise-free covariance matrix since it wrongly rescales the shape-noise component and possibly over-estimates the cosmology changes. Finally, we note that in Eq. (16) the determinant of the covariance matrix changes with cosmology as well and needs to be recalculated.

Using our fiducial setup, we determine the posterior distribution in two distinct ways: first, by varying the covariance matrix alongside the model vector at each step of the MCMC, and second, by scaling the covariance matrix to the MAP value. For the latter approach, we use an iterative process, where we first estimate the MAP with the fiducial covariance matrix, then use the MAP parameters to scale the covariance matrix and find new MAP parameters; we repeated that process 100 times. As seen in Fig. A.7 after approximately 20 iterations the MAP values converged. The results are shown in Fig. 10, where the red posteriors used a covariance rescaled to the converged MAP value; the blue posteriors are for a full parameter-dependent covariance matrix varied in the MCMC; the black posteriors show the fiducial covariance. The red and black posteriors are almost identical, which is not surprising given the fact that the MAP values are very close to the parameters used to determine the covariance matrix. However, the blue contours slightly differ from the other two but are still within half $1\,\sigma$; we are therefore not concerned about the impact on our constraints of this analysis choice. In Stage IV surveys, this will be even less important due to the tighter posterior and the, therefore, smaller cosmology variation.

7.3. Red and Blue split

In this section, we present our final investigation, dividing the KiDS-bright sample into red and blue galaxies according to their colour as described in Sect. 3.1, and carry out a joint analysis. The motivation for this is to learn more about the behaviour of different galaxy types and as a cosmological robustness check. As for the main analysis, we use the best estimated $n(z)$, result-

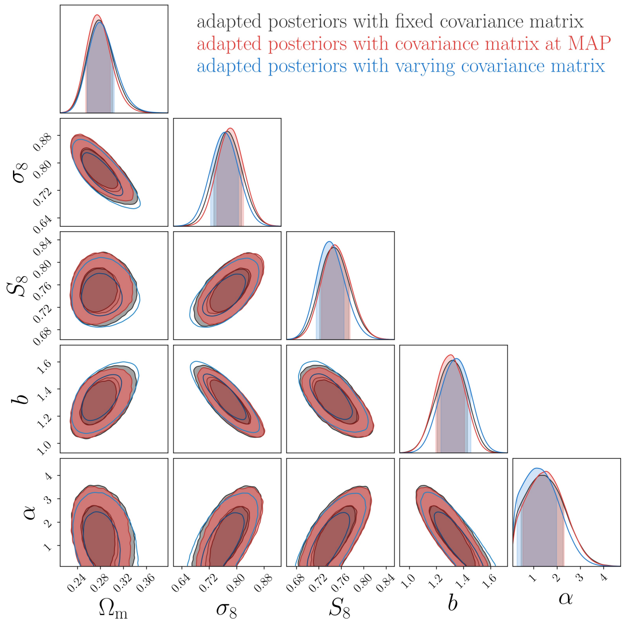

Fig. 10: Comparison between the posteriors obtained from our fiducial setup (with the covariance matrix calculated at the initial cosmology, see the black contours), with those obtained after scaling the covariance at the best-fit parameters (red) and to those obtained by varying the covariance with the parameters.

ing from smoothing the photometric redshifts after applying a $z_{\rm ph} > 0.1$ cut. In this setup, our data vector has 168 elements. But given the likelihood modelling described in Sect. 5, we are still confident in our results with respect to the remaining noise in the covariance matrix. As shown in Table 4, the reduced χ^2/d.o.f. = 1.07 indicates a valid fit. The resulting posteriors are shown in Fig. 11 and the MAP values are stated in Table 4.

First, we notice that the cosmological parameters of the full KiDS-bright sample analysis and the joint red and blue analysis are consistent and within $0.35\,\sigma$. Of particular interest in this investigation are the results obtained for the two astrophysical parameters, where we see that, as expected, the blue (red) sample prefers a smaller (larger) linear galaxy bias b compared to the full sample. This is in line with the fact that red galaxies are known to be more strongly clustered than blue galaxies and therefore have a larger galaxy bias (Mo et al. 2010). Furthermore, we find that the α parameter for the blue sample is significantly larger than unity, whereas the red sample tends to be below one. This shows that blue galaxies follow a super-Poisson distribution and red galaxies a sub-Poisson distribution. Following the results of Friedrich et al. (2022) who found that a higher satellite fraction leads to a higher α value, the blue sample has more satellites. The full sample overlaps with the blue and red posteriors and is consistent with a normal-Poisson distribution ($\alpha = 1.0$).

8. Summary and conclusions

In this work, we present an unblinded density split statistic analysis of the fourth data release of the Kilo-Degree survey (KiDS-1000). The analytical model used to infer cosmological and astrophysical parameters was first developed in Friedrich et al. (2018) then modified in Burger et al. (2022), and we further validated it on realistic simulated data. The lenses used to construct the foreground density map are taken from the KiDS-bright sample described in Bi21, while for our sources, we used the fourth and fifth tomographic redshift bins of the KiDS-1000 data described in H21.

We investigated for the first time the impact of baryons and IA on the DSS. While the effect of the former is suppressed due to the implied smoothing of the density map, IA can have an important role if the redshift distributions of the lenses and sources overlap. We carried out a full analysis on contaminated mock data without overlapping redshift distributions and found that for our selected data, we are immune to both of the systematic effects at the level of the inferred posteriors.

Table 4: Overview of the MAP values and 68% confidence intervals resulting from MCMC chains shown in Fig. 11. The first column is the same as in Table 3. We fixed $h = 0.6898$, $w_0 = -1$ and $n_s = 0.969$ but marginalised over the $\delta\langle z\rangle$ and m-bias uncertainties. If limits are not given they are dominated by priors.

adapted	full	red + blue	
Ω_m	$0.28^{+0.02}_{-0.02}$	$0.28^{+0.03}_{-0.02}$	
σ_8	$0.78^{+0.04}_{-0.04}$	$0.78^{+0.04}_{-0.03}$	
S_8	$0.74^{+0.03}_{-0.02}$	$0.75^{+0.03}_{-0.01}$	
b	$1.32^{+0.12}_{-0.10}$	$1.86^{+0.11}_{-0.14}$	$1.03^{+0.05}_{-0.10}$
α	$1.35^{+0.79}_{-0.91}$	$0.10^{+0.67}$	$2.25^{+0.34}_{-0.15}$
χ^2/d.o.f.	0.80	0.99	
p-value	0.91	0.51	

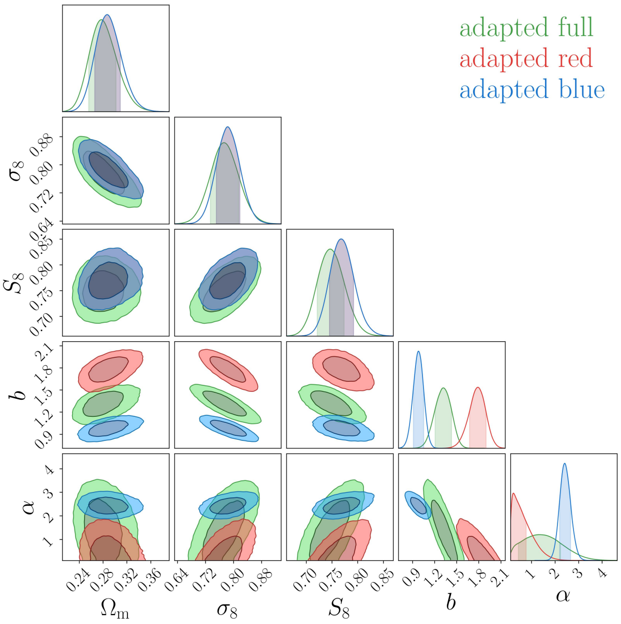

Fig. 11: Same as Fig. 9, but including a colour split. The posterior for the full KiDS-bright sample is shown in green, while the joint red+blue posteriors represent the results of the colour-selected samples. Note that in the latter case, the red and blue samples share the same cosmology (the dark blue contours) by construction. The resulting measured and best-fit predicted shear profiles for the red and blue samples are displayed in Fig. B.2 and the corresponding mean aperture number values are seen in Fig. B.3.

We explored the uncertainty of the redshift distribution of the lenses by investigating the impact on the posterior of changing the mean and the shape of the $n(z)$. In particular, we used for this the photometric redshift distribution $n(z_{\rm ph})$ with and without smoothing, as well as the distribution obtained directly from the overlapping spectroscopic GAMA galaxies. We found that the posteriors vary by less than $\sim 0.5\,\sigma$. Notably, we observed that of all parameters, $\Omega_{\rm m}$ is the most affected and is generally lower for broader $n(z)$; in contrast, σ_8 is increased, leaving S_8 values changed by $\sim 0.3\,\sigma$. We assigned an extra error term to this uncertainty, resulting in $S_8 = 0.743^{+0.030}_{-0.024} \pm 0.01$ for the $n(z)$ shape after marginalising over the other systematic effects. These constraints are competitive to and consistent with the KiDS-1000 cosmic shear constraints from Asgari et al. (2021).

Furthermore, we investigated the impact of varying the covariance matrix with cosmological parameters, where once we used an iterative process to scale the covariance matrix to the MAP best-fit parameters, and once we varied alongside the parameters in the MCMC process; for all cases, we record no significant deviations.

As our final result, we divided the full KiDS-bright sample into red and blue galaxies as a cosmology robustness check and to learn more about different galaxy types. For this, we performed a joint analysis of the red and blue samples with a joint covariance matrix with the smoothed version of $n(z_{\rm ph})$ as our best redshift estimate. The resulting posteriors of the full and joint red+blue analyses agree on the cosmological parameters within $0.35\,\sigma$. Furthermore, it shows the expected behaviour of the linear galaxy bias, where blue (red) galaxies have a lower (higher) bias than the full sample. The α parameter, which accounts for super-/sub-Poisson shot noise, also revealed interesting results. Whereas red galaxies have an α value that tends to be smaller than one ($\approx 1\,\sigma$), blue galaxies have an α value significantly larger than one ($\approx 6\,\sigma$), meaning that blue galaxies are super-Poisson distributed and red galaxies sub-Poisson distributed. According to Friedrich et al. (2020) this reveals information about the halo occupation distribution, with samples with a larger fraction of satellite galaxies tending to have larger α values than central.

We conclude from our results that the density split statistic is a valuable tool with a major advantage in the $\Omega_{\rm m}$-σ_8 degeneracy breaking. Besides this, it also yields a new way to measure the galaxy bias on linear scales and the Poissanity of different galaxy types. We save for future analysis the inference of the dark-energy-equation of state w, which can be achieved by a tomographic analysis of high-precision lensing and clustering data. Another aspect for future analysis is the modelling of a more complex galaxy bias model, and lastly the impact of the filter size, where we expect that smaller filter sizes are more constraining but also more sensitive to non-linear scales and baryonic analysis.

Acknowledgements. This paper went through the KiDS review process, where we especially want to thank the KiDS-internal referee Benjamin Joachimi for his fruitful comments to improve this work. Further, we would like to thank Mike Jarvis for maintaining `treecorr`, and Alessio Mancini to develop the `CosmoPower` emulator, which improved our work significantly. Lastly, we thank Sven Heydenreich, Laila Linke, Patrick Simon and Jan Luca van den Busch for very valuable discussion. PAB acknowledges support by the Deutsche Forschungsgemeinschaft, project SCHN342-13 and from the German Academic Scholarship Foundation. JHD acknowledges support from an STFC Ernest Rutherford Fellowship (project reference ST/S004858/1). OF gratefully acknowledges support by the Kavli Foundation and the International Newton Trust through a Newton-Kavli-Junior Fellowship and by Churchill College Cambridge through a postdoctoral By-Fellowship. MB is supported by the Polish National Science Center through grants no. 2020/38/E/ST9/00395, 2018/30/E/ST9/00698, 2018/31/G/ST9/03388 and 2020/39/B/ST9/03494, and by the Polish Ministry of Science and Higher Education through grant DIR/WK/2018/12. HH is supported by a Heisenberg grant of the Deutsche Forschungsgemeinschaft (Hi 1495/5-1) as well as an ERC Consolidator Grant (No. 770935). AHW is supported by a European Research Council Consolidator Grant (No. 770935). TC is supported by the INFN INDARK PD51 grant and the FARE MIUR grant 'ClustersXEuclid' R165SBKTMA. KD acknowledges support by the COMPLEX project from the European Research Council (ERC) under the European Union's Horizon 2020 research and innovation program grant agreement ERC-2019-AdG 882679 and by the Deutsche Forschungsgemeinschaft (DFG, German Research Foundation) under Germany's Excellence Strategy - EXC-2094 - 390783311. The calculations for the *Magneticum* simulations were carried out at the Leibniz Supercomputer Center (LRZ) under the project pr83li and with the support by M. Petkova through the Computational Center for Particle and Astrophysics (C2PAP). CH acknowledges support from the European Research Council under grant number 647112, and support from the Max Planck Society and the Alexander von Humboldt Foundation in the framework of the Max Planck-Humboldt Research Award endowed by the Federal Ministry of Education and Research. BJ acknowledges support by STFC Consolidated Grant ST/V000780/1. KK acknowledges support from the Royal Society, and Imperial College NM acknowledges support from the Centre National d'Etudes Spatiales (CNES) fellowship. HYS acknowledges the support from CMS-CSST-2021-A01 and CMS-CSST-2021-B01, NSFC of China under grant 11973070, the Shanghai Committee of Science and Technology grant No.19ZR1466600 and Key Research Program of Frontier Sciences, CAS, Grant No. ZDBS-LY-7013. TT acknowledges support from the Leverhulme Trust.
Author contributions: all authors contributed to the development and writing of this paper. The authorship list is given in three groups: the lead authors (PAB, OF, JHD, PS), where we ordered (OF, JHD, PS) alphabetically. PAB lead the paper, JHD provided all necessary simulations, OF and PS contributed to the modelling, and all four helped in the development of the analysis. The first author group is followed by two further alphabetical groups. The first alphabetical group includes those who are key contributors to both the scientific analysis and the data products. The second group covers those who have either made a significant contribution to the data products or to the scientific analysis.

References

Abbott, T. M. C., Abdalla, F. B., Alarcon, A., et al. 2018, Phys. Rev. D, 98, 043526
Amon, A., Gruen, D., Troxel, M. A., et al. 2022, Phys. Rev. D, 105, 023514
Arnouts, S., Cristiani, S., Moscardini, L., et al. 1999, MNRAS, 310, 540
Asgari, M., Lin, C.-A., Joachimi, B., et al. 2021, A&A, 645, A104
Asgari, M., Tröster, T., Heymans, C., et al. 2020, A&A, 634, A127
Barthelemy, A., Codis, S., & Bernardeau, F. 2021, MNRAS, 503, 5204
Bergé, J., Amara, A., & Réfrégier, A. 2010, ApJ, 712, 992
Bilicki, M., Dvornik, A., Hoekstra, H., et al. 2021, A&A, 653, A82
Bilicki, M., Jarrett, T. H., Peacock, J. A., Cluver, M. E., & Steward, L. 2014, ApJS, 210, 9
Bridle, S. & King, L. 2007, New Journal of Physics, 9, 444
Brouwer, M. M., Demchenko, V., Harnois-Déraps, J., et al. 2018, MNRAS, 481, 5189
Brown, M. L., Taylor, A. N., Hambly, N. C., & Dye, S. 2002, MNRAS, 333, 501
Burger, P., Friedrich, O., Harnois-Déraps, J., & Schneider, P. 2022, A&A, 661, A137
Burger, P., Schneider, P., Demchenko, V., et al. 2020, A&A, 642, A161
Carron, J. 2013, A&A, 551, A88
Castro, T., Borgani, S., Dolag, K., et al. 2021, MNRAS, 500, 2316
Chisari, N., Codis, S., Laigle, C., et al. 2015, MNRAS, 454, 2736
Chisari, N. E., Alonso, D., Krause, E., et al. 2019, ApJS, 242, 2
de Jong, J. T. A., Verdoes Kleijn, G. A., Boxhoorn, D. R., et al. 2015, A&A, 582, A62
de Jong, J. T. A., Verdoes Kleijn, G. A., Erben, T., et al. 2017, A&A, 604, A134
DES Collaboration, Abbott, T. M. C., Aguena, M., et al. 2021, arXiv e-prints, arXiv:2105.13549
Di Valentino, E., Anchordoqui, L. A., Akarsu, Ö., et al. 2021a, Astroparticle Physics, 131, 102605
Di Valentino, E., Anchordoqui, L. A., Akarsu, Ö., et al. 2021b, Astroparticle Physics, 131, 102604
Driver, S. P., Hill, D. T., Kelvin, L. S., et al. 2011, Monthly Notices of the Royal Astronomical Society, 413, 971
Edge, A., Sutherland, W., Kuijken, K., et al. 2013, The Messenger, 154, 32
Eifler, T., Schneider, P., & Hartlap, J. 2009, A&A, 502, 721
Fenech Conti, I., Herbonnet, R., Hoekstra, H., et al. 2017, MNRAS, 467, 1627
Friedrich, O., Gruen, D., DeRose, J., et al. 2018, Phys. Rev. D, 98, 023508
Friedrich, O., Halder, A., Boyle, A., et al. 2022, MNRAS, 510, 5069
Friedrich, O., Uhlemann, C., Villaescusa-Navarro, F., et al. 2020, MNRAS, 498, 464

Fu, L., Kilbinger, M., Erben, T., et al. 2014, MNRAS, 441, 2725
Giblin, B., Heymans, C., Asgari, M., et al. 2021, A&A, 645, A105
Górski, K. M., Hivon, E., Banday, A. J., et al. 2005, ApJ, 622, 759
Gruen, D., Friedrich, O., Amara, A., et al. 2016, MNRAS, 455, 3367
Gruen, D., Friedrich, O., Krause, E., et al. 2018, Phys. Rev. D, 98, 023507
Hamana, T., Shirasaki, M., Miyazaki, S., et al. 2020, PASJ, 72, 16
Harnois-Déraps, J., Amon, A., Choi, A., et al. 2018, MNRAS, 481, 1337
Harnois-Déraps, J., Giblin, B., & Joachimi, B. 2019, A&A, 631, A160
Harnois-Déraps, J., Martinet, N., Castro, T., et al. 2021, MNRAS, 506, 1623
Harnois-Déraps, J., Martinet, N., & Reischke, R. 2022, MNRAS, 509, 3868
Harnois-Déraps, J., Pen, U.-L., Iliev, I. T., et al. 2013, MNRAS, 436, 540
Hartlap, J., Simon, P., & Schneider, P. 2007, A&A, 464, 399
Heitmann, K., Lawrence, E., Kwan, J., Habib, S., & Higdon, D. 2014, ApJ, 780, 111
Heydenreich, S., Brück, B., Burger, P., et al. 2022, arXiv e-prints, arXiv:2204.11831
Heymans, C., Tröster, T., Asgari, M., et al. 2021, A&A, 646, A140
Hilbert, S., Hartlap, J., & Schneider, P. 2011, A&A, 536, A85
Hildebrandt, H., van den Busch, J. L., Wright, A. H., et al. 2021, A&A, 647, A124
Hildebrandt, H., Viola, M., Heymans, C., et al. 2017, MNRAS, 465, 1454
Hirschmann, M., Dolag, K., Saro, A., et al. 2014, MNRAS, 442, 2304
Jarvis, M., Bernstein, G., & Jain, B. 2004, MNRAS, 352, 338
Joachimi, B., Lin, C. A., Asgari, M., et al. 2021, A&A, 646, A129
Joudaki, S., Blake, C., Johnson, A., et al. 2018, MNRAS, 474, 4894
Joudaki, S., Hildebrandt, H., Traykova, D., et al. 2020, A&A, 638, L1
Kaiser, N. 1992, ApJ, 388, 272
Kilbinger, M. & Schneider, P. 2005, A&A, 442, 69
Kodwani, D., Alonso, D., & Ferreira, P. 2019, The Open Journal of Astrophysics, 2, 3
Kuijken, K., Heymans, C., Dvornik, A., et al. 2019, A&A, 625, A2
Kuijken, K., Heymans, C., Hildebrandt, H., et al. 2015, MNRAS, 454, 3500
Martinet, N., Castro, T., Harnois-Déraps, J., et al. 2021, A&A, 648, A115
Miller, L., Heymans, C., Kitching, T. D., et al. 2013, MNRAS, 429, 2858
Mo, H., van den Bosch, F. C., & White, S. 2010, Galaxy Formation and Evolution
Peacock, J. A. & Bilicki, M. 2018, MNRAS, 481, 1133
Percival, W. J., Friedrich, O., Sellentin, E., & Heavens, A. 2022, MNRAS, 510, 3207
Pires, S., Leonard, A., & Starck, J.-L. 2012, MNRAS, 423, 983
Planck Collaboration, Aghanim, N., Akrami, Y., et al. 2020, A&A, 641, A5
Pyne, S. & Joachimi, B. 2021, MNRAS, 503, 2300
Ragagnin, A., Dolag, K., Biffi, V., et al. 2017, Astronomy and Computing, 20, 52
Reimberg, P. & Bernardeau, F. 2018, Phys. Rev. D, 97, 023524
Sadeh, I., Abdalla, F. B., & Lahav, O. 2016, PASP, 128, 104502
Sánchez, A. G., Scoccimarro, R., Crocce, M., et al. 2017, MNRAS, 464, 1640
Schneider, P. 1996, MNRAS, 283, 837
Schneider, P. 1998, ApJ, 498, 43
Seitz, C. & Schneider, P. 1997, A&A, 318, 687
Sellentin, E. & Heavens, A. F. 2016, MNRAS, 456, L132
Smith, A., Cole, S., Baugh, C., et al. 2017, MNRAS, 470, 4646
Springel, V. 2005, MNRAS, 364, 1105
Spurio Mancini, A., Piras, D., Alsing, J., Joachimi, B., & Hobson, M. P. 2022, MNRAS, 511, 1771
Takahashi, R., Hamana, T., Shirasaki, M., et al. 2017, ApJ, 850, 24
van Daalen, M. P., Schaye, J., Booth, C. M., & Dalla Vecchia, C. 2011, MNRAS, 415, 3649
van den Busch, J. L., Wright, A. H., Hildebrandt, H., et al. 2022, arXiv e-prints, arXiv:2204.02396
van Uitert, E., Joachimi, B., Joudaki, S., et al. 2018, MNRAS, 476, 4662
Wright, A. H., Hildebrandt, H., van den Busch, J. L., et al. 2020, A&A, 640, L14
Xavier, H. S., Abdalla, F. B., & Joachimi, B. 2016, MNRAS, 459, 3693
Zürcher, D., Fluri, J., Sgier, R., et al. 2022, MNRAS, 511, 2075

Appendix A: Additional plots

In this section, we show additional plots which belong to the main text. We start by visualising the shear profiles that result in different threshold values for the effective area above which pixels are used for the analysis in Fig. A.1.

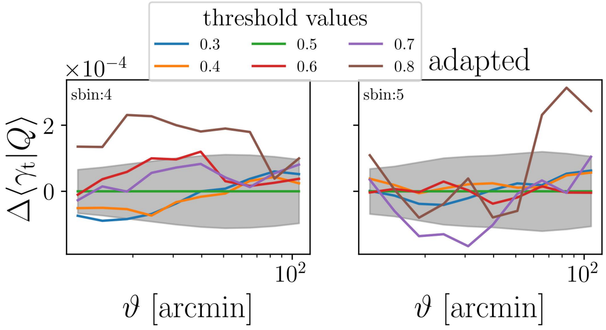

Fig. A.1: Residual shear profiles of the highest quantile filter for different threshold values that the effective area must exceed to be used with respect to the shear profiles with a 0.5 threshold. It is seen that for threshold values above 0.6 the shear profiles deviate more than one standard deviation (grey band) due to decreasing remaining area.

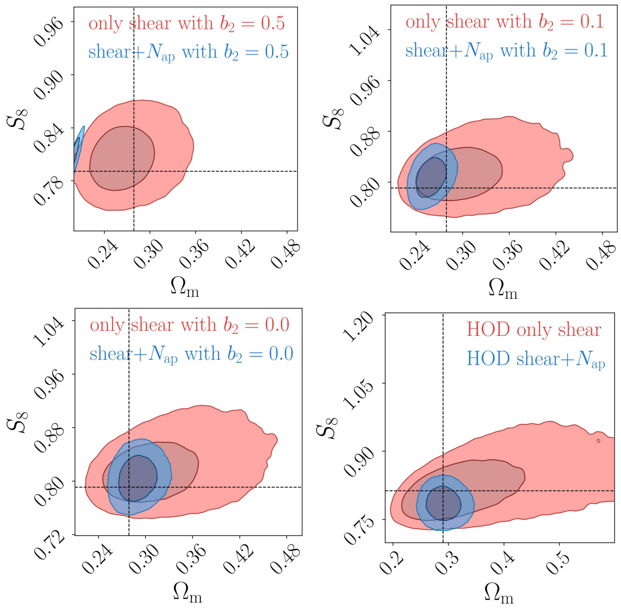

Fig. A.2: Posterior distributions, using different b_2 values to distribute galaxies to the same density contrast, from which a data vector is measured. The lower right panel shows the posterior results from simulations, where galaxies are distributed with a HOD. The model vector uses for all four cases a linear galaxy bias model.

In Fig. A.2 we show different posterior distributions, to test whether our analytical model with a linear galaxy bias model gives robust cosmological results even if galaxies are placed with Poisson process with mean $\lambda = n_{\rm eff}[1 + b_1\,\delta_{\rm m,2D}(\boldsymbol{\theta}) + b_2\,(\delta^2_{\rm m,2D}(\boldsymbol{\theta}) - \langle\delta^2_{\rm m,2D}\rangle)]$, where $\delta_{\rm m,2D}$ is the projected density contrast or with with an halo occupation distribution (HOD) description (Smith et al. 2017). For the Poisson process test, we use the simulation of Takahashi et al. (2017) with sources that mimic the fourth and fifth KiDS-1000 bins and lenses that mimic the KiDS-bright sample. For the HOD analysis, we measure the data vector, and the covariance from 614 SLICS realisations with noisy KiDS-1000 sources and GAMA lens mocks (see Harnois-Déraps et al. 2018, for a detailed description), where the covariance is scaled to approximately match the KIDS-1000 footprint. It is clearly seen that the posterior for $b_2 > 0$ are strongly biased if shear and $N_{\rm ap}$ information are used, whereas using only shear information, the posterior are unbiased as they are almost insensitive to the galaxy bias model. Although the HOD analysis already shows that the linear galaxy bias assumption is sufficient, if the posterior using shear and $N_{\rm ap}$ information is consistent with the posterior using only shear information gives additional confidence that $b_2 \approx 0$.

In Fig. A.3 we show that negligible difference of the lens $n(z)$ if the Lorentzian fitting parameters (a and s) are estimated from different patches of the sky.

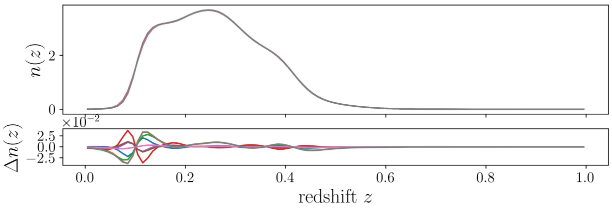

Fig. A.3: Redshift distribution of the full KiDS-bright sample resulting from Lorentzian fitting parameters (a and s), which in turn are determined from different patches on the sky. In the bottom panel, the absolute differences to the best estimated $n(z)$ are shown.

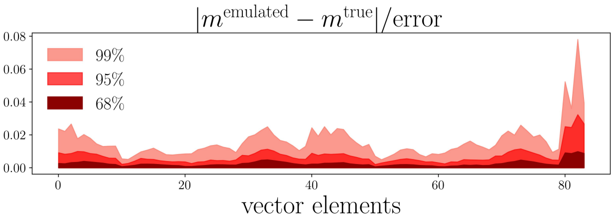

Fig. A.4: Upper panel: Relative difference of the χ^2 predicted from the emulator to ones predicted from the model. The mean and standard deviation is shown in the legend indicate the predictions from the emulator to be mostly below 0.5%. Lower panel accuracy of the emulated full model data vector $m(\boldsymbol{\Theta})$ scaled by the expected KiDS-1000 uncertainty. Both plots indicate that the error of the emulator is negligible.

In Fig. A.4 we display the accuracy of the emulator, and in Fig. A.5, that the third tomographic bin is indeed contaminated by IA, in Fig. A.6 the χ^2 distribution of mock data vectors around the MAP for the adapted filter with the best estimated $n(z)$, and lastly in Fig. A.7 the iterative process to find the optimal MAP values by scaling the covariance matrix to the previously found MAP.

Appendix B: Additional material for the red and blue analysis

Here in this chapter, we show the complementary plots for the joint red+blue analysis. In Fig. B.1 the redshift distribution for the red and blue samples is shown, resulting from the smoothing method described in Sect.3.1. In Fig. B.2 we show the shear

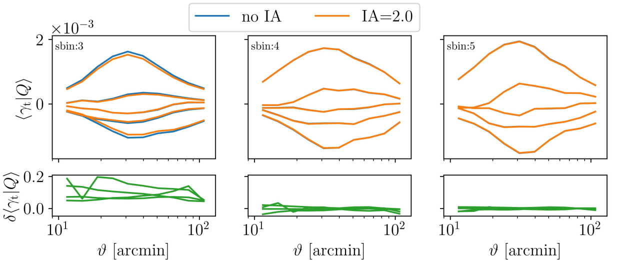

Fig. A.5: Shear profiles of the cosmo-SLICS for the bright lens and all three source mocks with the $n(z)$ shown in Fig. 1 for two different IA amplitudes for the adapted filter. The third source tomographic bin is strongly contaminated by IA due to the significant overlap with the lens $n(z)$ and is therefore excluded from this analysis.

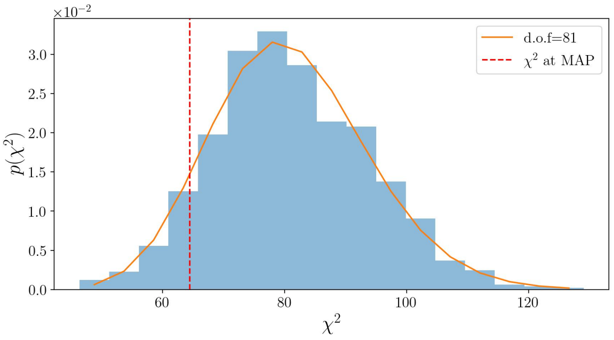

Fig. A.6: Distribution of χ^2 values of mock data vectors that follow from multivariate Gaussian distributions, where the mean is the model prediction at MAP and the covariance is the corresponding covariance for that particular model. The red line shows the χ^2 values using the real data vector. The orange line is a χ^2 distribution with d.o.f. = 81, which is slightly smaller than the 84 elements of the data vector.

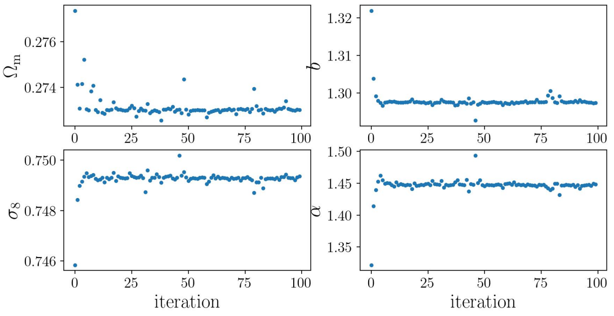

Fig. A.7: Change of MAP values due to scaling of the covariance to the previously measured MAP values. Roughly after 10 iterations, the process converged, where the occasional outliers happened if the minimisation process stopped to early by coincidence.

profiles; in Fig. B.3 the mean aperture number values for both samples which are used as the model and data vectors.

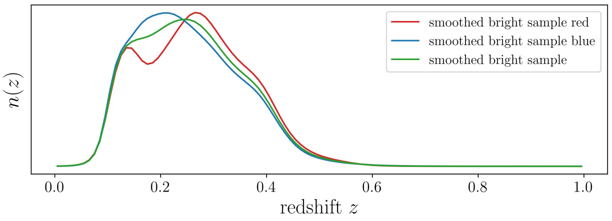

Fig. B.1: Best estimated redshift distributions of the red and blue KiDS-bright samples in red and blue, with the full KiDS-bright sample in green.

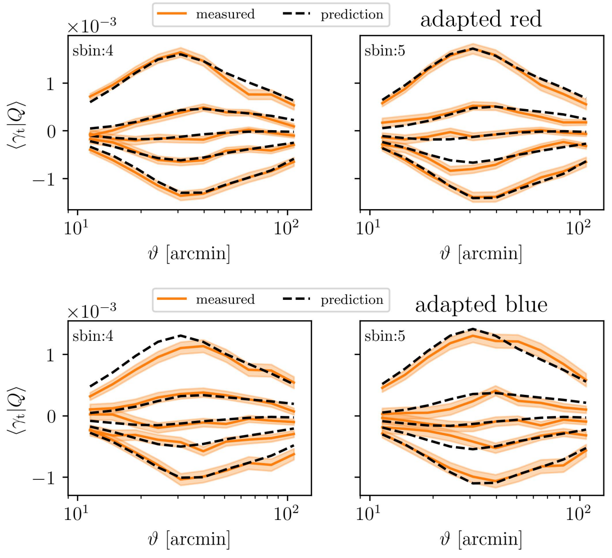

Fig. B.2: Measured and predicted shear profiles at the MAP values for the adapted filter for the red and blue samples. The shaded region is the expected KiDS-1000 uncertainty estimated from the 1000 `FLASK` realisations with shape noise.

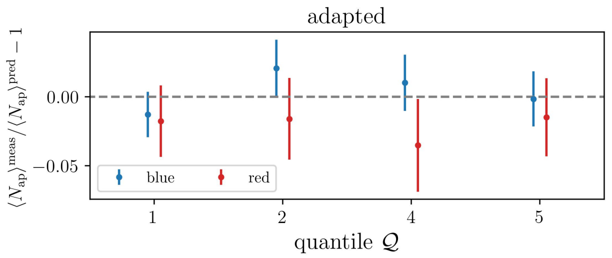

Fig. B.3: Mean aperture number of the red and blue sample, where the predictions follow from a joint minimisation process. Different to the full bright sample the measured $p(N_{\mathrm{ap}})$ is smaller than the predicted Map, resulting in the measured $\langle N_{\mathrm{ap}}\rangle$ being smaller.

Appendix C: Top-hat filter analysis

This section shows the corresponding plots that belong to the analysis with the top-hat filter. We start by showing in Fig. C.1 the validation for the top-hat with the cosmo-SLICS, which shows that the true parameters are always inside $1\,\sigma$. The discussion from Sect. 7.1 about the impact of different redshifts distributions is summarised for the top-hat filter in Table C.1, which shows with the given reduced χ^2 and corresponding p-value that the model is well fitted to the data given the covariance matrix, and result in parameters that are consistent to the ones constrained with the adapted filter.

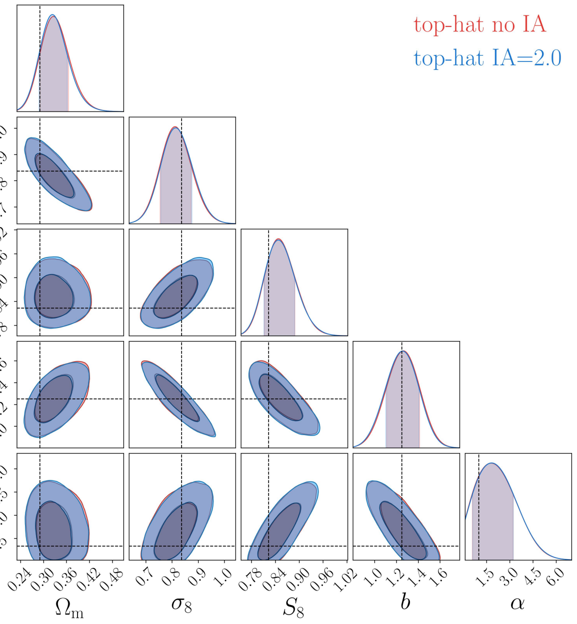

Fig. C.1: MCMC results for the top-hat filter using the model and simulations where we infused the pure shear signal with different amplitudes of IA.

Table C.1: Overview of the marginalised MAP values and 68% confidence intervals resulting from MCMC chains where Ω_m, σ_8, the α and the linear galaxy bias parameter are varied. We fixed $h = 0.6898$, $w_0 = -1$ and $n_\mathrm{s} = 0.969$ but marginalised over the $\delta\langle z\rangle$ and m-bias uncertainties. If limits are not given, they are dominated by priors.

top-hat	$n(z)$	$n(z_\mathrm{ph})$	$n(z_\mathrm{spec})$
Ω_m	$0.31^{+0.04}_{-0.03}$	$0.34^{+0.05}_{-0.04}$	$0.36^{+0.05}_{-0.04}$
σ_8	$0.68^{+0.05}_{-0.05}$	$0.65^{+0.05}_{-0.05}$	$0.62^{+0.05}_{-0.05}$
S_8	$0.68^{+0.04}_{-0.02}$	$0.69^{+0.04}_{-0.01}$	$0.68^{+0.04}_{-0.02}$
b	$1.66^{+0.14}_{-0.20}$	$1.69^{+0.15}_{-0.22}$	$1.73^{+0.15}_{-0.23}$
α	$0.10^{+2.09}$	$0.10^{+2.12}$	$0.10^{+2.24}$
χ^2/d.o.f.	1.02	1.03	1.04
p-value	0.44	0.41	0.39

Finally we show in Fig. C.2 and Table C.2 the analogous results for the top-hat filter to the adapted filter as shown in Fig. 11 and Table 4. The p-value for the joint red+blue indicates that the given d.o.f. has a significant tension between the measured data and the best fit model. Although this reduced χ^2 is not ideal for the given d.o.f., we still perform the analysis, but note that the posteriors should be taken with caution, which is already true because we are uncertain about the true $n(z)$ of the sub-samples. Overall the results show the same trends as for the adapted filter, where the blue galaxies result in smaller bias b and larger α than the red galaxies. The reason for the top-hat filter performing worse than the adapted filter is unclear. Nevertheless, besides the fact that the $n(z)$ of the red and blue sample is quite uncertain, both filters are probing on fundamentally different scales so that different behaviours are not surprising.

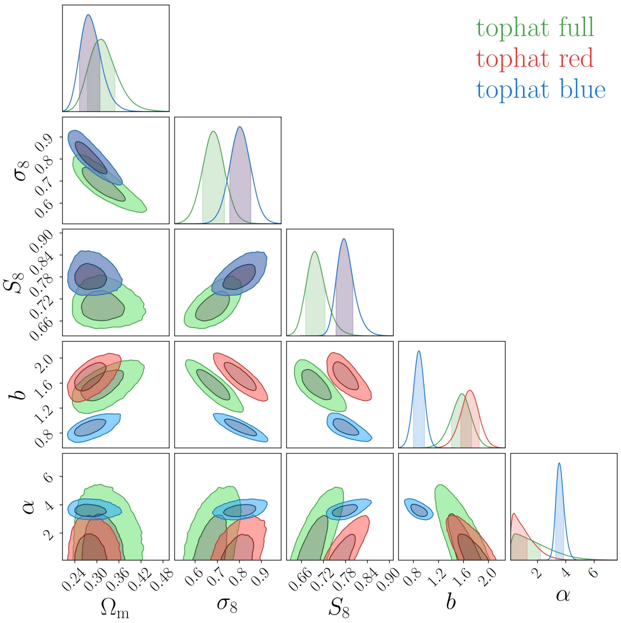

Fig. C.2: The posterior for the full KiDS-bright sample is shown in green, while the joint red+blue posteriors represent the results of the individual colour-selected samples. Note that in the latter case, by construction, the red and blue samples share the same cosmology (the dark blue contours).

Table C.2: Overview of the MAP values resulting from MCMC chains shown in Fig. C.2. We fixed $h = 0.6898$, $w_0 = -1$ and $n_\mathrm{s} = 0.969$ but marginalised over the $\delta\langle z\rangle$ and m-bias uncertainties. If limits are not given, they are dominated by priors.

top-hat	full	red + blue	
Ω_m	$0.31^{+0.04}_{-0.03}$	$0.27^{+0.03}_{-0.02}$	
σ_8	$0.68^{+0.05}_{-0.05}$	$0.79^{+0.06}_{-0.04}$	
S_8	$0.68^{+0.04}_{-0.02}$	$0.76^{+0.04}_{-0.01}$	
b	$1.66^{+0.14}_{-0.20}$	$1.78^{+0.10}_{-0.20}$	$0.94^{+0.08}_{-0.11}$
α	$0.10^{+2.09}$	$0.10^{+1.20}$	$3.35^{+0.44}_{-0.15}$
χ^2/d.o.f.	1.02	1.35	
p-value	0.44	0.001	

Contribution summary

In this additional chapter, I summarise all my work during my PhD.

In the publication B20, I derived in cooperation with Peter Schneider a new filter function for the density split statistic (DSS), that is optimised in terms of signal-to-noise ratio (S/N). Although this work is based on my master's thesis, I started writing the paper during the first period of my PhD, updated several results during this process, and went through the full Kilo-Degree Survey (KiDS) consortium review process.

The first main project of my PhD was then published in B22a, where I modified in cooperation with Peter Schneider and Oliver Friedrich the original DSS model presented in Friedrich et al. (2018, hereafter F18) in such a way that it can use general filter functions. During this work, I changed the mathematical calculations and the implementation of all necessary components of the analytical model, introducing entirely new approaches to the solution. Furthermore, using the public available Takahashi et al. (2017, hereafter T17) simulations, I created the lens and source galaxy catalogues that mimic the fourth data release of the Kilo-Degree Survey (KiDS-1000) data. With these mocks, I tested, validated and calibrated the model. Afterwards, I tested the calibrated model with the independent Scinet Light Cone Simulations (SLICS) simulations. As many of the lens catalogues of the SLICS were originally done for me, I also contributed by analysing them to their accuracy.

In B22b, I published the last major project, where I analysed the real KiDS-1000 data using the DSS. While measuring the DSS data vector, I discovered that a subset of the KiDS-1000 tiles demonstrated an offset between the galaxy tile centroids and their corresponding mask centroids. This discovery resulted in a new data release (DR 4.1), which was used for the DSS analysis (and all subsequent KiDS-1000 analyses). Furthermore, I measured the covariance matrix using the FLASK simulations (Xavier et al., 2016). I implemented an inference pipeline, which can predict converged posterior distributions within a minute, by running Markov chain Monte Carlo (MCMC) samplers on a graphics processing unit (GPU) using the CosmoPower emulator (Spurio Mancini et al., 2022). In this work, I also tested the robustness of the DSS model concerning baryonic feedback processes, intrinsic alignment (IA), the assumption of the linear galaxy bias, the shape of the lens galaxy redshift distribution, and the impact on the posterior if the covariance matrix is changed with cosmological parameters. Finally, after these validation steps, I analysed the KiDS-1000 data. Additionally, I split the bright sample of the KiDS-1000 release (KiDS-bright) sample into red and blue galaxies and analysed them jointly.

Besides the central DSS project, I also contributed to other works during my PhD, which I will summarise next.

The most significant additional contribution was in the work of Heydenreich et al. (2022b). This work performs a cosmological parameter analysis with third-order cosmic shear using the shear three-point correlation functions Γ_i and the third-order aperture statistics $\langle M_{\rm ap}^3 \rangle$. My first contribution to this work was to measure a $\langle M_{\rm ap}^3 \rangle$ KiDS-1000-like covariance matrix and data vector using the T17 simulations. This covariance and data vector were used for the key figure, which forecasts the constraining power of second-order aperture statistics, third-order aperture statistics and their combination. My second contribution to this work was that I implemented the inference pipeline to measure the posterior distributions using the CosmoPower emulator, which enabled the determination of MCMC chains on a GPU within several minutes. Lastly, I wrote those parts of the paper that I also analysed. In a companion paper by Linke et al. (in preparation), which develops an analytic description of the covariance matrix of the third-order aperture statistic $\langle M_{\rm ap}^3 \rangle$, the T17-covariance matrix is used as a reference with which the analytic covariance matrix should agree. Furthermore, the inference pipeline used for Heydenreich et al. (2022b) is also used in Linke et al. (in preparation) to compare the constraining power of different covariance matrices.

In another side project, I contributed in Heydenreich et al. (2022a). The idea of this project, which is similar to peak statistics (Harnois-Déraps et al., 2021) or Minkowski functionals (Shirasaki and Yoshida, 2014), is to cut off an aperture mass map at a certain threshold and count the number of holes and connected components. By varying the threshold and keeping track of when these features are 'born' and 'die', it is shown in Heydenreich et al. (2021) that persistent Homology is at least as informative, if not better than the peak statistics. My contributions to this paper are many statistical notes regarding the evaluation during the weekly meetings, the measurement of two-point statistics for comparison with the persistent homology statistics, and partial writing of the paper.

As further side project, I implemented python modules for CosmoSIS (Zuntz et al., 2015), that can read in the power spectrum emulator CosmoPower. CosmoSIS is a modular cosmological parameter estimation tool used for many state-of-the-art analyses (Asgari et al., 2021; Heymans et al., 2021). Using CosmoPower instead of Camb (Lewis et al., 2000) reduced the run-time to predict the power spectrum from ~ 2.1 s to ~ 0.04 s. The publication Johnston et al. (in prep) uses these modules to improve their analysis, which the previous runtime of Camb prevented. Also, I have already implemented Python modules that calculate power spectra of the halo model from CosmoSIS, which in turn will be used to train CosmoPower.

The last project, which resulted in a presentation at a KiDS busy week, is a simulation-based inference using convolutional neural networks (CNN). The CNN is trained on $M_{\rm ap}$ maps measured from the cosmo-SLICS, which have several different cosmologies. The overall idea was that the CNN could learn features in the $M_{\rm ap}$ maps that are correlated with cosmological parameters. Although I achieved some exciting results, the feasibility of using a CNN is highly correlated with the number of training sets, which will significantly increase for the next generation of surveys like Euclid or LSST.

Acknowledgement

This whole work would not have been possible without the help of many who contributed scientifically and mentally. Independent of their contribution, I am grateful for all their support on the way to my PhD.

The greatest contribution to this thesis was doubtless from my supervisor Prof. Dr. Peter Schneider. Although a long time during my PhD happened in isolation due to the Covid-19 pandemic, we discussed my project in weekly meetings and, if needed, even in between. In all these numerous meetings, Peter not only supported me with a lot of scientific help but also encouraged me to accomplish things I did not think I could do myself. Furthermore, I am also grateful for the opportunity of tutoring, which helped me to understand the material of astronomy and astrophysics in a new level of detail. Peter also encouraged me to apply for the German National Academic Foundation scholarship. I am very grateful for their support for a whole year.

Next, I would like to thank Prof. Dr. Hendrik Hildebrandt. He introduced me to the Kilo Degree Survey (KiDS) team. Besides the many friends and colleagues I found at the Argelander Institut of Astronomy (AIfA), the KiDS team always felt like my big scientific family. Especially the meetings held twice a year (even if some were only remote) always motivated me to deliver the best results and helped me to stay positive even in difficult times. Hendrik also supported me with a lot of scientific advice during my master's and PhD. An immense contribution is also made by Joachim Harnois-Déraps. During all the years, he always helped with any kind of questions that came to mind and provided me with all the necessary simulations that were of invaluable importance for my work. KiDS member Jan Luca van den Busch is especially important to me. Apart from the fact that I could always discuss any scientific question with him, no matter how stupid, he also became a very good friend with whom I spent many board game evenings. I want to thank also all other KiDS members regardless if they made a scientific impact on my work.

Special thanks to Oliver Friedrich because we met every two weeks to discuss all my projects for almost two years. He helped me with numerous assistance to modify his analytical model. Similar to Peter, he also motivated me to solve problems that seemed unsolvable to me at first.

During my time at AIfA, I met many interesting colleagues who increased my productivity and provided a harmonious work environment. Sandra Unruh is particularly noteworthy. She guided me through my first steps and helped me with all the stupid and naive questions (even at inappropriate times) a young scientist has. Laila Linke and Sven Heydenreich have also been of great importance to me, as they both attended the weekly meetings with Peter Schneider and contributed interesting ideas that improved my work. I am also very grateful for the occasional

gatherings organised by Sven, which contributed a lot to team building inside the AIfA. I also would like to thank all other members of AIfA, who are not mentioned by name here. This also includes the technical support team, which has made it possible for me to use (except on hot days with more than 30 degrees) highly functional computing resources. Here I would like to highlight Andreas Bödewig, who helped me throughout the years with every technical issue.

Abschließend möchte ich mich bei meiner Familie und meinen Freunden bedanken, auch wenn sie nur indirekt zu dieser Arbeit beigetragen haben. Sei es das Korrekturlesen englischer Texte, lustige Spieleabende oder die Ablenkung durch Sportarten wie Tennis oder Tischtennis. Diese ganzen Leistungen wären ohne Euch nicht möglich gewesen.

Besonders bedanken möchte ich mich hier allerdings bei meinen Eltern und meiner Frau Marie. Ohne meinen Vater Karl hätte ich wahrscheinlich nicht einmal eine wissenschaftliche Laufbahn eingeschlagen, denn er hat mich schon früh für die Naturwissenschaften begeistert. Und nicht nur das, er hat mir die Mathematik in vielen, manchmal etwas lauten, Sitzungen näher gebracht als jeder andere Lehrer oder Professor in meinem Leben. Dafür werde ich ihm auf ewig dankbar sein. Außerdem möchte ich mich nochmal bei Ihm bedanken, dass er seine komplette Freizeit meiner sportlichen Karrier geopfert hat und mich als Jugendlicher in ganz Deutschland herumgefahren hat. Das ist absolut keine Verständlichkeit, was ich damals noch nicht zu würdigen wusste. Dankbar bin ich auch für meinen Vater Michi, der einen großen Anteil daran hatte, dass ich der Mensch geworden bin, der ich heute bin. Wie Karl hat auch er mich in allen möglichen Dingen unterstützt und fasziniert. Die Aufzählung wäre hier sehr lang, aber sehr wichtig für mich ist, dass er mir wie kein anderer das handwerkliche Geschick beigebracht hat. Erst neulich haben wir ein ganzes Haus gebaut. Natürlich darf ich meine Mutter nicht vergessen, denn sie war und ist die Person, die das größte Vertrauen in mich hat. Dieses Vertrauen ist von unschätzbarem Wert, denn es gab mir die Kraft, weiterzumachen und den Glauben daran, meine Ziele zu erreichen. Übrigens waren die leckeren Pflaumenkuchen immer eine große Hilfe, auch wenn ich sie erst um Mitternacht nach getaner Arbeit essen konnte. Ich weiß, dass sie es nicht immer leicht mit mir hatte, was meine Dankbarkeit ihr gegenüber nur noch vergrößert.

Abschließend möchte ich noch ein paar Worte an meine Frau richten. Ich weiß, dass ich manchmal nicht der einfachste Mensch der Welt bin und ziemlich stur sein kann. Aber ich liebe dich über alles und bin unendlichdankbar Dankbar, dass du mir mehr Toleranz gelehrt und meine Blick auf die Welt verändert hast. Ohne dich hätte ich niemals mit dem Studium der Physik und auch Astrophysik begonnen und wäre heute sicherlich ganz woanders.

Obwohl ich noch weiter gehen und mehr Geschichten erzählen könnte, werde ich hier aufhören und mich auf die vor mir liegende Reise mit Euch allen freuen. Meine letzten Gedanken gelten meinem Vater und meinem Großvater, die während meines Studiums verstorben sind. Papa und Opa, ich werde euch immer vermissen.